



Norwegian  
Meteorological  
Institute

**METreport**

No. 3/2021

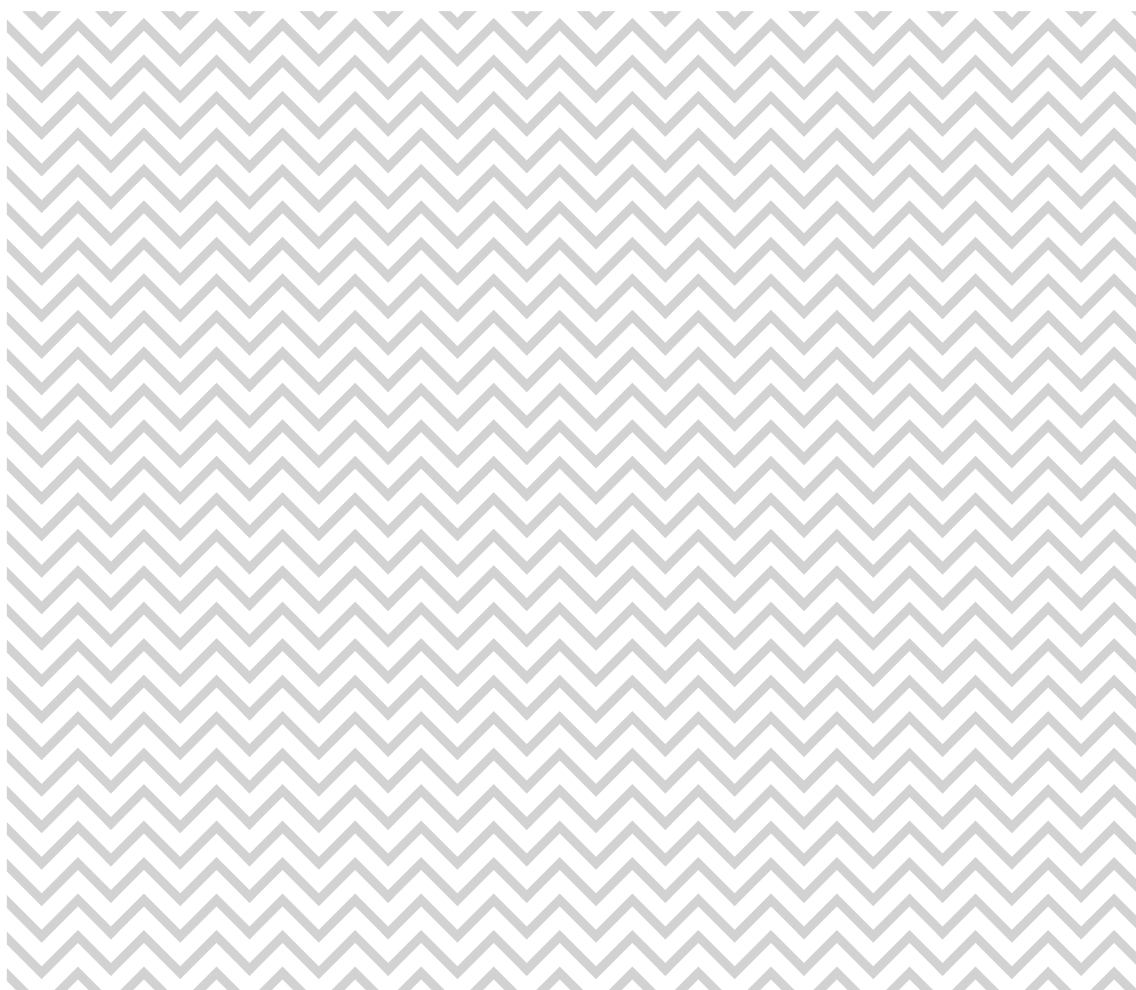
ISSN 2387-4201

Oceanography

# **Wave conditions in Sulafjorden, Vartdalsfjorden, Halsafjorden and Julsundet**

Fjordcrossing E39

Birgitte R. Furevik and Ole Johan Aarnes





Norwegian  
Meteorological  
Institute

# METreport

<b>Title</b> Wave conditions in Sulafjorden, Vartdalsfjorden, Halsafjorden and Julsundet	<b>Date</b> July 21, 2021
<b>Section</b> ...	<b>Report no.</b> 3/2021
<b>Author(s)</b> Birgitte Rugaard Furevik & Ole Johan Aarnes	<b>Classification</b> <input checked="" type="radio"/> Free <input type="radio"/> Restricted
<b>Client(s)</b> Statens Vegvesen	<b>Client's reference</b> Magne Gausen, Jørn Arve Hasselø
<b>Abstract</b> <p>This report presents an overview of wave conditions in Sulafjorden, Vartdalsfjorden, Julsundet and Halsafjorden, Norway, based on 13+ years of hindcast model simulations with the wave model SWAN. The work is performed in connection with planning of fjord-crossings in the Coastal Highway E39 project in mid-Norway. Spatial variations in wave conditions are addressed as well as calculations of extreme values of significant wave height and the joint distribution of significant wave height and peak period, joint statistics (scatter diagrams) of significant wave height and peak period/wind, and a description of wave spectral shape over frequency and direction for all buoy locations. An analysis of historical storms and extreme events is included to support the extreme value calculations in Sulafjord. The general quality of the hindcast data sets with SWAN is assessed by comparing with observations from buoys deployed by the Norwegian Public Roads Administration (NPRA) and results of the analyses are compared to the observations throughout the report.</p>	
<b>Keywords</b> significant wave height, peak period, mean wave period, wind speed, return value estimates, scatter diagrams, wind roses, wave roses, SWAN, NORA10	

---

Disciplinary signature  
Øyvind Breivik

Responsible signature  
Øyvind Breivik

## Abstract

This report presents an overview of wave conditions in Sulafjorden, Vartdalsfjorden, Julsundet and Halsafjorden, Norway, based on 13+ years of hindcast model simulations with the wave model SWAN. The work is performed in connection with planning of fjord-crossings in the Coastal Highway E39 project in mid-Norway. Spatial variations in wave conditions are addressed as well as calculations of extreme values of significant wave height and the joint distribution of significant wave height and peak period, joint statistics (scatter diagrams) of significant wave height and peak period/wind, and a description of wave spectral shape over frequency and direction for all buoy locations. An analysis of historical storms and extreme events is included to support the extreme value calculations in Sulafjord. The general quality of the hindcast data sets with SWAN is assessed by comparing with observations from buoys deployed by the Norwegian Public Roads Administration (NPRA) and results of the analyses are compared to the observations throughout the report.

# Contents

<b>1 Summary</b>	<b>6</b>
<b>2 Scope of report</b>	<b>8</b>
<b>3 Data</b>	<b>10</b>
3.1 Wind/wave forcing - NORA10 . . . . .	10
3.2 Wind input - WRF / NORA10 . . . . .	12
3.3 Wave model - SWAN . . . . .	12
3.4 Measurements . . . . .	16
<b>4 Point statistics</b>	<b>19</b>
4.1 Validation . . . . .	19
4.2 Frequency tables / scatter plots . . . . .	24
4.2.1 Significant Wave Height vs Peak Period . . . . .	24
4.2.2 Significant Wave Height vs Wind Speed . . . . .	24
4.3 Contours - $H_s/T_p$ . . . . .	27
4.4 Spectral shape . . . . .	30
4.5 Return Value Estimates . . . . .	39
4.5.1 Recommendation . . . . .	44
<b>5 Spatial statistics</b>	<b>47</b>
5.1 Transects . . . . .	47
5.2 Return value estimates . . . . .	56
<b>6 Selected storms</b>	<b>60</b>
<b>7 Appendix</b>	<b>73</b>
7.1 Extreme statistics . . . . .	73
7.1.1 Generalized Extreme Value Distribution . . . . .	73
7.1.2 Generalized Pareto Distribution . . . . .	74
7.1.3 Weibull Distribution . . . . .	75
7.1.4 Fitting procedure . . . . .	76
7.1.5 LoNoWe - Joint distribution of $H_s$ and $T_p$ . . . . .	76
7.2 Validation plots . . . . .	77

7.3	Return value plots . . . . .	83
7.4	Spectral characteristics . . . . .	87
7.4.1	Three highest $H_s$ cases . . . . .	100
7.5	Frequency tables . . . . .	107
7.5.1	Significant Wave Height vs Peak Period . . . . .	107
7.5.2	Significant Wave Height and Wind Speed . . . . .	142
7.6	Validation NORA10 . . . . .	146
<b>References</b>		<b>151</b>

# 1 Summary

This report describes the wave conditions in Breisundet, Sulafjord, Vartdalsfjord, Julsundet and Halsafjord as input to the planned fjord crossings along the coastal highway E39 in mid-Norway. Based on a 13-year hindcast we present extreme value analysis of significant wave height and joint distribution of significant wave height and peak period, frequency tables (scatter diagrams) of significant wave height and peak period/wind, variation in wave conditions along the possible fjord crossings and a description of wave spectral shape over frequency and direction. The general quality of the hindcast data set is assessed against observations from buoys deployed by the Norwegian Public Roads Administration (NPRA) and results of the analyses are compared to the observations throughout the report.

In general, the model has a positive bias in Sulafjord and Halsafjord, but the maximum values in the outer part of Sulafjord are lower than observed. In Vartdalsfjord the model overestimates the wave conditions. With regard to extreme values, we have emphasized on analysing the uncertainty by focusing on historical storms and re-sampling (bootstrap) both measured and modelled time series.

Based on observations alone, we get 100-year return values of 6m and 3.6m at location A and B in Sulafjord, 2.3m at location C, 2.5m at location F in Vartdalsfjord and 1.8m at location G in Halsafjord. In accordance with the validation referred to above, return values based on model data concurrent with the observation period is only slightly lower at A (5.7m), very similar at B, and higher at C, F and G. When we extend to the 13-year data set, the return values are reduced for all sites. This indicates that the measurement period (2016-2020) was relatively stormy compared to the full hindcast period (2007-2020). We get 5.3m and 3.5m with a confidence interval considering all methods of 4.6 - 5.4m and 3.2 - 3.7m at A and B, respectively. Based on an analysis of storm situations from the NORA10 hindcast period 1957-2020, we define and run SWAN for an extreme, yet realistic, scenario in Sulafjord. This experiment yields a result of  $H_s$  5.6m at A and 4.1m at B.

Preferably, the hindcast should be extended to a minimum of 30 years to obtain a more solid climatology and more reliable 100-year return value estimates. At present this is not possible, because we lack the wind input to run SWAN for such a time period. An attempt to use winds from the offshore hindcast NORA10 was made, but resulted in underestimation of significant wave height at several locations. Therefore, this solution

was abandoned. However, the data set (20 years) and model setup was useful for the study and provides re-runs of historical storms in this report.

The wave conditions across the outer fjord-crossing (at A), and in particular the inner crossing (at B) of Sulafjord, are quite inhomogeneous. The difference from west to east during the 1% highest storms is 1m in significant wave height at the inner crossing (B). In this study we have not focused on swell intrusion inwards in the fjords, i.e. we have not performed partitioning of the wave spectra - separating windsea and swell. However, based on the observed peak period, swell up to 8s is observed in Vartdalsfjord (at F) and peak periods up to 10-12s in Halsafjord. For Halsafjord, the model seems to have too little reduction of swell inwards the fjord, indicating peak periods of up to 16s. At location F, the modelled wave climate is mainly windsea dominated, probably due to the strong wind forcing in this area.

Generally, wave spectra at location A conform to a JONSWAP spectrum for windsea dominated cases (high  $H_s$ ) with  $\gamma$  of 1.1 – 1.5. The two-peaked Torsethaugen spectrum provides a better fit for swell dominated cases and very young windsea cases (moderate  $H_s$ ). Both cases are probably a mix of equally large peaks of windsea and swell. At location C, and partially at location B, the sea state is often more complex, indicating bi-modal spectra closer to Torsethaugen.

## 2 Scope of report

Coastal Highway E39 is crossing several wide fjords on the west coast of Norway between Kristiansand and Trondheim where the ferry crossings are considered replaced by fixed road connections such as floating bridges, suspension bridges with floating or fixed towers or submerged tunnels. Several of the possible constructions are sensitive to waves and wave conditions are necessary to consider during a construction phase. This work is performed in order to investigate the wave conditions in Sulafjord, Vartdalsfjord, Julsundet and Halsafjord in collaboration between the Norwegian Public Roads Administration (NRPA) and the Norwegian Meteorological Institute (MET). The report provides a general documentation of the wave conditions and includes point wave statistics as well as some spatial analyses.

For offshore areas, MET has developed a high-quality wind and wave hindcast NORA10 Reistad et al. [2011]. NORA10 is a downscaling of ERA-40 using High Resolution Limited-Area Model (HIRLAM) and the Wave Model WAM both on a 10 km grid covering the Nordic Seas. While 10 km resolution is insufficient in coastal areas, NORA10 provides excellent boundary spectra for fine-scale wave modelling along the Norwegian Coast. By applying the wave model Simulating waves Nearshore (SWAN), wave hindcasts for Sulafjord, Vartdalsfjord, Julsundet and Halsafjord has been conducted. The wave model setup is run with boundary spectra from NORA10 and surface wind input from Kjeller Vindteknikk/Norconsult (KVT) using the mesoscale atmosphere model WRF on 500m x 500m grid. WRF winds are available for over 13 years (January 2007- February 2020) in Sulafjord, Vartdalsfjord and Julsundet and in Halsafjord (January 2007 - July 2020). WRF winds and NORA10 spectra were used to run SWAN in a nested setup with 1 km and 250 m grid resolution. Results from this data set were reported (2007-2017), but not validated, in Harstveit et al. [2018].

The model data set is described in chapter 3 and validated against observations in section 4.1. Analysis of wave parameters useful for planning fjord crossings are presented in the following sections, primarily based on the model data, but supported by the observations (frequency tables,  $H_s/T_p$  contours, analysis of spectral shape and return value estimates). Spatial statistics like transects of significant wave height ( $H_s$ ) and peak period ( $T_p$ ) and maps of return value estimates of  $H_s$  are included in chapter 5. Summary of the most extreme storms in the data sets: NORA10, SWAN and observations, is provided in chapter 6.

The chapters summarise results and show examples of results from some locations, while plots from all locations are included in the Appendix. A description of the extreme statistics applied to obtain return value estimates are also presented in the Appendix.

## 3 Data

### 3.1 Wind/wave forcing - NORA10

NORA10 (Norwegian Reanalysis 10 km) is a well recognized atmospheric and wave hindcast produced at the Norwegian Meteorological Institute (MET). The three-dimensional atmospheric model HIRLAM is run with 10 km resolution to downscale global reanalysis ERA40 [Uppala et al., 2005] and operational data from the European Centre for Medium-Range Weather Forecasts (ECMWF). The wave model, WAM, is set up on the same 10 km grid as the atmospheric model. Boundary values are provided by a coarser (50km grid) wave model covering the North Atlantic and adjacent seas. The NORA10 hindcast data are in good agreement with measurements, examples from Ekofisk and Heidrun platforms are shown in figure 1. In figure 113 and 114 a comparison of significant wave height and peak period at Ami, Heidrun, Draugen, Gullfaks, Sleipner and Ekofisk over the period 2002-2011 is presented. For more details on the hindcast archive and validation against measurements see Reistad et al. [2007, 2011]. In the following, two-dimensional (frequency, direction) wave spectra from NORA10 is used as boundary conditions for the SWAN-simulations.

The original 10m wind speeds ( $U_{10}^{org}$ ) from NORA10 are considered weak for the highest percentiles and are often calibrated by adding an extra 20% to the excess wind speed of 15 m/s:

$$U_{10} = U_{10}^{org} + 0.2 \times (U_{10}^{org} - 15), \quad \text{for } U_{10}^{org} > 15 \text{ m/s} \quad (1)$$

Figure 115 illustrates calibrated NORA10 wind speed at 5 locations, similar to fig. 113, validated wind speed obtained at 5 locations. Offshore wind speed measurements are based on the original wind speeds obtained at measuring height, reduced to 10m using the wind profile recommended in DNVGL [2017]. Wind speed from NORA10 is used in chapter 6 as input to SWAN, but without calibration.

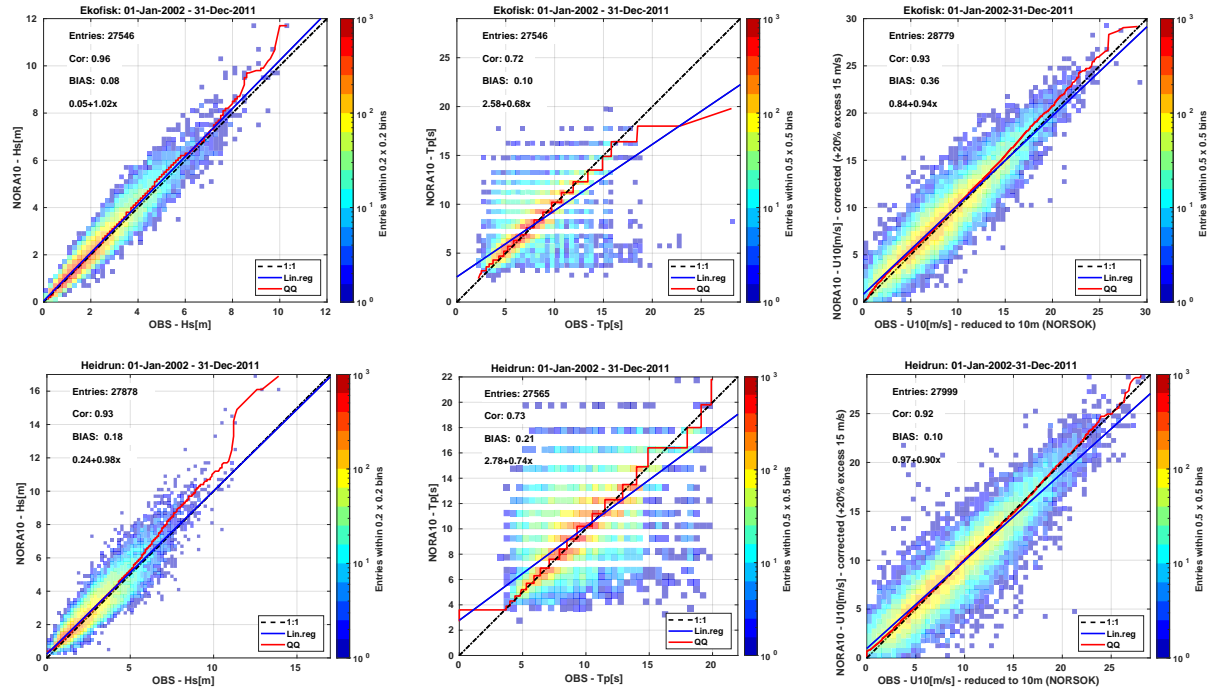


**Figure 1:** NORA10 validated against observations at Ekofisk (top) and Heidrun (bottom) over the period 2002-2011 -  $H_s$  (left),  $T_p$  (center) and wind speed (right). Wave observations are based on 20-min periods, while wind speeds are taken over a 10 minute - both sampled every three hours, at corresponding hours with NORA10. Wind measurements are reduced to 10 m from rig height and NORA10 winds are adjusted according to eq. 1. More validation of NORA10 is presented in appendix.

### **3.2 Wind input - WRF / NORA10**

The Weather Research and Forecasting (WRF) numerical weather prediction model is run by Kjeller Vindteknikk/Norconsult (KVT) to downscale the global ERA interim reanalysis down to 500 m grid spacing for Storfjorden (Sulafjord/Vartdalsfjord) and Halsafjorden [Christakos et al., 2020]. 10 m wind from WRF is used as input to a nested setup with an outer domain of 1 km x 1 km and two inner domains (for Storfjord, including Vartdalsfjord and Sulafjord, and for Julsund) with 250 m x 250 m grid (in Storfjord this corresponds to the SWAN-WRF0.5 setup in Christakos et al. [2020]) and similar for Halsafjord. Wind input is available for January 2007 to February 2020 for Sulafjorden (including Vartdalsfjorden and Julsundet) and to July 2020 for Halsafjorden. These data sets are default in this report, or referred to as SWAN, SWAN250 or SWAN-WRF.

Since WRF only covers 13 years, a additional setup with SWAN for Sulafjord on 150 m x 150 m with both winds and boundary spectra from NORA10 was run for 20 years (1999 - 2018) and for additional historical storms in 1977, 1988 and 1992. The winds from NORA10 are the original HIRLAM winds, i.e. not calibrated. In this setup, SWAN is run without nesting. This setup is only used in chapter 6 and is referred to as SWAN150. The different domains are compared in the map in figure 2.

### **3.3 Wave model - SWAN**

SWAN is a phase-averaged wave model especially developed for shallow water and coastal areas. It is a so-called third generation wave model which defines the latest generation of operational wave models. SWAN simulates the development of the two dimensional (2D) wave spectrum in time and space, which is mainly controlled by three source terms; wind input, wave dissipation and non-linear wave interaction.

In this study the model is set up with a spectral resolution of 35 frequency bands (0.04 - 1.0 Hz) and 36 directional sectors, i.e. 10° resolution. The spatial resolution is 250 m. Due to the implicit numerical scheme of SWAN, the model is not subject to the Courant criterion of numerical stability. So, we use a time step of 10 min, and store model output every hour.

Figure 3 shows the model domains with the applied bathymetry (<http://www.emodnet-bathymetry.eu/>), covering both offshore and inshore areas. The model is run with nesting, i.e, it is set up with an outer domain with 1 km grid spacing, providing boundary conditions (2D wave spectra every hour) to two inner domains for Julsundet and Sulafjorden with grid

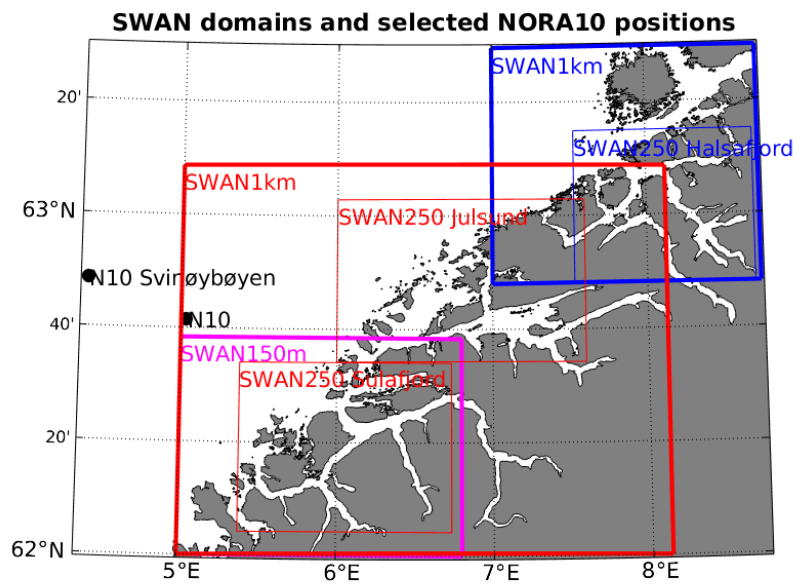


**Figure 2:** Boxes showing the SWAN domains. SWAN250 for Sulafjord and Julsund is a nested setup from a grid spacing of 1km x 1km to 250m x 250m using WRF winds (red domains). SWAN250 for Halsafjord is a similar nested setup (blue domains). SWAN150 has a grid spacing of 150m x 150m (no nesting) and is using NORA10 winds. All receive NORA10 2D wave spectra along the open boundaries. The two positions from NORA10 (points in black) are referred to in chapter 6.

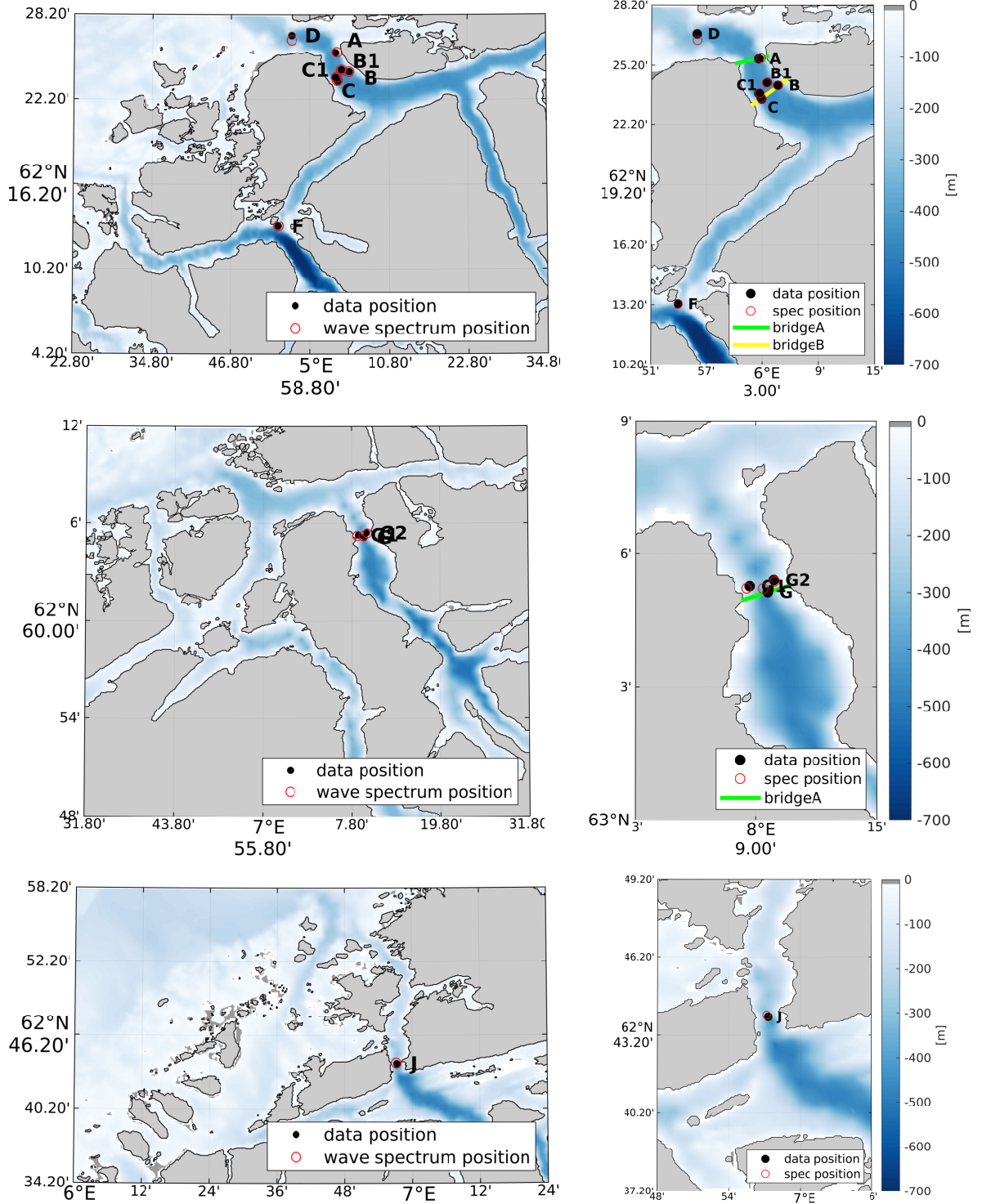


**Figure 3:** SWAN250 inner model domains and the corresponding bathymetry (<http://www.emodnet-bathymetry.eu/>). Sulafjorden/Vartdalsfjorden/Halsafjorden/Julsundet; the approximate locations of the available wave buoys and the chosen data positions used herein.

spacing 250m [Christakos et al., 2020]. Realistic offshore conditions are maintained by running the outer model with wave boundary spectra from the WAM (10km) model which constitute the wave part of the NORA10 hindcast [Komen et al., 1994], [Reistad et al., 2011], hereafter denoted as WAM10 or NORA10, depending on the context. Winds are obtained from WRF as described in section 3.2. This potentially leads to some inconsistency between the input wind and waves as WAM10 is forced by the wind part of NORA10 (atmosphere model HIRLAM). A similar nested setup is used for Halsafjord with an outer domain with 1km grid spacing and an inner domain with 250m grid spacing.

A number of wave parameters are available as output from the wave model SWAN, based on the calculated 2D wave spectrum  $E(f, \theta)$  of the model. These are described in the following.

The 2D wave spectrum may be reduced by integrating  $E(f, \theta)$  over all directions,  $\theta$ , or by integrating over all frequencies,  $f$ , where

$$E(f) = \int_0^{2\pi} E(f, \theta) d\theta \quad (2)$$

is known as the 1D frequency spectrum and

$$E(\theta) = \int_0^{1Hz} E(f, \theta) df \quad (3)$$

is referred to as the directional wave spectrum, or  $\theta$ -spectrum. The shape of the 2D wave spectrum may be further simplified by the n-th order moment

$$m_n = \int_0^{\infty} f^n E(f) df \quad (4)$$

In this study we emphasize on the most commonly used integrated parameters, i.e.:

- **Significant wave height** -  $H_{m0}$  or  $H_s$

$$H_{m0} = 4\sqrt{m_0} \quad (5)$$

- **Peak wave period** -  $T_p$ ; defined as the peak frequency of eq. 2.

- **Mean wave period** -  $T_m$  ( $T_{m02}$ )

$$T_{m02} = \sqrt{\frac{m_0}{m_2}} \quad (6)$$

- **Mean wave direction - Mdir**

$$Mdir = \tan^{-1} \left[ \frac{\int_0^{2\pi} \int_0^{\infty} E(f, \theta) \sin(\theta) df d\theta}{\int_0^{2\pi} \int_0^{\infty} E(f, \theta) \cos(\theta) df d\theta} \right] \times \frac{180}{\pi} \quad (7)$$

- **Peak wave direction - Pdir;** defined as the peak direction of eq. 3.

Notice that we use **meteorological convention** throughout the study, i.e., all statistics are presented as *coming from* the direction noted - wind and waves.

The emphasis of this study is to investigate the metocean conditions in the locations that may be relevant for E39 to cross the fjords. These locations are two in Sulafjord (at buoys A and B), one in Vartdalsfjord at buoy F, one in Julsundet (no buoy, but we use a center position which we denote J), and one in Halsafjord (buoy G). However, in Sulafjord and Halsafjord, several other buoys are deployed (described in section 3.4). Therefore point statistics herein will focus on the buoy locations (A-D, F, G) and the center of Julsund, listed in table 1, see figure 3. In these locations, 2D wave spectra every hour are stored from the model.

### 3.4 Measurements

Wind and wave measurements are carried out by Fugro Ocean using SEAWATCH Wavescan buoys. The data are transferred to MET and made available through the MET Norway Thredds Service [Furevik et al., 2016]. Integrated wave parameters, wind speed and direction (4.1 m height) is available every 10 minutes. Raw wave data are provided in separate files and are used to calculate wave spectra [Christakos, 2020]. An overview of the buoys is given in table 1 and in figure 5.

Wave spectra are calculated from the raw data files<sup>1</sup> on thredds. The average wave spectra from B, B1, C and C1 over the winter period 2019/2020 are shown in figure 4. The peak of the spectrum, i.e the energy level, is generally reduced from B to B1 to C1 and to the lowest energy level at C. The location of the peak, the peak frequency, increase from B and B1 to C and C1. Thus the peak wave period is generally reduced the most to C and C1. The peak period at C and C1 is approximately the same.

---

<sup>1</sup>For example [https://thredds.met.no/thredds/dodsC/obs/buoy-svv-e39/2020/01/202001\\_E39\\_A\\_Sulafjorden\\_raw\\_wave.nc](https://thredds.met.no/thredds/dodsC/obs/buoy-svv-e39/2020/01/202001_E39_A_Sulafjorden_raw_wave.nc)

Buoy	Area	Measurement period	Position	Depth
A	Sulafjord	2016.10.13 -	62.4263 6.0447	375
B	Sulafjord	2016.10.13 -	62.4038 6.0806	325
B1	Sulafjord	2019.02.08 -	62.4051 6.0585	445
C	Sulafjord	2017.04.27 -	62.3922 6.0509	445
C1	Sulafjord	2019.02.14 -	62.3964 6.0459	445
D	Breisundet	2016.10.14 -	62.4464 5.9336	345
F	Vartdalsfjorden	2017.11.29 -	62.2208 5.8994	217
G	Halsafjorden	2016.10.18 -	63.0856 8.1575	495
G1	Halsafjorden	2016 - 2019	63.0872 8.1426	
G2	Halsafjorden	2016. - 2019	63.0898 8.1656	
J	Julsund	-		

**Table 1:** Buoy name, area, day of deployment and last day of measurements (- if ongoing), position (degrees latitude and longitude) and depth (m).

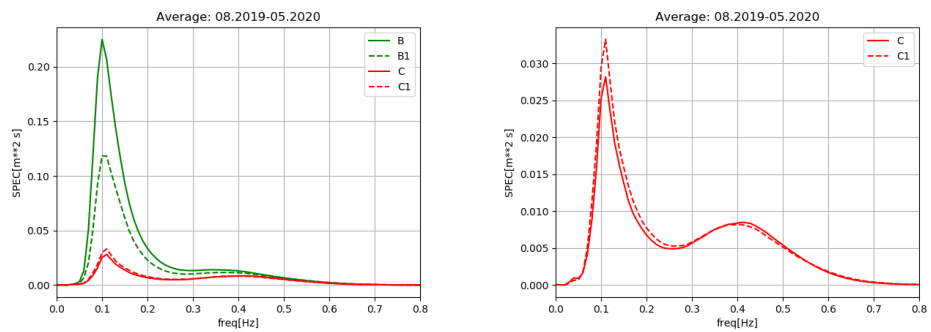


**Figure 4:** Mean observed wave spectra at B, B1, C and C1 (left) and only C and C1 (right) over 10 months.

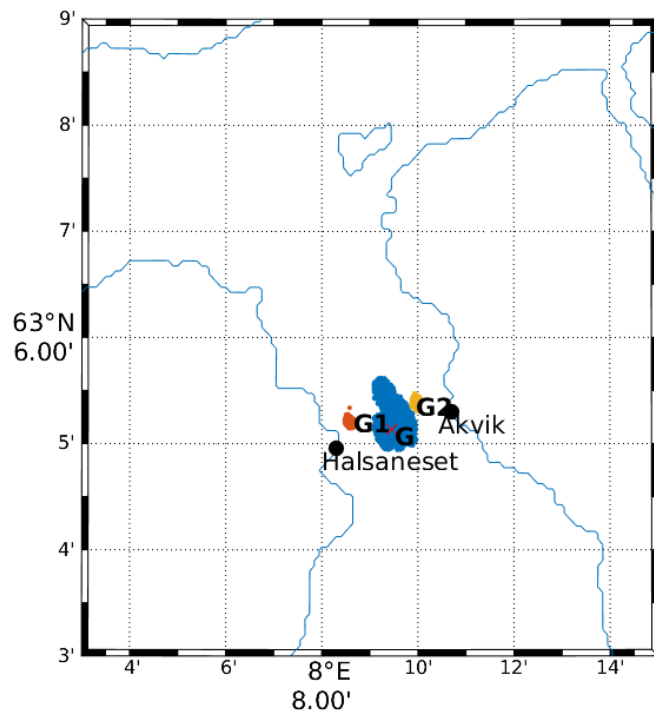
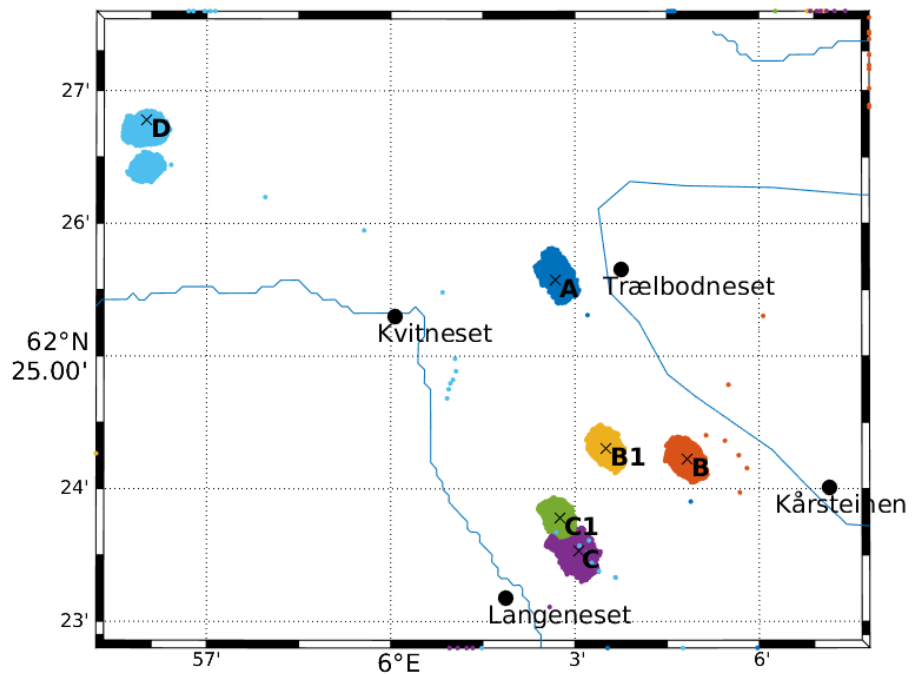


**Figure 5:** Map of Sulafjord (top) and Halsafjord (bottom) with location of the buoys marked with x and the recorded position of the buoys 2016-2020 marked with colors. Land-based masts are marked with black dots.

## 4 Point statistics

The purpose of running a 13 year long hindcast is to obtain a solid climatology - sufficient to capture both normal and extreme events/years. In the following section we present standard plots typically used to describe local wave climate. We focus on scatter plots (frequency tables), describing the joint distribution of different sea state parameters and wind. We further want to assess the spectral shape of the wave energy and the possibility to generalize the sea state into different well-known empirical shapes, i.e. JONSWAP Hasselmann et al. [1973] and Torsethaugen [Torsethaugen et al., 2004]. In the end, return value estimates of significant wave height and  $H_s/T_p$  contours are presented.

Our results and statistics are primarily based on model output, but observations are included to assess the validity of the model estimates. First, we start off with some general model validation.

### 4.1 Validation

The model simulations used herein are validated with various metrics. For better readability, the majority of results are presented in the Appendix. In the following we focus on a few plots to illustrate some of the findings.

The overall model performance is effectively illustrated by regression plots for different parameters. In figure 6 we presents regression plots for significant wave height ( $H_s$ ),  $FF$  (wind speed), peak period ( $T_p$ ) and mean period ( $T_{m02}$ ) at location A. Equivalent plots at location B, B1, C, C1, D, F, G, G1 and G2 are presented in the Appendix (section 7.2) according to the different parameters.

In terms of significant wave height  $H_s$ , one of the main findings is that SWAN overestimates  $H_s$  on all locations. However, the positive bias is small, with a maximum of 19 cm at location B1. For the highest  $H_s$  events, represented by the quantile-quantile line, the situation is somewhat different; SWAN underestimates the highest events at location D, does a good job at location A and becomes increasingly high going into the fjords. At location F  $H_s$  is clearly too high at the high end of the distribution. This characteristic will further influence the accuracy of return value estimates based on SWAN. In general, correlation is high, but decreasing going into the fjords.

Several of the features seen in the validation of  $H_s$  is also apparent in wind speed. Generally, the correlation in wind speed is decreasing going into the fjord. All stations

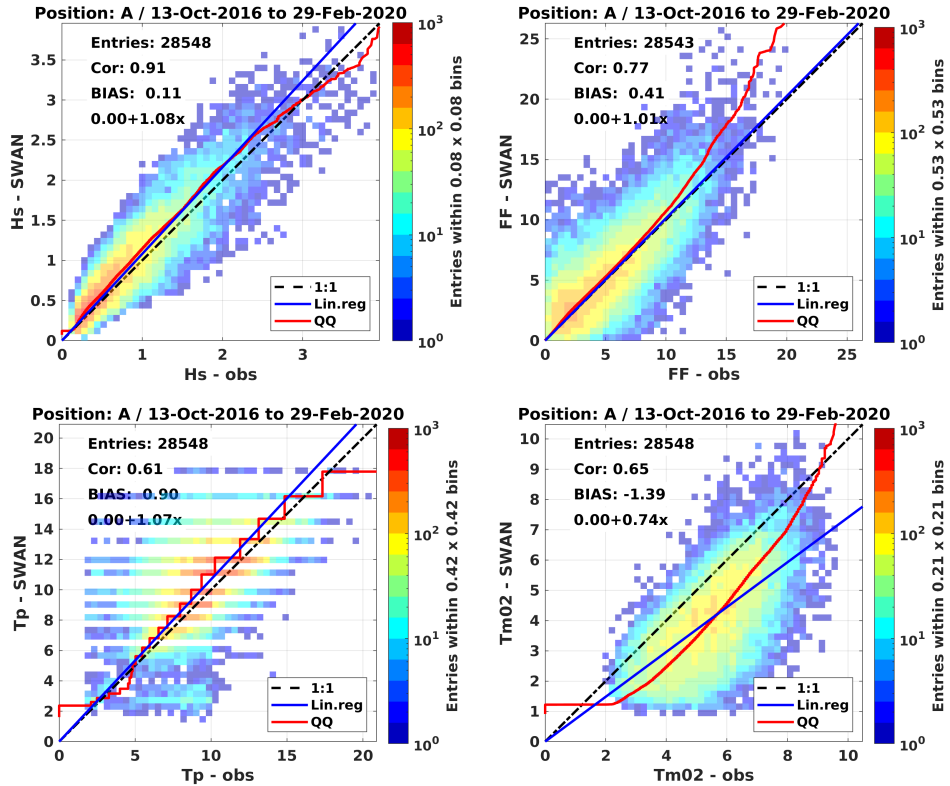


**Figure 6:** Regression plots of  $H_s$  (top left), wind speed at sensor height (top right),  $T_p$  (bottom left) and  $T_{m02}$  (bottom right) at position A; observations (x-axis) and SWAN (y-axis). Validation period is presented in the title, while the number of corresponding data (entries), correlation (cor), bias and regression slope (blue line) is provided in the legend. The quantile-quantile line is given in red.

indicate WRF (model) to be too high at high wind events. This can partly be attributed to the fact that observed wind speed is valid at sensor height, which is approximately 4m above sea level. If observed wind speed had been adjusted to 10m, equivalent to WRF, validation would be nuanced. However, WRF is still likely to be high for extremes and is probably causing SWAN to overestimate  $H_s$  inwards the fjord.

The performance of SWAN is not reaching the same quality as  $H_s$  for the two different wave periods; mean wave period ( $T_{m02}$ ) and peak period ( $T_p$ ), see Appendix (section 7.2). Mean period from SWAN is generally too low (negative bias), although showing improvement at the high end of the distribution. In Halsafjorden,  $T_{m02}$  is clearly showing a split into two populations in the regression plot, one following the 1:1 line (perfect fit), and one where SWAN is low and observed  $T_{m02}$  is increasing. This could indicate that there are instances where more swell penetrate the fjord than indicated by SWAN. Still, these events are likely associated with low  $H_s$  events. In terms of peak period, the validation shows low correlation, which is expected due to the nature of  $T_p$ . As seen for  $T_{m02}$ , there is large scatter in Halsafjorden, where both observed and model indicates the presence of swell, but not at corresponding hours.

The directional distribution of significant wave height and wind speed for Sulafjorden and Halsafjorden is shown in figure 7 and 8; observed and modelled. Overall, both models, SWAN and WRF, perform satisfactory. Waves are primarily following the bathymetry/geometry of the fjord, while winds are more often blowing across the fjord. Still, areas like location F (Vartdalsfjorden) is clearly influenced by the geometry of the fjord.

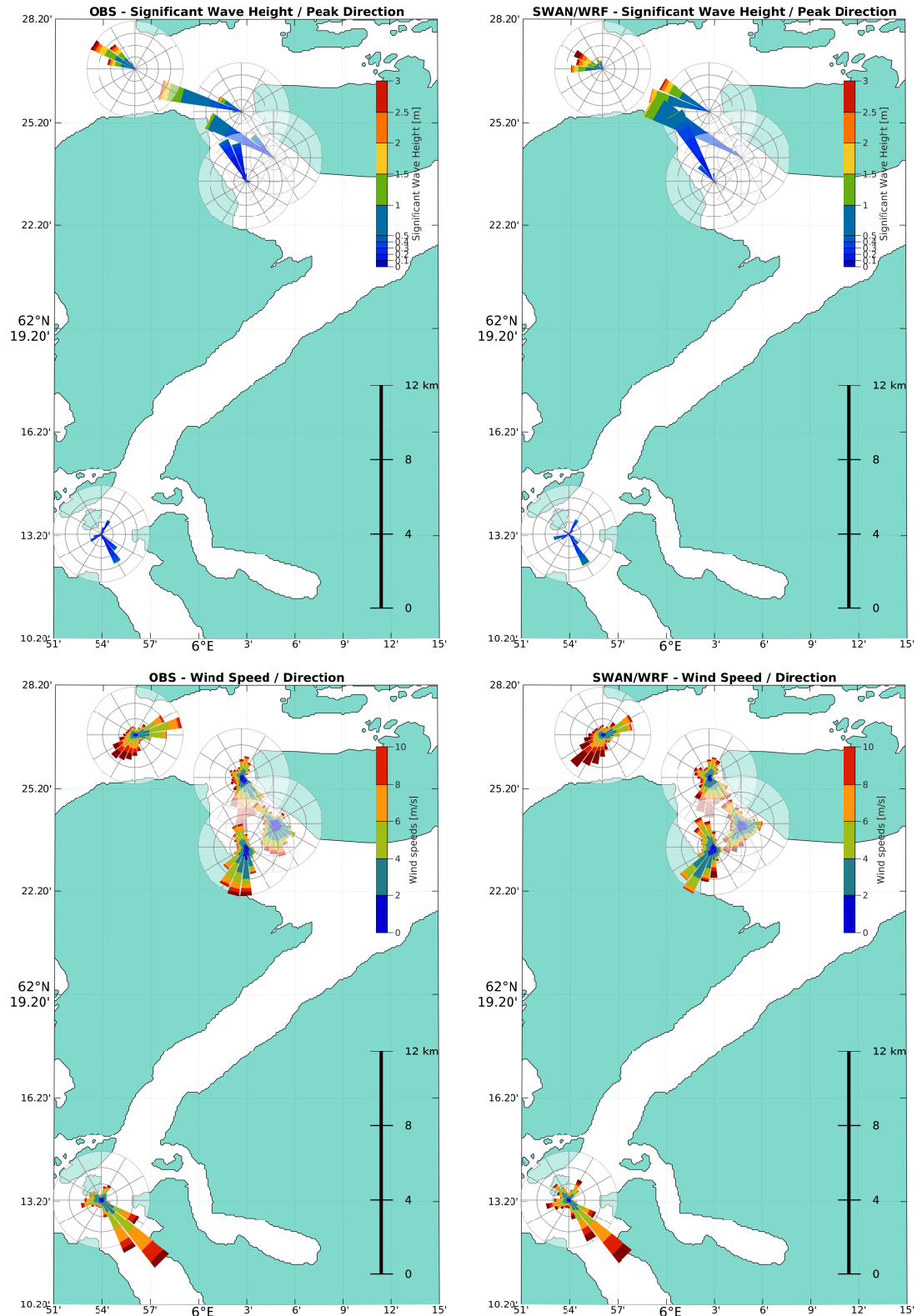


**Figure 7:** Directional distribution of significant wave height (top) and wind speed (bottom) at corresponding hours. Left: Observations. Right: SWAN.

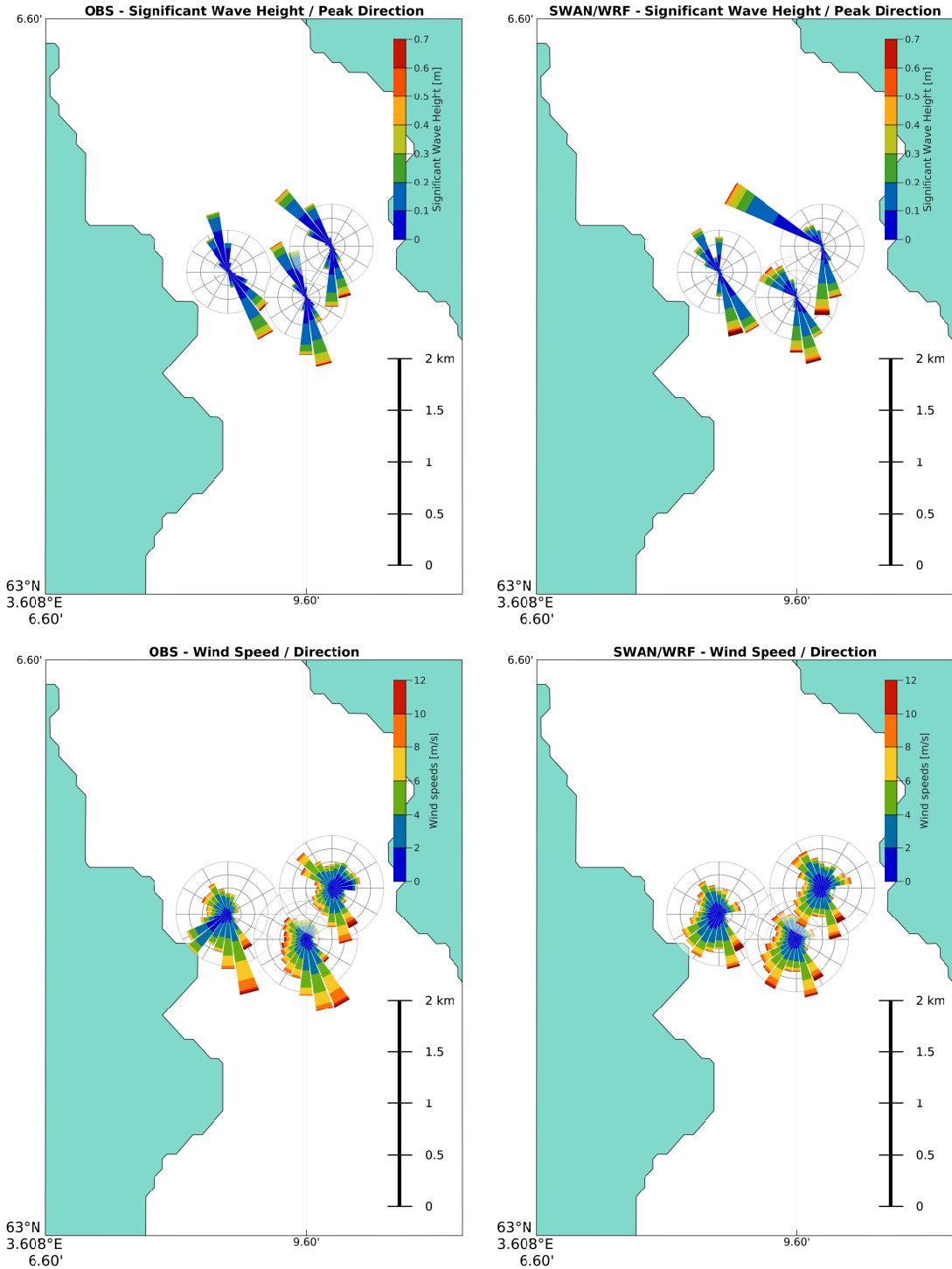


**Figure 8:** Directional distribution of significant wave height (top) and wind speed (bottom) at corresponding hours. Left: Observations. Right: WRF (model).

## 4.2 Frequency tables / scatter plots

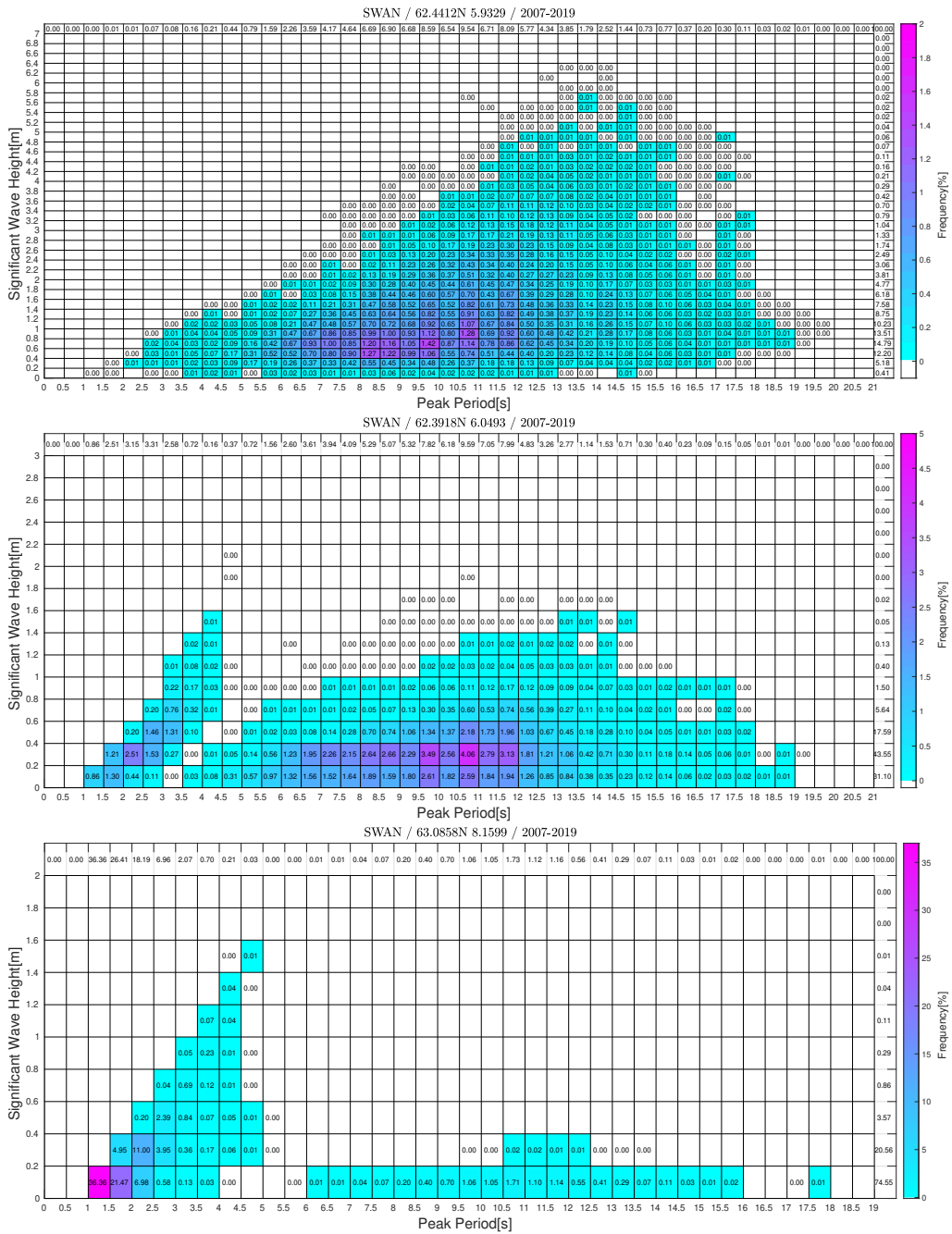
### 4.2.1 Significant Wave Height vs Peak Period

Figure 9 presents frequency tables (aka scatter plots) of corresponding  $H_s$  and  $T_p$  data obtained with SWAN at location D, C and G. The marginal distributions of the respective parameters are found at the far right and the top of the table.  $H_s/T_p$ -bins of pinkish color are the most frequent conditions. Notice that the three sites portray highly different wave climate; location D illustrates a coherent wave climate, where all sea states ( $H_s/T_p$ -bins) link smoothly together. Since location D is exposed to offshore conditions, the sea state will be a mix of local windsea and swell, and often transition from being windsea-dominated to swell-dominated and vice-versa. At location C windsea and swell seem clearly separated into two different populations; steep wave conditions (lower  $T_p'$ s) and sea states of longer wave periods. At location G this becomes even more evident. Still, one should keep in mind that although these plots indicate highly binary conditions, the sea state may very well be a mix of both, even at location G. These conditions are recognized by bimodal wave spectra, where the two peaks are clearly separated.

In the Appendix (section 7.5.1) we present  $H_s/T_p$  frequency tables for all sites, including monthly tables.

### 4.2.2 Significant Wave Height vs Wind Speed

Due to the nature of waves; once generated, waves propagate with or without the force of local wind. Especially in the open ocean, swell is known to move across large distances without much loss of energy. In semi enclosed fjords wave energy is more efficiently damped due to the interaction with bathymetry and coastline. Still, relative high sea states may potentially be accompanied by low winds. As different combinations of wind and waves may have different implications for different types of structures (bridge concepts), coherent wind and wave climate needs to be accounted for. In figure 10 we present frequency tables of wind and  $H_s$  from location D, C and G. In general, all sites show clear correlation between wind speed and wave height. The more uncommon combination of high waves and low winds are most frequent at location D and becomes less apparent inwards the fjord. In the Appendix (7.5.2) we present frequency tables of  $H_s$  and wind speed for all sites.



**Figure 9:** Frequency tables of  $H_s/T_p$  at location D (top), C (middle) and G (bottom).

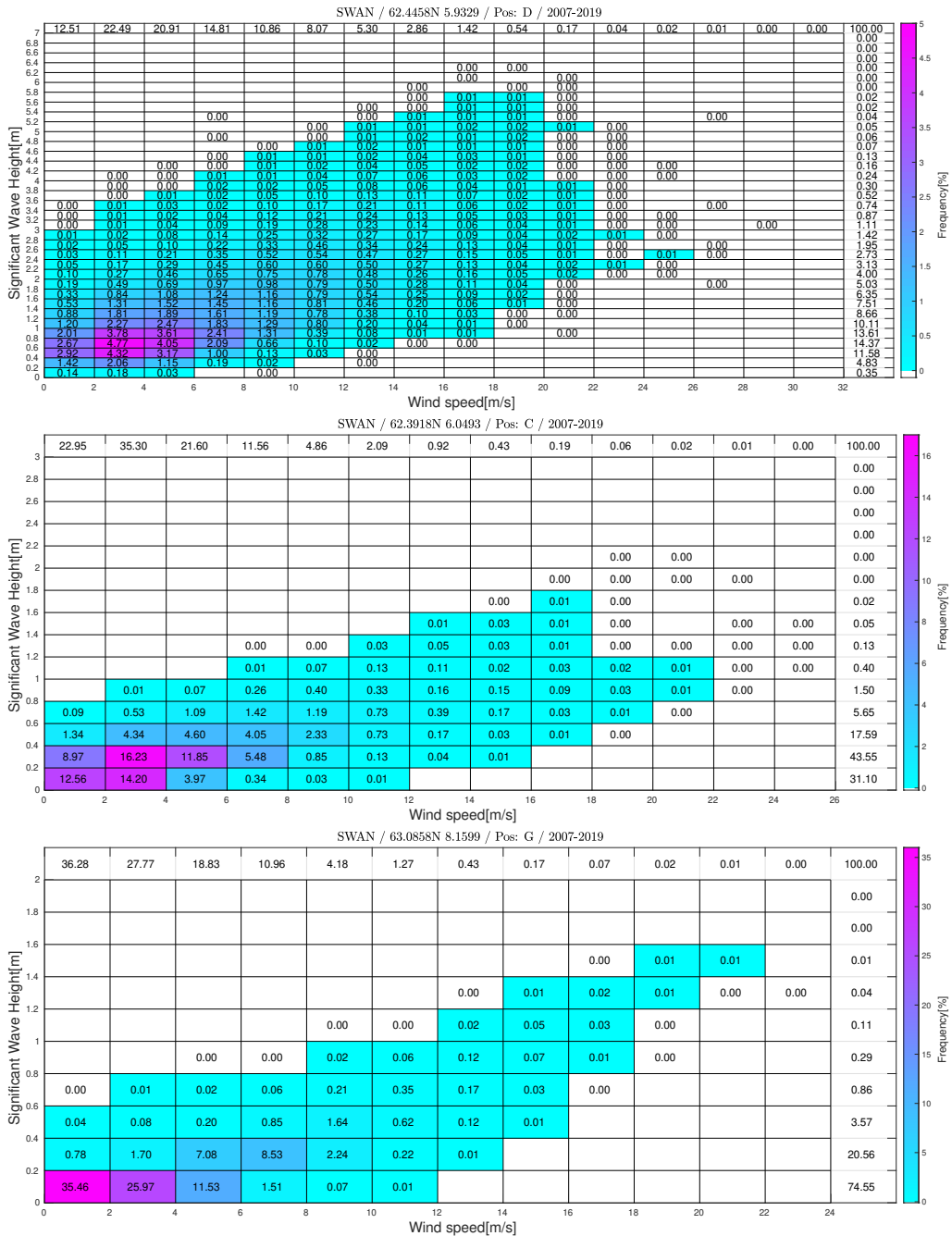


**Figure 10:** Frequency tables of wind speed and  $H_s$  at location D (top), C (middle) and G (bottom).

### 4.3 Contours - $H_s/T_p$

Scatter plots of  $H_s/T_p$  are especially informative for moderate to high sea states. However, in order to describe extreme combinations of  $H_s/T_p$ , joint distributions of  $H_s/T_p$  are needed - often represented by contours enveloping the data. In the following we present both  $H_s/T_p$ -contours fitted to the SWAN-data and scatter plots of  $H_s/T_p$  based on SWAN and observations at corresponding hours. The latter works as validation and is meant to illustrate any shortcomings of the model. The results are presented in figure 11 and 12. Here, the omni 100-year return value contours of  $H_s/T_p$  are presented together with the joint  $H_s$  and  $T_p$  (data). Due to the fact that several locations have two separated populations of  $H_s/T_p$ -data, we have split the analysis into two categories, i.e. swell-dominated or windsea-dominated sea states. For those locations where swell-dominated seas are representing the highest  $H_s$ -cases, the contours are adjusted to correspond to the marginal 100-year return value estimate of  $H_s$  presented in section 4.5. If windsea-dominated seas are representing the highest  $H_s$ -cases, this is done in a similar fashion.

In general, the contours are obtained as follows (see section 7.1.5); first, we find the  $T_p$  estimate corresponding to the 100-year return value of  $H_s$ , given by eq. 30. Second, we establish the joint probability of  $H_s/T_p$  using the 100-year return value of  $H_s$  and the corresponding  $T_p$ . This probability level defines the contour by "cutting through" the joint probability density function (pdf). We also include the steepness criteria defined by DNVGL [2017], i.e.

$$S_p = \frac{2\pi}{g} \frac{H_s}{T_p^2} \quad (8)$$

, where  $S_p = 1/15$  for  $T_p \leq 8$  s and  $S_p = 1/25$  for  $T_p \geq 15$  s and is linearly interpolated between the boundaries. In theory, no sea states are physically possible beyond this steepness limit.

In general, the contours have a poorer fit for low to moderate  $H_s$  and high  $T_p$ , i.e. for less steep wave conditions. For these combinations of  $H_s$  and  $T_p$ , the contours should be used cautiously. This is especially prominent in figure 12; at location F observations clearly indicate intrusion of some longer period waves ( $T_p > 4$ s), which is not reflected in the model, i.e. SWAN has no swell-dominated cases at all. This may be a result of too strong wind forcing, causing local windsea to dominate the sea state in the model. At location G, we see an opposing effect, where the the swell-dominated cases in SWAN is not reduced enough compared to the observations.

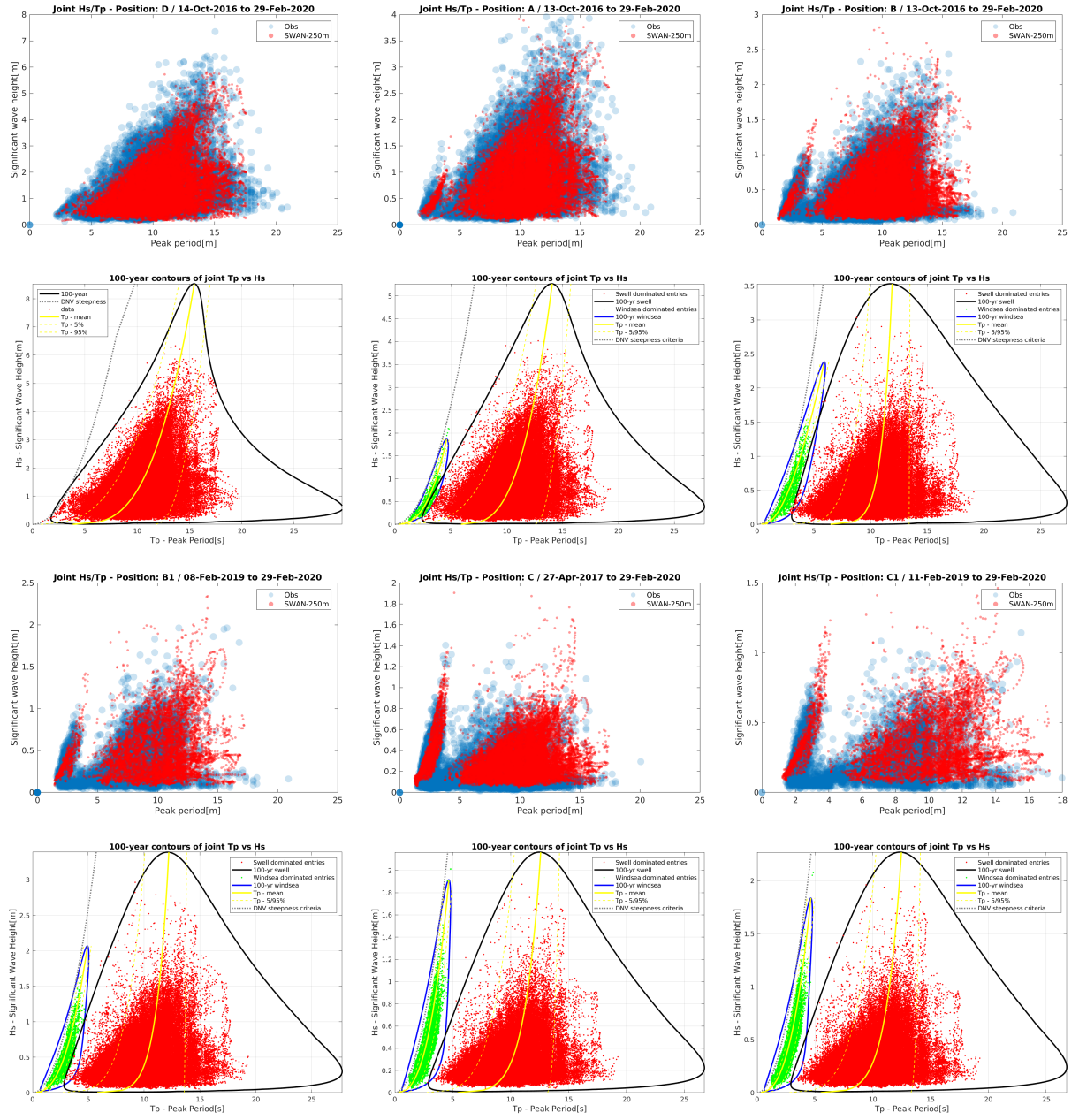


**Figure 11:** Scatter plots of  $H_s/T_p$  (top and second from bottom) at location D, A, B, B1, C and C1 at corresponding hours; SWAN (red) and observations (blue). And, joint  $H_s/T_p$ -contours (second from top and bottom) representing the 100-year return value fitted to SWAN data over the 13 year period. Notice that windsea-dominated cases are illustrated by green dots and corresponding contours.

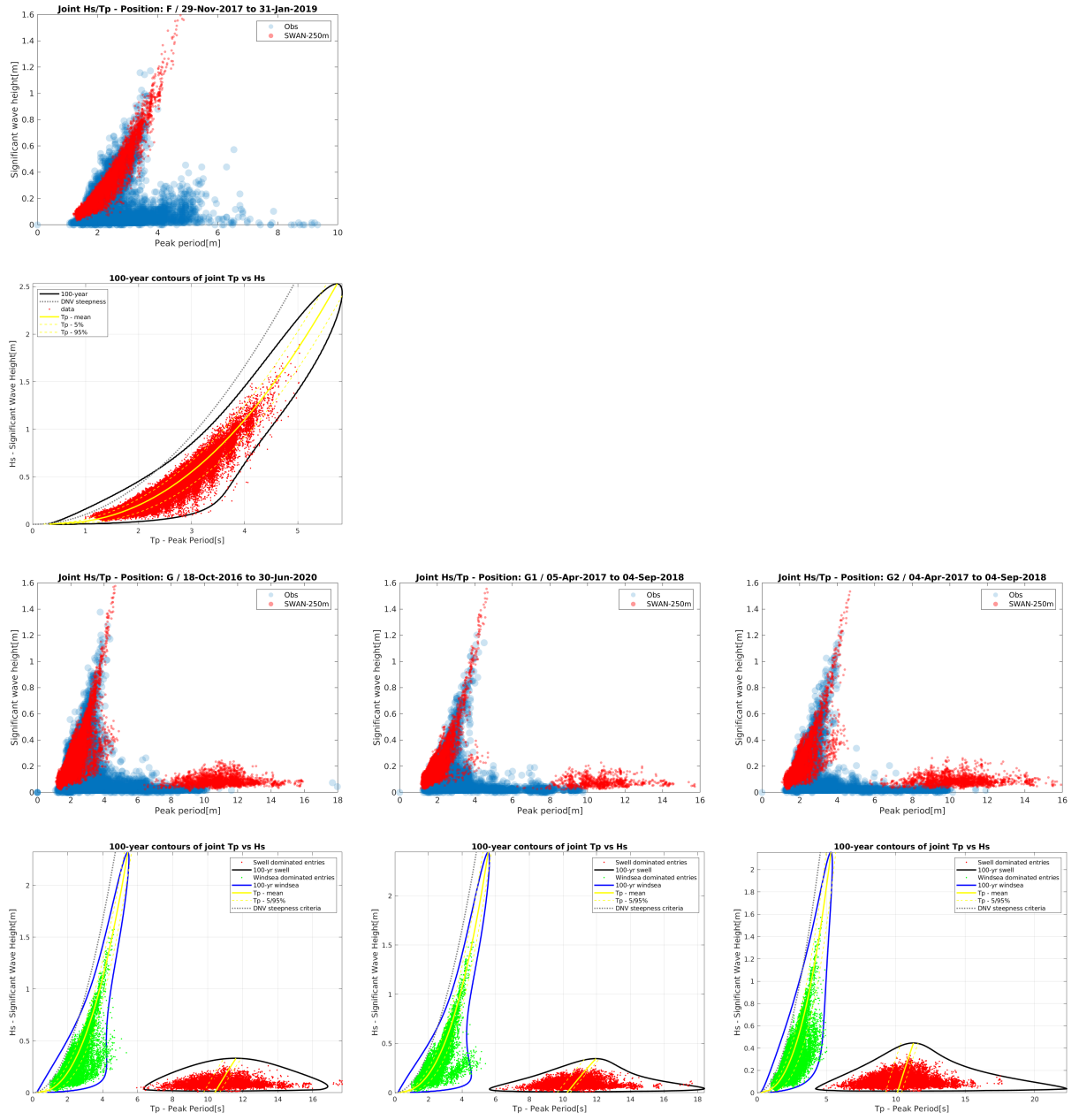


**Figure 12:** Scatter plots of  $H_s/T_p$  (top and second from bottom) at location F, G, G1 and G2 at corresponding hours; SWAN (red) and observations (blue). And, joint  $H_s/T_p$ -contours (second from top and bottom) representing the 100-year return value fitted to SWAN data over the 13 year period. Notice that windsea-dominated cases are illustrated by green dots and corresponding contours at location G, G1 and G2.

## 4.4 Spectral shape

Once the joint distribution of  $H_s$  and  $T_p$  is established, a description of spectral shape (wave energy distribution over frequency) within each  $H_s/T_p$ -bin is needed. Ideally, we would like to assign a spectral shape which is representative in all sea states. However, this is difficult when sea states are a mix of swell and windsea. For some of the locations of interest (possible bridge crossings) the sea states are typically less complex, but still too variable to determine a spectral shape applicable in all situations.

In order to illustrate some of the differences between the areas of interest, we start off by focusing on extreme events. We have analysed the three highest  $H_s$ -events (from independent storms), and fitted the JONSWAP spectrum to the data [Hasselmann et al., 1973];

$$E(f) = \alpha g^2 (2\pi)^{-4} f^{-5} \exp \left[ -\frac{M}{N} \left( \frac{f_p}{f} \right)^N \right] \gamma^{\exp \left[ -\frac{1}{2} \left( \frac{f/f_p - 1}{\sigma} \right)^2 \right]} \quad (9)$$

$$\sigma = \begin{cases} \sigma_a, & \text{if } f < f_p \\ \sigma_b, & \text{if } f \geq f_p \end{cases} \quad (10)$$

$$M = 5, \quad N = 4 \quad (11)$$

$$\alpha = 5.061 \frac{H_{m0}^2}{T_p^4} (1 - 0.287 \ln(\gamma)) \quad (12)$$

Here, we have applied two different fitting techniques; parametric and curve fitting. The commonly applied parametric method assumes  $\sigma_a = 0.07$  and  $\sigma_b = 0.09$  and a peakedness-parameter defined by;

$$\gamma = \exp \left\{ 3.484 (1 - 0.1975 (0.036 - 0.0056 T_p / \sqrt{H_{m0}}) T_p^4 / H_{m0}^2) \right\} \quad (13)$$

When curve fitting the JONSWAP spectrum to the data, we use different combinations of the three shape parameters;  $\sigma_a$ ,  $\sigma_b$  and  $\gamma$ , where they are set to vary or kept constant. In the following we emphasize on the approach where  $\sigma_a = 0.07$  and  $\sigma_b = 0.09$  and  $\gamma$  is set to vary. An upper limit of  $\gamma = 7$  has been applied. We also included the Torsethaugen spectrum which is a bimodal spectrum designed to represent both swell and windsea, consisting of two JONSWAP-shaped spectra; one with variable  $\gamma$  (dominant peak) and one with  $\gamma = 1$  (Pierson-Moskowitz) [Torsethaugen et al., 2004].

The results from station D and C are presented in figure 13 and 14, respectively (see section 7.4.1 for all stations). Notice the clear distinction between the two sites; D has a uni-modal spectrum, while location C clearly portraits a bi-modal spectrum. For the remaining locations, the distinction is less obvious. Further; the conclusion of the analysis is that the parametric approach, although commonly applied, is not suitable to represent the SWAN spectra. The parametric approach offers too sharp spectra, i.e. too high  $\gamma$ . The curve fitted JONSWAP-spectra are generally better. Still, it is important to stress that SWAN probably offers unrealistically smooth representations of the true wave spectrum, which is addressed later in the report.

Following this, we also present observed spectra from the three strongest storms in Sulafjorden ( $H_s > 4m$  at buoy A) during the measurement period, and two situations from Vartdalsfjorden ( $H_s > 1m$  at buoy F) in chapter 6 (figures 41 and 42).

We have also analysed the directional spreading of the three highest  $H_s$ -cases from SWAN in Sulafjorden and found the value of  $s$  which offers the best conformity between the theoretical spreading function [DNVGL, 2017];

$$D(\theta) = \frac{\Gamma(s+1)}{2\sqrt{\pi}\Gamma(s+1/2)} \cos^{2s} \left( \frac{1}{2}(\theta - \theta_p) \right), \quad |\theta - \theta_p| \leq \pi \quad (14)$$

and the SWAN data. As a reference;  $s$  usually lies somewhere between 4-9 in growing wave conditions offshore. For swell the spreading is smaller and  $s$  usually exceeds 13. As illustrated in Figure 13 and 14 (bottom plots), the wave energy at location C is more focused than seen at location D. In general, our locations of interest offer extreme sea states where the wave energy is fairly focused as all extreme  $H_s$ -cases exceed  $s = 13$ , with the exception of location F. This is due to the fact that waves follow the topography/bathymetry of the fjords.

The spectral analysis based on the three highest  $H_s$ -cases are summarized in Table 2.

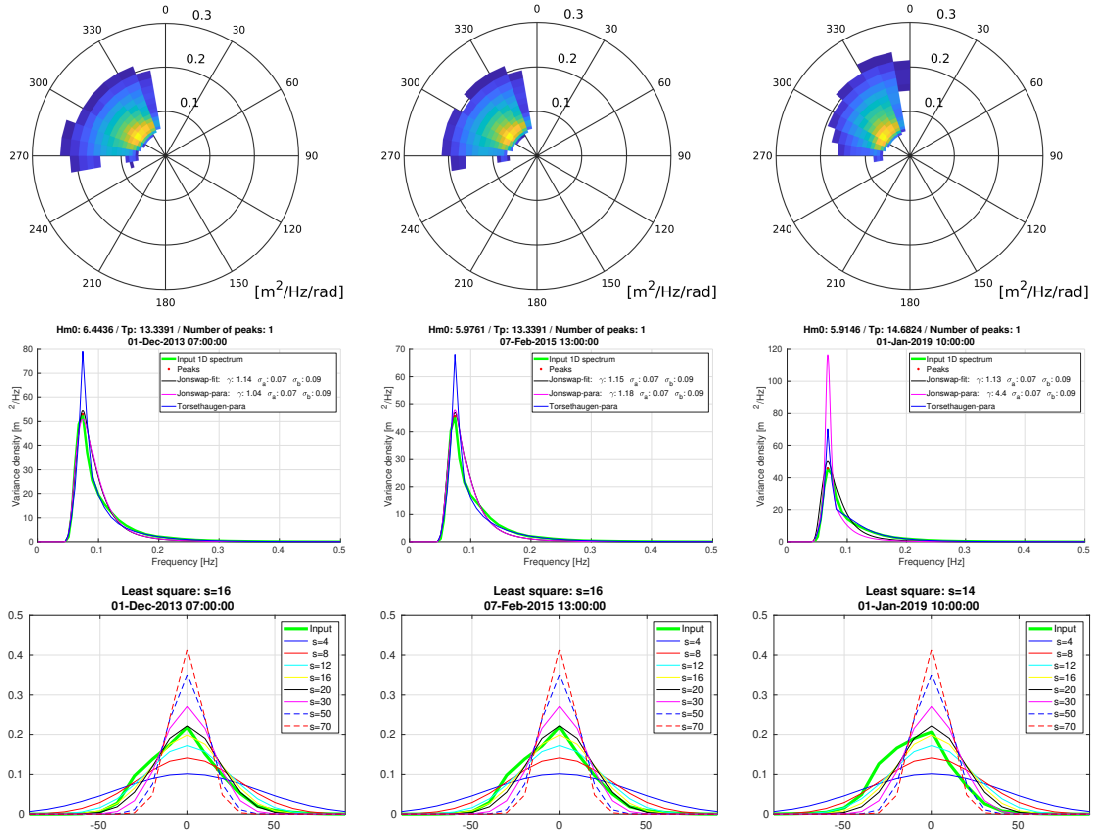


**Figure 13:** Top row: 2D wave spectra from the three highest  $H_s$ -cases over the period 2007-2019 at position D. Model is represented by the green line in the two lower rows. Middle row: Modelled 1D spectra and different fitted JONSWAP-spectra and Torsethaugen. The corresponding shape parameters are presented in the legend. Bottom row: Directional spreading (normalized) according to eq. 14 for different  $s$ .

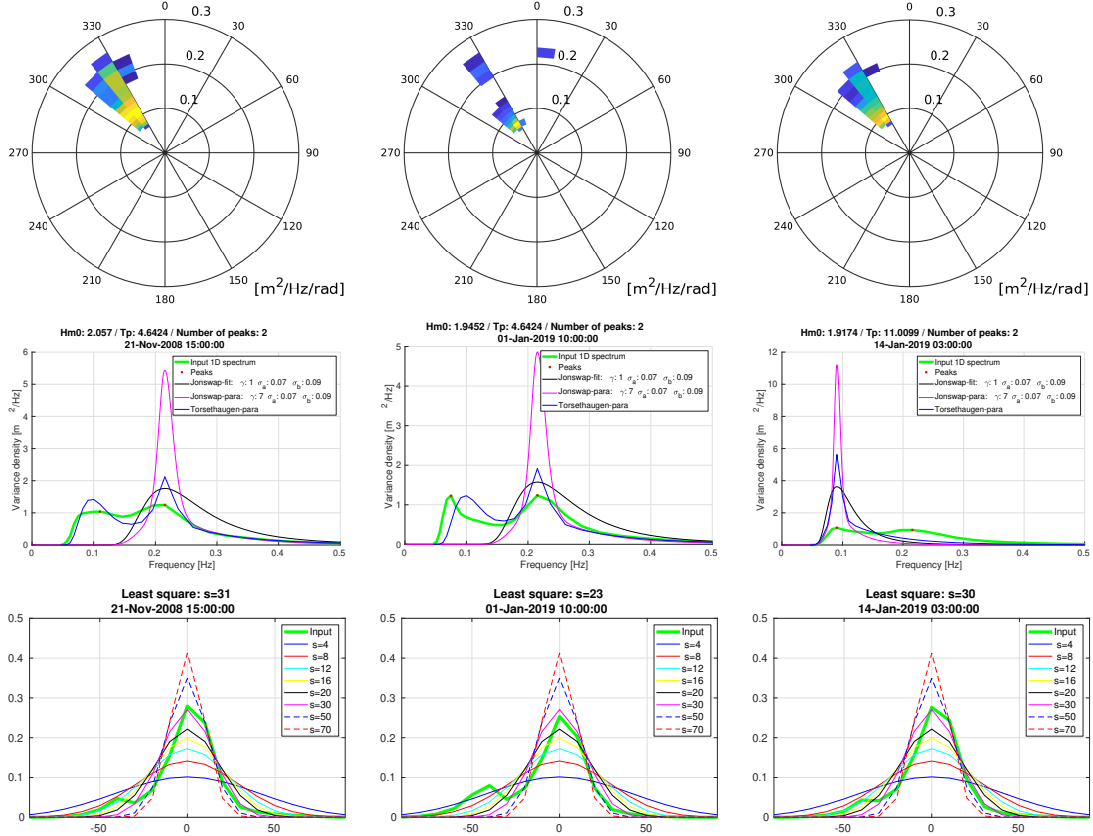


**Figure 14:** Top row: 2D wave spectra from the three highest  $H_s$ -cases over the period 2007-2019 at position C. Model is represented by the green line in the two lower rows. Middle row: Modelled 1D spectra and different fitted JONSWAP-spectra and Torsethaugen. The corresponding shape parameters are presented in the legend. Bottom row: Directional spreading (normalized) according to eq. 14 for different  $s$ .

**Table 2:** The three highest  $H_s$ -cases and corresponding  $T_p$  within Sulafjorden (A-F), together with the peakedness-parameter ( $\gamma$ ) of JONSWAP based on the parametric and the curve fitted approach. The directional spreading parameter  $s$  corresponding to eq. 14 is presented at the bottom row. Notice that the two  $\gamma$ -estimates diverge significantly. The curve fitted estimates conform better to the SWAN-spectra, but is probably somewhat low because the model is a smooth representation of the true sea state.

	A			B			C			D			F			C1			B1		
	1st	2nd	3rd																		
$H_{m0}$ [m]	4.0	4.0	3.8	3.1	3.0	2.9	2.1	1.9	1.9	6.4	6.0	5.9	1.9	1.9	1.8	2.0	2.0	1.7	2.8	2.6	2.4
$T_p$ [s]	13.3	14.7	14.7	9.1	11.0	10.0	4.6	4.6	11.0	13.3	13.3	14.7	5.1	5.1	4.6	11.0	13.3	14.7	11.0	13.3	14.7
$\gamma$ - par fit ( $\sigma_a = 0.07$ , $\sigma_b = 0.09$ )	7.0	7.0	7.0	1.0	7.0	2.9	7.0	7.0	1.0	1.2	4.4	4.7	4.4	6.3	7.0	7.0	7.0	7.0	7.0	7.0	7.0
$\gamma$ - curve fit ( $\sigma_a = 0.07$ , $\sigma_b = 0.09$ )	1.0	1.0	1.0	1.0	1.0	1.0	1.0	1.0	1.1	1.1	1.1	1.1	1.8	1.8	1.8	1.0	1.0	1.0	1.0	1.0	1.0
Directional spreading - s	62.0	65.0	75.0	57.0	55.0	58.0	31.0	23.0	30.0	16.0	16.0	14.0	15.0	11.0	12.0	29.0	23.0	31.0	41.0	42.0	50.0

We have extended the same analysis (as above) to all sea states. In figure 15 we present tables of JONSWAP- $\gamma$ , mean and 90-percentile, respectively, based on the curve fitting approach and binned according to  $H_s$  and  $T_p$  at location A. Here, it is illustrated that SWAN generally produce spectra of low  $\gamma$  and that the variability in  $\gamma$  is minimal for high sea states.

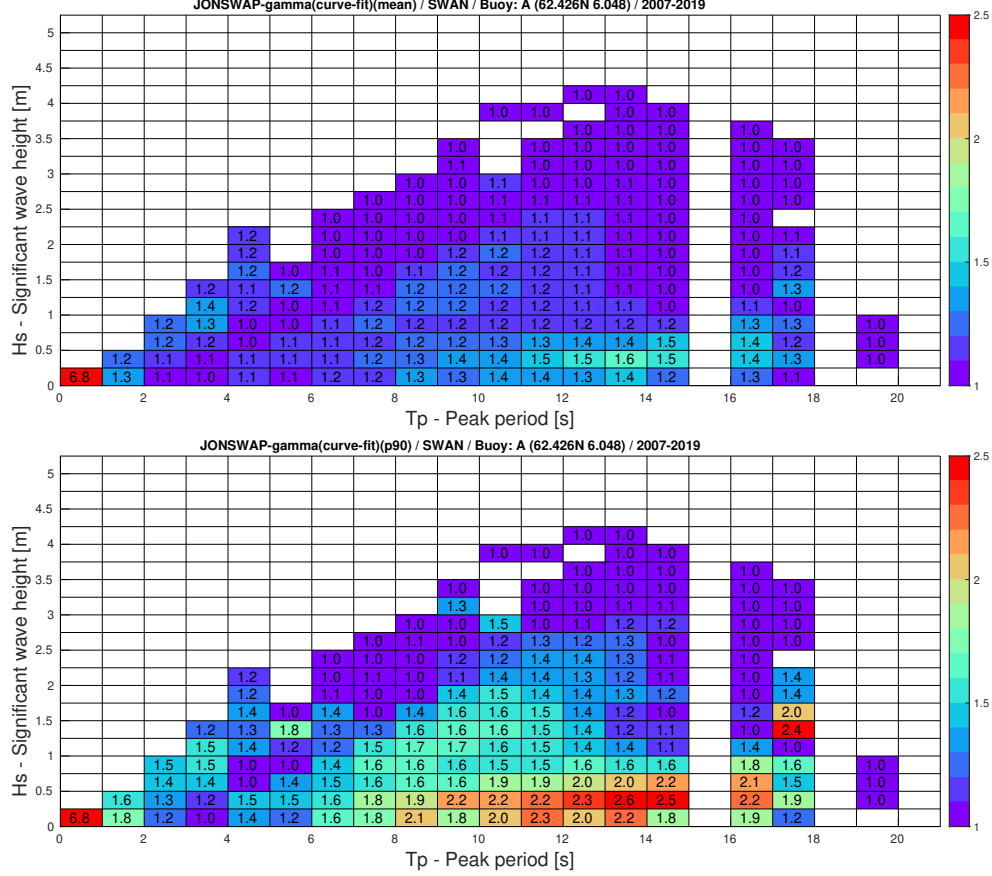


**Figure 15:** JONSWAP- $\gamma$  (curve fitted) at location A binned according to peak period and significant wave height; top: mean and bottom: 90-percentile.

Similarly, we have made the same exercise based on the fitted directional spreading parameter  $s$  of eq. 14. In figure 16 we present a table of mean fitted  $s$ , binned according to  $H_s$  and  $T_p$ . It is shown that the widest spread (lowest  $s$ ) is typically found in steeper wave conditions.

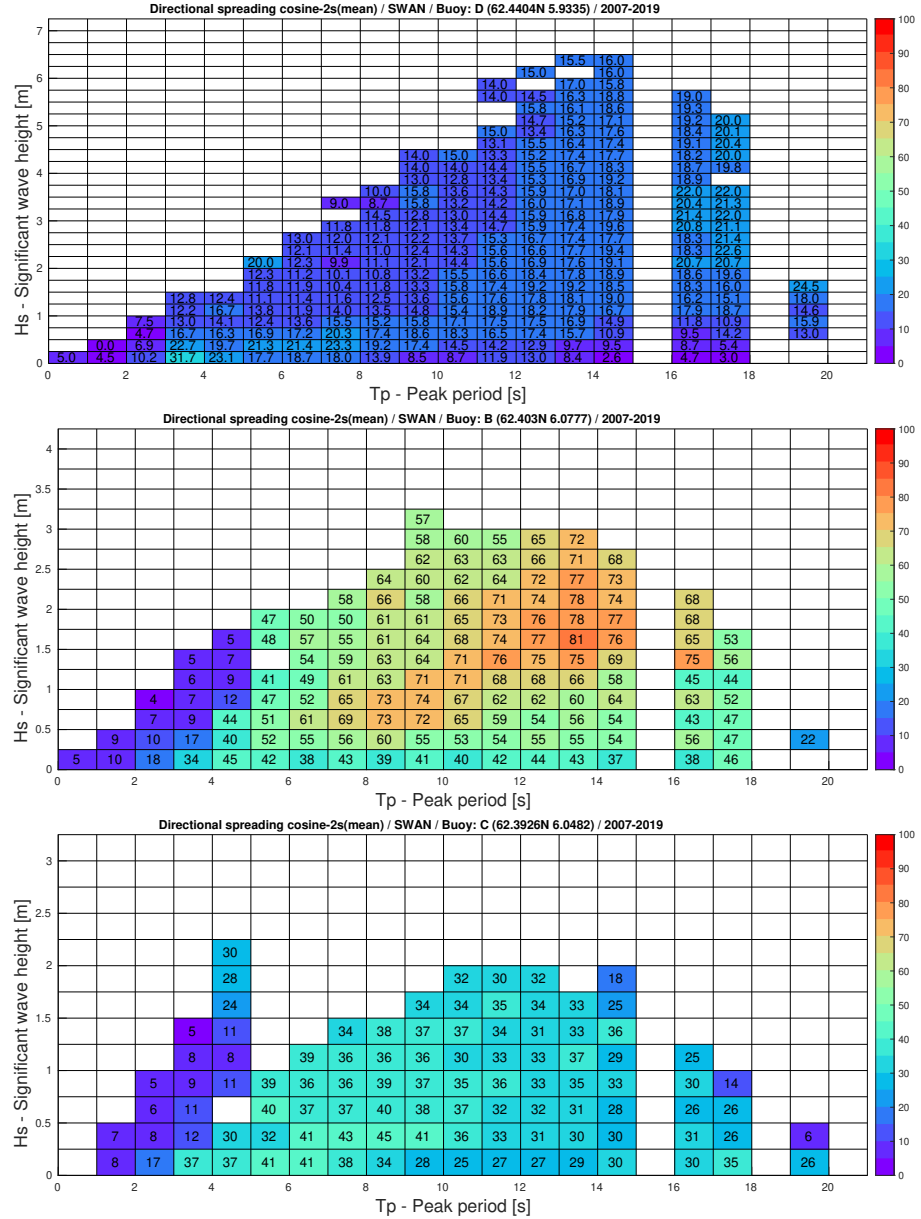


**Figure 16:** Mean directional spread  $s$  of eq. 14 binned according to peak period versus significant wave height.

So far, we have only investigated conformity between the idealized spectra (JONSWAP and Torsethaugen) and SWAN for the three highest  $H_s$ -events. Maybe more importantly is the validity of the idealized spectra compared to observed spectra. In the following, we have made the same exercise as above, but for all observed spectra. Here, we present the results based on location A. All other sites are provided in the Appendix (section 7.4). In figure 17 (top) we present the mean JONSWAP- $\gamma$  based on observed spectra. This plot is equivalent to figure 15 (top) which is based on SWAN. As indicated, the observed spectra are slightly more elevated near the peak frequency (peaked), ie. showing higher JONSWAP- $\gamma$ . However, the difference is less than expected.

In figure 17 (center) we have made an attempt to illustrate the conformity of JONSWAP (curve fitted) relative to observations. The plot shows the mean energy offset ("fit score"), in percent, based on all available spectra, ie. the amount of observed wave energy displaced (exceeding) relative to JONSWAP. A crude threshold may be set at 20%. So, if the wave energy displacement exceeds 20%, JONSWAP is not considered applicable for the associated  $H_s/T_p$ -bin. In this example, for location A, it is seen that JONSWAP is relevant for the highest  $H_s$ -events (shaded in blues). For moderate  $H_s$  and long period  $T_p$ 's JONSWAP provides a poor fit. This is as expected, since these sea states are more often a mix of swell and windsea, ie. bimodal spectra. Since JONSWAP is a unimodal spectrum, conformity is not possible. On the other hand, Torsethaugen is designed to capture bimodal sea states. So, by doing the same exercise, only based on Torsethaugen, a better fit is expected in the same sea states (where JONSWAP is inadequate). In figure 17 (bottom) we illustrate the difference in "fit score" between JONSWAP and Torsethaugen. Sea states in reds indicate better conformity between JONSWAP and observation, while sea states in blues indicate better conformity between Torsethaugen and observations. Clearly Torsethaugen is the better option for moderate  $H_s$  and long period  $T_p$ , but also for moderate  $H_s$  and very short  $T_p$ . The latter is less intuitive, but can probably be attributed those cases where swell is present, but where local windsea is starting to build (presumably from the south at location A), and barely exceeding the energy peak of the swell from the north at location A. Similar plots for all locations are provided in the Appendix (section 7.4).

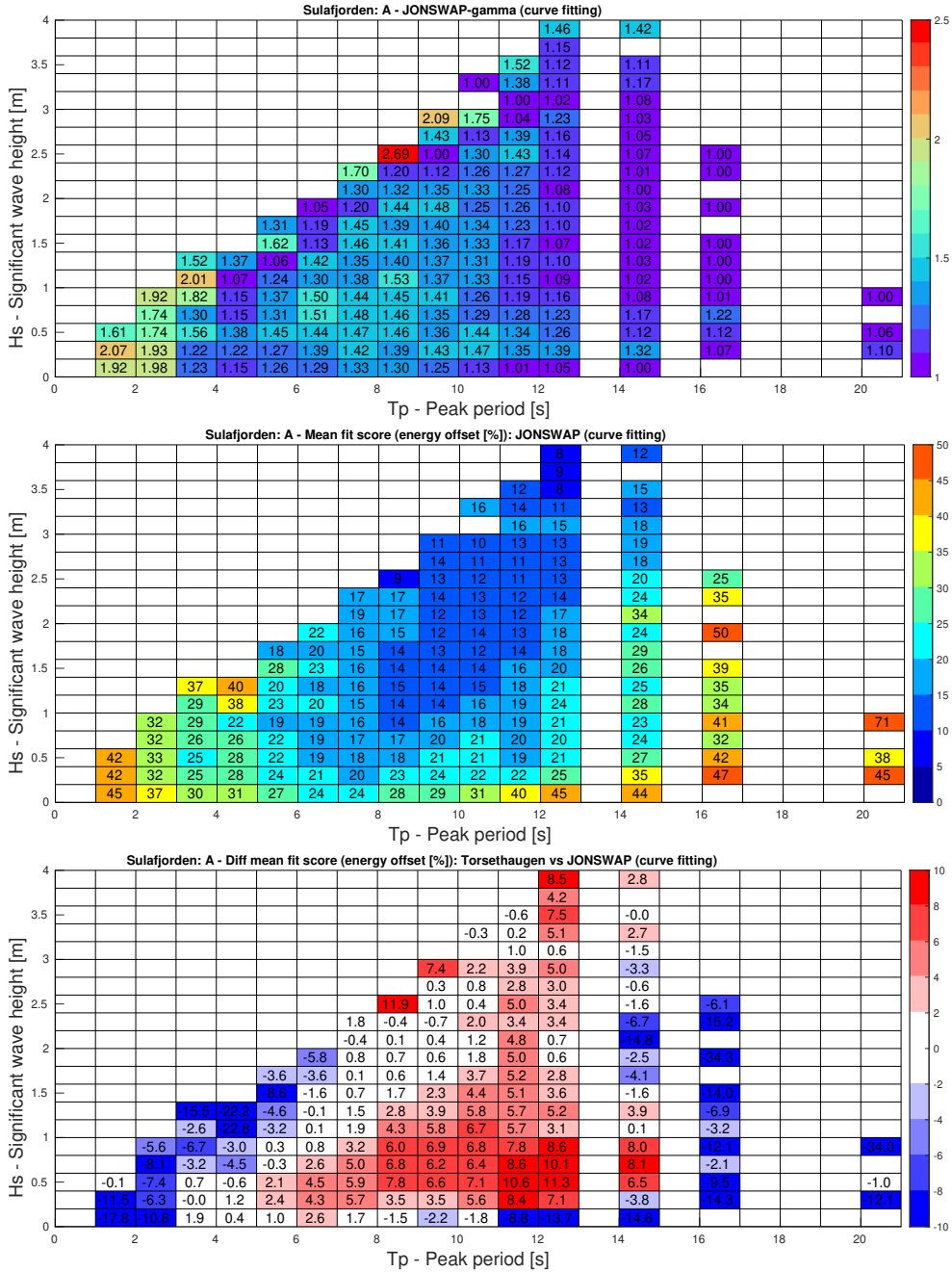


**Figure 17:** Observed spectral properties at location A. Top: Mean JONSWAP-gamma binned according to peak period and significant wave height. Center: Mean fit score - JONSWAP vs observed spectra - represented by the amount of displaced energy (in percent). Bottom: Discrepancy in fit score; Torsethaugen vs JONSWAP. Reds indicating superior fit between JONSWAP and observed spectra. Blues indicating superior fit between Torsethaugen and observed spectra.

## 4.5 Return Value Estimates

Return value estimates are usually based on traditional extreme statistics, or alternative methods that have become established and standardized over time. Although the purpose is the same, different approaches will provide slightly different results. Often this can be attributed to the length of the underlying data. Some approaches should not be extrapolated more than 3-4 times the length of the initial data Lopatoukhin et al. [2000]. In other words; you need approximately 30 years of data to obtain reliable 100-year return value estimates. So, with only 13 years of data, it would be preferable to simulate a longer period.

In the following study, we have tested and compared several approaches, all presented in the Appendix. However, in order to present a somewhat tidy result, we have focused on one approach, which has been used extensively by the offshore industry on the Norwegian Continental Shelf. Unlike traditional extreme statistics, where only a subset of the initial data is used (above some threshold), here, we use all data. This is usually referred to as the *initial distribution* approach. A three-parametric Weibull distribution is then fitted to the data, and extrapolated to the desired return period. We have applied two different fitting techniques, i.e. the *method of moments* (MOM) and the *least square* (LS).

Here, we want to utilize the full length of the SWAN model simulation, ie. 13 years of data. However, in order to validate the quality of the estimates, we also apply the same approach to the observations. For the validation to be comparable, we extract SWAN and observations at corresponding hours. Altogether, we present 100-year return value estimates based on 13 years of SWAN data, together with equivalent estimates based on both SWAN and observations at corresponding hours. The results from location A is presented in figure 18. Similar plots for the remaining locations are found in the Appendix (section 7.3). This is illustrated by so-called return value plots where the empirical cumulative distribution of the underlying data and the theoretical distribution (three-parametric Weibull) are plotted together to illustrate conformity between the two. For the most part, all distributions fit the data fairly well and it is not obvious which approach provide the most accurate estimate.

In order to illustrate some of the inherent uncertainty in the 100-year return value estimates, we have re-sampled each of the three data sets 500 times (bootstrap). Each re-sample contains the same number of data ( $N$ ) as the initial data sets. For each re-sample we have fitted the three-parametric Weibull distribution. In the end we get 500

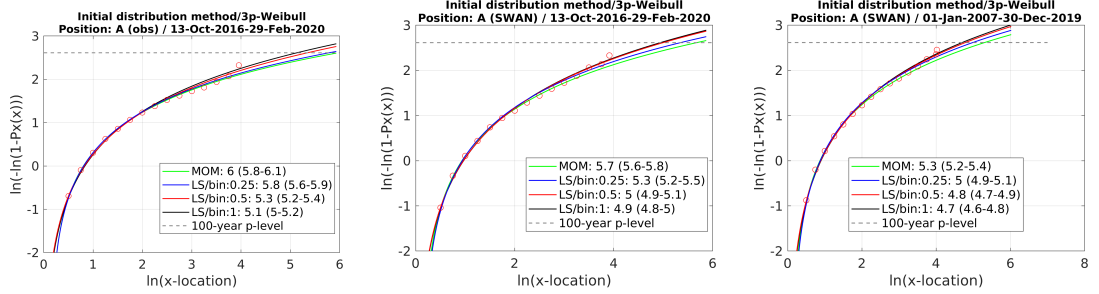


**Figure 18:** Return value plots at location A based on observations for the period 13-Oct-2016 to 29-Feb-2020 (left), SWAN for the period 13-Oct-2016 to 29-Feb-2020 (center) and SWAN for the period 01-Jan-2007 to 30-Dec-2019 (right). 100-year return value estimates are presented in the legend. MOM represents the method of moments estimates, while LS represents least square estimates for different bin-sizes of  $H_s$ . 95%-confidence intervals are provided in brackets.

versions of the return value plots illustrated in figure 18. These data are then used to find the lower 2.5-percentile and the upper 97.5-percentile of the 100-year return value estimate based on the different approaches, where the range between the two represent the 95% confidence interval. Confidence intervals are presented in the legend of figure 18. Paradoxical some of the 95% confidence intervals do not overlap, which only comes to show that estimates are more uncertain than indicated by the confidence intervals. As mentioned above, some of the explanation is related to the relative length of the initial data, which is short compared to the desired return period (100-year). However, statistical approach also influence the estimates.

In table 3 and 4 we present 100-year return value estimates based on the different approaches/periods for Sulafjorden/Vartdalsfjorden and Halsafjorden, respectively. We have made the choice to emphasize the estimates based on the 13-year long SWAN data and the MOM approach, presented in bold text in the tables. Still, we need to stress the fact that SWAN indicates a bias relative to the observations at several locations (based on the validation period). **In general, the SWAN estimates are probably on the low side at location D, fair or slightly (0.2-0.3m) low at location A, fair at location B, and high at location B1, C, C1, F, G1, G and G2.** Any best estimate could be subjectively adjusted according to findings made in the validation period.

In figure 19 we present the 100-year return value estimates at Julsundet. Again, we emphasize the estimates based on the MOM approach, which is 1.9m at location J. With no observations available at Julsundet, it is difficult to indicate the validity of the esti-

	D	A	B	B1	C	C1	F
OBS: start	14-Oct-2016	13-Oct-2016	13-Oct-2016	08-Feb-2019	27-Apr-2017	11-Feb-2019	29-Nov-2017
OBS: end	29-Feb-2020	29-Feb-2020	29-Feb-2020	29-Feb-2020	29-Feb-2020	29-Feb-2020	31-Jan-2019
MOM	10 (9.7-10.3)	6 (5.8-6.1)	3.6 (3.5-3.8)	2.8 (2.6-3)	1.9 (1.8-2)	1.7 (1.6-1.7)	1.6 (1.5-1.7)
LS1	9.4 (8.3-9.5)	5.1 (5-5.2)	3.2 (3-3.2)	2.9 (2.7-3)	2 (1.7-2.1)	1.6 (1.4-1.6)	1.7 (1.5-1.8)
LS2	9.4 (8.6-9.9)	5.3 (5.2-5.4)	3.3 (3.1-3.3)	2.8 (2.6-2.9)	2.1 (1.8-2.2)	1.6 (1.4-1.6)	1.7 (1.5-1.8)
LS3	9.6 (9.2-9.9)	5.8 (5.6-5.9)	3.4 (3.2-3.5)	3.1 (2.8-3.2)	2.1 (1.9-2.2)	1.6 (1.5-1.7)	1.7 (1.5-1.8)
SWAN: start	14-Oct-2016	13-Oct-2016	13-Oct-2016	08-Feb-2019	27-Apr-2017	11-Feb-2019	29-Nov-2017
SWAN: end	29-Feb-2020	29-Feb-2020	29-Feb-2020	29-Feb-2020	29-Feb-2020	29-Feb-2020	31-Jan-2019
MOM	9.2 (8.9-9.4)	5.7 (5.6-5.8)	3.6 (3.5-3.7)	3.3 (3.2-3.4)	2.3 (2.2-2.5)	2 (1.9-2.1)	2.5 (2.3-2.6)
LS1	7.2 (7.1-7.2)	4.9 (4.8-5)	3.5 (3.2-3.5)	3 (2.7-3.4)	2.6 (2.4-2.8)	1.9 (1.8-2)	2.3 (2.2-2.4)
LS2	7.8 (7.7-7.8)	5 (4.9-5.1)	3.5 (3.3-3.6)	3.1 (2.9-3.2)	2.6 (2.4-2.7)	1.9 (1.8-2)	2.3 (2.2-2.4)
LS3	8.4 (8.2-8.6)	5.3 (5.2-5.5)	3.7 (3.4-3.8)	3.2 (2.9-3.3)	2.5 (2.3-2.6)	2.1 (2-2.1)	2.4 (2.3-2.5)
SWAN: start	01-Jan-2007						
SWAN: end	30-Dec-2019						
<b>MOM</b>	<b>8.5 (8.4-8.6)</b>	<b>5.3 (5.2-5.4)</b>	<b>3.5 (3.5-3.6)</b>	<b>3.4 (3.3-3.4)</b>	<b>2.2 (2.1-2.3)</b>	<b>2.3 (2.2-2.3)</b>	<b>2.5 (2.5-2.6)</b>
LS1	7.2 (6.9-7.4)	4.7 (4.6-4.8)	3.5 (3.2-3.6)	3.4 (3.2-3.4)	2.4 (2.4-6.9)	2.4 (2.4-6.7)	2.3 (2.2-2.3)
LS2	7.5 (7.3-7.6)	4.8 (4.7-4.9)	3.6 (3.4-3.7)	3.5 (3.3-3.6)	2.5 (2.2-2.6)	2.5 (2.3-2.6)	2.3 (2.2-2.3)
LS3	7.9 (7.7-8.1)	5 (4.9-5.1)	3.6 (3.5-3.7)	3.5 (3.4-3.6)	2.4 (2.3-2.5)	2.5 (2.3-2.6)	2.3 (2.2-2.3)

**Table 3:** Summary of 100-year return value estimates in Sulafjorden/Vartdalsfjorden based on three different data sets; Observations (OBS), SWAN at corresponding period as observations and SWAN over 13 years. Each station A-F (columns) are presented with 100-year return value estimates based on different approaches; MOM represents the method of moments estimates, while LS represents least square estimates for different bin-sizes (1-3) of  $H_s$ . 95%-confidence intervals are provided in brackets. **Estimates presented in bold text are used as input to the contours presented in section 4.3.**

mates. Based on the findings made at Sulafjorden and Halsafjorden, there are reasons to believe that 1.9m might be biased high.

	G1	G	G2
OBS: start	05-Apr-2017	18-Oct-2016	04-Apr-2017
OBS: end	04-Sep-2018	30-Jun-2020	04-Sep-2018
MOM1	2.1 (1.9-2.3)	1.8 (1.7-1.9)	2.1 (1.9-2.2)
LS11	2.1 (1.8-2.2)	2 (1.7-2.2)	2 (1.8-2.1)
LS21	2.1 (1.9-2.3)	2 (1.7-2.1)	2 (1.8-2.2)
LS31	2.2 (1.9-2.4)	1.9 (1.8-2.1)	2.1 (1.9-2.3)
SWAN: start	05-Apr-2017	18-Oct-2016	04-Apr-2017
SWAN: end	04-Sep-2018	30-Jun-2020	04-Sep-2018
MOM2	3.7 (3.3-3.9)	2.5 (2.4-2.7)	3.2 (2.9-3.4)
LS12	2.9 (2.7-3.1)	2.5 (2.3-2.7)	2.7 (2.5-2.9)
LS22	3.2 (2.8-3.6)	2.6 (2.4-2.7)	2.9 (2.6-3.2)
LS32	3.8 (3.3-4.1)	2.6 (2.4-2.7)	3.2 (2.9-3.5)
SWAN2: start	01-Jan-2007	01-Jan-2007	01-Jan-2007
SWAN2: end	30-Dec-2019	30-Dec-2019	30-Dec-2019
<b>MOM</b>	<b>2.5 (2.4-2.6)</b>	<b>2.4 (2.3-2.4)</b>	<b>2.2 (2.2-2.3)</b>
LS13	2.1 (2-2.2)	2.1 (2-2.1)	2 (1.9-2.1)
LS23	2.2 (2.1-2.3)	2.2 (2.1-2.2)	2.1 (2-2.2)
LS33	2.4 (2.3-2.5)	2.3 (2.2-2.4)	2.2 (2.1-2.2)

**Table 4:** Summary of 100-year return value estimates in Halsafjorden based on three different data sets; Observations (OBS), SWAN at corresponding period as observations and SWAN over 13 years. Each station G1, G and G2 (columns) are presented with 100-year return value estimates based on different approaches; MOM represents the method of moments estimates, while LS represents least square estimates for different bin-sizes (1-3) of  $H_s$ . 95%-confidence intervals are provided in brackets. **Estimates presented in bold text are used as input to the contours presented in section 4.3.**

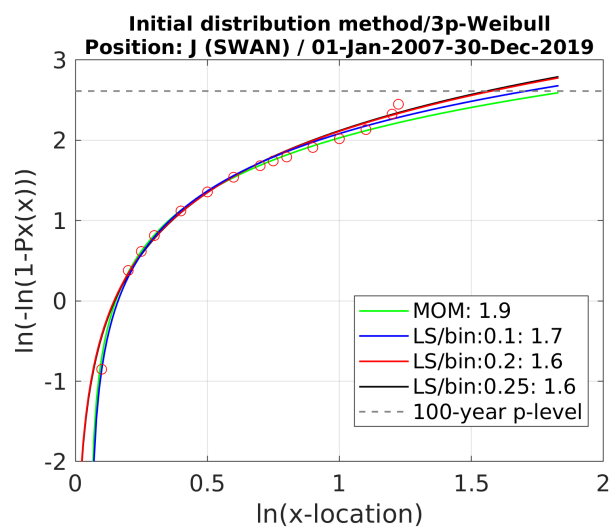


**Figure 19:** Return value plot at location J based on SWAN for the period 01-Jan-2007 to 30-Dec-2019 (right). 100-year return value estimates are presented in the legend. MOM represents the method of moments estimates, while LS represents least square estimates for different bin-sizes of  $H_s$ .

#### 4.5.1 Recommendation

So far the presented 100-yr return value estimates are mainly based on SWAN data and compared against coinciding observations, see table 3 and 4. Here, we want to emphasise the observed wave data. We use all available data, but limit the data sets by full years, i.e. each data set starts from the earliest date of available data and are prolonged by complete years. In this way the final data set should have the same number of e.g. November-data as May-data, and no months are over-represented. This is not fully satisfied as some periods lack data. However, we have checked the total coverage and the amount of missing data is minor, providing a fairly uniform distribution of data over the full calendar year.

The original wave data are sampled every 10 min<sup>2</sup> and constitute the most comprehensive data set. The 10-min sampling interval is somewhat arbitrary, therefore, we also want to investigate the effect of sub-sampling the original data. Here, we sub-sample the original data every three hours. Notice that the sub-sampled data sets are extracted at coinciding hours as NORA10 (1958-2020), which reduce the total data set with 1 year at B1, C and C1. In figure 20 we present 100-year return value estimates based on both the original data and the sub-sampled data set, together with the data period and the total number of years. For both data sets, we apply two extreme value approaches, i.e. the IDM/three-parametric Weibull and the POT/exponential, see section 7.1. As shown, the return value estimates are affected by the sub-sampling, but - for the most part - no more than expected given the length of the data period relative to the desired 100-year return period.

With no more than four years of available data, return value estimates will be affected by any longer period oscillations in storm activity (decadal), e.g. North Atlantic Oscillation (NAO). In order to investigate whether the period is slow/moderate/extreme in a climatic sense, we want to utilize the full length of the NORA10 data set (1958-2020). So, by calibrating NORA10 (obtained from a near offshore location, i.e. 62.43N 05.69E) against the available observations, we are able to produce synthetic data sets for each buoy location covering 63 years (1958-2020). The calibration is obtained by linear regression between NORA10 and the observed data, separated into the sectors 15 – 225°, 225 – 255°, 255 – 285°, 285 – 315° and 315 – 15° based on the NORA10 mean wave direction. The correlation between NORA10 and the buoy data is provided in figure 20, before and after

---

<sup>2</sup>Each 10-minute value is based on 17 minutes (2048 2 Hz samples) with 7 minutes overlap in time with the previous.

calibration. Location F and G (G1/G2) show poor correlation before/after calibration, and should not be used. The highest correlation is (obviously) obtained between the locations situated closest to NORA10, i.e. location A and D, where the calibrated data sets exceed 0.9 relative to NORA10. Further; the calibrated NORA10 data sets are used to obtain 100-year return value estimates for the full period (1958-2020) and the shorter period of coinciding data. Depending on extreme value approach, the comparison shows slightly different results. With IDM/three-parametric Weibull the two periods show highly similar estimates. For the POT/exponential, the shorter period shows higher estimates, indicating that the period with available observations is more extreme in a climatic sense. However, there are different reasons why this result should be used carefully; first, the period of coinciding data is short. Second, the POT/exponential is highly sensitive to threshold selection. Last, the correlation between observations and the calibrated data sets are moderate. All in all, the return value estimates based on the coinciding period seem representative in a longer perspective. If anything, the 100-year return value estimates are on the high side (conservative).

In order to conclude, we present subjective 100-year return value estimates in figure 20 together with the estimates obtained with SWAN (2007-2019) presented in table 3 and 4. Our subjective estimates are mostly affected by the original 10-min observations (coinciding period), but slightly adjusted based on the estimates obtained with the sub-sampled data and the calibrated NORA10 data. Still, it must be emphasized that the final estimates are uncertain, primarily due to the length of the original data set (4 years or less). And, as the measured data series are prolonged, the 100-year return value estimates are expected to be affected slightly.

		OBS (10 min) original		OBS (3-hrly) coinciding w/NORA10		NORA10 cal	NORA10 cal (3-hrly) short	NORA10 cal (3-hrly) 1958-2020	SWAN 2007- 2019	SUB
Station	Period	Num year	3p-WBL (L-S-bin)	EXP (thres)	3p-WBL (L-S-bin)	corr OBS (omni)	3p-WBL (L-S-bin)	EXP (thres)	3p-WBL (L-S-bin)	3p-WBL MOM
<b>A</b>	13-Oct-2016..to..12-Oct-2020	4	5.8 (0.25)	6.2 (2.0)	5.5 (0.25)	6.0 (1.8)	0.85	0.9	5.2 (0.25)	5.3 (0.25)
<b>B</b>	13-Oct-2016..to..12-Oct-2020	4	3.4 (0.25)	3.7 (1.2)	3.2 (0.25)	3.6 (1.0)	0.84	0.87	3.2 (1.0)	2.8 (0.25)
<b>B1</b>	08-Feb-2019..to..07-Feb-2021	2 (1)	2.9 (0.25)	2.9 (1.1)	2.9 (0.1)	3.0 (0.91)	0.78	0.81	2.2 (0.1)	2.7 (0.74)
<b>C</b>	27-Apr-2017..to..26-Apr-2021	4 (3)	2.1 (0.1)	2.1 (0.68)	1.8 (0.1)	1.8 (0.61)	0.76	0.78	1.3 (0.1)	1.4 (0.4)
<b>C1</b>	11-Feb-2019..to..10-Feb-2021	2 (1)	1.8 (0.1)	1.9 (0.74)	1.7 (0.1)	1.7 (0.77)	0.78	0.8	1.4 (0.1)	1.6 (0.53)
<b>D</b>	14-Oct-2016..to..13-Oct-2020	4	10.1 (0.5)	10.8 (3.3)	9.1 (0.5)	10.2 (2.9)	0.9	0.93	8.7 (0.5)	9.5 (2.8)
<b>F</b>	29-Nov-2017..to..27-Nov-2020	3	1.7 (0.1)	1.7 (0.74)	1.5 (0.1)	1.5 (0.61)	0.46	0.65		8.7 (0.5)
<b>G</b>	18-Oct-2016..to..17-Oct-2020	4	2.1 (0.1)	2.2 (0.81)	1.8 (9.1)	1.9 (0.53)	0.32	0.43		
<b>G1</b>	05-Apr-2017..to..04-Apr-2018	1	2.2 (0.1)	2.3 (0.61)	2.2 (0.1)	2.2 (0.46)	0.23	0.29		
<b>G2</b>	04-Apr-2017..to..03-Apr-2018	1	2.1 (0.1)	2.3 (0.62)	2.3 (0.1)	2.3 (0.53)	0.31	0.36		
									2.2	2.2

**Figure 20:** 100-year return value estimates (100yr-RVE) based on different data sets. Table is organized as follows (columnwise); Location name, period of utilized observations, total number of years (number of years coinciding with NORA10 data), 100yr-RVE based on IDM/3p-Weibull (bin-size least square) and POT/GP (threshold), 100yr-RVE based on sub-sampled data and IDM/3p-Weibull (bin-size least square) and POT/GP (threshold), correlation between observations and calibrated NORA10 (62.43N 05.69E), 100yr-RVE based calibrated NORA10 for coinciding period; IDM/3p-Weibull (bin-size least square) and POT/GP (threshold), 100yr-RVE based on NORA10 for 1958-2020; IDM/3p-Weibull (bin-size least square) and POT/GP (threshold), 100yr-RVE based on SWAN (2007-2019), see table 3 and 4 and subjective 100yr-RVE estimates based on all data.

## 5 Spatial statistics

### 5.1 Transects

In this section we will focus on the spatial variation across the fjords in terms of significant wave height,  $H_s$ , and peak period,  $T_p$ , and on the highest events in terms of percentiles.  $T_p$  is everywhere related to the significant wave height and it should be noted that swell may be present even if the peak period is low. We show results from three transects; A: from Kvitneset to Trælbodneset in Sulafjorden going through the position of buoy A, B: From Langeneset through buoy C and B locations and further to the coast of Sula, G: From Halsaneset to Åkvik in Halsafjorden through buoys G, G1 and G2. The model represents 13 years of wave climate, but as we want to relate the information from the model to observations, the data are presented both for the full model data set and for concurrent data of model and buoys.

**Sulafjorden** We have extracted values of significant wave height and peak period along the transects A (green line) and B (yellow line) shown in figure 21. The map also shows the actual location of all 5 buoys in Sulafjord (A, B, B1, C, C1) buoys in Sulafjord for concurrent whole hours up to 2020.

Percentiles and maximum of  $H_s$  along the transects are calculated and presented in figure 22. The figure show both the result from the full model data set (top row) and when co-located in time to observations. Since the buoys have been deployed at different times, the concurrent data set can be extracted in several ways. Using concurrent data based on model and all 5 buoys in Sulafjord (A, B, B1, C, C1) results in a quite small data set of only 6405 data points (lower row) (figure 21). Since buoys A, B, C have been in operation for the longest time period, we also retrieve a data set of concurrent data based on just these three buoys. This results in 21032 data points. The result from this data set is shown in the middle row of figure 22.

The figure show the variation in  $H_s$  across the fjord. The gradient is large over transect B where the 99<sup>th</sup> percentile based on the full data set vary from 1.5 m in the east to 0.75 m in the western side. The maximum  $H_s$  is 4m (3m) for transect A (B). The concurrent data sets show that the percentiles from the model show a positive bias of around 0.2 – 0.3m compared to the buoys (middle row), while the maximum values are underestimated<sup>3</sup>.

---

<sup>3</sup>Spurious values have been removed, as well as recorded values when the buoys were not in the vicinity

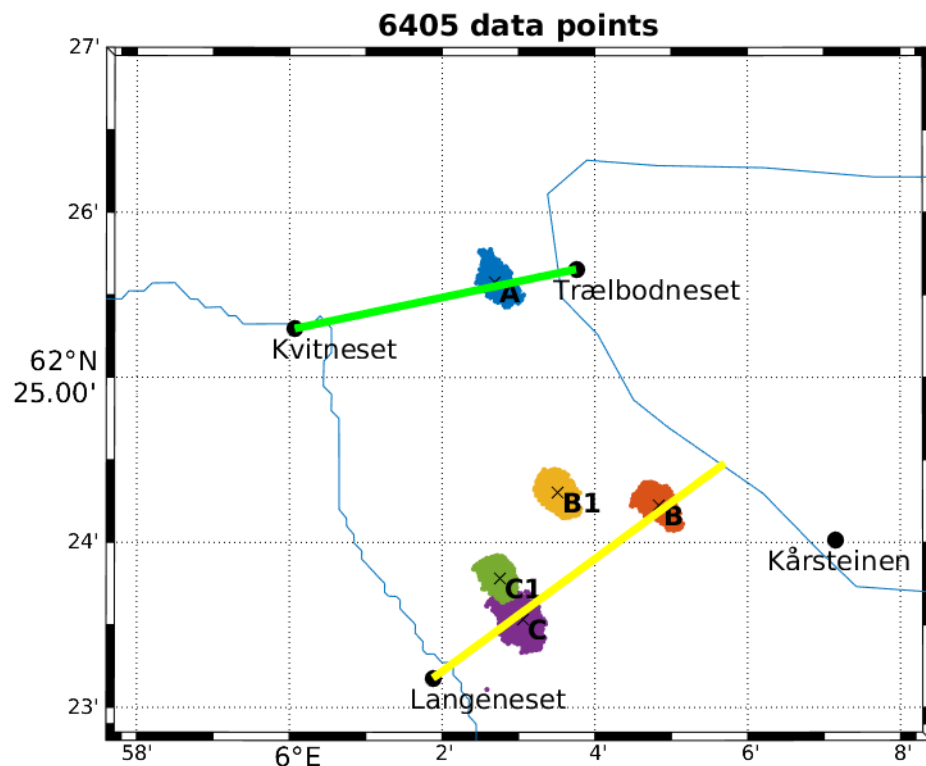


**Figure 21:** Location of the five buoys in Sulafjord for concurrent times with swan model output (6405 hours). Model data for figures 22 - 24 are extracted along the green and yellow transects (named transect A and B).

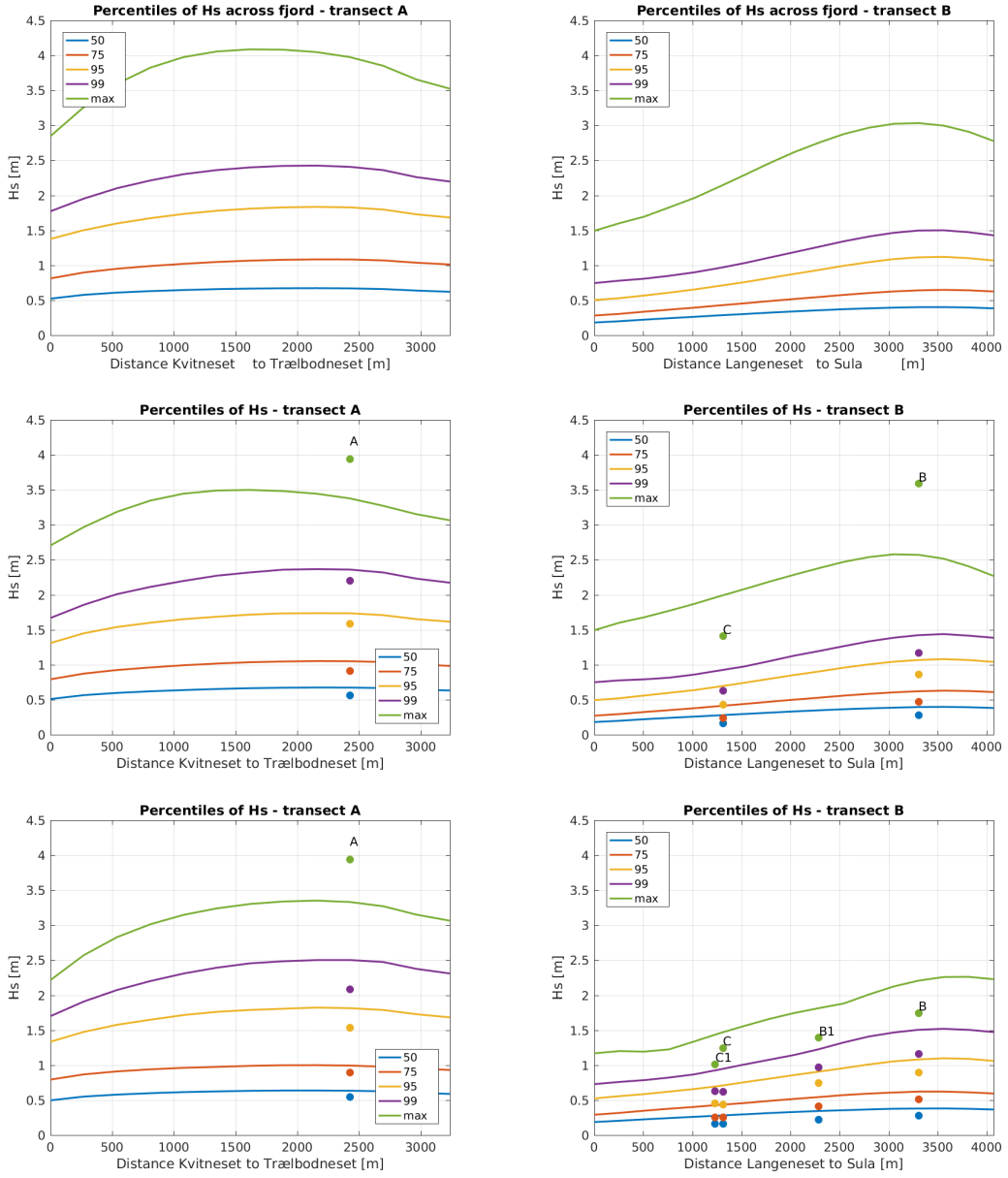


**Figure 22:** Percentiles and maximum of significant wave height at transect A and B from model (lines) and buoys (points). Top row: Model data only. Middle row: Concurrent data (21032 hours) from model and buoys A, B, C. Lower row: Concurrent data (6405 hours) from model and buoys A, B, B1, C and C1.

The 99<sup>th</sup> percentile of significant wave height at the center of transect A is 2.4 m and 1.2 m in the center of transect B which we consider thresholds for the upper 1% situations at each transect. In figure 23 and 24 we have selected the 1% situations (single transects) exceeding these thresholds in the center and shown these data in boxplots of  $H_s$  and  $T_p$ , respectively. As for figure 22, the top row is based on all model data, the middle row is concurrent data for buoys A, B, C and the lower row includes also B1 and C1. The boxplots give the median variation along the transects for the 1% highest situations with the variability indicated by the box (+/- 25%) and whiskers (minimum and maximum values). A value which is considered an outlier is plotted with plus-signs for the model and circles for the buoys. During storm events, the inhomogeneity in  $H_s$  (figure 23) along the transects may be more pronounced than when looking at percentiles at each location. This is the case at transect B, while at A the variation is similar for the 99th percentile (figure 22) and the 1% storm cases (figure 23). The buoys confirm the variations at transect B, but the model is generally biased high. As noted in the introduction to this section, we need to be careful when looking at peak period, since a low peak period related to a local wind sea does not rule out the presence of swell. This also explains the large range in peak period for transect B (figure 24), where in particular the western side close to Langeneset is sheltered and wind sea may be the dominant wave system. The model shows typical peak periods of 12 – 13 s during these storm events. These values are high, compared to the observations. The model is overestimating  $T_p$  by around 1 s at location A and by 2 s at B. Closer to Langeneset (at C and C1), the model show larger differences to measured  $T_p$ . In other words, SWAN retains too much low frequency energy in this area, indicating more swell than what is actually being measured. See also  $H_s/T_p$  scatter plots in section 4.3 (figures 11 and 12).

**Halsafjorden** The location of the transect in Halsafjord from Halsaneset to Åkvik is shown in figure 25. The map also shows the actual location of the buoys for concurrent whole hours up to 2020.

Like in Sulafjord, the model tend to overestimate the waves in Halsafjord with a positive bias of 0.1-0.2 m and also the maximum values are slightly higher than observed (figure 26). The peak period is low, below 5 s, which shows that the wind sea is typically dominant in storm situations in Halsafjord. The wave conditions across Halsafjord are quite homogeneous, only with slightly higher waves in the center of the fjord. This is

---

of their fixed geographical position.

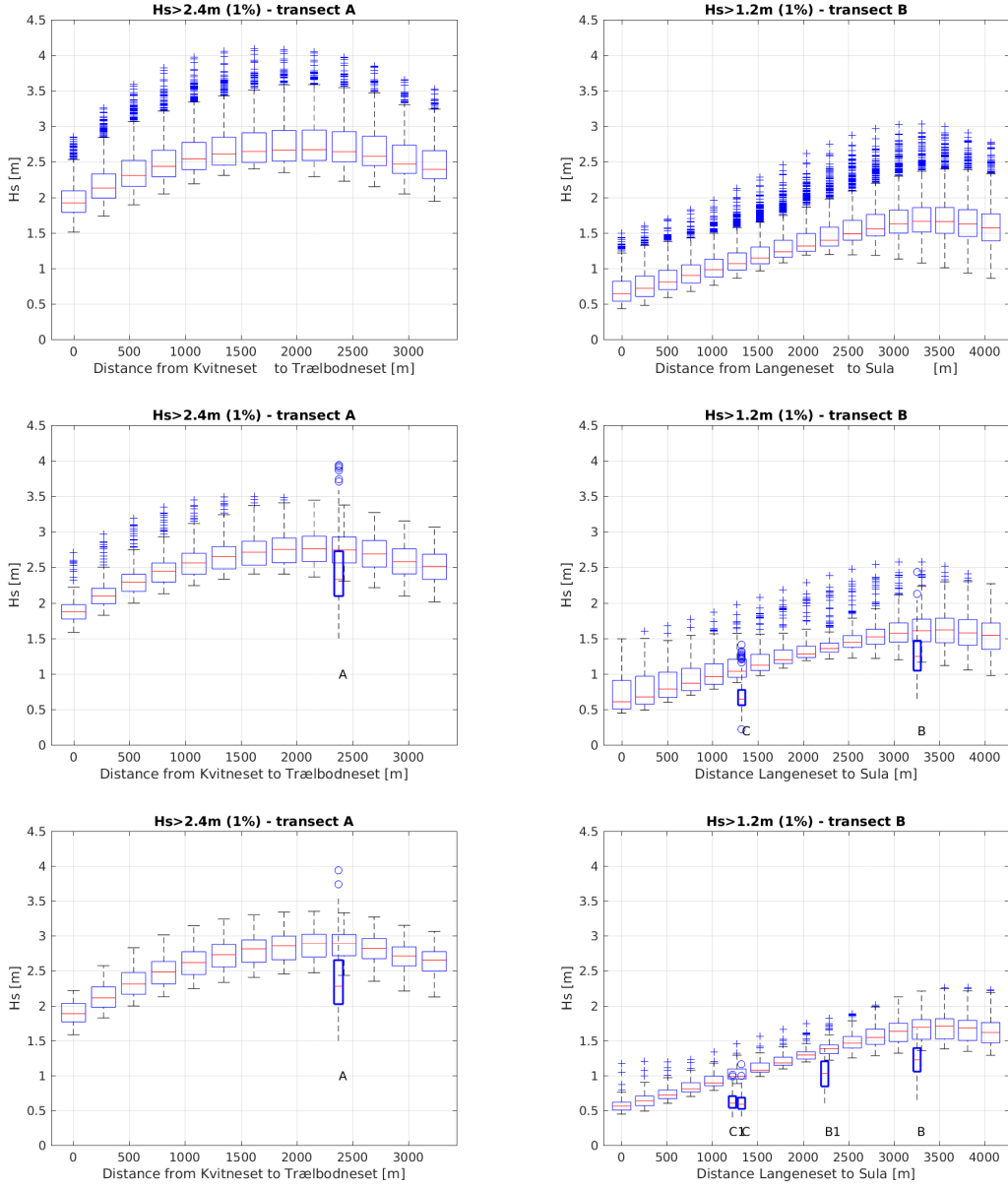


**Figure 23:** Box plot of significant wave height at transects A and B of the 1% highest situations selected from significant wave height at the center of each transect. The corresponding boxes for observations are shown in bold. Each box gives the 25 to 75 percentiles and the red line shows the median. Top row: Model data only. Middle row: Based on concurrent data from model and buoys A, B, C. Lower row: Based on concurrent data from model and buoys A, B, B1, C and C1.

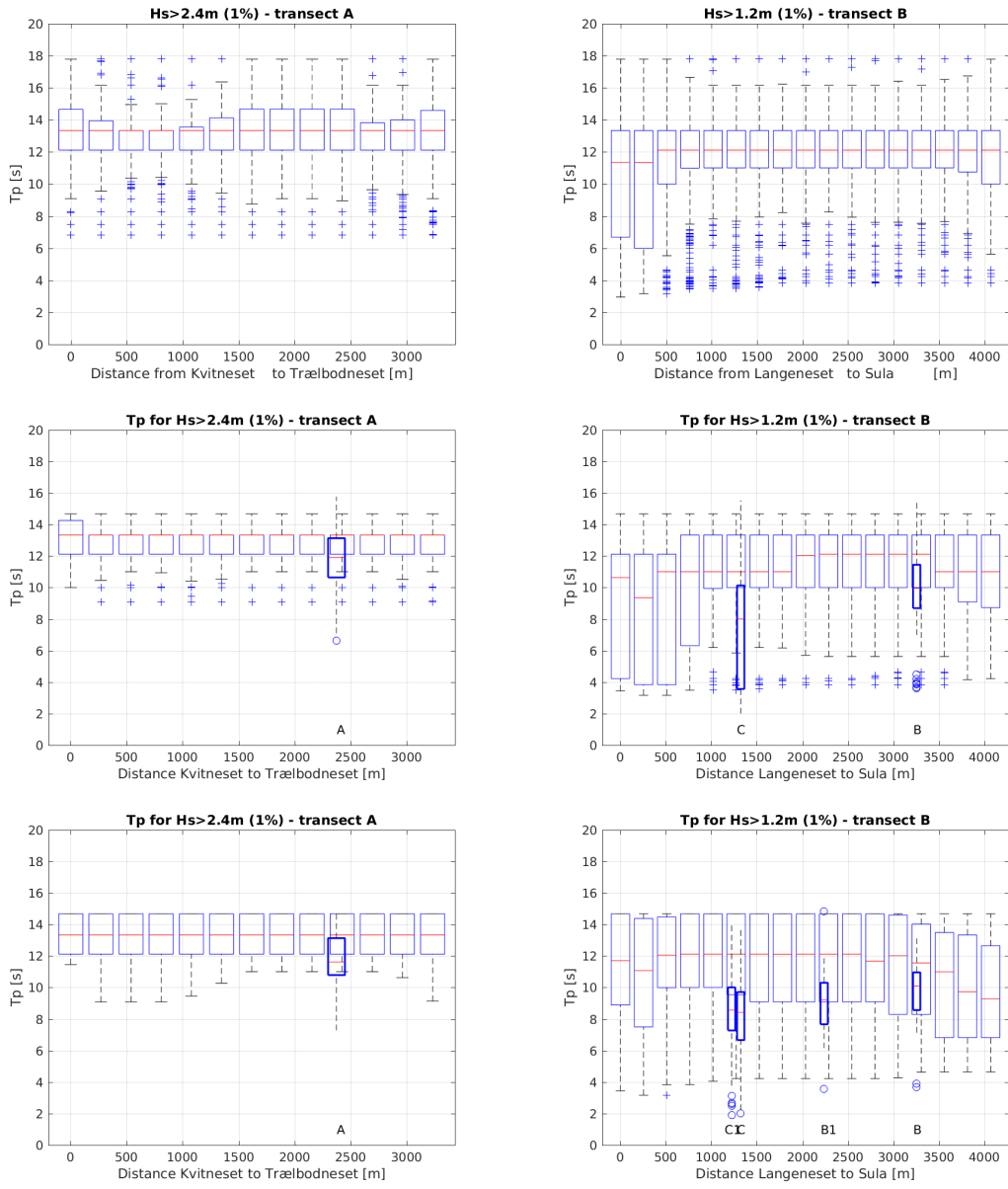


**Figure 24:** Box plot of peak period at transects A and B of the 1% highest situations selected from significant wave height at the center of each transect. The corresponding boxes for observations are shown in bold. Each box gives the 25 to 75 percentiles and the red line shows the median. Top row: Model data only. Middle row: Based on concurrent data from model and buoys A, B, C. Lower row: Based on concurrent data from model and buoys A, B, B1, C and C1.

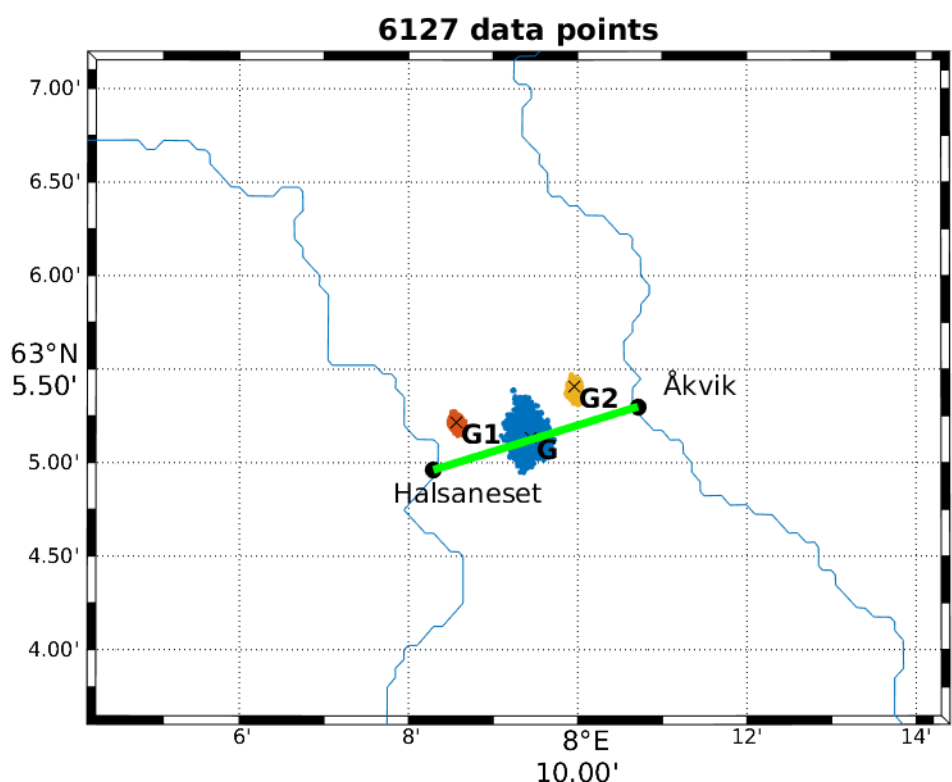


**Figure 25:** Location of the three buoys in Halsafjord for concurrent times with swan model output (6127 hours). Model data for figures 26 and 27 are extracted along the green transect (named transect G).

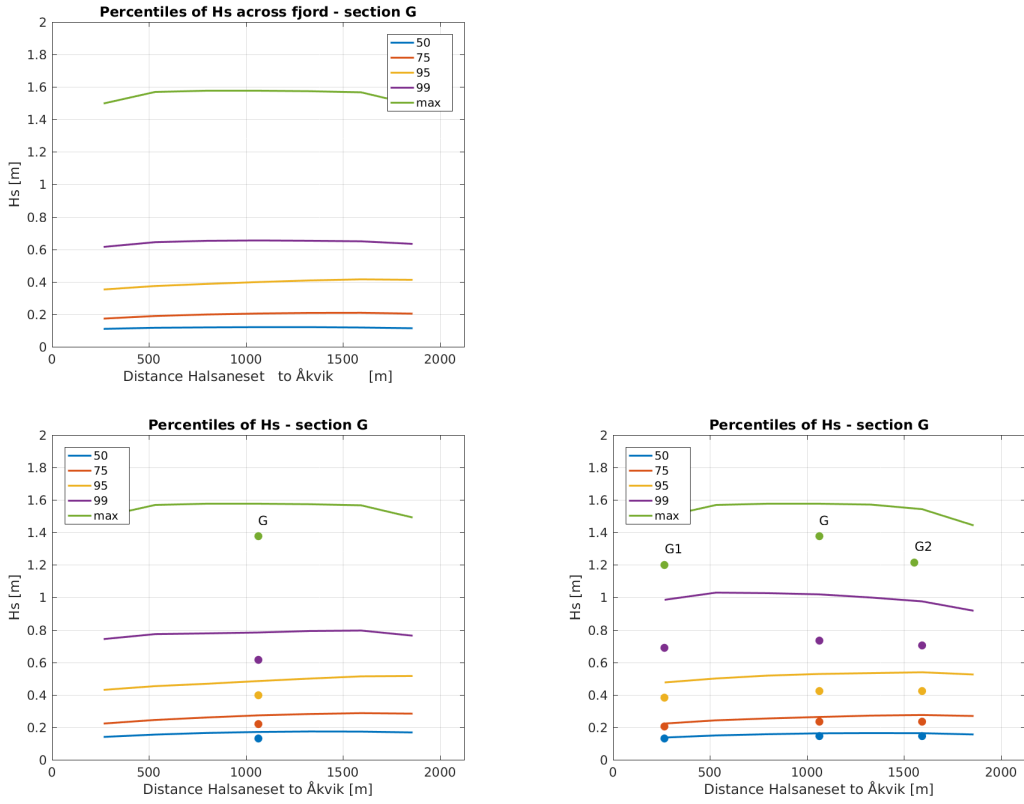


**Figure 26:** Percentiles and maximum of significant wave height at transect A and B from model (lines) and buoys (points). Top : Model data only. Lower left: Concurrent data (21141 hours) from model and buoy G. Lower right: Concurrent data (6127 hours) from model and buoys G, G1 and G2.

confirmed by the buoys in figure 27.

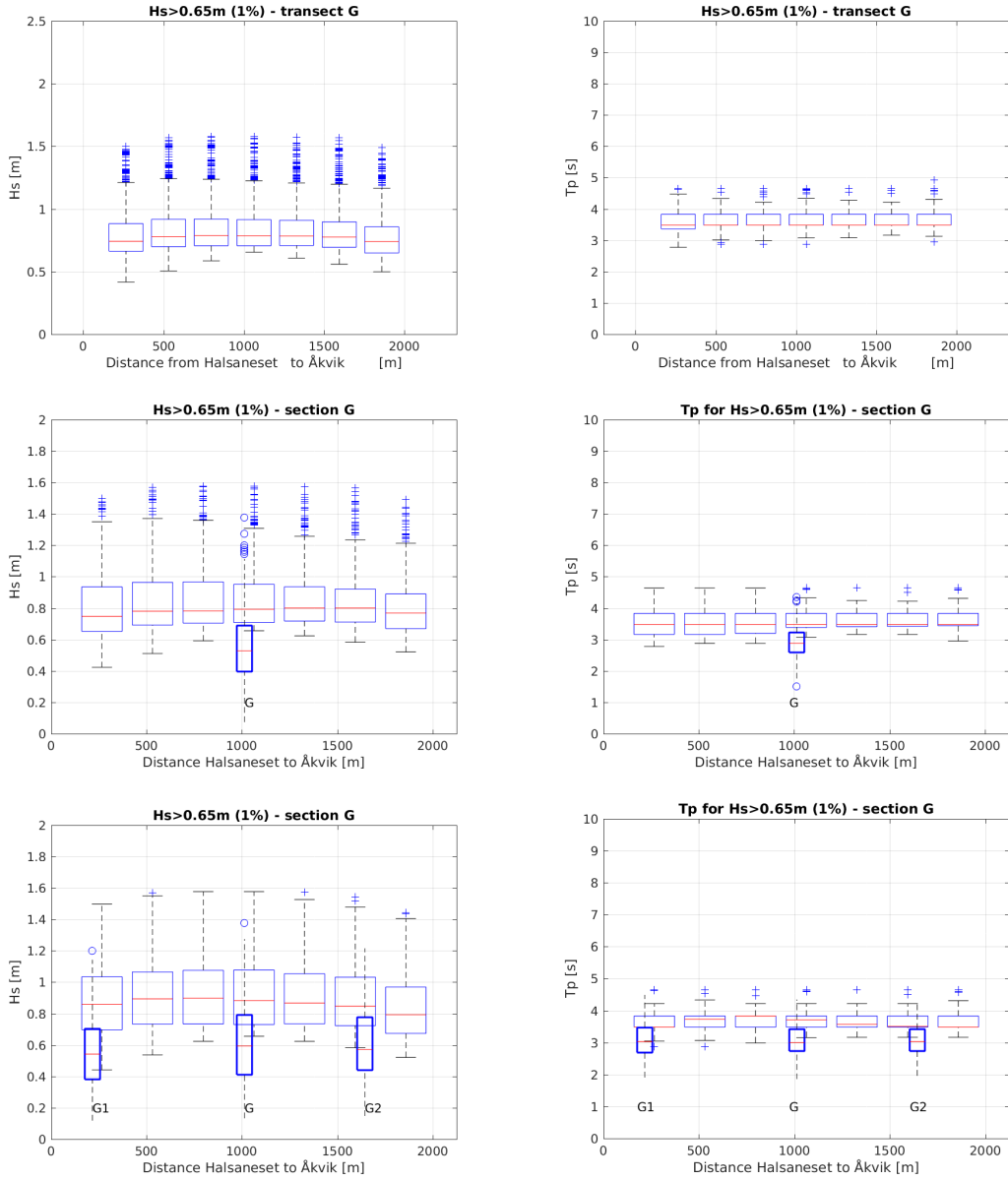


**Figure 27:** Box plot of significant wave height (left column) and peak period (right column) at transect G of the 1% highest situations selected from significant wave height at the center of the transect. The corresponding boxes for observations are shown in bold. Each box gives the 25 to 75 percentiles and the red line shows the median. Top row: Model data only. Middle row: Based on concurrent data from model and buoy G. Lower row: Based on concurrent data from model and buoys G, G1, G2.

## 5.2 Return value estimates

In order to illustrate the spatial variability in extreme  $H_s$ , we present maps of 100-year return value estimates. These plots are based on the *generalized extreme value* (GEV) distribution fitted to the annual maxima data, altogether 13 data entries (2007-2019), which is short relative to the desired 100-year return period. Method is described in section 7.1. Notice that *Gumbel* is a special case of the GEV. Below, we present estimates based on both distributions. Also note that the following estimates may deviate from the 100-year statistics presented in section 4.5, due to the different applied approach.

In figure 28, we present 100-year return value estimates for the three different model domains; Sulafjorden, Halsafjorden and Julsundet. All three plots indicate 100-year returns above 16m offshore, while corresponding estimates are effectively reduced to 2m and below going inwards the fjord.

In figure 29-31 we zoom in on the areas of interest, i.e. the planned bridge crossings. Again, the two plots will deviate from the estimates presented in section 4.5, however, illustrates very well spatial variability in extreme conditions.

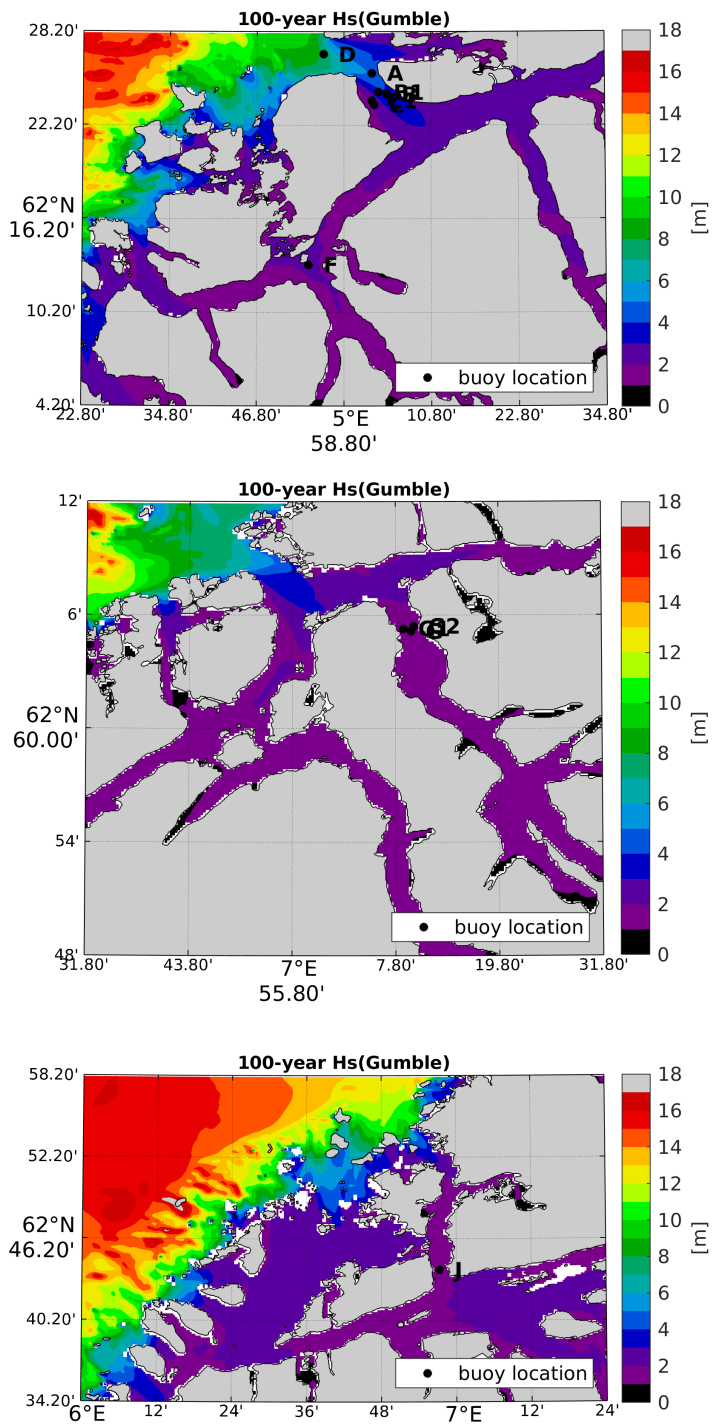


**Figure 28:** Return value estimates of  $H_s$  based on the Gumbel distribution fitted to annual maxima over the period 2007 - 2019 at Sulafjorden (top), Halsafjorden (center) and Julsundet (bottom).

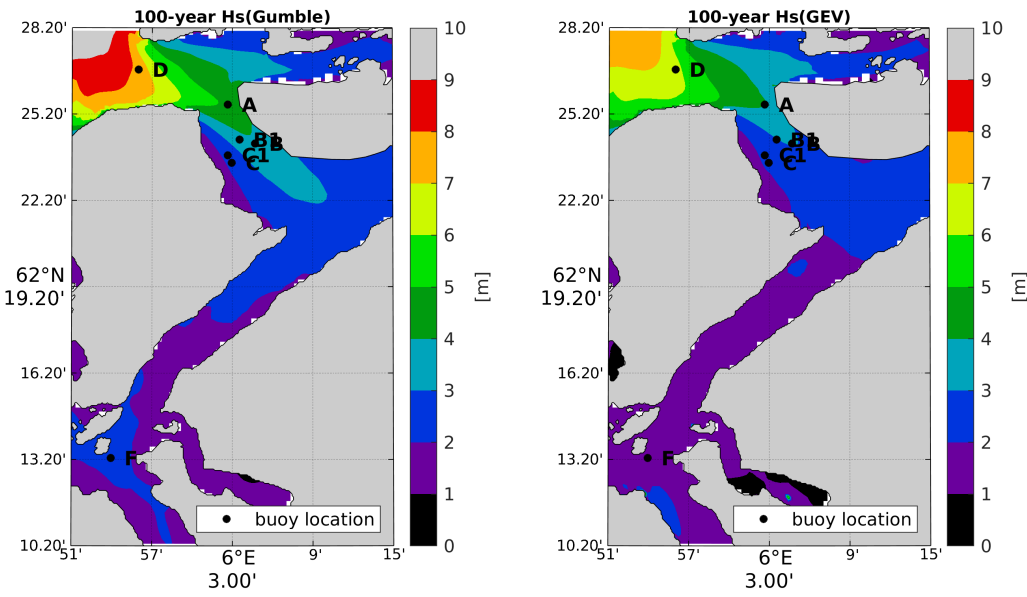


**Figure 29:** Sulaffjorden; Return value estimates of  $H_s$  based on the Gumbel (left) and the Generalized Extreme Value (GEV) distribution (right) fitted to annual maxima over the period 2007 - 2019.

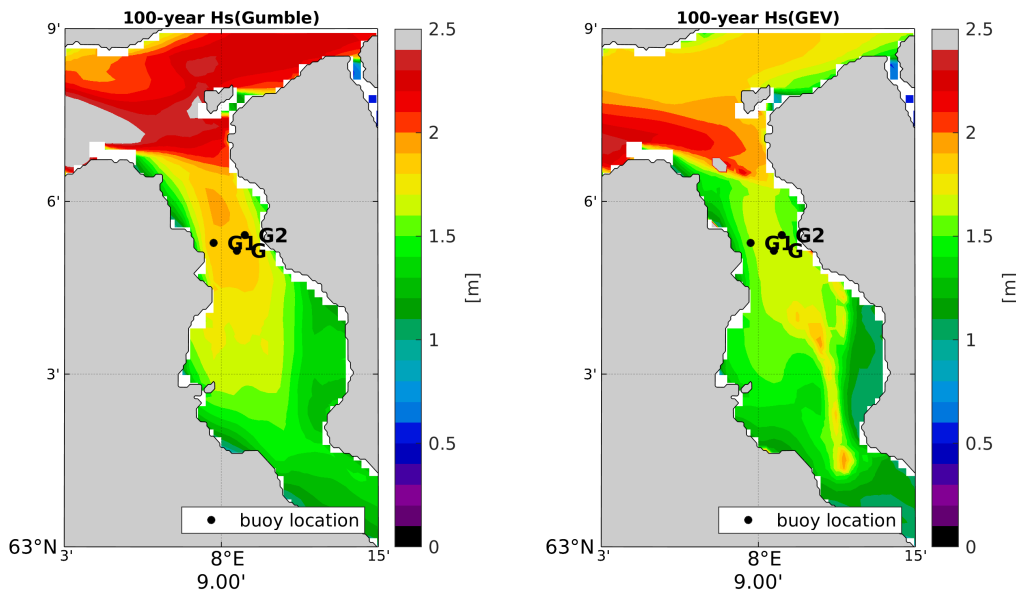


**Figure 30:** Halsaffjorden; Return value estimates of  $H_s$  based on the Gumbel (left) and the Generalized Extreme Value (GEV) distribution (right) fitted to annual maxima over the period 2007 - 2019.

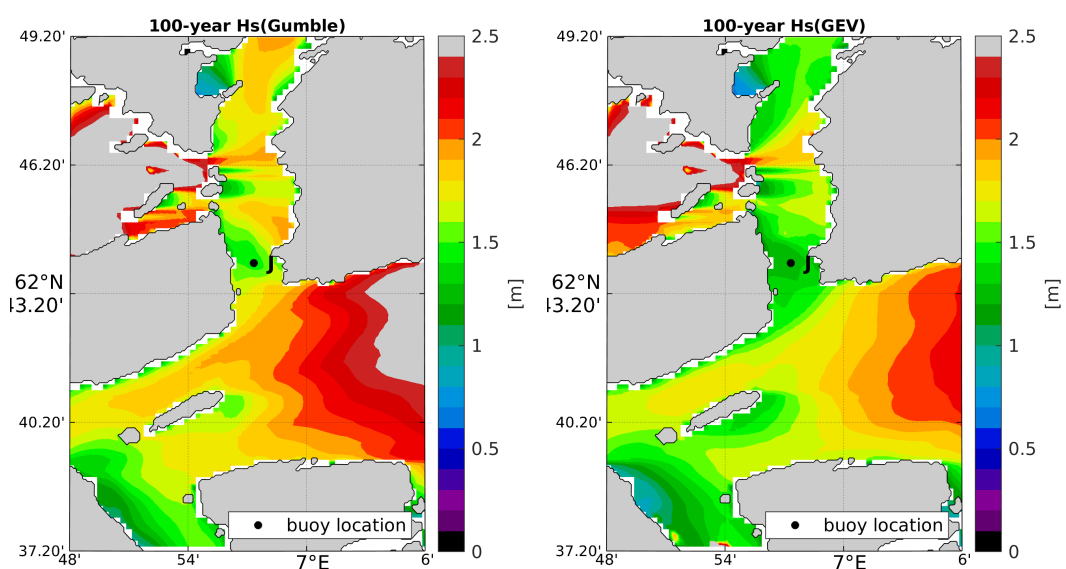


**Figure 31:** Julsundet; Return value estimates of  $H_s$  based on the Gumbel (left) and the Generalized Extreme Value (GEV) distribution (right) fitted to annual maxima over the period 2007 - 2019.

## 6 Selected storms

In this chapter, storms are selected from the data set at location A (observations and models) and from a NORA10-location offshore in order to analyse what could be the most extreme situation to have occurred in Sulafjord during the NORA10 hindcast period 1957-2020. The cases are summarised in table 5 with case number, date and time,  $H_s$  and  $T_p$  in NORA10 at the offshore position 62.69N 5.03E close to the border of the SWAN-domains ,  $H_s$  and  $T_p$  from SWAN simulations (SWAN150 with NORA10 winds / SWAN250 with WRF winds) at buoy location A, observed  $H_s$  and  $T_p$  at buoy A (October 2016 - present ) and a comment on the reason for including the case. Case number S1 and S2 are stationary runs with SWAN using JONSWAP spectra on the border. SWAN250 (13+ year hindcast used in the remaining of the report) and SWAN150 (20 year hindcast) are described in section 3.2. A map with an overview of model domains and NORA10 positions referred to in this chapter is found in figure 2.

$H_s$  -  $T_p$  combinations for the selected storms (figure 32) show that the selection covers most of the extreme cases at A. Case 9-12 which were selected based on peak direction offshore are not the highest cases, but case 10 results in  $H_s$  of 3.7 m at location A for SWAN250 which is quite high. The maximum  $T_p$  in NORA10 is 21.5 s (case 1 and 5) and the wave period transfers to A with  $T_p$  of 19.6 – 20.7s for case 5, but for case 1 the wind sea is dominating at A.

Time series from the two strongest storms covered in the SWAN250-simulations (December 2011 case 4, and December 2013 case 8, figure 33) show that the local wind speed in 2013 was similar in NORA10 and WRF. However, in during the extreme weather in December 2011 WRF only had around 10 m/s in Sulafjord. Simulations using winds from WRF (SWAN250) therefore give somewhat low values for  $H_s$  at location A for the extreme weather *Dagmar* (case 4).  $H_s$  from SWAN150 (forced with NORA10 winds) is 0.6 m higher at A than SWAN250.

From observations, the highest  $H_s$  in location A occurred January 2017 ( $H_s = 4.4\text{m}$ ). Time series offshore and from the two simulations as well as observations from A in figure 34 show that the waves start to decrease before the peak in the observations. The wind from the buoy agree very well with both simulations, but it is not adjusted for the observation height of 4.1m, which means that the local wind speed in the simulations might be too low. The peak period agree well with observations.

In August 2019, a Wavescan buoy was deployed by Geophysical Institute, University

of Bergen and NPRA on the shelf edge *Storegga* around 90 km from the coast at Sulafjord. The buoy operated during the winter 2019-2020. The station is called *Svinøy* as it is close to a oceanographic section, *Svinøysnittet*, regularly monitored by the Institute of Marine Research. The highest waves during the time of the *Svinøy*-buoy were recorded 8 January 2020. We include this case in order to validate the boundary conditions from NORA10 to SWAN. Time series from NORA10 (both at the reference location and from the grid point closest to the buoy 62.81N 4.40E) agree well with the observations for  $H_s$  and  $T_p$  (figure 35). SWAN250 also agree well with buoy A in Sulafjord except for too high values of peak period. Overall,  $H_s$  and  $T_p$  from NORA10 has a correlation to observations of 0.95 and 0.7, respectively, with 6% overestimation in  $H_s$  (figure 35 lower plots).

The three cases in 2019 (case 11-13) occurring during the time of Sulafjord measurements are interesting to include (figure 36). In all three cases long period waves enter Sulafjord and are recorded by the buoys.  $T_p$  registered at B shift between wind sea and the incoming swell/ocean waves, while SWAN keeps the swell/ocean waves as the dominant waves.

The fiercest storms in the NORA10 archive for this region occurred on 22 December 1988, 1 January 1992 and 25 December 2011 (case 2-4) with offshore  $H_s$  of 14-16m. Case 4 is presented in figure 33. We have simulated the old cases, case 2 and 3, with SWAN150 using NORA10 winds (figure 37). In none of the cases the local wave height exceeds 4.4m at A which is maximum modeled and observed at A. However, NORA10 winds are very coarse and are considered too low in coastal regions. The wind speed during the 1992-hurricane was estimated<sup>4</sup> to have reached 46 m/s at *Svinøy* lighthouse and 36 m/s at *Vigra*, representing a 200-year event at that time [Aune and Harstveit, 1992]. The wind speed at *Vigra* was later adjusted to 30 m/s and this value is archived in the observation database of MET (the API frost.met.no). We have performed a downscaling of the global reanalysis ERA5 using the atmosphere model AROME to a grid of 750m x 750m (figure 38). The downscaling reproduces the *Vigra* winds of 30 – 32 m/s from southwest (but not the 46 m/s at *Svinøy*), while NORA10 has around 29 m/s at *Vigra* and decrease further inland. It is therefore possible that the  $H_s$  was higher in Sulafjord during the hurricanes than given in table 5.

To investigate a worst case scenario based on this, we have included two stationary simulations. Instead of NORA10 spectra on the boundaries, we use a JONSWAP spectrum ( $\gamma = 2.2$ , with integrated parameters  $H_s = 16\text{m}$ ,  $T_p = 18\text{s}$  as for case 2) on the border

---

<sup>4</sup>The instruments were not recording above approximately 31 m/s.

of the SWAN-domain. In S1, winds (32 m/s over the whole domain) and waves both act from NW ( $300^\circ$ ). In S2 we simulate the propagation of waves without wind. As seen in table 5 and figure 39 the effect of including wind on this large domain means a difference of 2.4 m in  $H_s$  at A. The peak period in the fjord is connected to the windsea in S1, i.e  $T_p$  around 8 s, due to the strong wind (figure 39).

The SWAN wave spectra from case S2 at D, A and B fit a JONSWAP-distribution quite well (figure 40 - lower plots). Adding wind to the simulation results as expected in wider bi-modal spectra at both A, B and C with a larger directional spread (lower  $s$ -value) (figure 40 - upper plots). These spectra conform better to Torsethaugen spectra. Please note that this is the result of a stationary solution and in reality the wind could be higher offshore and lower but very turbulent in some locations in the fjord, such as at C.

Finally, we have compared 1-D spectra from SWAN with observed spectra during three storms in Sulafjord (marked with \* in table 5) and two storms in Vartdalsfjord (figure 41-42) [Christakos, 2020]. The intention is to show the variability of the 10-minute spectra (raw data used for calculating the spectra are provided every 10 minutes, but contain data for 1024s) and how poor/well SWAN spectra compare. The wind sea appears as a peak for frequencies above approximately 0.15 Hz at the inner locations B, B1 and C, but generally the ocean waves/swell is dominating. An interesting case is the bi-modal spectrum at location C on 1 January 2019 where SWAN and observations agree very well. In comparison location F in Vartdalsfjord only show a single peak during the same storm. During storm situations we showed earlier that the observed spectra conform well to a JONSWAP spectrum. Location F is treated extensively in Christakos et al. [2020] and Christakos et al. [2021].

In summary; based on the analysis of this chapter and the result of our stationary simulation (case S1), it is possible that during a hurricane like case 3 (1 January 1992) but from northwest instead of southwest, the significant wave height at A can reach 5.6 m with a peak period of 17 s. As illustrated here, the wind conditions naturally plays a very important role.

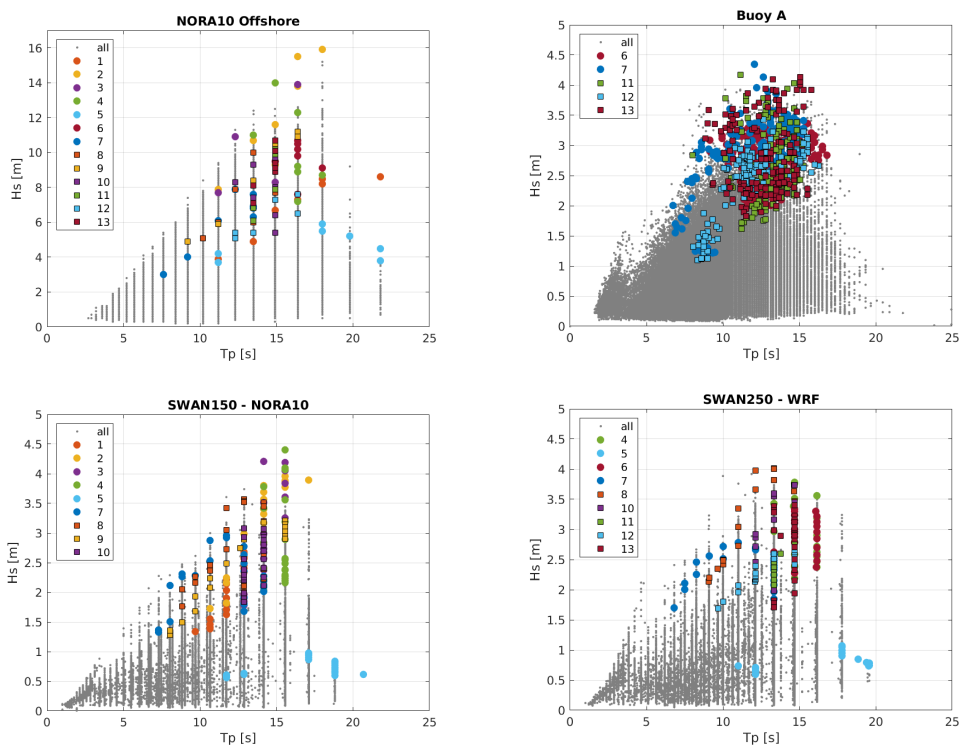


**Figure 32:**  $H_s$ - $T_p$  scatter diagrams for the NORA10 offshore location and location A in Sulafjord for data from the buoy, SWAN150 and SWAN250 with the selected cases indicated in color. The numbers refer to the first column of table 5.

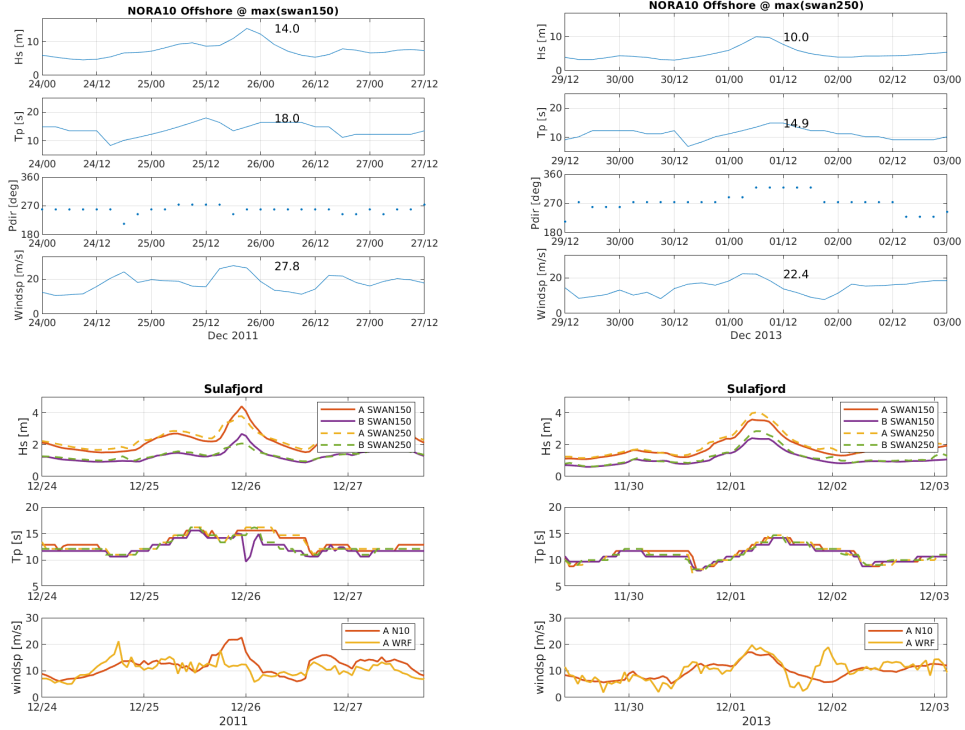


**Figure 33:** Time series with date / hour on the x-axis of offshore and location conditions during the two storms with the highest waves at A in the modelled data sets: case 4 and 8 in table 5 which were highest at A in SWAN150 and SWAN250, respectively. Top: NORA10 at an offshore location close to the border of SWAN. The highest values for each parameter during the storm is indicated in the plot. Below: Locations A and B. In the legend, "A SWAN150" and "B SWAN150" refers to SWAN150 with NORA10 winds at location A and B, "A SWAN250" and "B SWAN250" refers to SWAN250 with WRF winds. The same color is used for same location and data set for all the time series, e.g. SWAN150/NORA10 at A is orange, SWAN250/WRF at B is green etc. "A obs" and "B obs" are the observations from buoy A and B when available (after October 2016).

Case	Date and time	N10 $H_s T_p$	SWAN150/SWAN250 $H_s T_p$	Obs $H_s T_p$	Comment
1	15-Dec-1977 06:00	8.6 21.8	2.7/ 12.9/		Highest $H_s$ with max $T_p$ in NORA10
2	22-Dec-1988 15:00	15.9 18	4.0/ 17.1/		Max $H_s$ offshore in NORA10
3	01-Jan-1992 09:00	14 16.4	4.2/ 15.6/		200-yr repeat cycle in wind speed
4	25-Dec-2011 21:00	14 18	4.4/3.8 15.6/16.2		"Ekstremvær Dagmar". Max $H_s$ at A in SWAN150
5	07-Jan-2014 03:00	5.9 21.8	1.0/1.1 20.7/19.6		Max $T_p$ offshore in NORA10 with $H_s > 4m$
6	08-Jan-2020 21:00	10.7 18	/3.3 /16.2	3.4 16.8	Max $H_s$ on Svinøy buoy
7	03-Jan-2017 17:10	7.9 13.5	3.0/2.8 14.2/13.3	4.4 15.3	Max $H_s$ on A in observations, Nc1 *
8	01-Dec-2013 06:00	10 14.9	3.6/4.0 14.2/14.7		Max $H_s$ at A in SWAN250
9	24-Feb-2004 06:00	11.2 16.4	3.2/ 15.6/		$P_{dir}$ 275 - 315 offshore
10	16-Nov-2013 21:00	9.7 14.9	3.1/3.7 14.2/14.7		$P_{dir}$ 275 - 315 offshore
11	23-Mar-2019 18:00	10.2 14.9	/3.2/14.7	4.2 15.3	$P_{dir}$ 275 - 315 offshore, Nc14 *
12	11-Jan-2019 00:00	7.6 16.4	/2.7/14.7	3.4 16.3	$P_{dir}$ 275 - 315 offshore, Nc16
13	01-Jan-2019 12:00	10.7 14.9	/3.4/14.7	4.1 15.8	$H_s > 4m$ on A, Nc15 *
S1	-	16 18	5.6/- 17.1/-	-	Stationary run with 32m/s 300 deg. wind
S2	-	16 18	3.2/- 17.1/-	-	Stationary run without wind

**Table 5:** Selected storms in Sulafjord with maximum offshore (NORA10) and local (location A) conditions ( $H_s T_p$ ) during a 4 day interval centered at the date in column 2. Reason for selection of each case is indicated in the comment. Nc-number refers to the numbering of storms in Musch et al. [2019] (table 37, page 89 therein). Spectra from the three cases with \* are presented in figure 41.

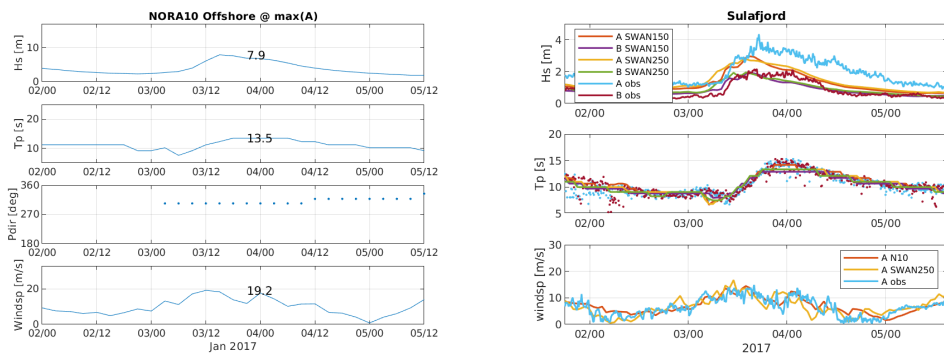


**Figure 34:** Time series of offshore and local conditions during the storm with the highest observed waves at A - case 7 in table 5.

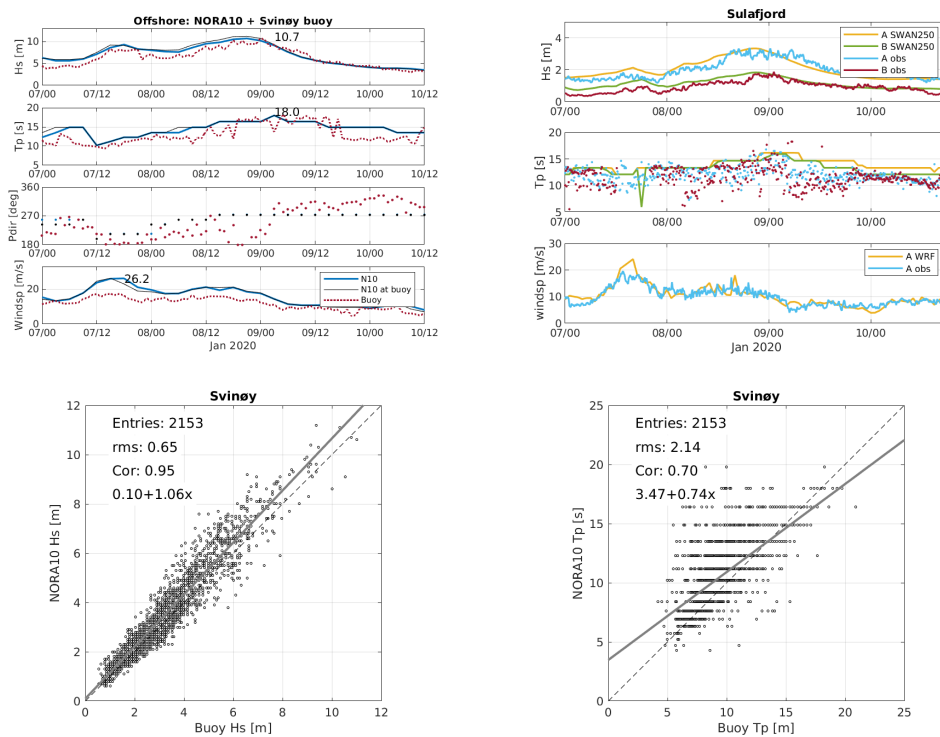


**Figure 35:** Top: Time series of offshore and local conditions during the storm with the highest observed waves at buoy location Svinøy (offshore) - case 6 in table 5. Bottom: Scatter plots of  $H_s$  and  $T_p$  of NORA10 against the offshore Svinøy-buoy.

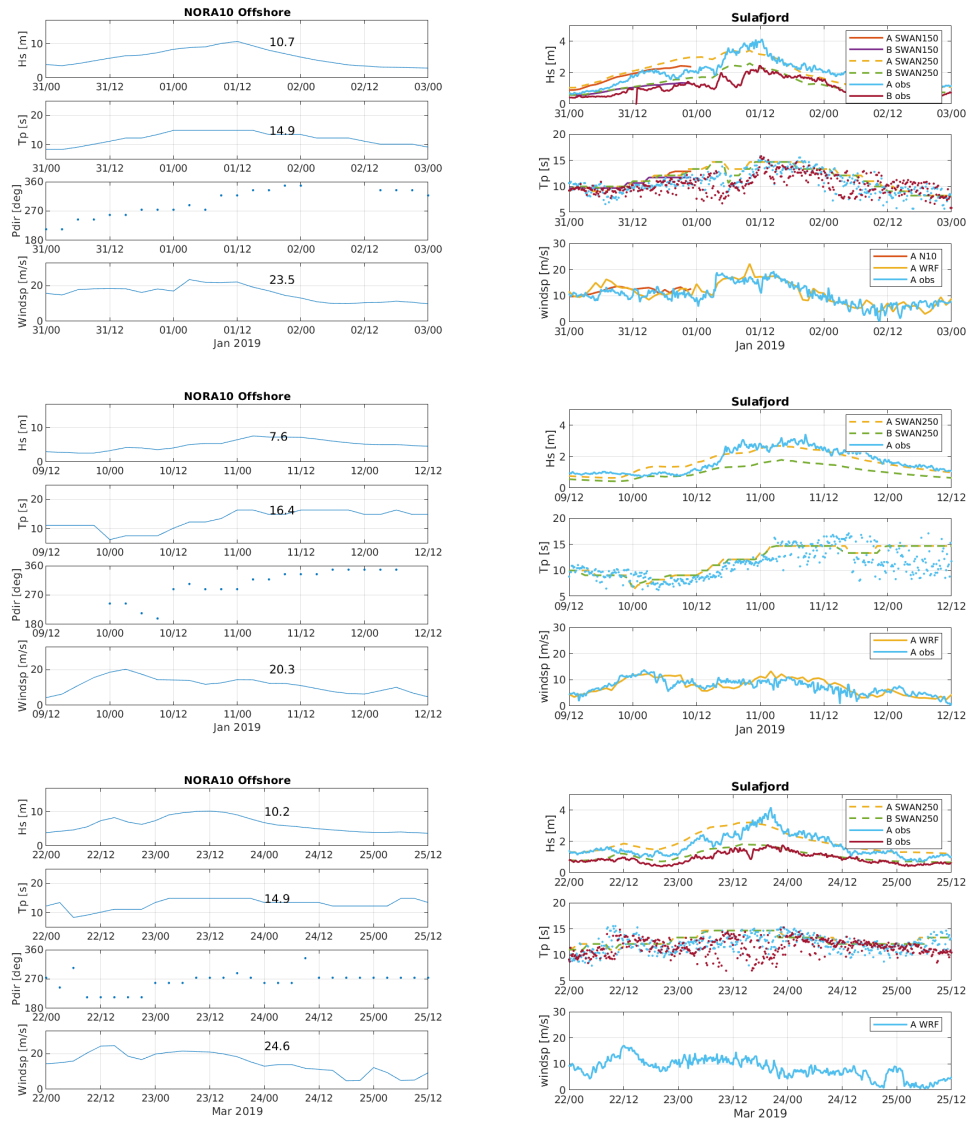


**Figure 36:** Time series of offshore and local conditions during three storms in 2019 - case 11\*, 12, 13\* in table 5. Buoy B have no observations for case 12. Observed spectra from case 11 and 13 are found in figure 41.

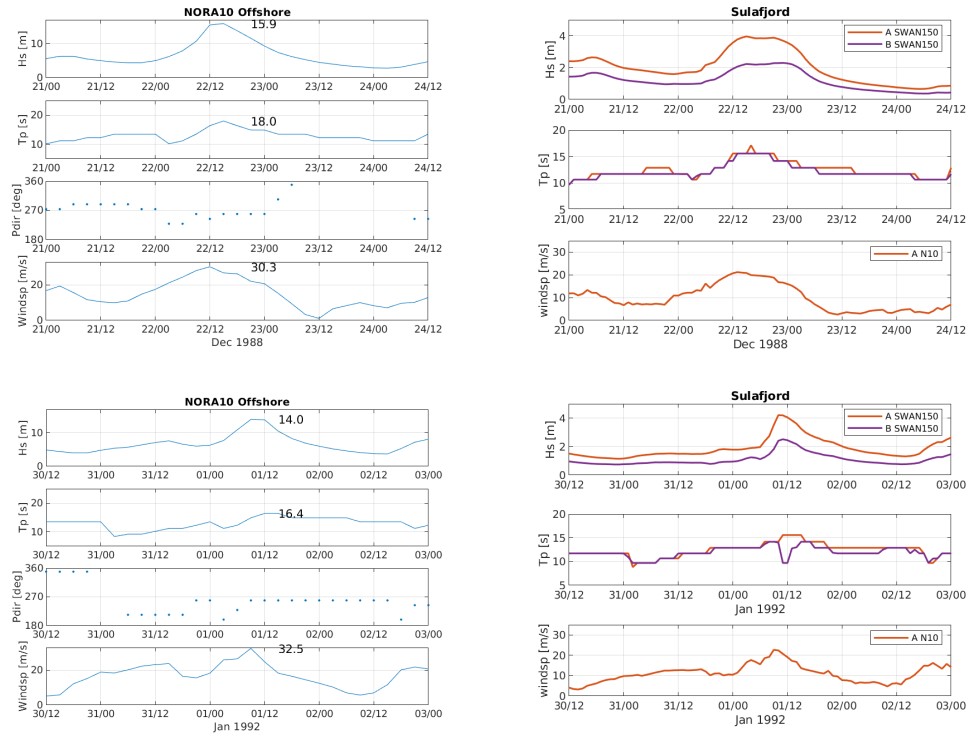


**Figure 37:** Time series of offshore and local conditions during the two strongest hurricanes in NORA10, case 2 and 3 in table 5.

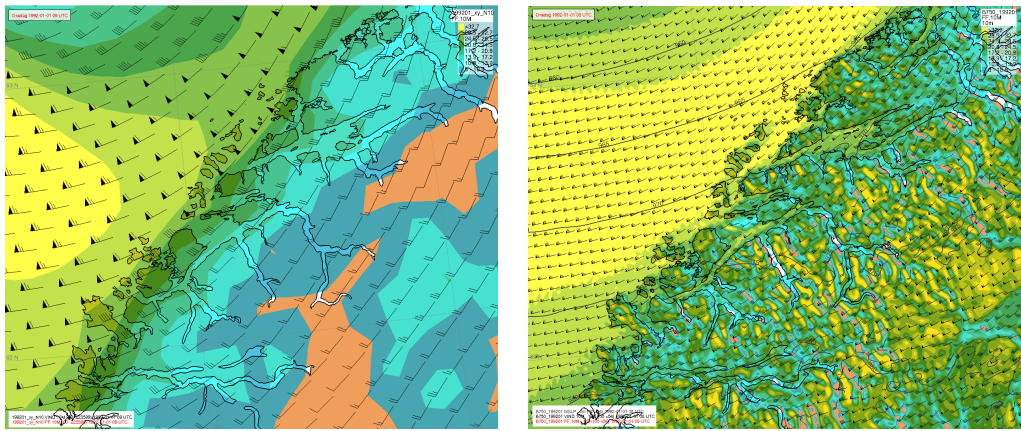


**Figure 38:** 10 m wind speed and wind vectors during the hurricane 1 January 1992 from NORA10 (HIRLAM with grid 10km x 10km) at 09 UTC (left) and from a downscaling of ERA5 with AROME (grid 750m x 750m) 07 UTC (right).

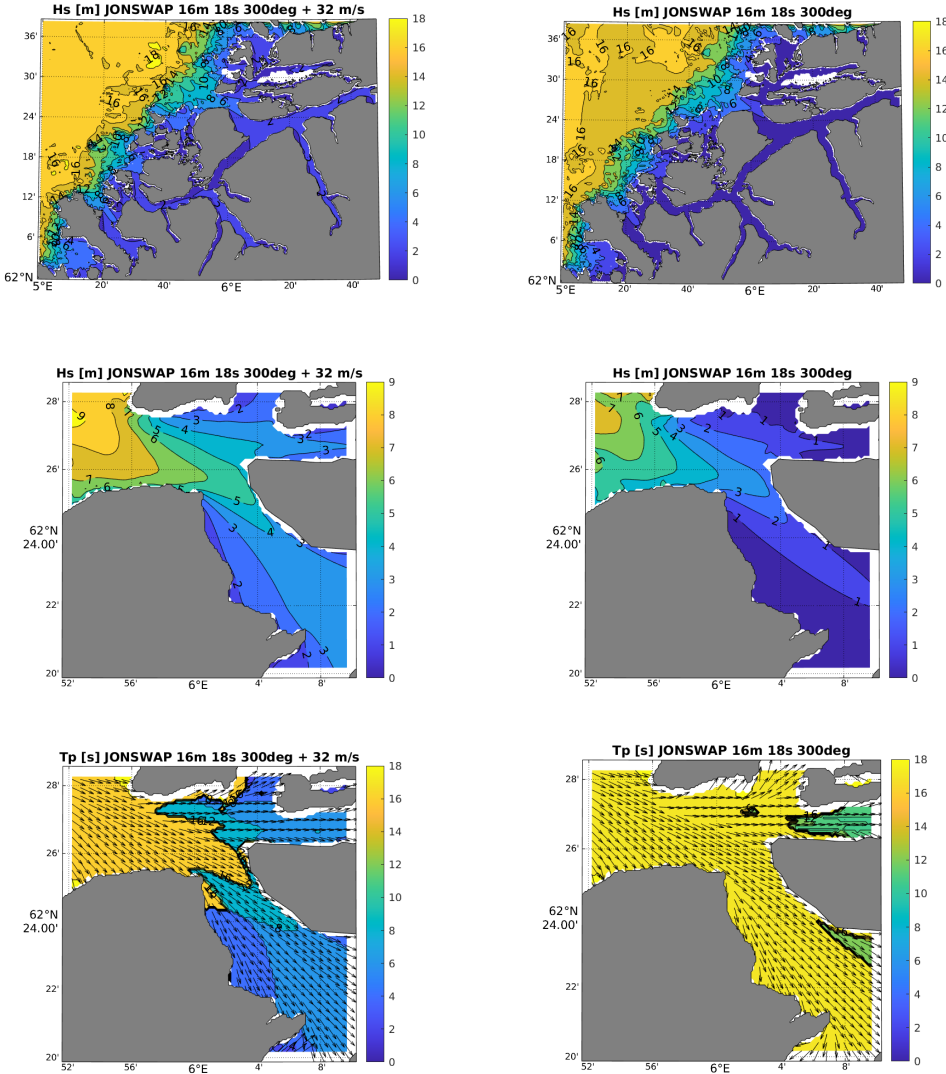


**Figure 39:** Maps of  $H_s$  for the full SWAN150 domain (top) and for a subsection around Sulafjord (middle) and maps of  $T_p$  and peak direction (below) for cases S1 (with 32 m/s wind from northwest) and S2 (without wind) in table 5 (left and right, respectively). The parameters used to define a JONSWAP spectrum on the border is  $H_s = 16$  m,  $T_p = 18$  s and peak direction  $300^{\circ}$ , as given in the titles.

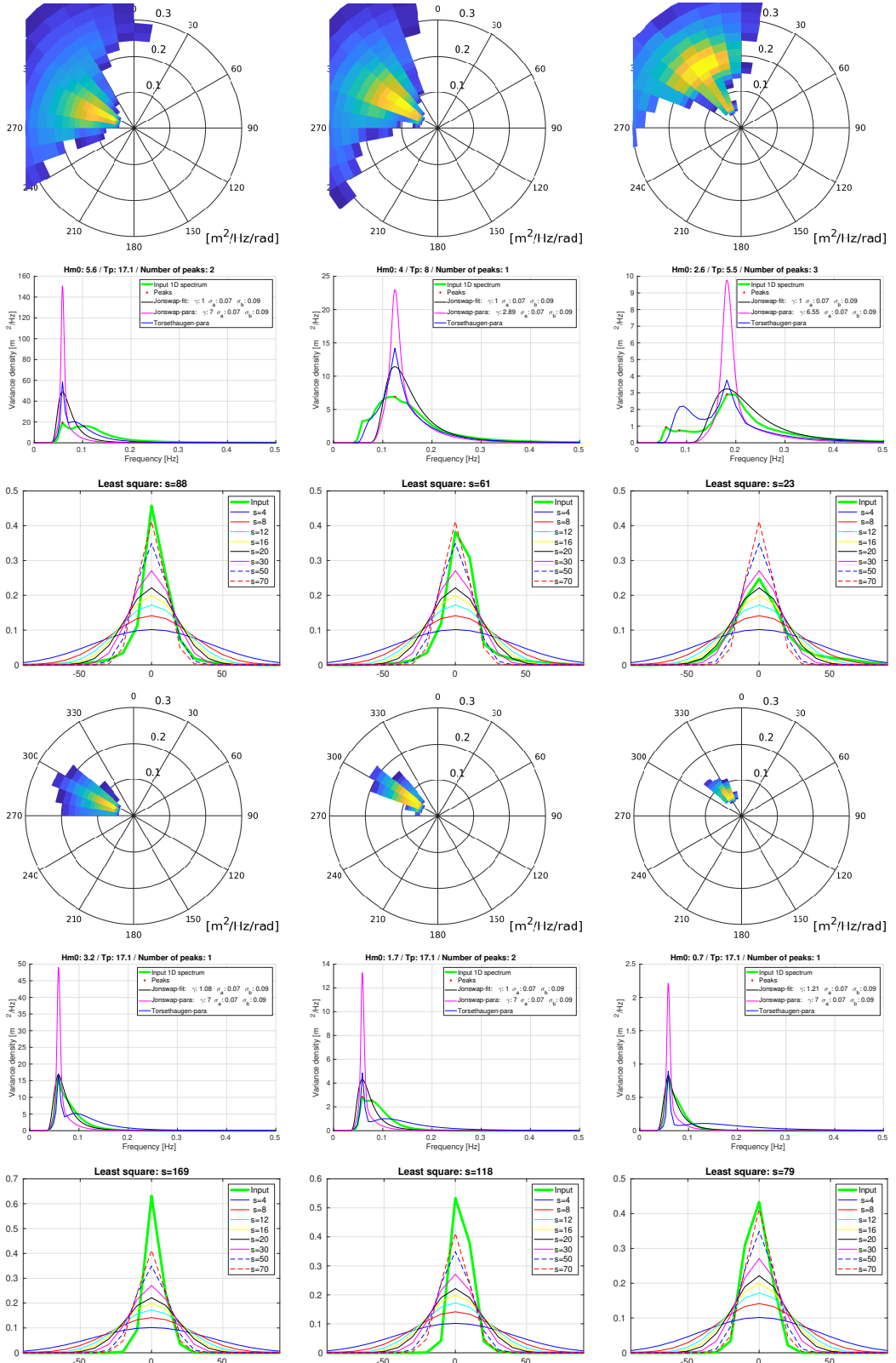


**Figure 40:** SWAN spectra from two stationary runs with (top) and without (bottom) wind forcing at position A (right), B (center) and C (right).

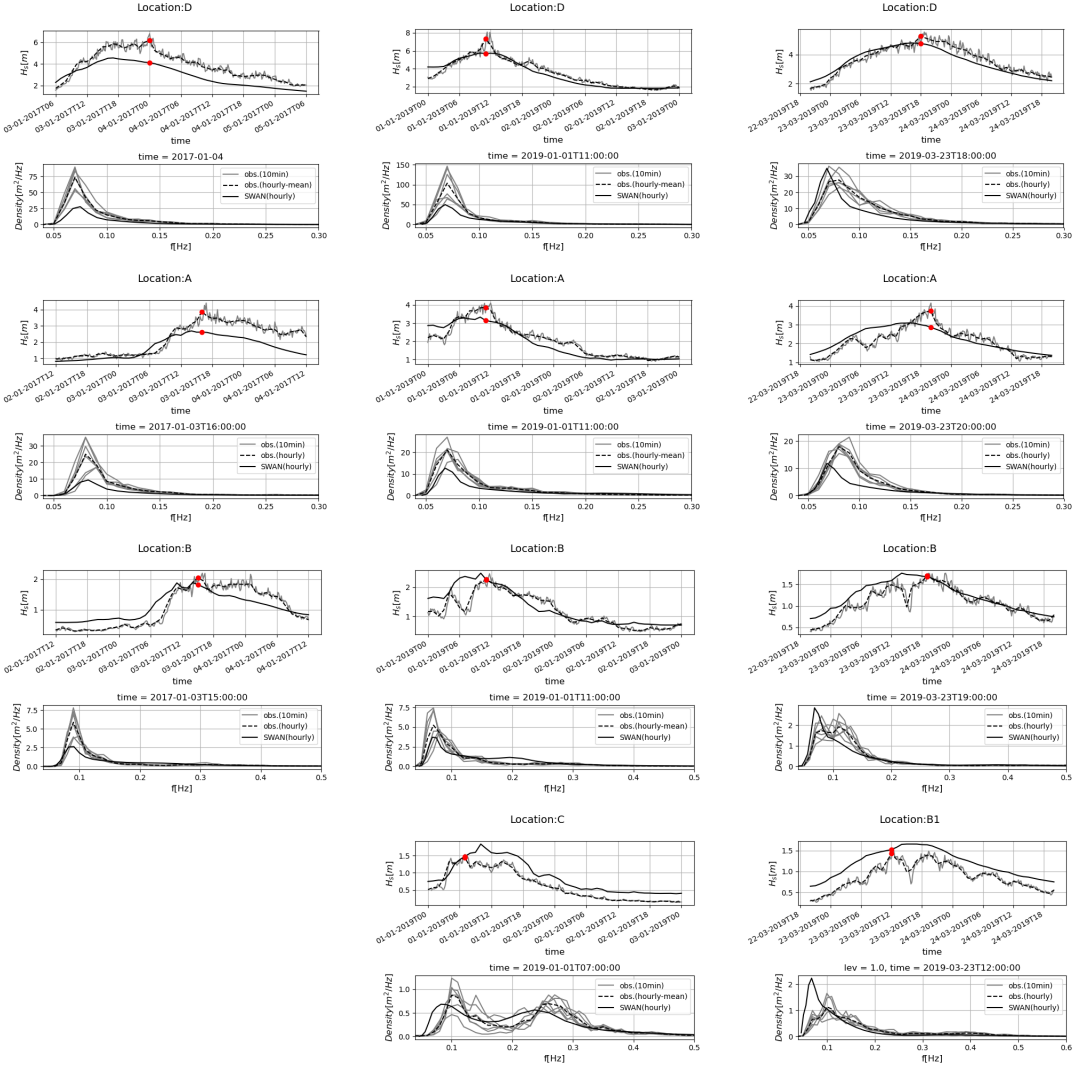


**Figure 41:** Time series and spectra at the time indicated by the red dot from buoys D, A, B, C (B1 from the last case) (dashed and gray lines) in Sulafjord during the three events (columns) with  $H_s$  measured above 4 m at buoy A. Time series and spectra from SWAN are included as full black lines. Please note the different scales on the plots.

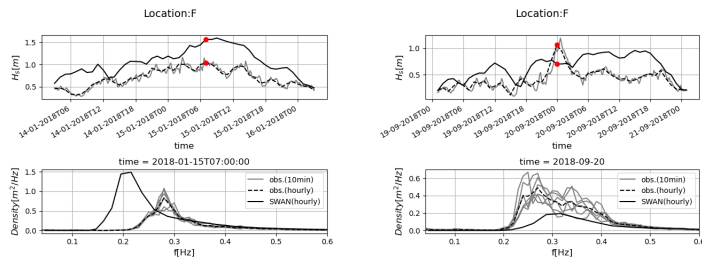


**Figure 42:** Time series and spectra at the time indicated by the red dot from buoy F (dashed and gray lines) in Vartdalsfjord during the two highest storms measured at F. Time series and spectra from SWAN are included as full black lines. Please note the different scales on the plots.

## 7 Appendix

### 7.1 Extreme statistics

In this study we consider three commonly applied extreme value models in our quest for reliable return value estimates, all presented in DNVGL [2019]. Primarily, these techniques differ in their way of utilizing the initial data. Two of the techniques retain only a smaller subset of the initial data to obtain a dataset that is independent and identical distributed (IID), while the third utilizes all available data (dependent data). The different subsets dictate the applied statistical distribution.

- Annual maximum data / Generalized Extreme Value distribution
- Peaks over threshold data / Generalized Pareto distribution
- Initial data / 3-parametric Weibull distribution

A brief presentation of each statistical distribution is presented below, i.e. the *Generalized Extreme Value* distribution, the *Generalized Pareto* distribution and the *Weibull* distribution. A more thorough description may be found in Coles [2001], Aarnes et al. [2012], DNVGL [2019].

In general, extreme value models may be extrapolated to any return period, but becomes somewhat speculative when exceeding the length of the dataset by a factor of 3-4 [Lopatoukhin et al., 2000]. In this work we use a time series of 13 years or less, making the 100-year return value estimates uncertain, but justifiable.

#### 7.1.1 Generalized Extreme Value Distribution

Instead of fitting a statistical distribution to the initial data set of a variable  $X$ , this approach only retains the annual maximum of the data  $M_n = \max \{X_1, \dots, X_n\}$ , also referred to as block maxima, where  $n$  represents the total number of entries per year. Given that the initial data belongs to the same statistical distribution (identical), the distribution of the renormalized block maxima  $\Pr \{(M_n - \mu)/\sigma \leq z\}$  should conform to the *Generalized Extreme Value* (GEV) distribution:

$$F_{GEV}(z) = \exp \left\{ - \left[ 1 + \xi \left( \frac{z - \mu}{\sigma} \right) \right]^{-1/\xi} \right\}, \quad (15)$$

The distribution is defined by three parameters, i.e. the location parameter  $\mu$ , the scale parameter  $\sigma$  and the shape parameter  $\xi$ . Depending on the sign of  $\xi$ , the tail characteristics of the distribution change. For  $\xi > 0$ , known as the Fréchet distribution, the distribution decays polynomially. For  $\xi = 0$ , known as the Gumbel distribution, the distribution decays exponentially. Both distributions are unbounded on  $z$ . For  $\xi < 0$ , the distribution is of the Weibull-type, and is bounded on  $z$ . Return value estimates of  $z$  is obtained by inverting eq. 15

$$z_p = \begin{cases} \mu - \frac{\sigma}{\xi} \left[ 1 - \{-\ln(1-p)\}^{-\xi} \right] & \text{for } \xi \neq 0 \\ \mu - \sigma \ln \{-\ln(1-p)\} & \text{for } \xi = 0, \end{cases} \quad (16)$$

where  $F_{GEV}(z) = 1 - p$  represents the probability of non-exceedance,  $p$  represents the probability of exceedance and the inverse of  $p$  corresponds to the return period in years. By setting  $y_p = -\ln(1-p)$ , equation 16 can be reformulated

$$z_p = \begin{cases} \mu - \frac{\sigma}{\xi} \left[ 1 - y_p^{-\xi} \right] & \text{for } \xi \neq 0 \\ \mu - \sigma \ln y_p & \text{for } \xi = 0, \end{cases} \quad (17)$$

The 1, 5, 10, 100, 1000 and 10000-year return value estimates corresponds to  $p$  equal to  $[0.63, 5^{-1}, 10^{-1}, 10^{-2}, 10^{-3}, 10^{-4}]$ .

The GEV distribution can be presented in a return value plot by plotting  $z_p$  against  $-\ln y_p$  (Gumbel paper). For  $\xi = 0$ , the distribution goes straight, otherwise the distribution will be non-linear and either bounded or unbounded on  $z$ . In order to validate the fit (goodness of fit) between the theoretical distribution and the distribution of the blocked maxima, each data entry is given the cumulative probability

$$P_r = \frac{r - b}{N + 1 - 2b} \quad (18)$$

and plotted in the same return value plot. Here,  $b$  equals 0 [Makkonen, 2006],  $r$  represents the rank of the block maxima and  $N$  the total number of maxima/years. Ideally the empirical distribution function of the blocked maxima line up perfectly with the theoretical distribution.

### 7.1.2 Generalized Pareto Distribution

The POT-approach (*peaks-over-threshold*) is a common alternative to the blocking procedure presented above. Rather than extracting only one entry per block (annual maximum), all peaks above some prescribed threshold are extracted. In order to keep the data

set uncorrelated (independent), a minimum of 24-48 hours between each peak is required, which is approximately the time span of the passing of an extratropical cyclone.

It can be shown that if eq. 15 is satisfied for  $z$ , the distribution of  $y = X - u$  is given by

$$F_{GP}(y) = 1 - \left(1 - \frac{\xi y}{\tilde{\sigma}}\right)^{-1/\xi}, \quad (19)$$

where  $\tilde{\sigma} = \xi(u - \mu)$  and  $u$  represents the threshold. When  $\xi \rightarrow 0$ , equation 19 becomes the exponential distribution.

$$F_{GP}(y) = 1 - \exp\left(-\frac{y}{\tilde{\sigma}}\right). \quad (20)$$

One of the potential benefits of using a threshold model is the possibility of utilizing more data for the distribution fitting. Even so, there exist no consensus on how to choose an optimal threshold. Therefore, in the following we carefully study the return value plots of the GP distribution as the threshold is let to vary. The return value plots are obtained by plotting the  $N$ -year return level,  $z_N$ , against  $-\ln(1 - p)$ . The  $N$ -year return value is the level expected to be exceeded on average once every  $N$  years. If there are a total of  $n_y$  observations per year (=2922 for three-hourly data), then the the  $N$ -year return level is defined by

$$z_N = \begin{cases} u + \frac{\sigma}{\xi} [(Nn_y \zeta_u)^\xi - 1] & \text{for } \xi \neq 0 \\ u + \sigma \ln(Nn_y \zeta_u) & \text{for } \xi = 0, \end{cases} \quad (21)$$

A natural estimator for  $\zeta_u$  is  $\hat{\zeta} = k/n$ , where  $k$  represents the number of peaks above the threshold  $u$  from a total of  $n$  data entries.

### 7.1.3 Weibull Distribution

Following DNVGL [2019], the threshold excesses obtained with the POT-approach should conform to the 2-parameter Weibull distribution

$$F_{2pW}(y) = 1 - \exp\left[-\left(\frac{y}{\alpha}\right)^\beta\right], \quad \text{for } y \geq 0 \quad (22)$$

where  $\alpha > 0$  is the scale parameter and  $\beta > 0$  is the shape parameter.

The  $N$ -year return level is defined by

$$z_N = u + \alpha \left[-\ln\left(\frac{1}{Nn_y \zeta_u}\right)\right]^{1/\beta} \quad (\text{real}) \quad (23)$$

In addition we confer with the 3-par Weibull using all data (Initial Distribution Method - IDM), using the fitting techniques method of moments (MOM) and least square (LS). The latter is conducted based on different bin-intervals of the data. For more information see [DNVGL, 2019].

#### 7.1.4 Fitting procedure

In this study we use three different fitting techniques; maximum likelihood, method of moments and least square. *Maximum likelihood* is often considered superior because the different parameter values are found such that they maximise the likelihood that the process described by the model produce the data sample at hand. This is obtained by maximizing the equation

$$L(\theta) = \prod_{i=1}^n f(z_i; \theta), \quad (24)$$

or more conveniently the log-likelihood function

$$\ell(\theta) = \ln L(\theta) = \sum_{i=1}^n \ln f(z_i; \theta), \quad (25)$$

where  $f$  represents the pdf and  $\theta = (\xi, \sigma, \mu)$ . The maximizing of eq. 25 is solved iteratively by numerical techniques.

Although, theoretical advantages, maximum likelihood can be difficult to work with in practice. *Method of moments* (MOM) is often less cumbersome as the distribution parameters are estimated from the statistical moments of the data sample, i.e mean, variance, skewness. MOM usually provide good fit to the mode of the distribution, however, not always to the extremes.

In order to provide more weight to the tail of the distribution, *least square* (LS) can be an easy and effectiv approach, where the sum of squared errors between the empirical distribution and the fitted probabilities are minimized. LS is typically more heavily dictated by the tail behaviour of the data than MOM and MLE.

#### 7.1.5 LoNoWe - Joint distribution of $H_s$ and $T_p$

The LoNoWe-model (LogNormal-Weibull) is developed to represent the long term joint distribution of significant wave height,  $H_s$ , and peak period,  $T_p$ . Most of this analysis follow the work by Moan et al. [2005], DNVGL [2017].

The LoNoWe joint density function is expressed by

$$f_{H_s, T_p}(h, t) = f_{H_s}(h) \cdot f_{T_p|H_s}(t|h) \quad (26)$$

where the marginal distribution of  $H_s$  is given by

$$f_{H_s}(h) = \frac{1}{\sqrt{2 \cdot \pi} \cdot \alpha \cdot h} \exp\left(-\frac{(\ln(h) - \Theta)^2}{2 \cdot \alpha^2}\right) \quad \text{for } h \leq \eta \quad (27)$$

representing the lowest part of the distribution (LogNormal) and

$$f_{H_s}(h) = \frac{\beta}{\rho} \left(\frac{h}{\rho}\right)^{\beta-1} \exp\left[-\left(\frac{h}{\rho}\right)^\beta\right] \quad \text{for } h > \eta \quad (28)$$

representing the high-end of the distribution (2p-Weibull). The shifting point between the two distributions is selected using a Chi-square test, fulfilling the principal of continuity between the two distributions, both for the pdf and the cumulative distribution function (cdf) at the shifting point.

The peak period  $T_p$  is assumed to follow a pure lognormal distribution, however, with a conditionality set on  $H_s$ :

$$f_{T_p|H_s}(t, h) = \frac{1}{\sqrt{2 \cdot \pi} \cdot \sigma \cdot t} \cdot \left(-\frac{(\ln(t) - \mu)^2}{2 \cdot \sigma^2}\right) \quad (29)$$

where

$$\mu = a_1 + a_2 \cdot h^{a_3} \quad \text{for } a_3 \leq 1 \quad (30)$$

$$\sigma^2 = b_1 + b_2 \cdot \exp(-b_3 \cdot h) \quad (31)$$

represent the mean and variance of  $\ln(T_p)$ , respectively, which are functions of  $H_s$ . Here, the simultaneous data of  $H_s$  and  $T_p$  are binned with respect to  $H_s$ , every 0.5 or 1 m, and the coefficients  $a_1$ ,  $a_2$ ,  $a_3$ ,  $b_1$ ,  $b_2$  and  $b_3$  are established by curve fitting eq. 30 and 31 to the mean and variance of  $\ln(T_p)$  within each  $H_s$ -bin.

## 7.2 Validation plots

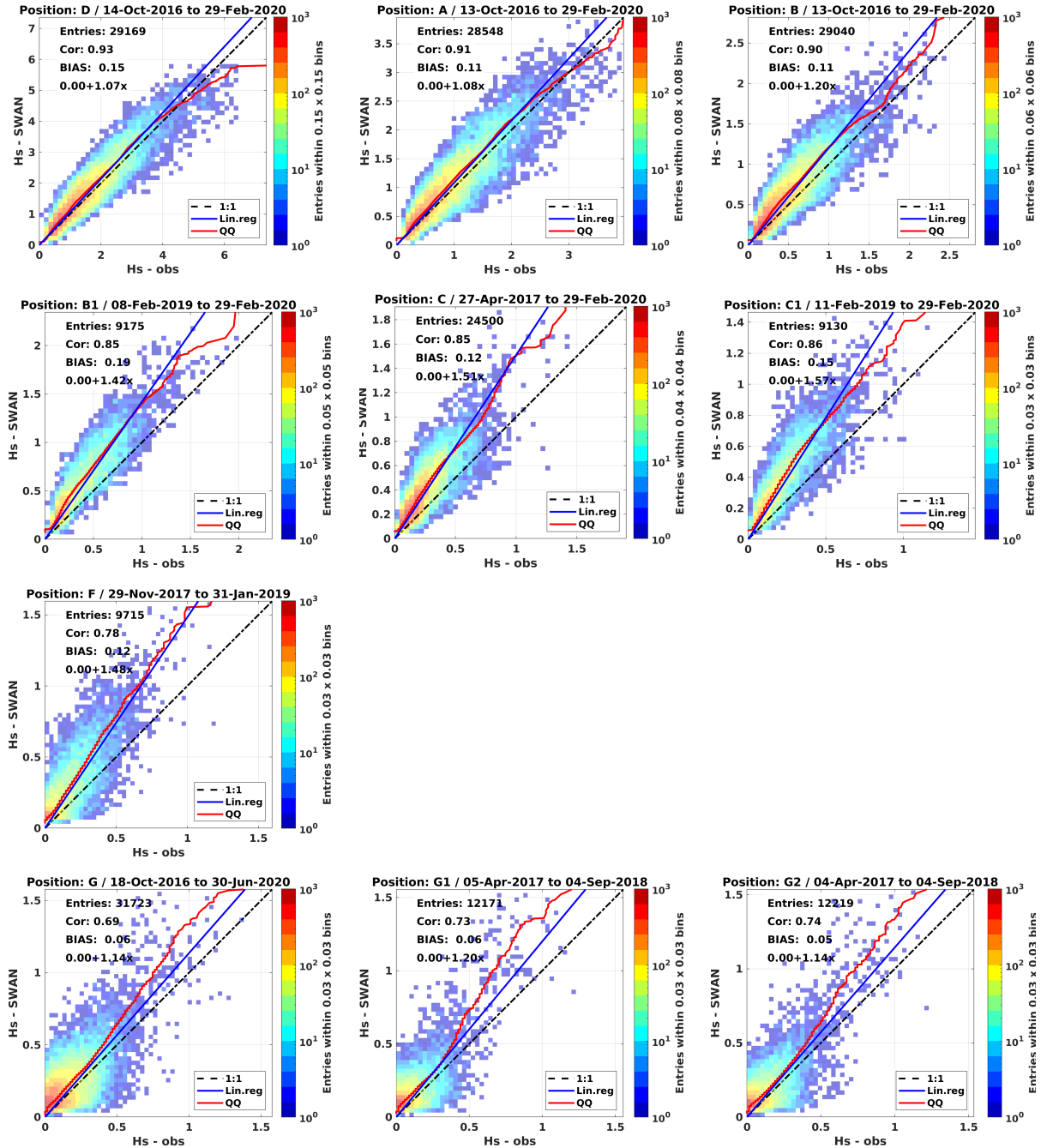


**Figure 43:** Regression plots of  $H_s$ ; observations ( $x$ -axis) and SWAN ( $y$ -axis). Station and validation period is presented in the title, while the number of corresponding data(entries), correlation (cor), bias and regression slope (blue line) is provided in the legend. The quantile-quantile line is given in red

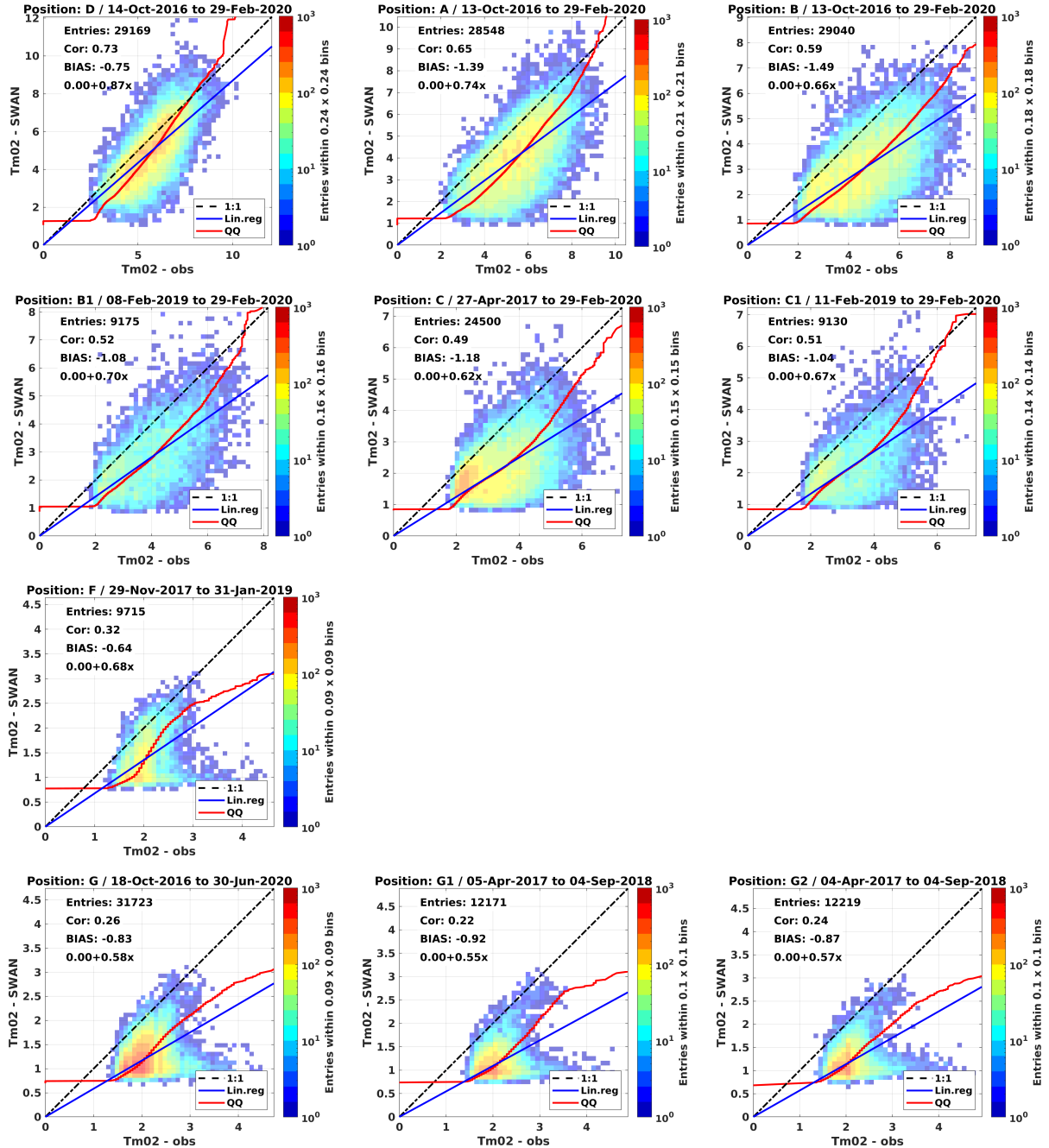


**Figure 44:** Regression plots of Tm02; observations (x-axis) and SWAN (y-axis). Station and validation period is presented in the title, while the number of corresponding data(entries), correlation (cor), bias and regression slope (blue line) is provided in the legend. The quantile-quantile line is given in red

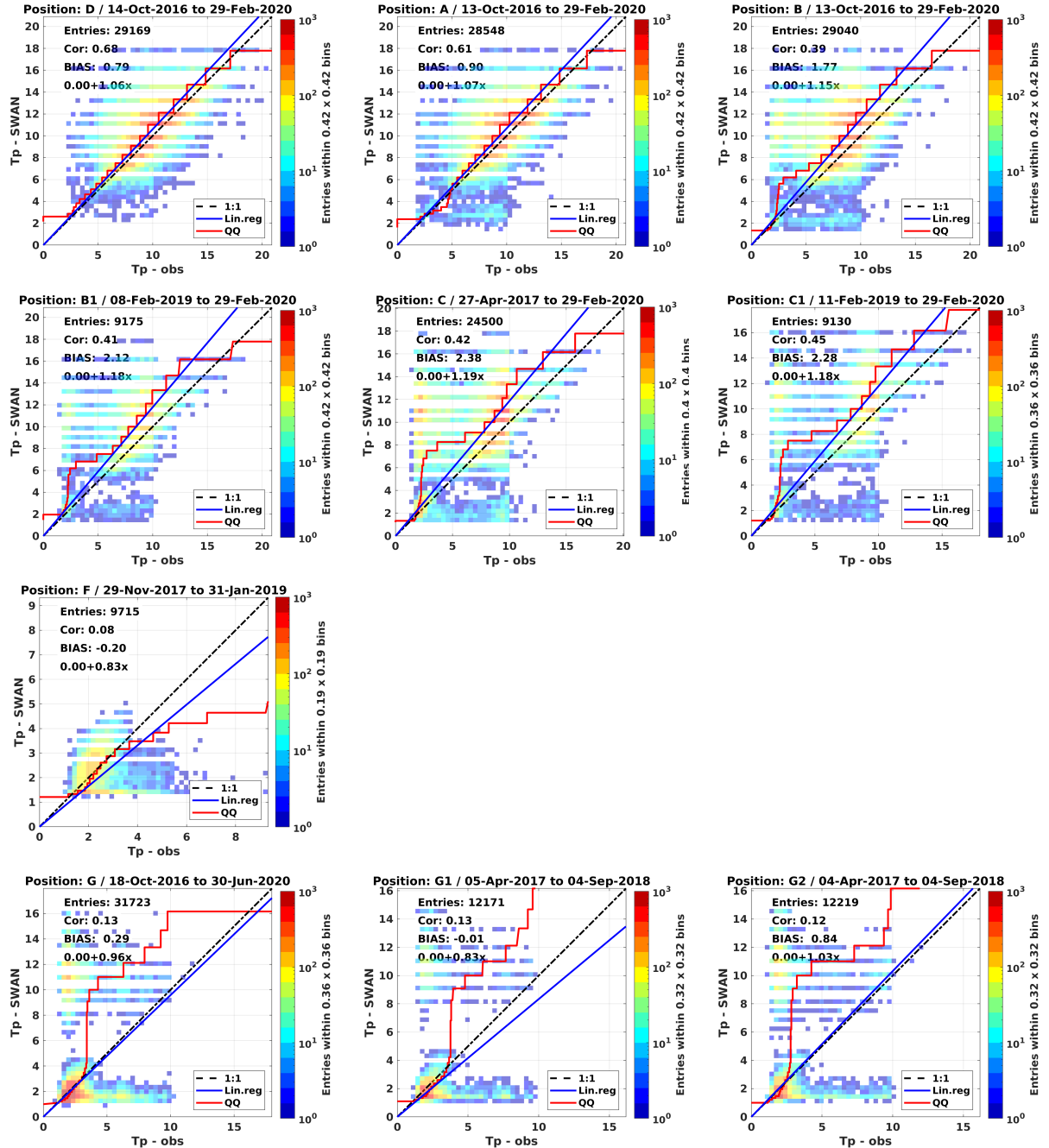


**Figure 45:** Regression plots of  $T_p$ ; observations ( $x$ -axis) and SWAN ( $y$ -axis). Station and validation period is presented in the title, while the number of corresponding data(entries), correlation (cor), bias and regression slope (blue line) is provided in the legend. The quantile-quantile line is given in red

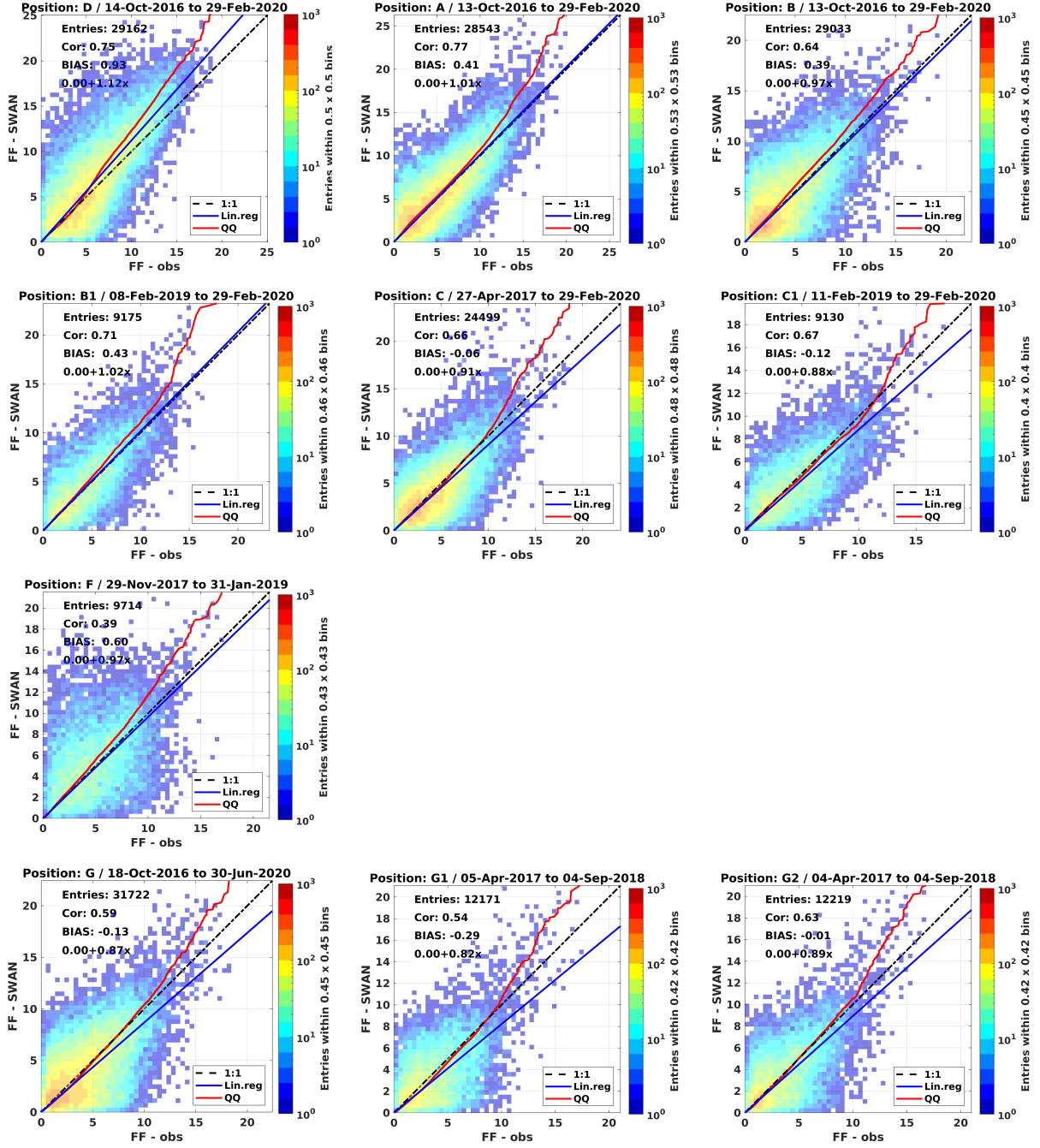


**Figure 46:** Regression plots of FF; observations (x-axis) and SWAN (y-axis). Station and validation period is presented in the title, while the number of corresponding data(entries), correlation (cor), bias and regression slope (blue line) is provided in the legend. The quantile-quantile line is given in red

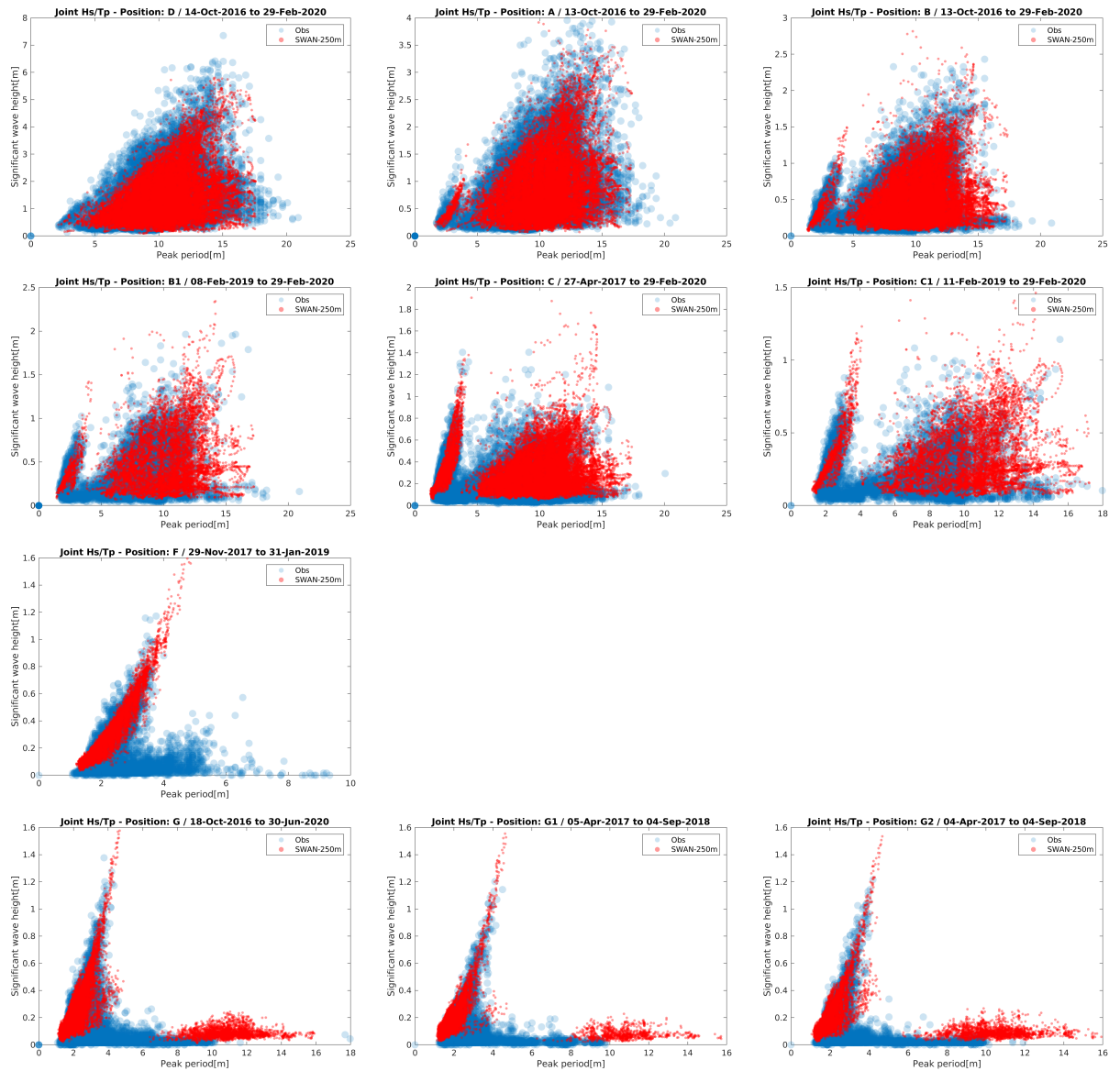


**Figure 47:** Scatter plots of  $Hs/Tp$  at corresponding hours; SWAN (red) and observations (blue).

### **7.3 Return value plots**

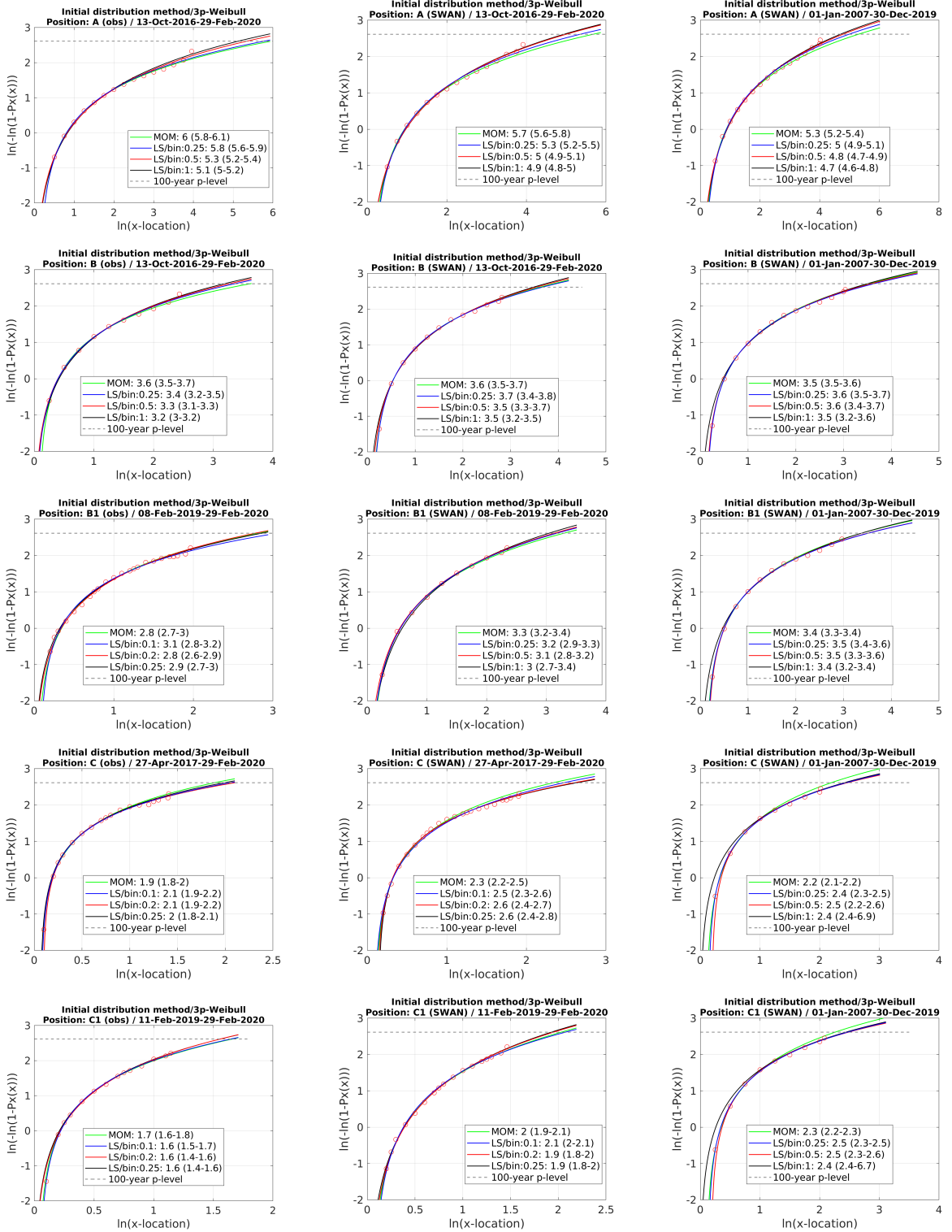


**Figure 48:** Return value plots in Sulafjorden based on observations (left), SWAN for the corresponding period (center) and SWAN for the period 01-Jan-2007 to 30-Dec-2019 (right). 100-year return value estimates are presented in the legend. MOM represents the method of moments estimates, while LS represents least square estimates for different bin-sizes of  $H_s$ . 95%-confidence intervals are provided in brackets.

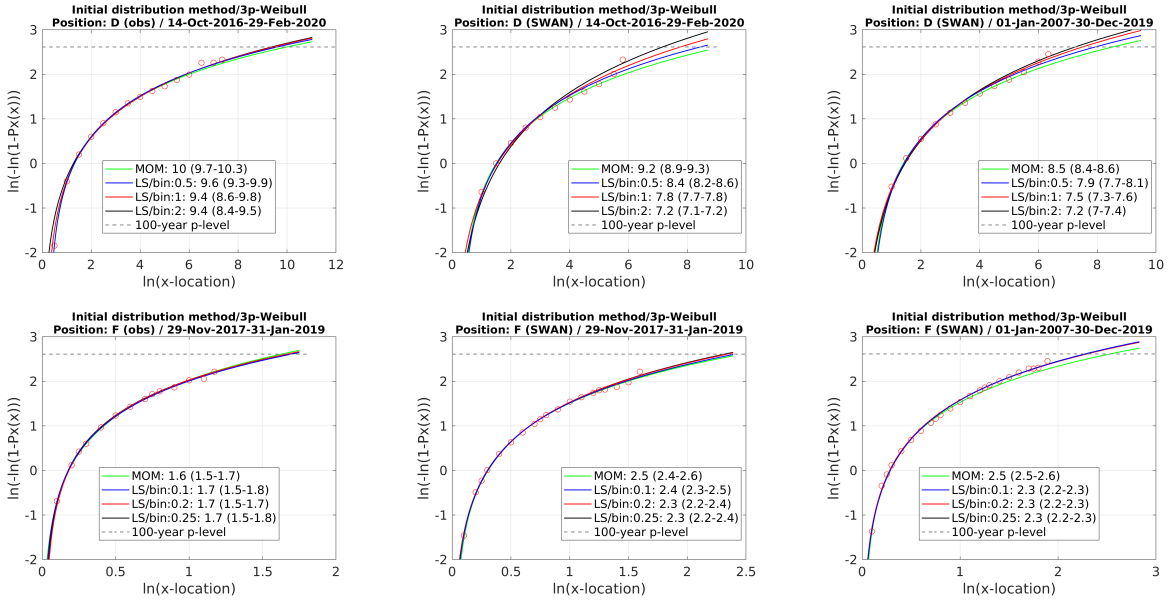


**Figure 49:** Return value plots in Sulafjorden based on observations (left), SWAN for the corresponding period (center) and SWAN for the period 01-Jan-2007 to 30-Dec-2019 (right). 100-year return value estimates are presented in the legend. MOM represents the method of moments estimates, while LS represents least square estimates for different bin-sizes of  $H_s$ . 95%-confidence intervals are provided in brackets.

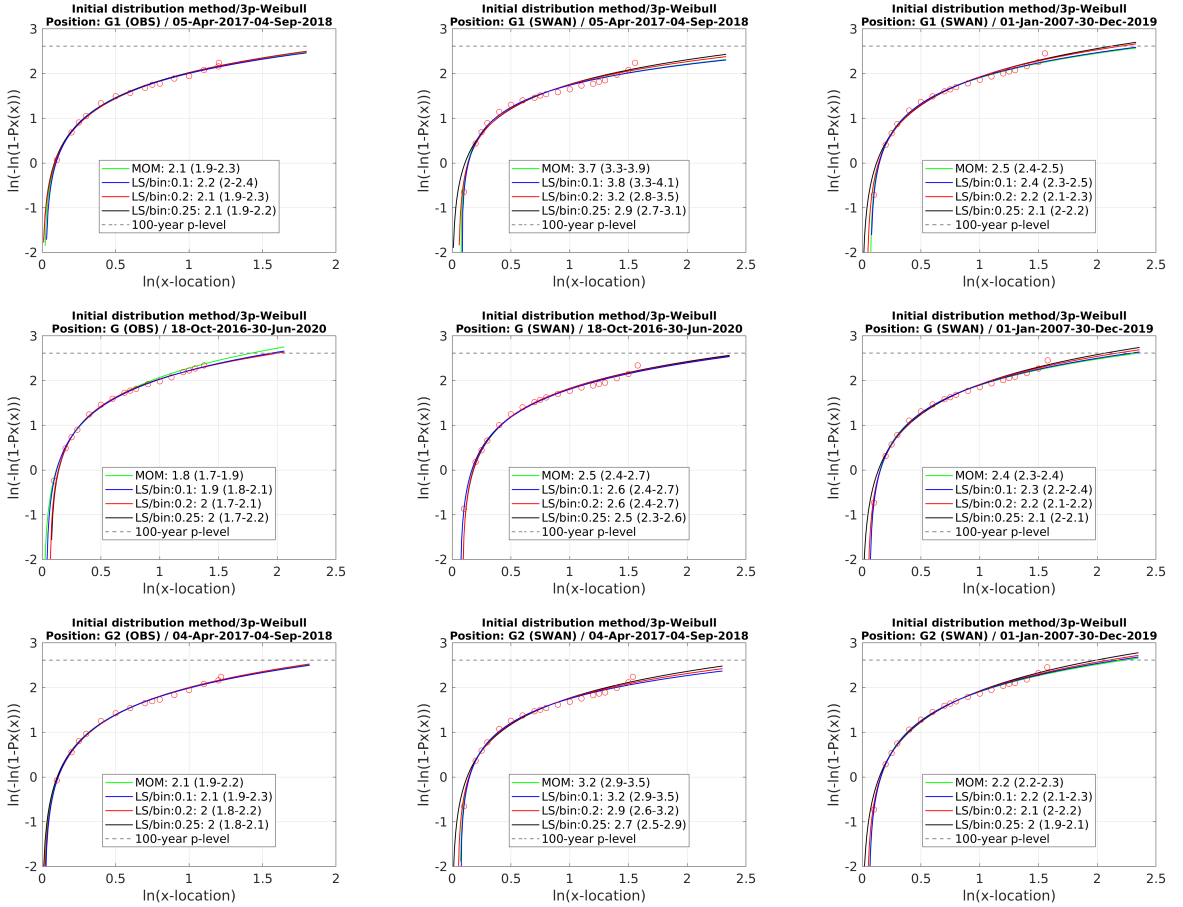


**Figure 50:** Return value plots in Halsafjorden based on observations (left), SWAN for the corresponding period (center) and SWAN for the period 01-Jan-2007 to 30-Dec-2019 (right). 100-year return value estimates are presented in the legend. MOM represents the method of moments estimates, while LS represents least square estimates for different bin-sizes of  $H_s$ . 95%-confidence intervals are provided in brackets.

## 7.4 Spectral characteristics

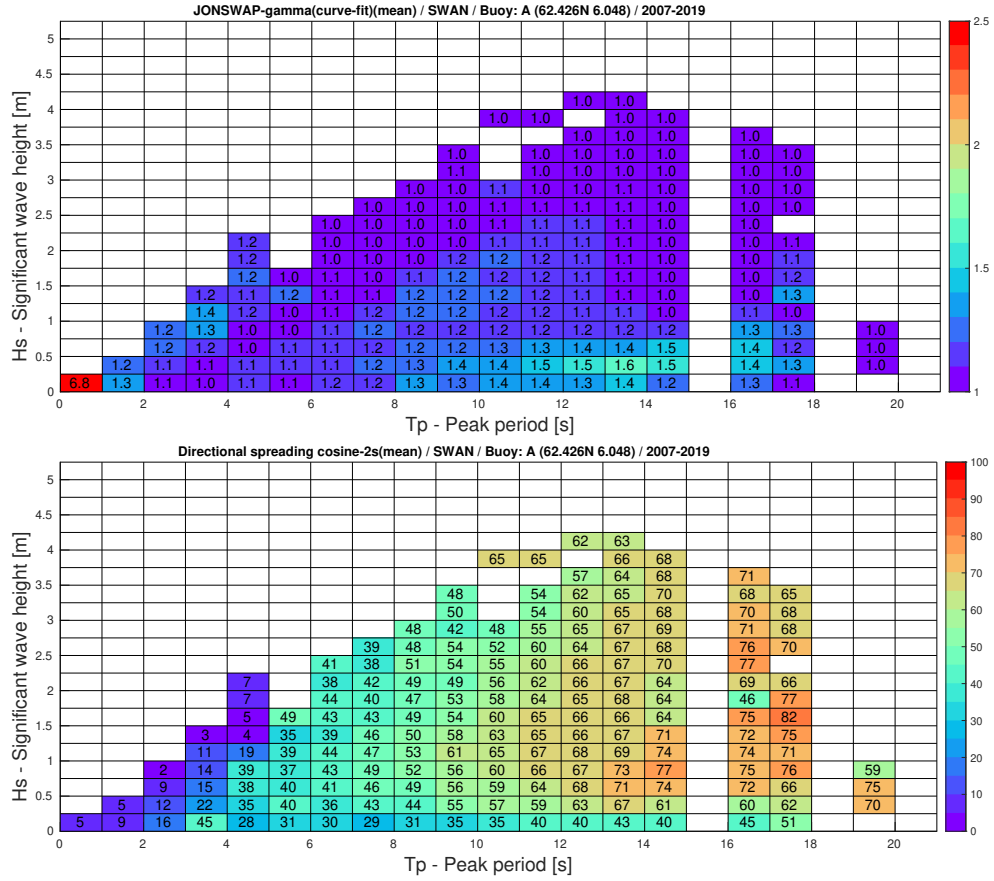


**Figure 51:** Modelled spectral properties at location A: Mean JONSWAP-gamma (top) and mean directional spread  $s$  of eq. 14 (bottom) binned according to peak period versus significant wave height.

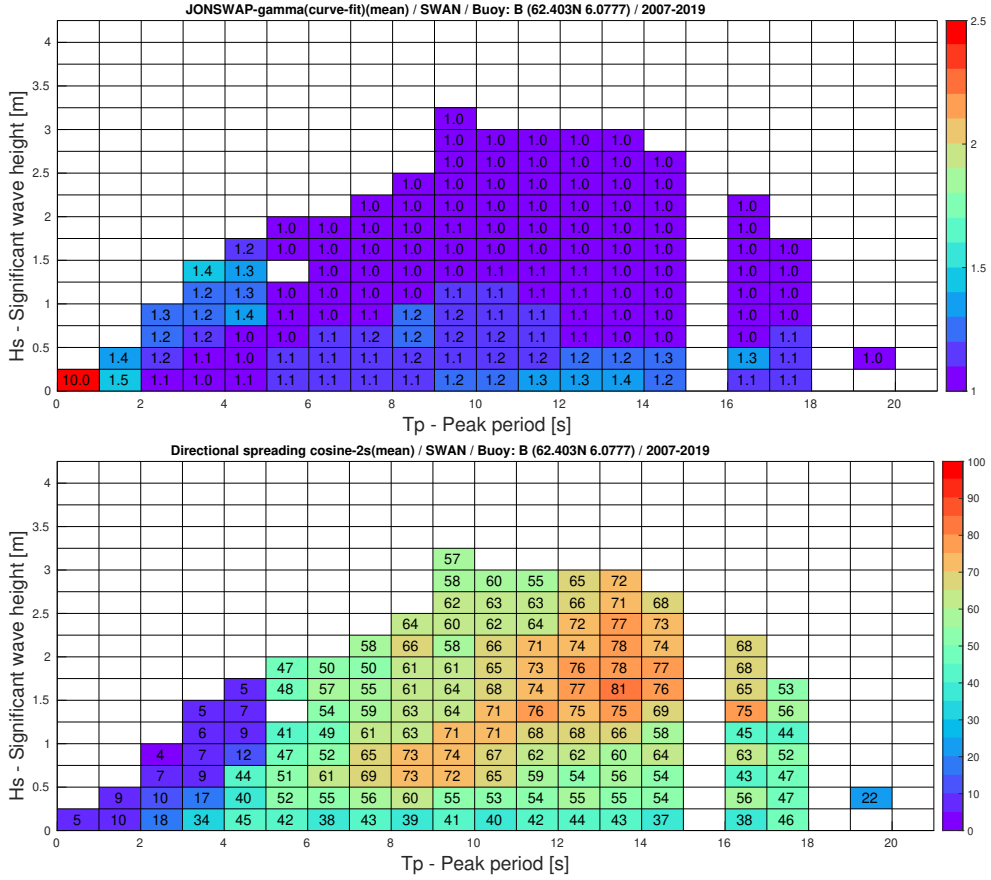


**Figure 52:** Modelled spectral properties at location B: Mean JONSWAP-gamma (top) and mean directional spread  $s$  of eq. 14 (bottom) binned according to peak period versus significant wave height.

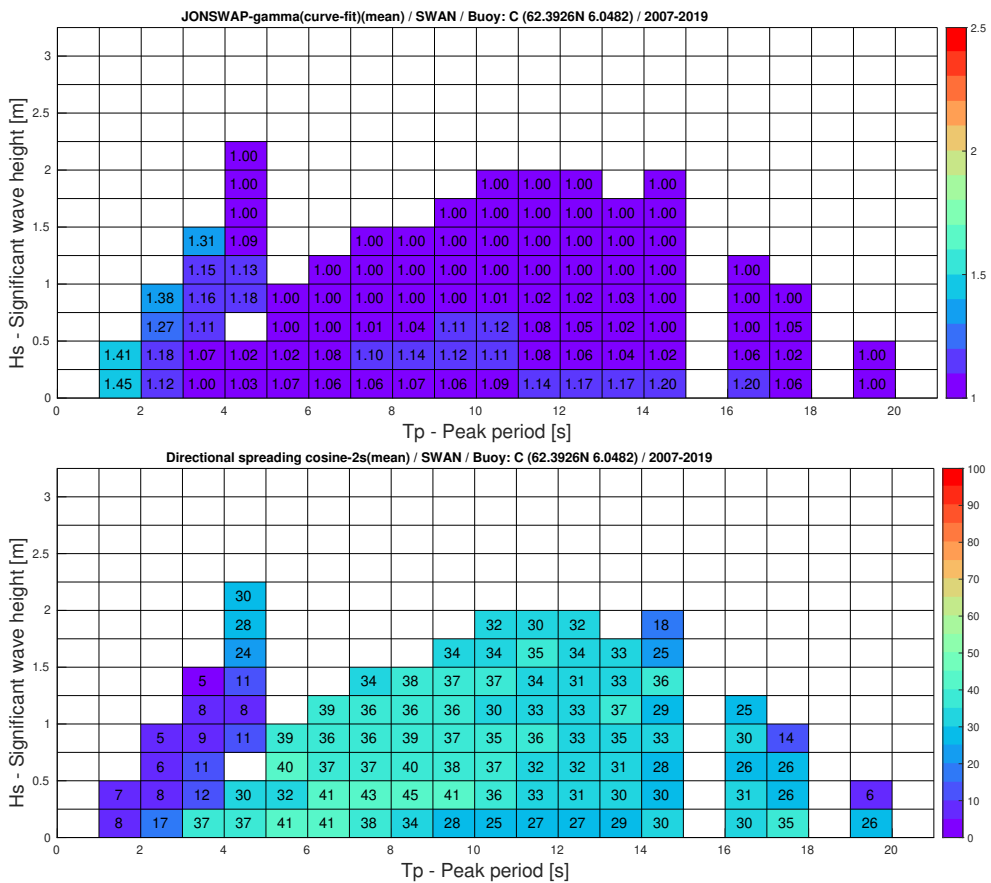


**Figure 53:** Modelled spectral properties at location C: Mean JONSWAP-gamma (top) and mean directional spread  $s$  of eq. 14 (bottom) binned according to peak period versus significant wave height.

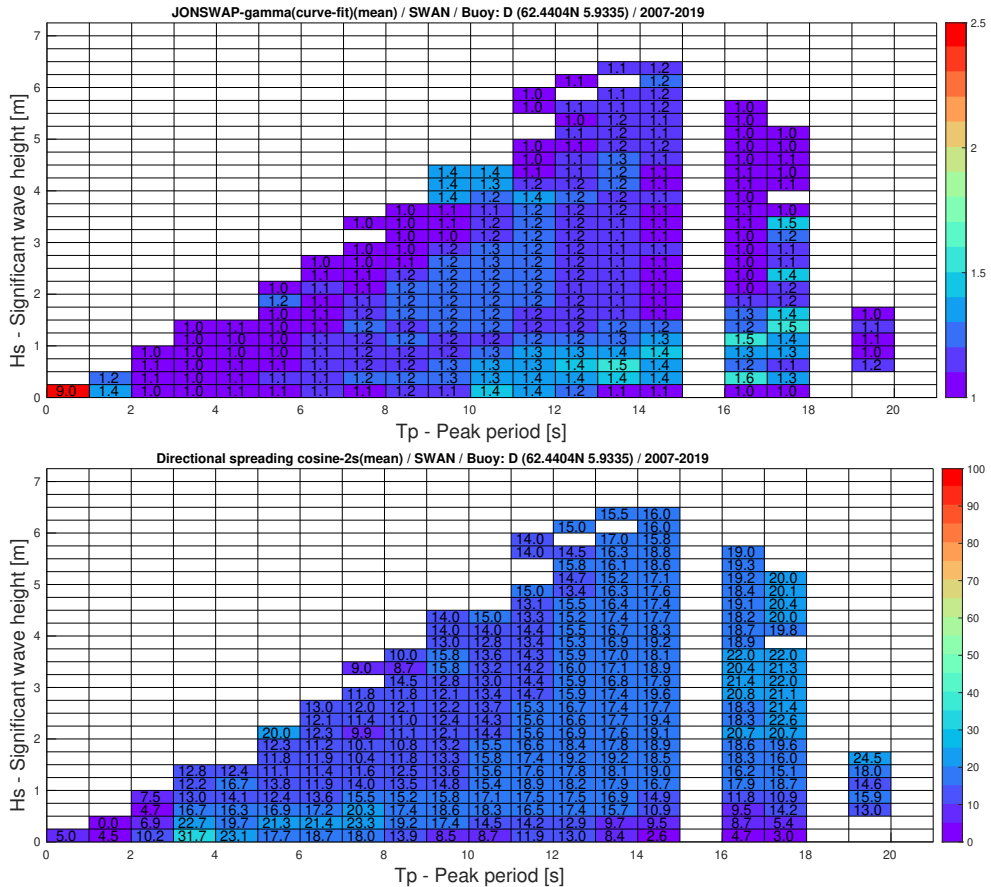


**Figure 54:** Modelled spectral properties at location D: Mean JONSWAP-gamma (top) and mean directional spread  $s$  of eq. 14 (bottom) binned according to peak period versus significant wave height.

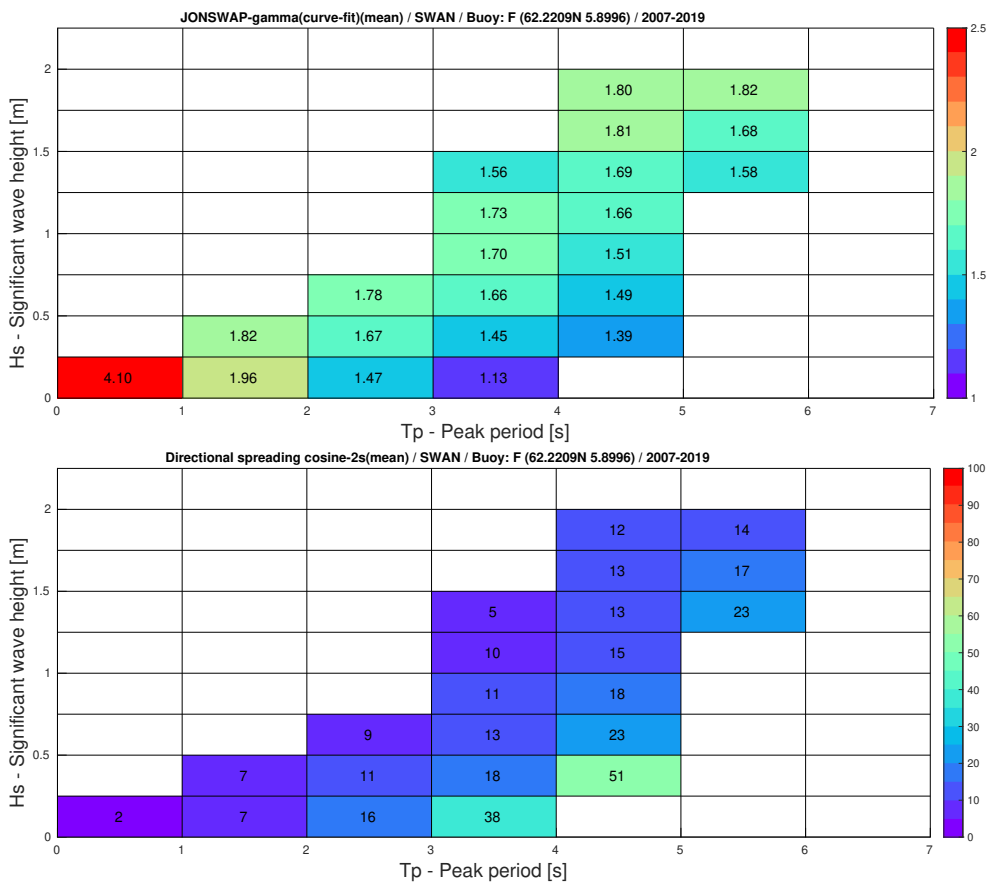


**Figure 55:** Modelled spectral properties at location F: Mean JONSWAP-gamma (top) and mean directional spread  $s$  of eq. 14 (bottom) binned according to peak period versus significant wave height.

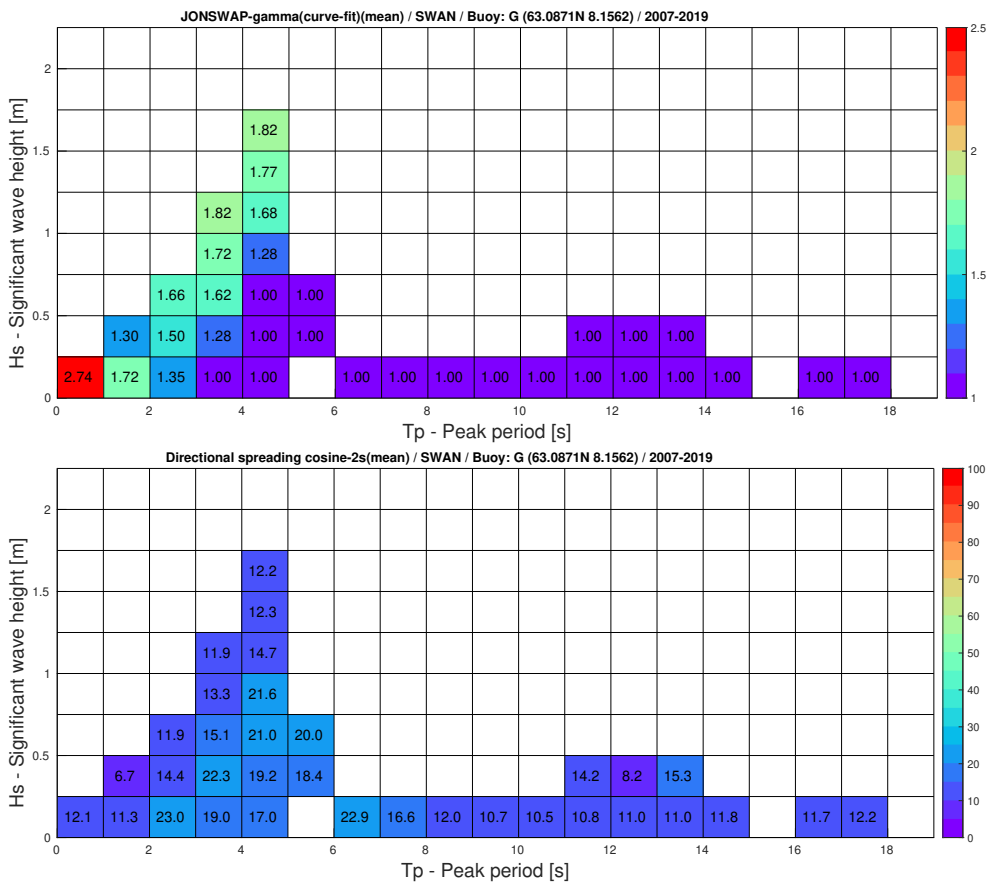


**Figure 56:** Modelled spectral properties at location G: Mean JONSWAP-gamma (top) and mean directional spread  $s$  of eq. 14 (bottom) binned according to peak period versus significant wave height.

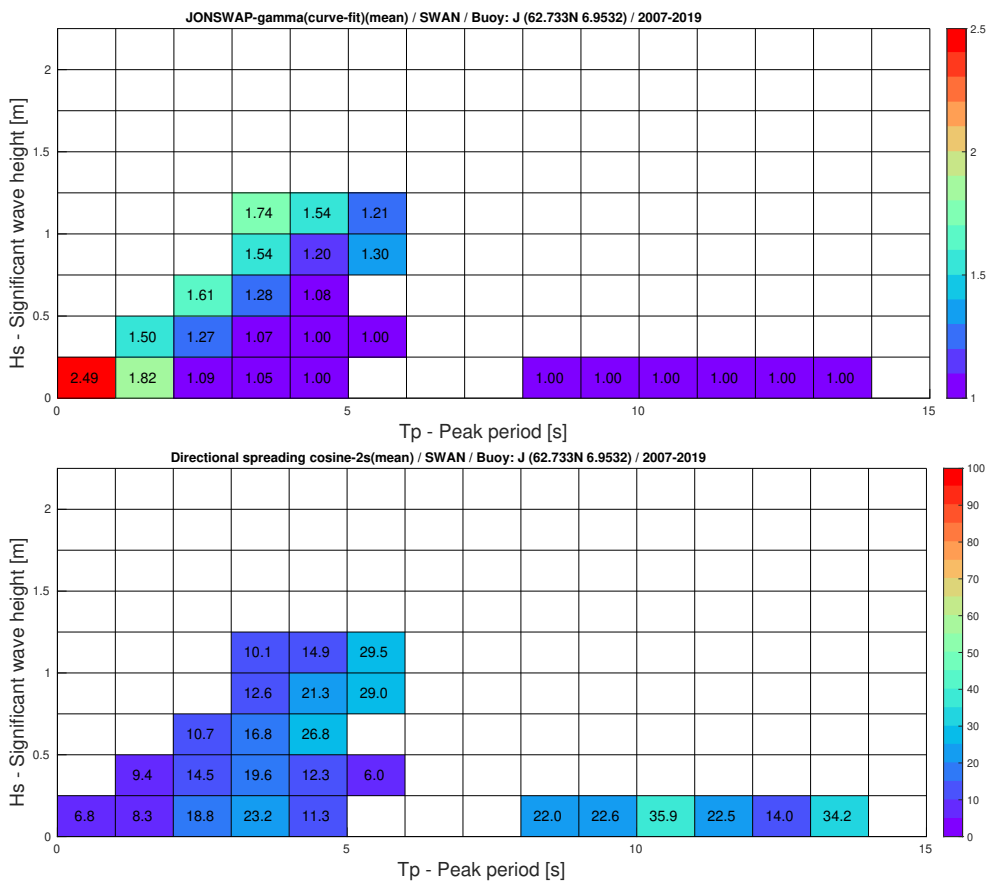


**Figure 57:** Modelled spectral properties at location J: Mean JONSWAP-gamma (top) and mean directional spread  $s$  of eq. 14 (bottom) binned according to peak period versus significant wave height.

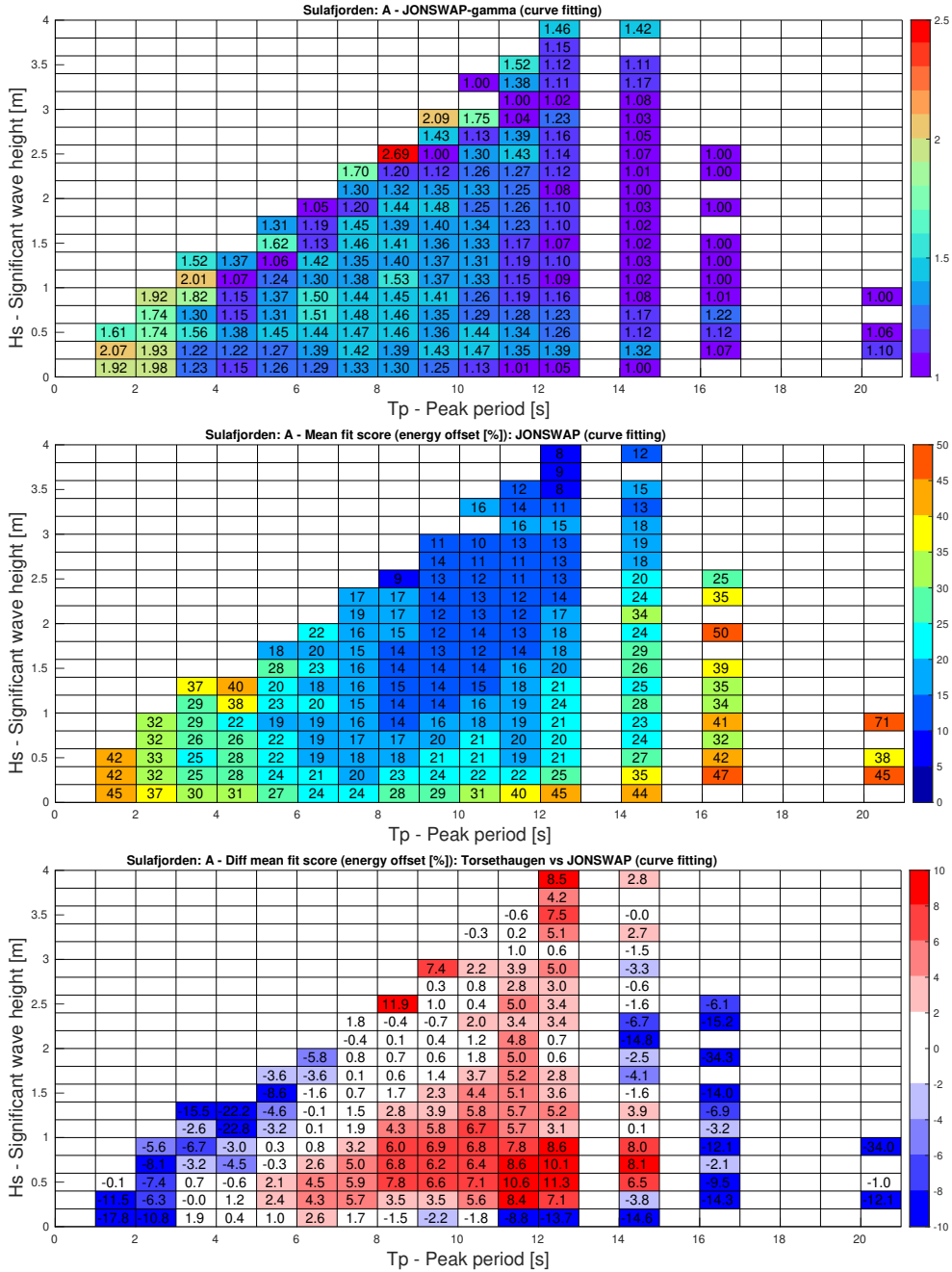


**Figure 58:** Observed spectral properties at location A. Top: Mean JONSWAP-gamma binned according to peak period and significant wave height. Center: Mean fit score - JONSWAP vs observed spectra - represented by the amount of displaced energy (in percent). Bottom: Discrepancy in fit score; Torsethaugen vs JONSWAP. Reds indicating superior fit between JONSWAP and observed spectra. Blues indicating superior fit between Torsethaugen and observed spectra.

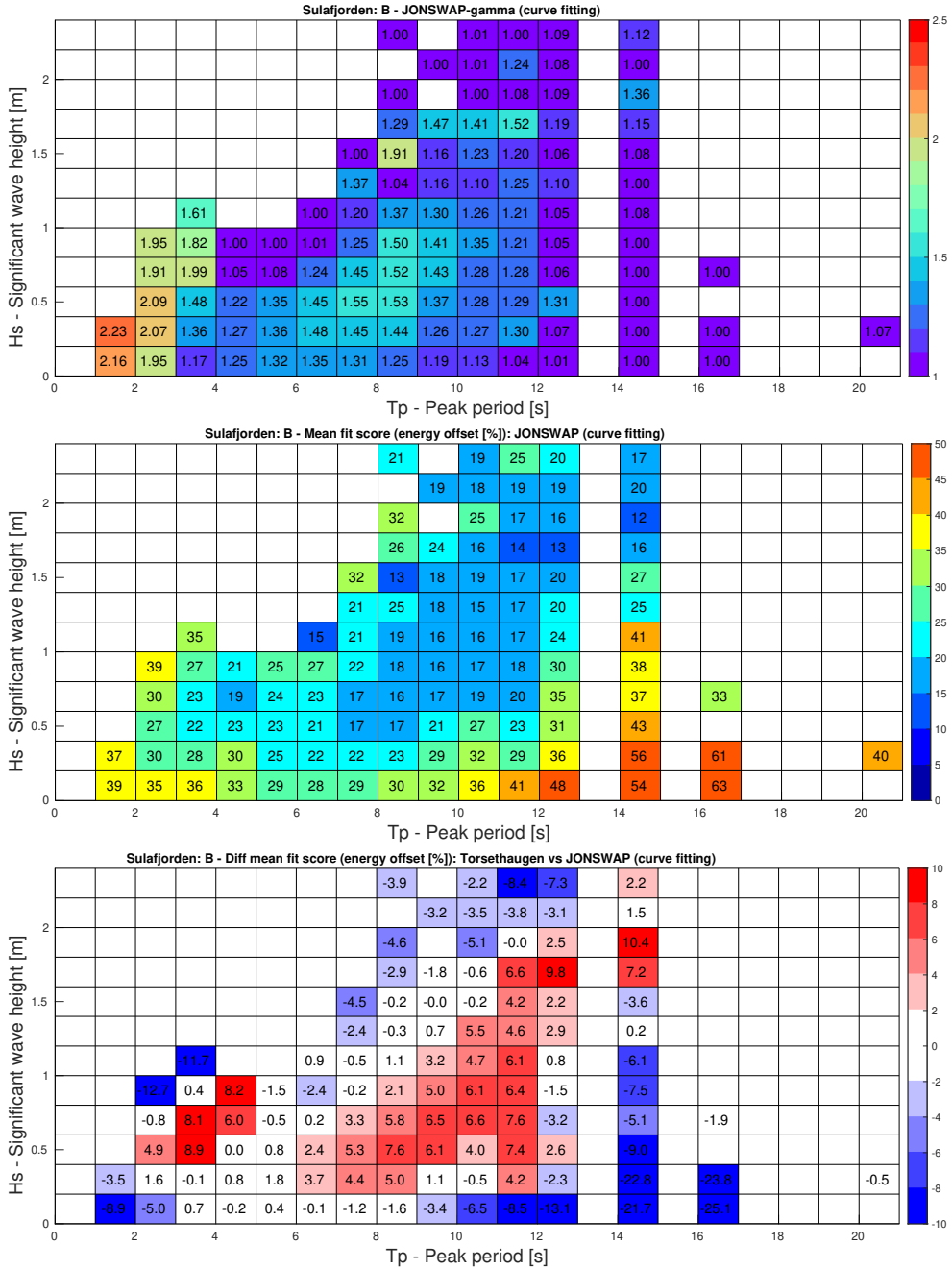


**Figure 59:** Observed spectral properties at location B. Top: Mean JONSWAP-gamma binned according to peak period and significant wave height. Center: Mean fit score - JONSWAP vs observed spectra - represented by the amount of displaced energy (in percent). Bottom: Discrepancy in fit score; Torsethaugen vs JONSWAP. Reds indicating superior fit between JONSWAP and observed spectra. Blues indicating superior fit between Torsethaugen and observed spectra.

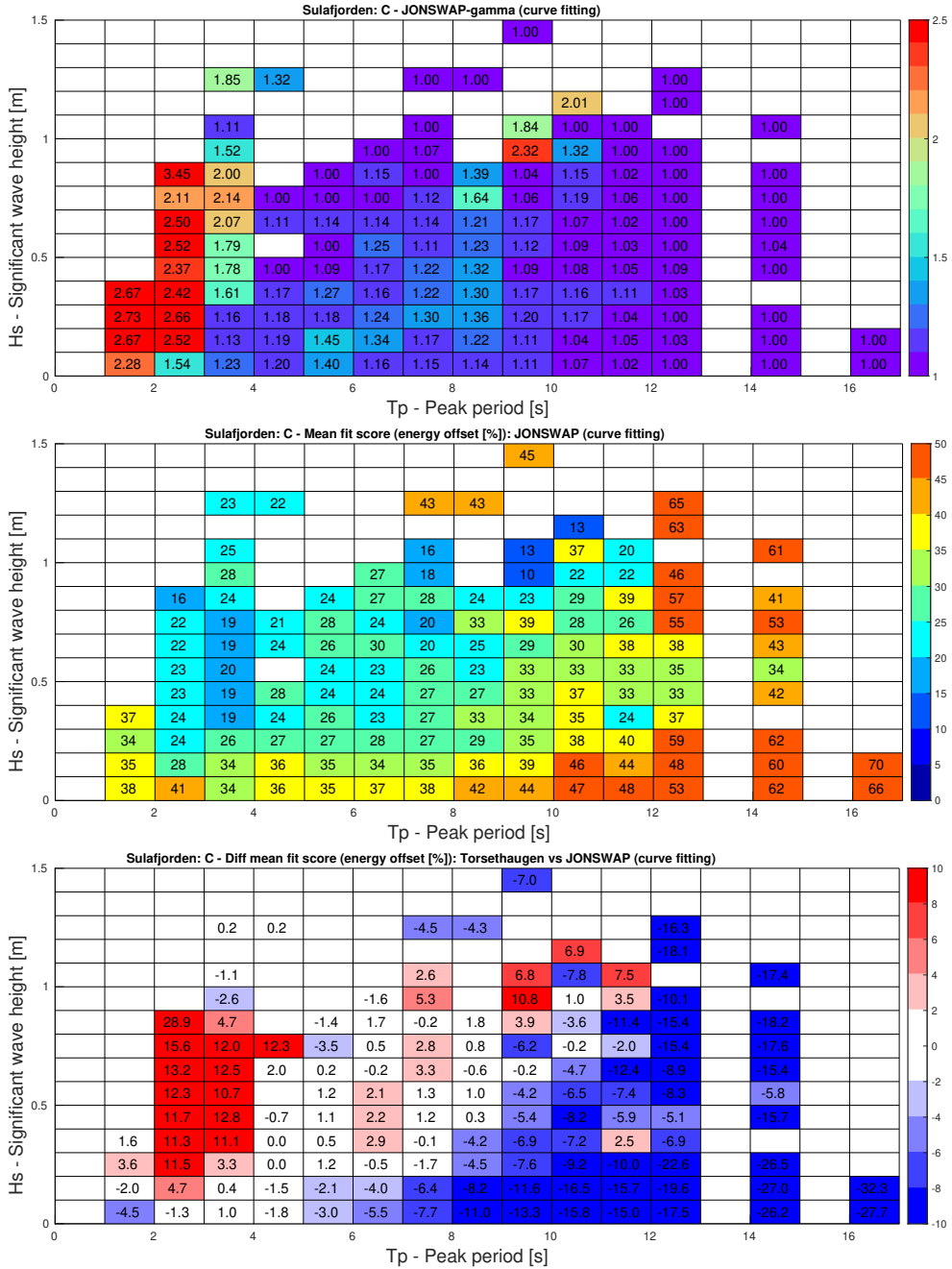


**Figure 60:** Observed spectral properties at location C. Top: Mean JONSWAP-gamma binned according to peak period and significant wave height. Center: Mean fit score - JONSWAP vs observed spectra - represented by the amount of displaced energy (in percent). Bottom: Discrepancy in fit score; Torsethaugen vs JONSWAP. Reds indicating superior fit between JONSWAP and observed spectra. Blues indicating superior fit between Torsethaugen and observed spectra.

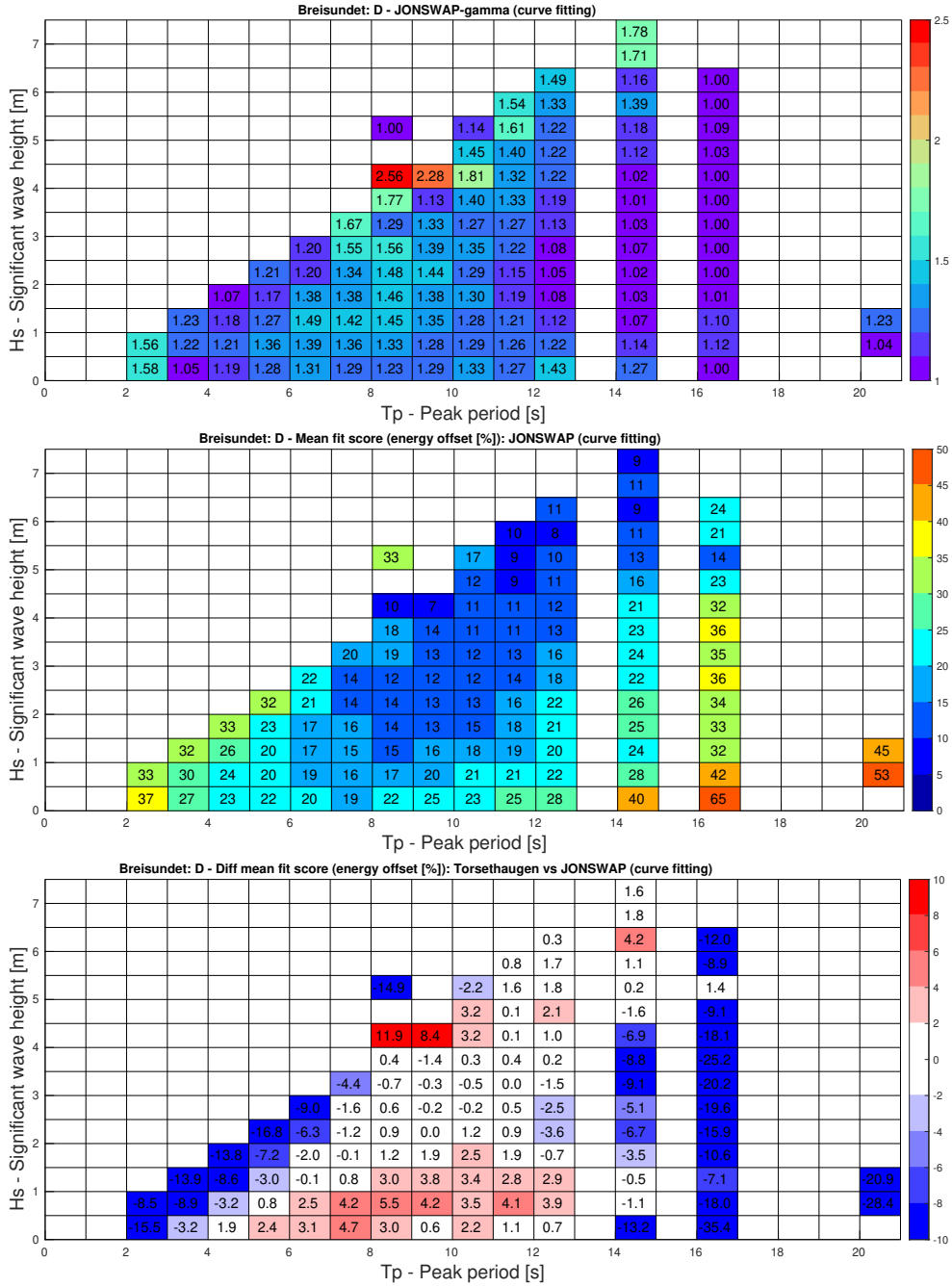


**Figure 61:** Observed spectral properties at location D. Top: Mean JONSWAP-gamma binned according to peak period and significant wave height. Center: Mean fit score - JONSWAP vs observed spectra - represented by the amount of displaced energy (in percent). Bottom: Discrepancy in fit score; Torsethaugen vs JONSWAP. Reds indicating superior fit between JONSWAP and observed spectra. Blues indicating superior fit between Torsethaugen and observed spectra.

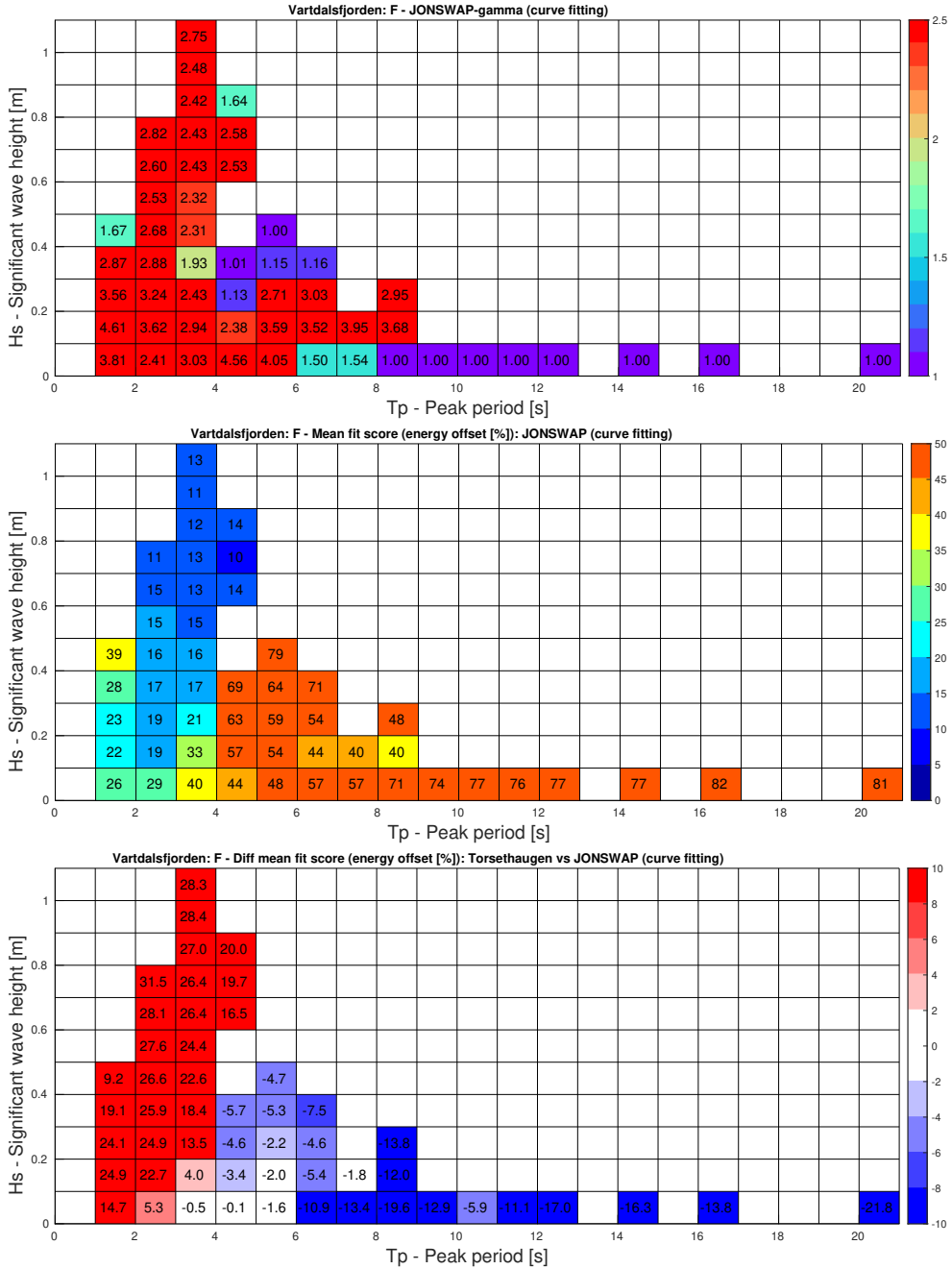


**Figure 62:** Observed spectral properties at location F. Top: Mean JONSWAP-gamma binned according to peak period and significant wave height. Center: Mean fit score - JONSWAP vs observed spectra - represented by the amount of displaced energy (in percent). Bottom: Discrepancy in fit score; Torsethaugen vs JONSWAP. Reds indicating superior fit between JONSWAP and observed spectra. Blues indicating superior fit between Torsethaugen and observed spectra.

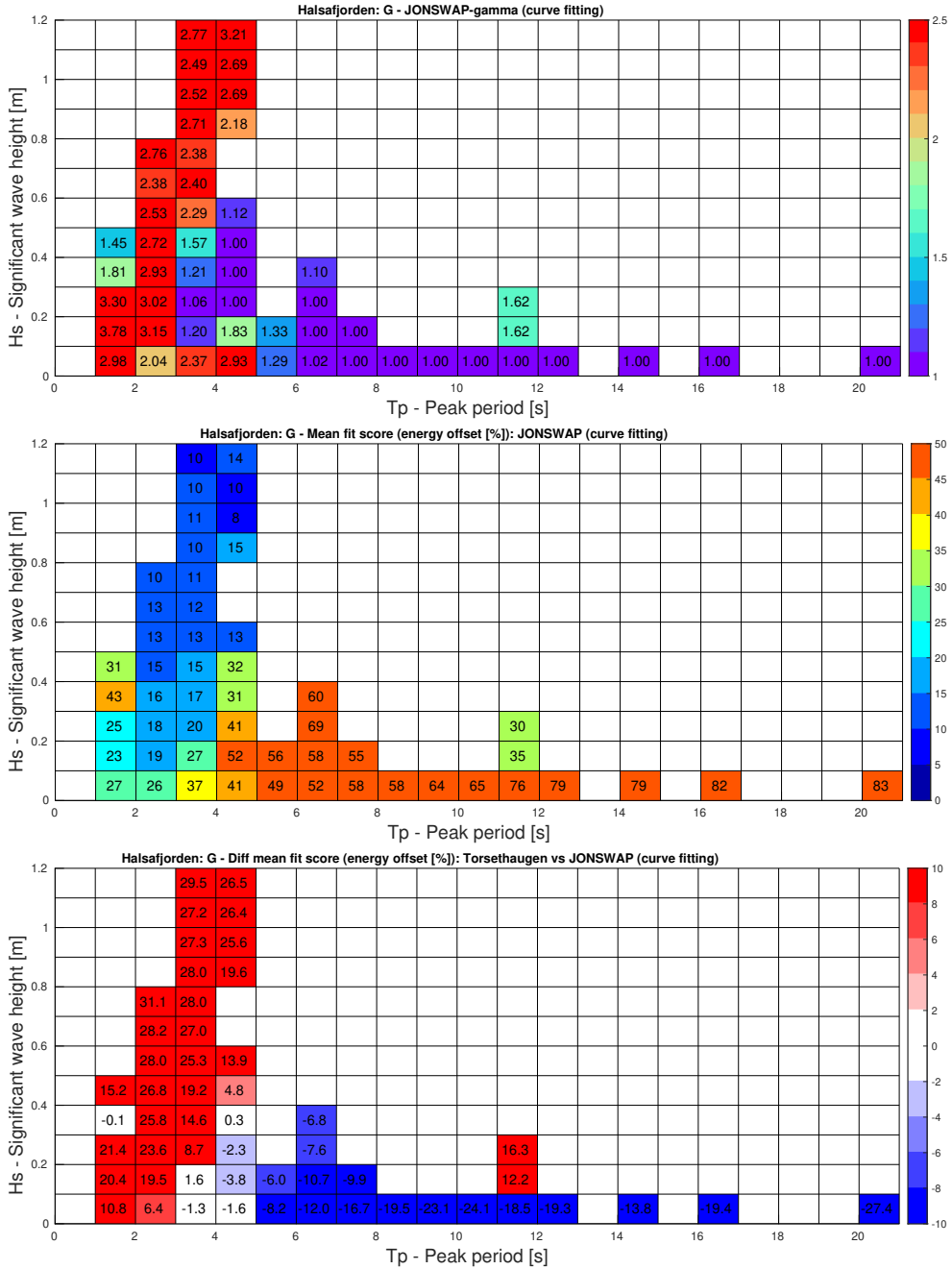


**Figure 63:** Observed spectral properties at location G. Top: Mean JONSWAP-gamma binned according to peak period and significant wave height. Center: Mean fit score - JONSWAP vs observed spectra - represented by the amount of displaced energy (in percent). Bottom: Discrepancy in fit score; Torsethaugen vs JONSWAP. Reds indicating superior fit between JONSWAP and observed spectra. Blues indicating superior fit between Torsethaugen and observed spectra.

### 7.4.1 Three highest $H_s$ cases

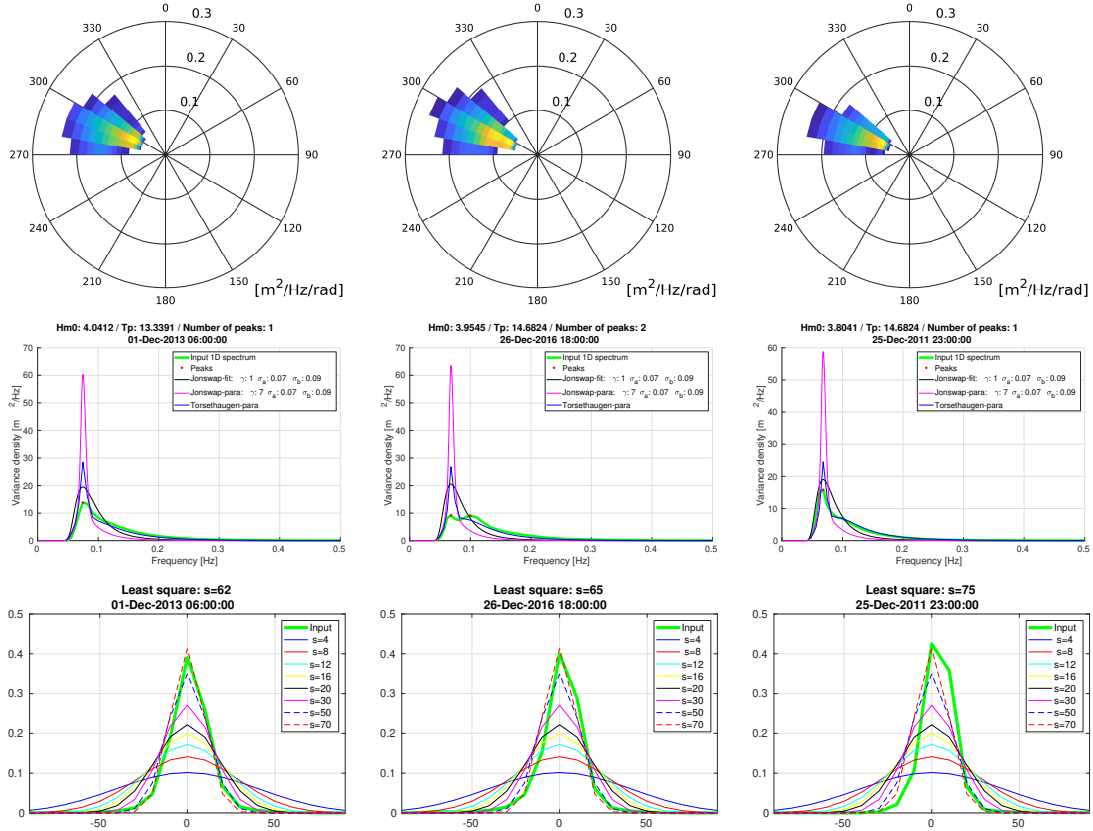


**Figure 64:** Top row: 2D wave spectra from the three highest  $H_s$ -cases over the period 2007–2019 at position A. Model is represented by the green line in the two lower rows. Middle row: Modelled 1D spectra and different fitted JONSWAP-spectra and Torsethaugen. The corresponding shape parameters are presented in the legend. Bottom row: Directional spreading (normalized) according to eq. 14 for different  $s$ .

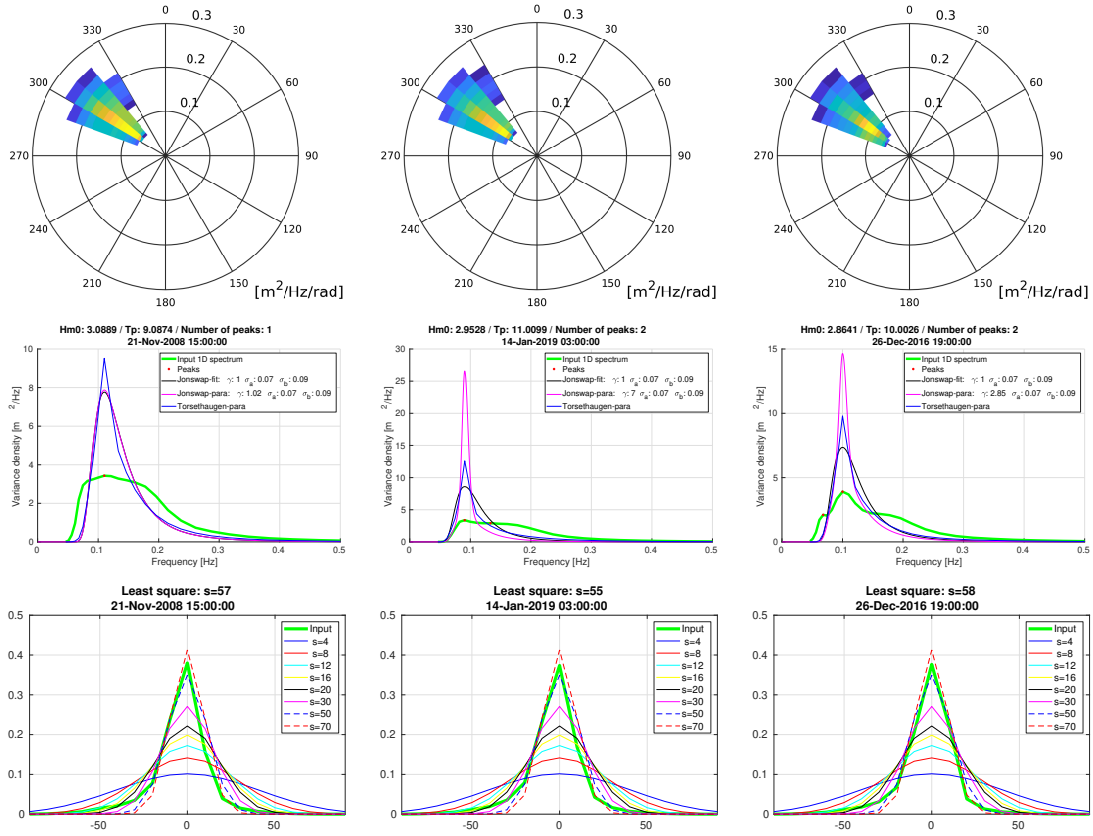


**Figure 65:** Top row: 2D wave spectra from the three highest  $H_s$ -cases over the period 2007-2019 at position B. Model is represented by the green line in the two lower rows. Middle row: Modelled 1D spectra and different fitted JONSWAP-spectra and Torsethaugen. The corresponding shape parameters are presented in the legend. Bottom row: Directional spreading (normalized) according to eq. 14 for different  $s$ .

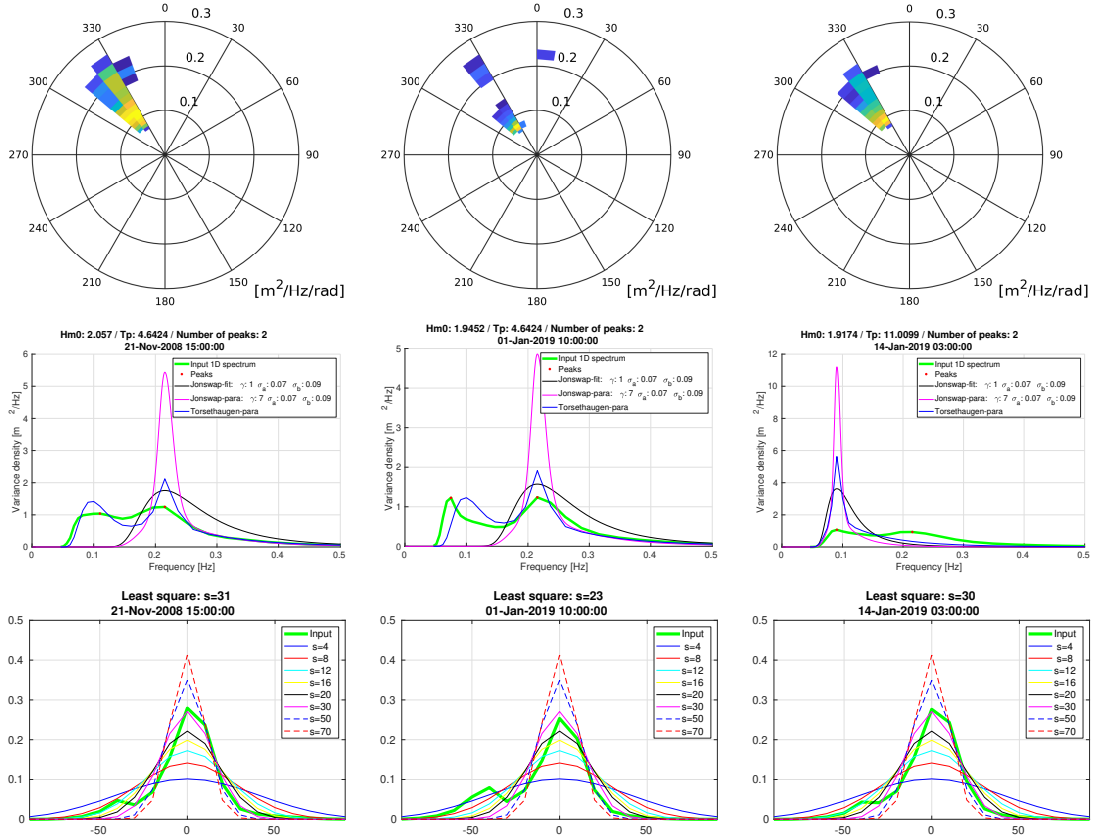


**Figure 66:** Top row: 2D wave spectra from the three highest  $H_s$ -cases over the period 2007-2019 at position C. Model is represented by the green line in the two lower rows. Middle row: Modelled 1D spectra and different fitted JONSWAP-spectra and Torsethaugen. The corresponding shape parameters are presented in the legend. Bottom row: Directional spreading (normalized) according to eq. 14 for different  $s$ .

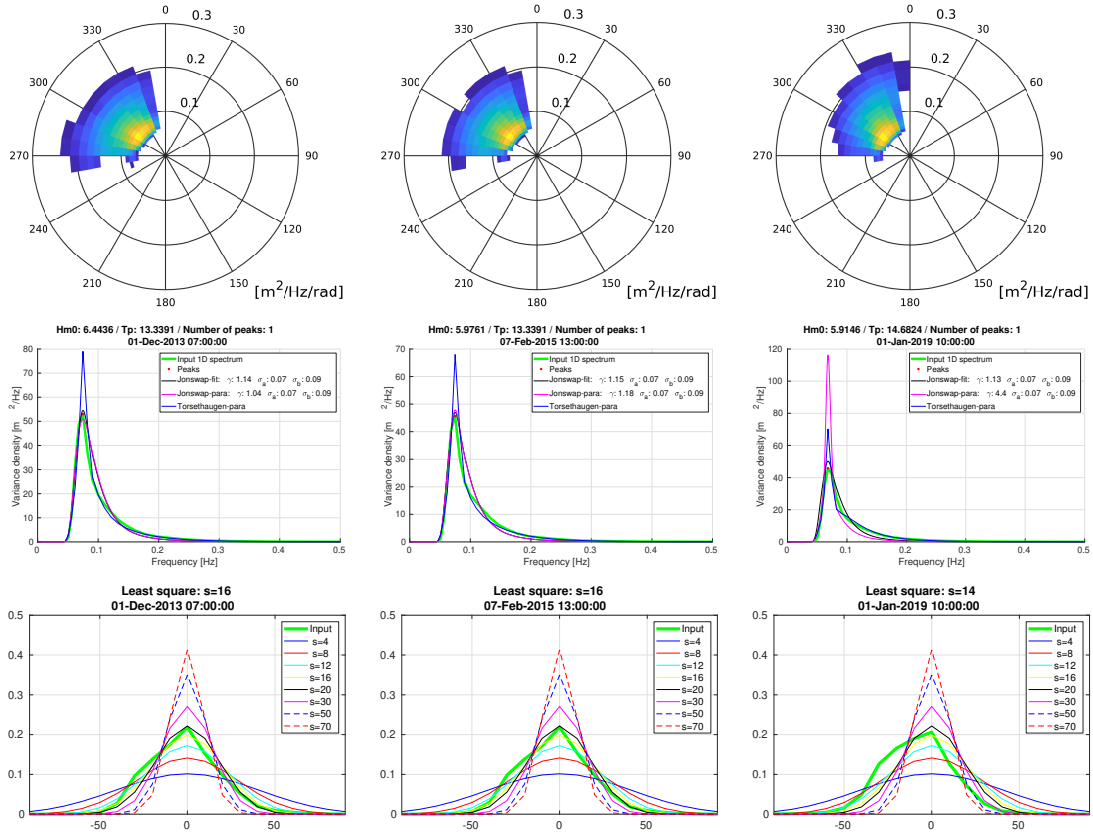


**Figure 67:** Top row: 2D wave spectra from the three highest  $H_s$ -cases over the period 2007–2019 at position D. Model is represented by the green line in the two lower rows. Middle row: Modelled 1D spectra and different fitted JONSWAP-spectra and Torsethaugen. The corresponding shape parameters are presented in the legend. Bottom row: Directional spreading (normalized) according to eq. 14 for different  $s$ .

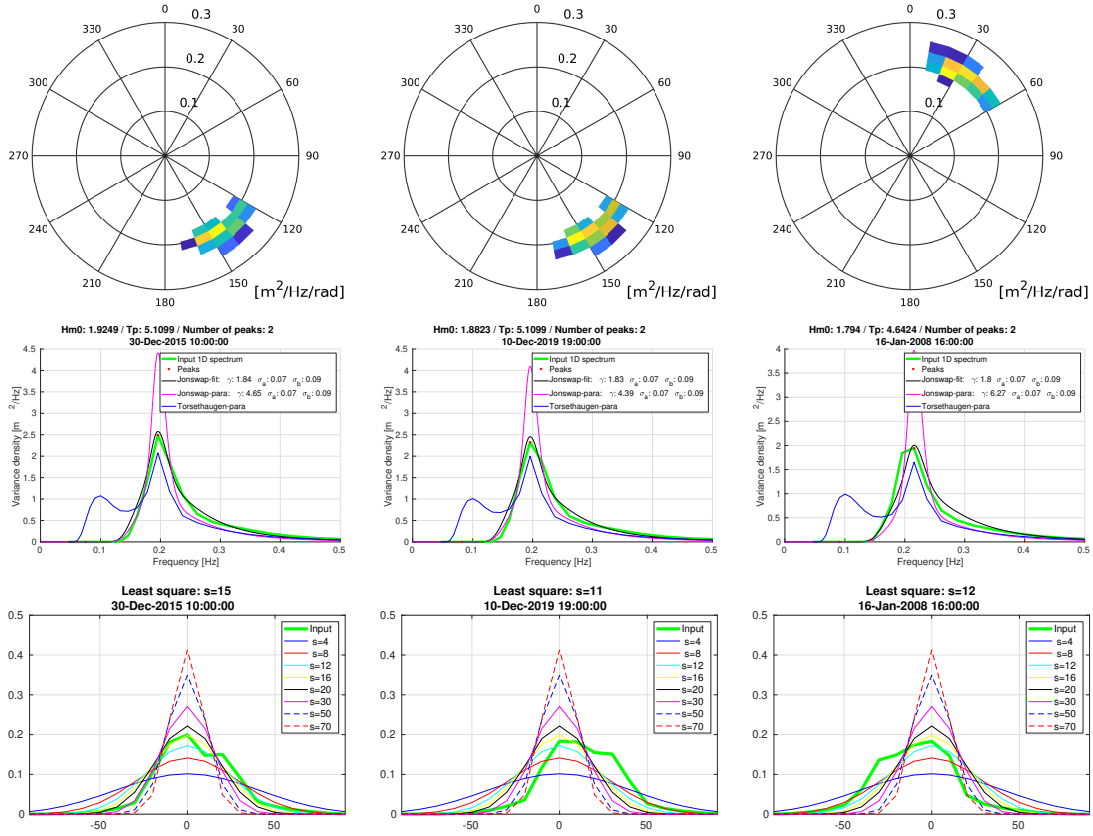


**Figure 68:** Top row: 2D wave spectra from the three highest  $H_s$ -cases over the period 2007-2019 at position F. Model is represented by the green line in the two lower rows. Middle row: Modelled 1D spectra and different fitted JONSWAP-spectra and Torsethaugen. The corresponding shape parameters are presented in the legend. Bottom row: Directional spreading (normalized) according to eq. 14 for different  $s$ .

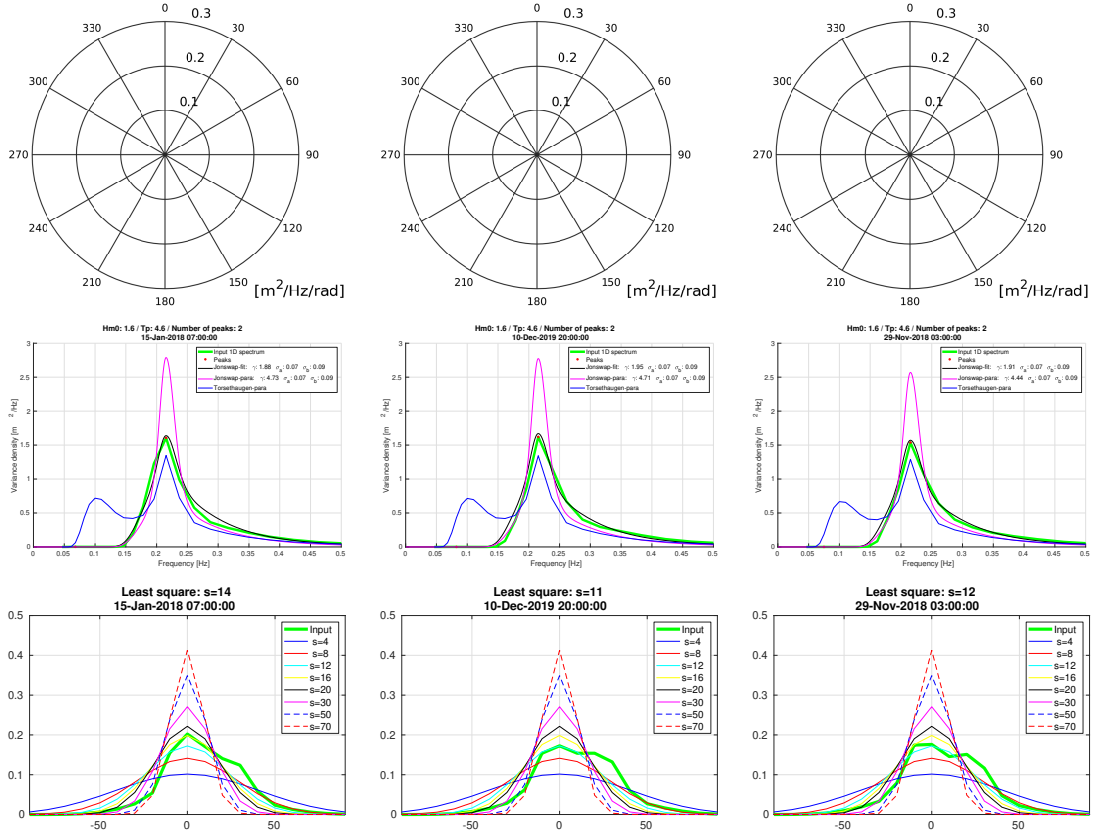


**Figure 69:** Top row: 2D wave spectra from the three highest  $H_s$ -cases over the period 2007-2019 at position G. Model is represented by the green line in the two lower rows. Middle row: Modelled 1D spectra and different fitted JONSWAP-spectra and Torsethaugen. The corresponding shape parameters are presented in the legend. Bottom row: Directional spreading (normalized) according to eq. 14 for different  $s$ .

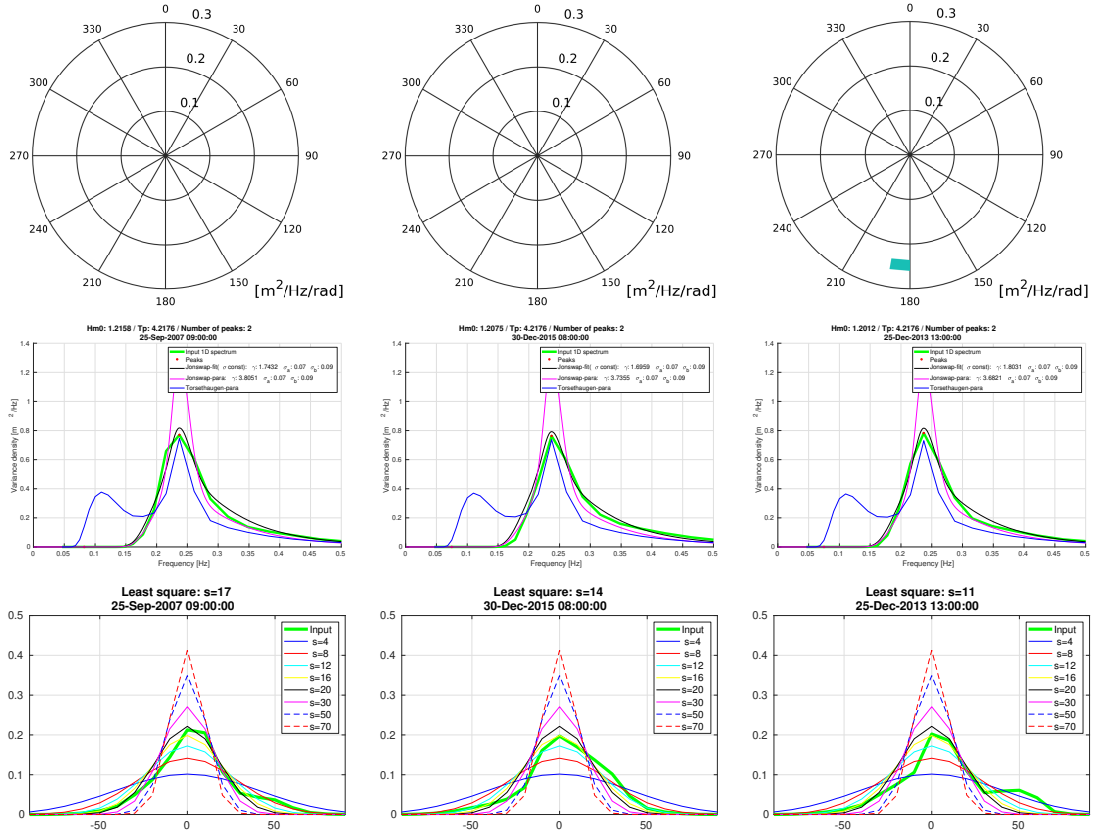


**Figure 70:** Top row: 2D wave spectra from the three highest  $H_s$ -cases over the period 2007-2019 at position J. Model is represented by the green line in the two lower rows. Middle row: Modelled 1D spectra and different fitted JONSWAP-spectra and Torsethaugen. The corresponding shape parameters are presented in the legend. Bottom row: Directional spreading (normalized) according to eq. 14 for different  $s$ .

## 7.5 Frequency tables

### 7.5.1 Significant Wave Height vs Peak Period

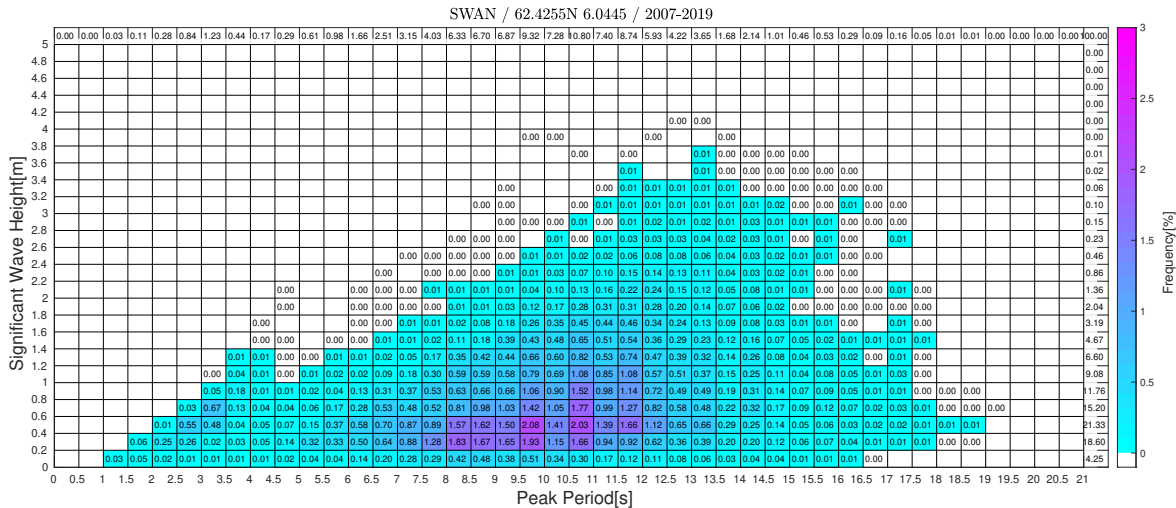


**Figure 71:** Frequency table of annual/omni  $H_s/T_p$  at location A.

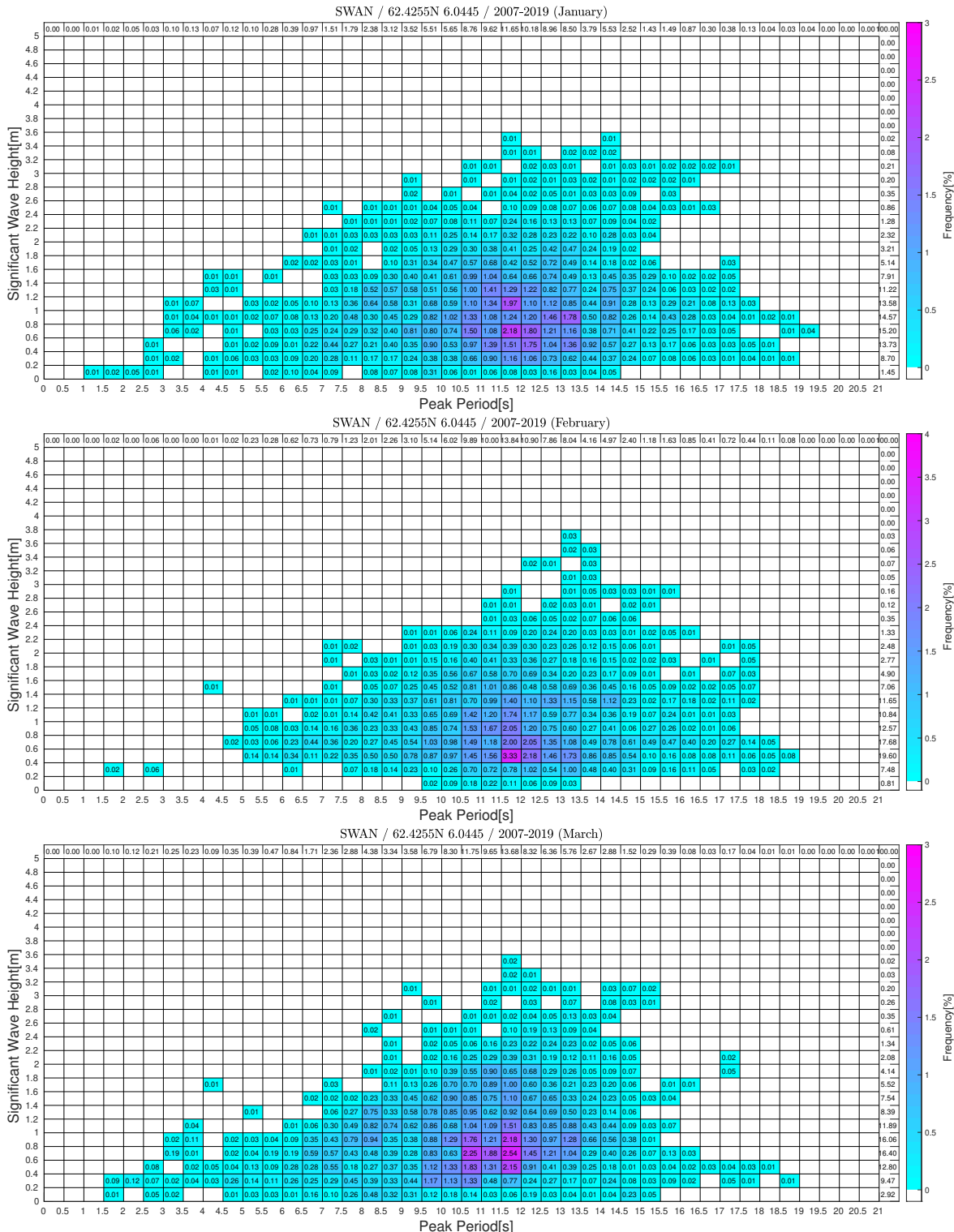


**Figure 72:** Monthly frequency tables of  $H_s/T_p$  at location A.

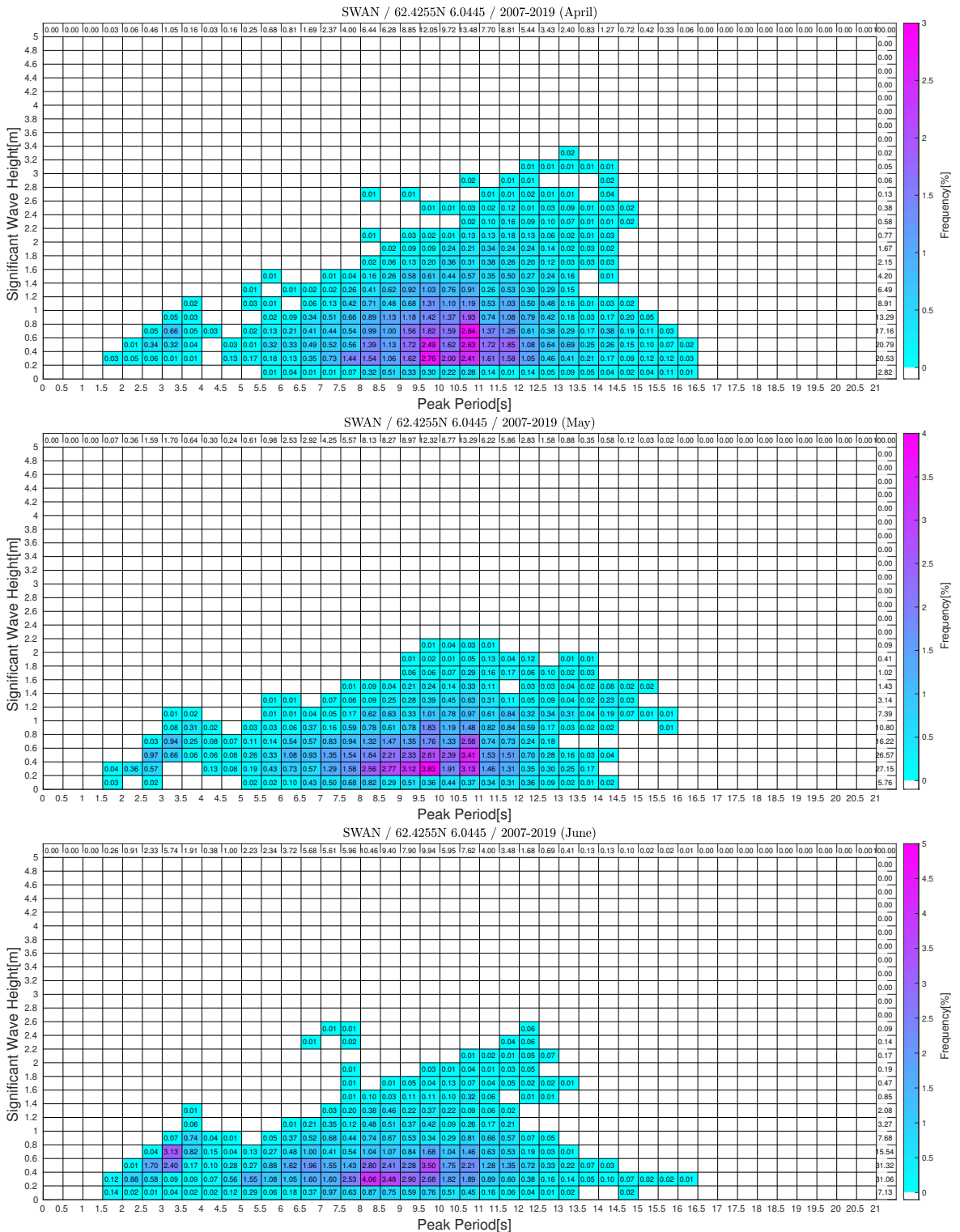


**Figure 73:** Monthly frequency tables of  $H_s/T_p$  at location A.

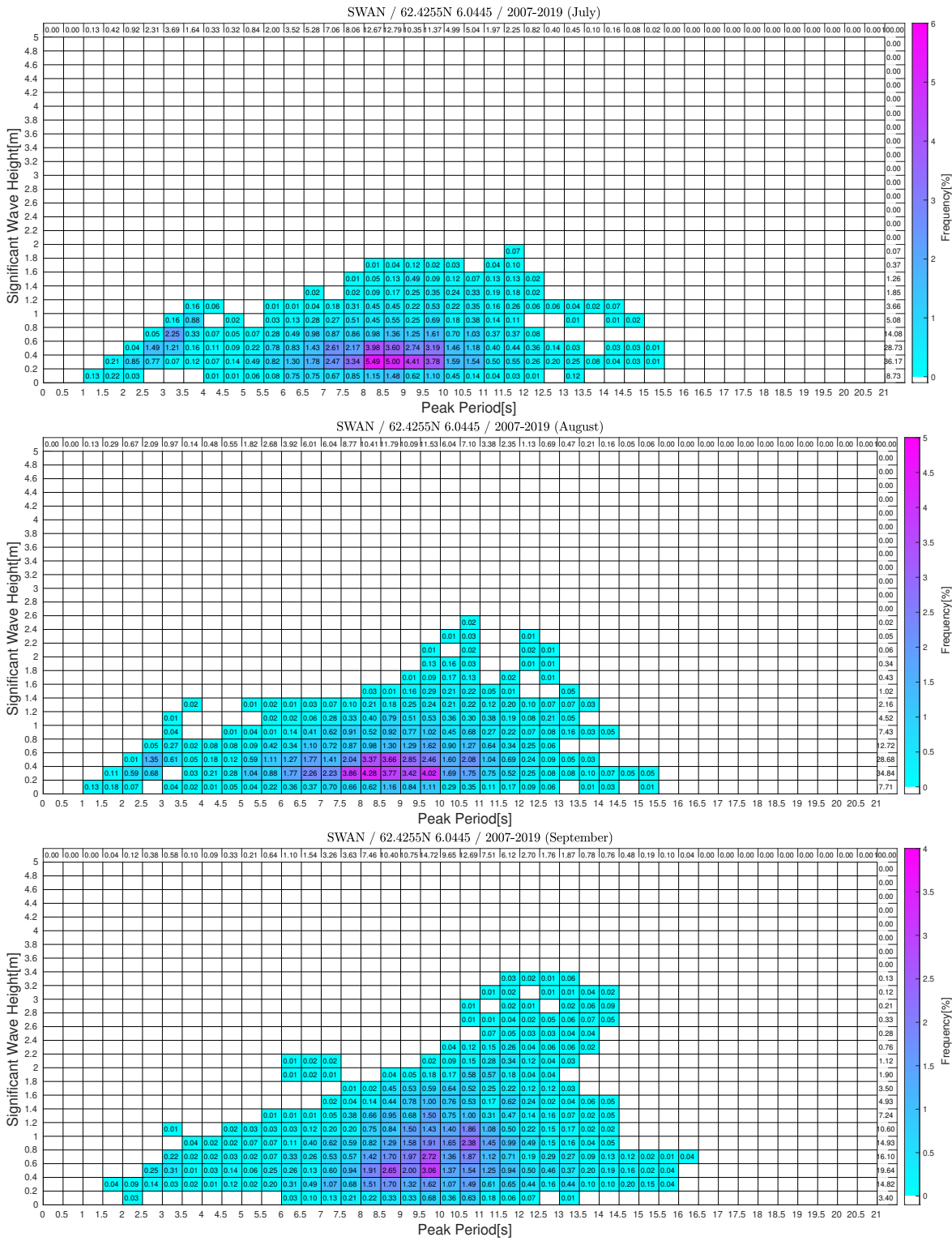


**Figure 74:** Monthly frequency tables of  $H_s/T_p$  at location A.

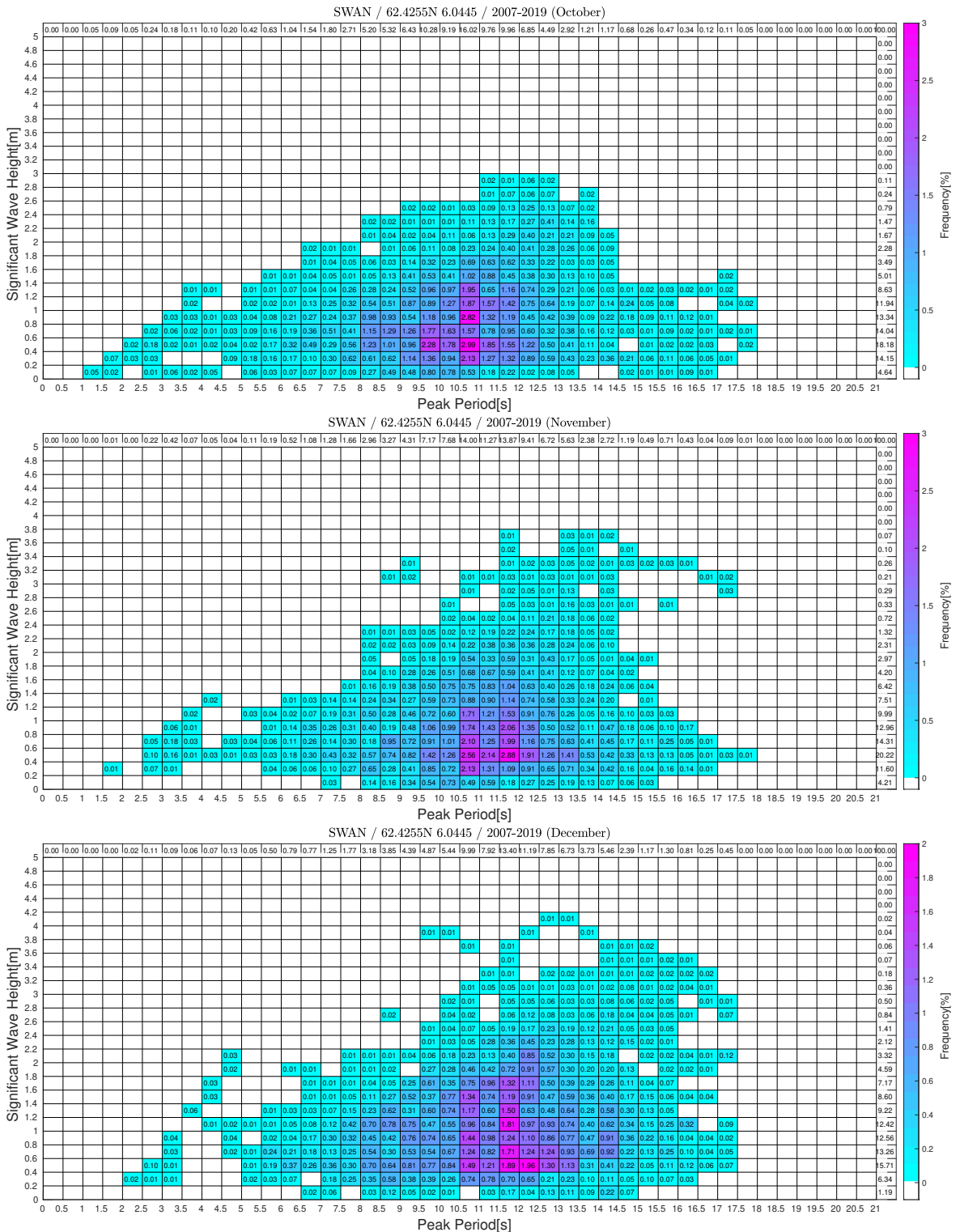


**Figure 75:** Monthly frequency tables of  $H_s/T_p$  at location A.

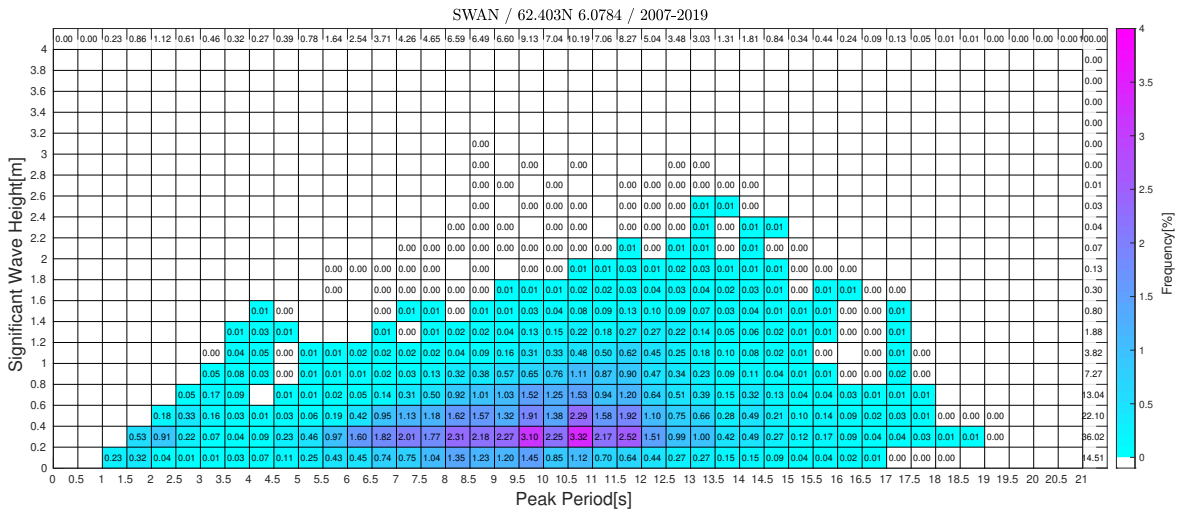


**Figure 76:** Frequency table of annual/omni  $H_s/T_p$  at location B.

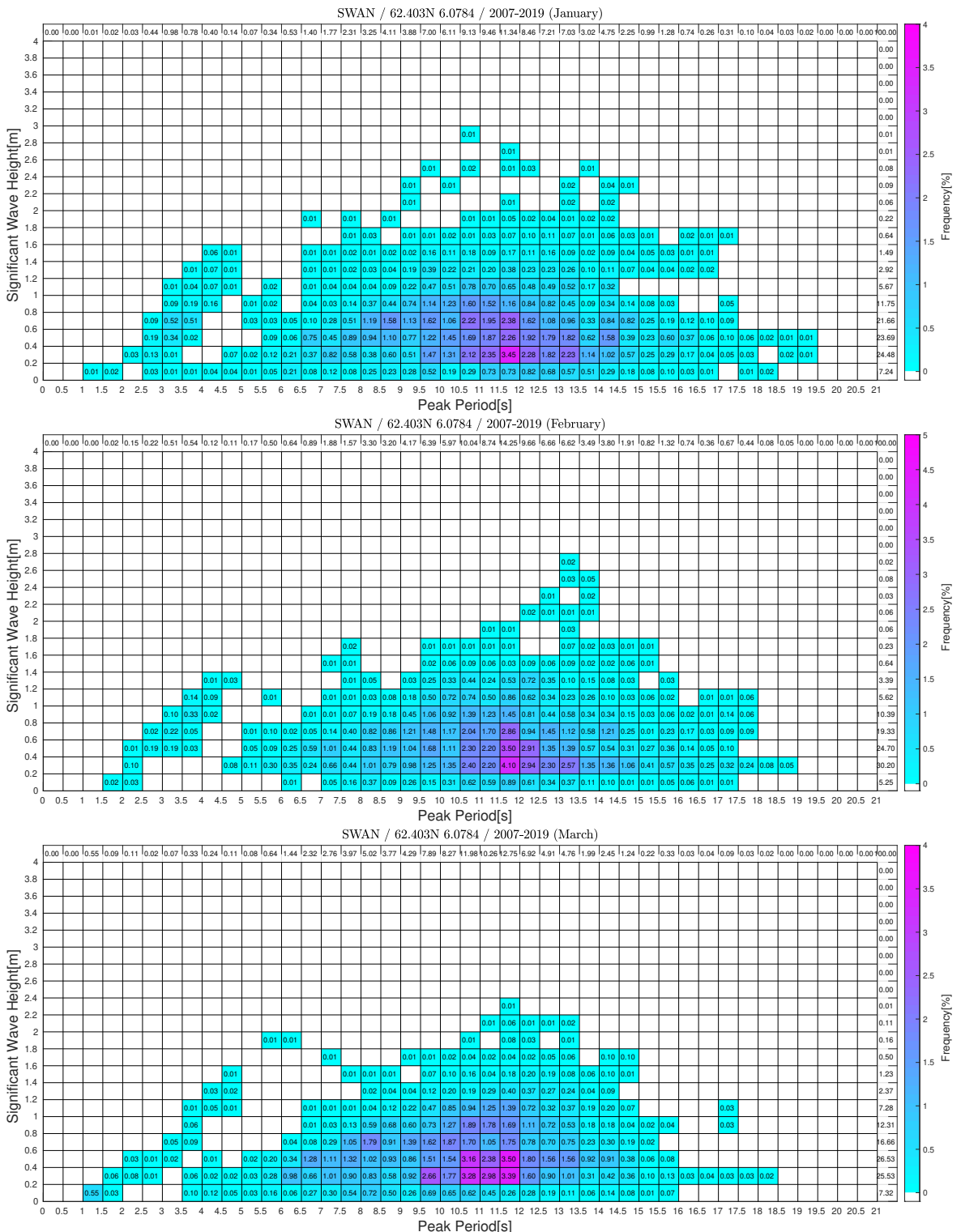


**Figure 77:** Monthly frequency tables of  $H_s/T_p$  at location B.

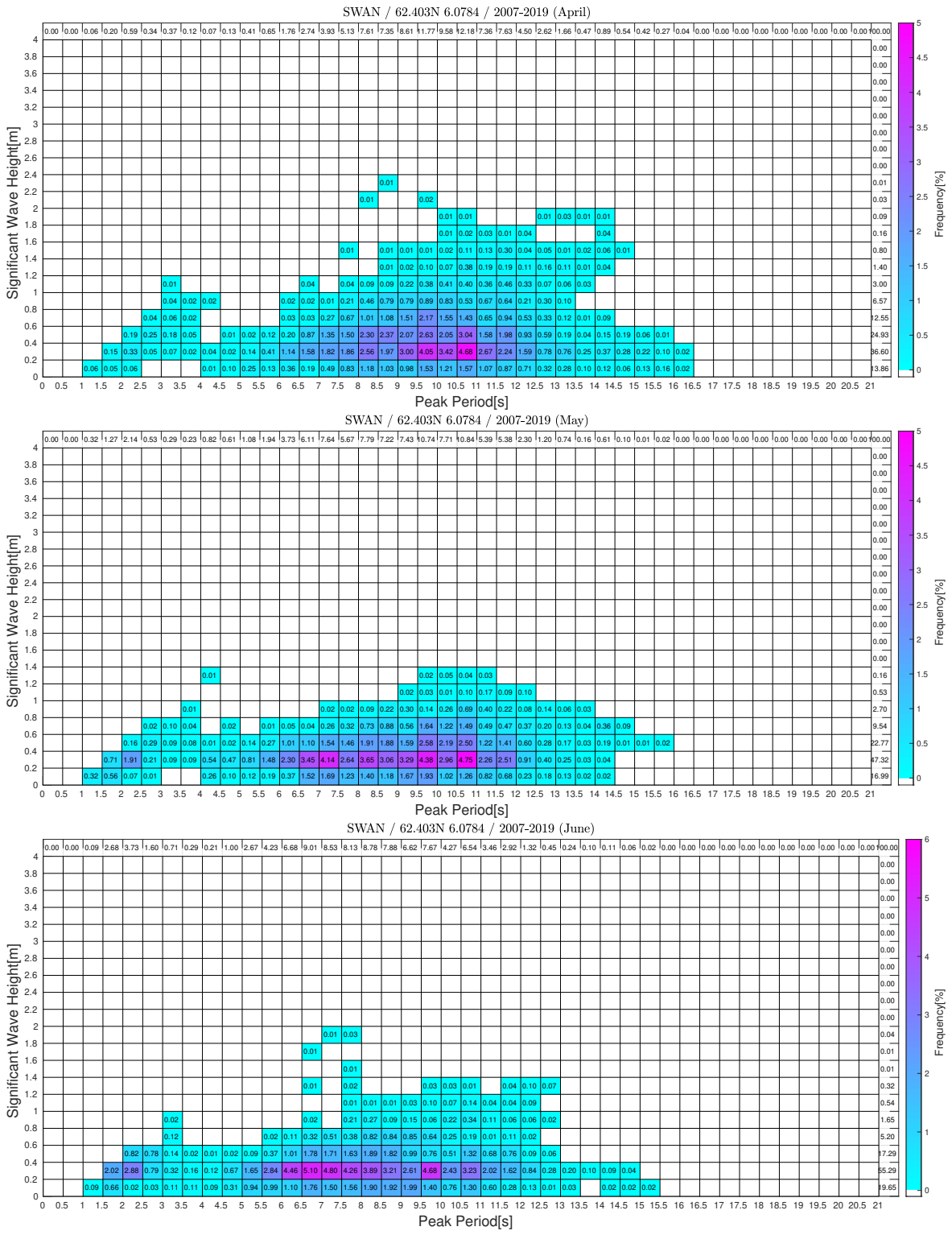


**Figure 78:** Monthly frequency tables of  $H_s/T_p$  at location B.

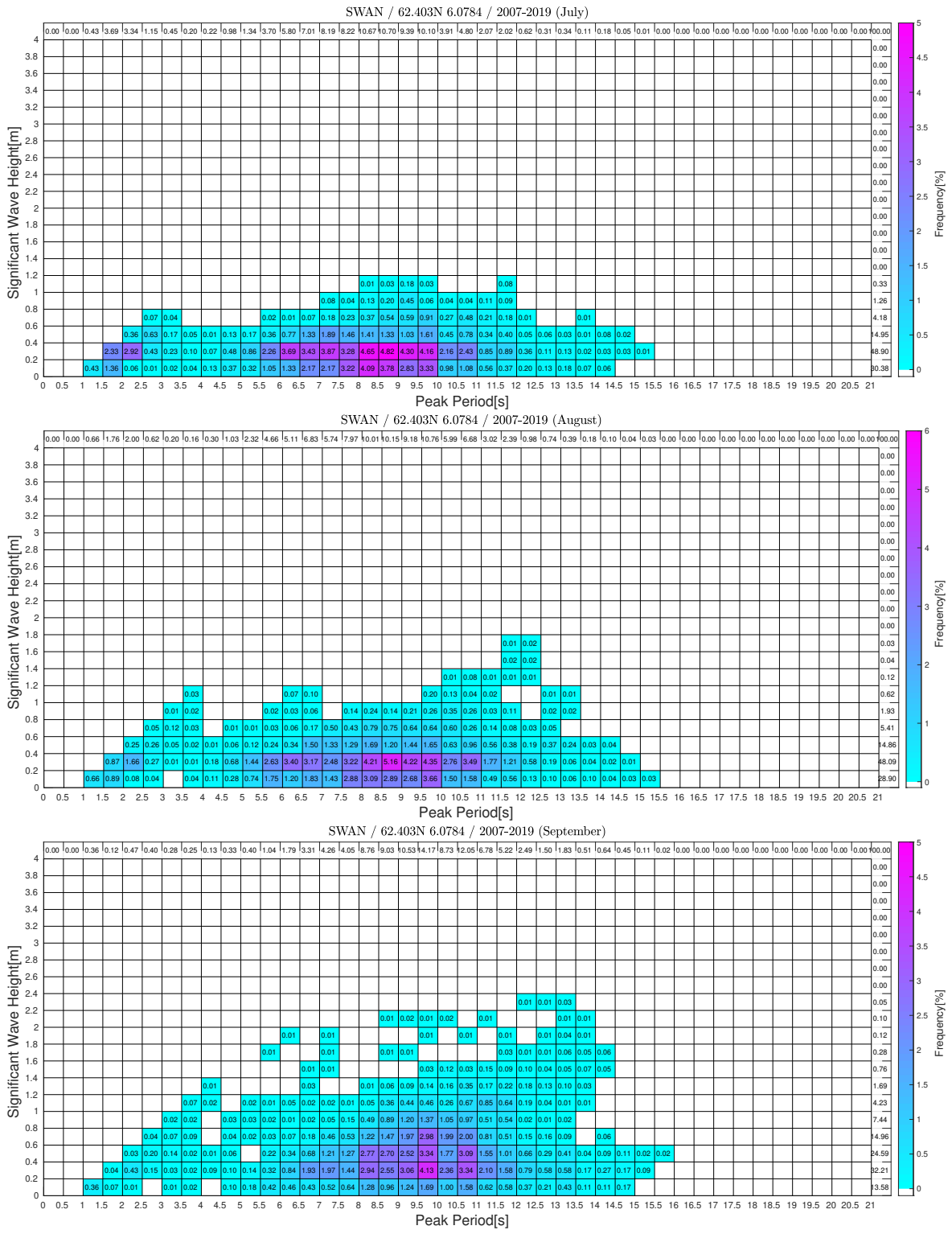


**Figure 79:** Monthly frequency tables of  $H_s/T_p$  at location B.

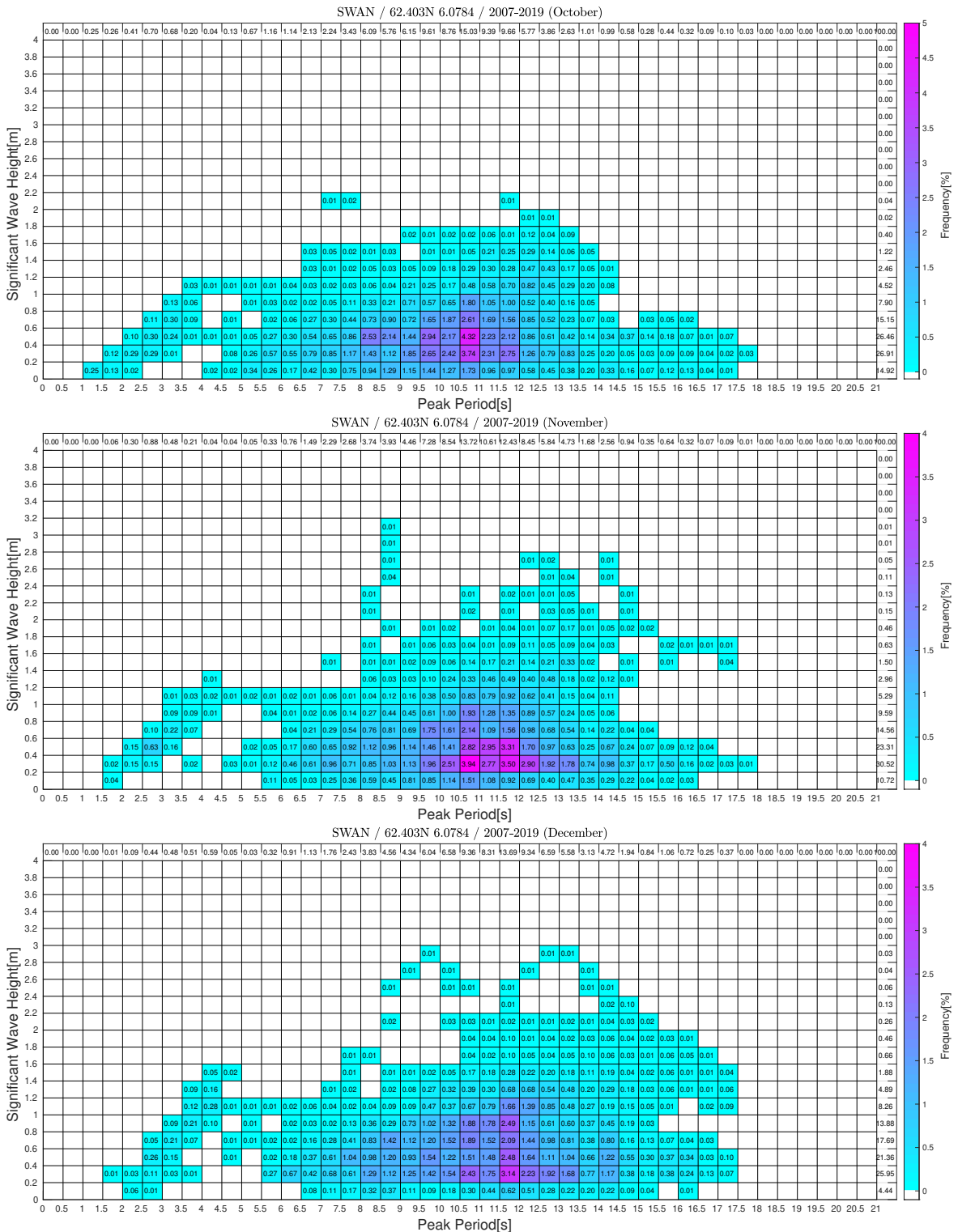


**Figure 80:** Monthly frequency tables of  $H_s/T_p$  at location B.

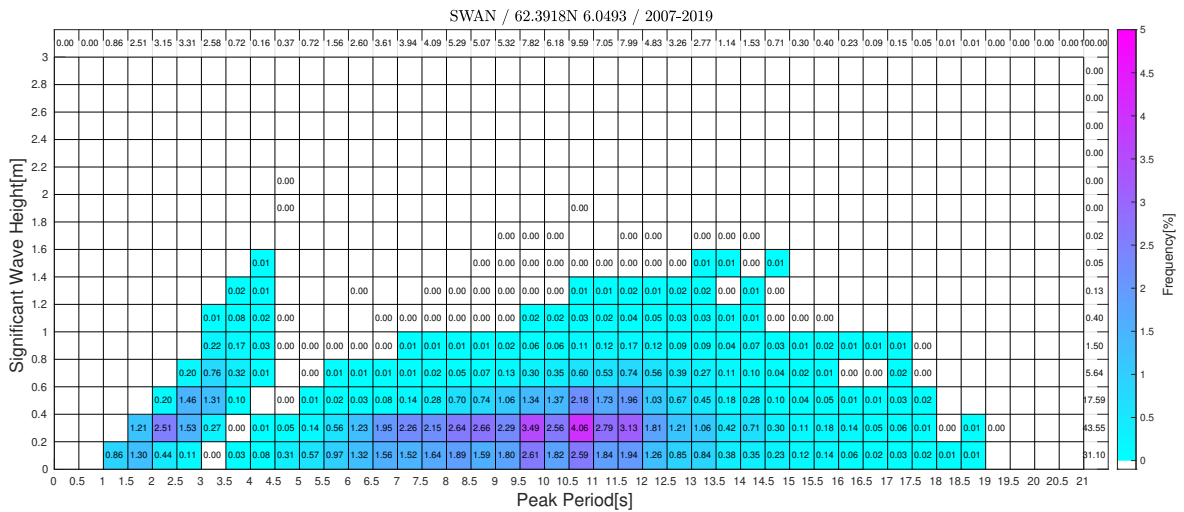


**Figure 81:** Frequency table of annual/omni  $H_s/T_p$  at location C.

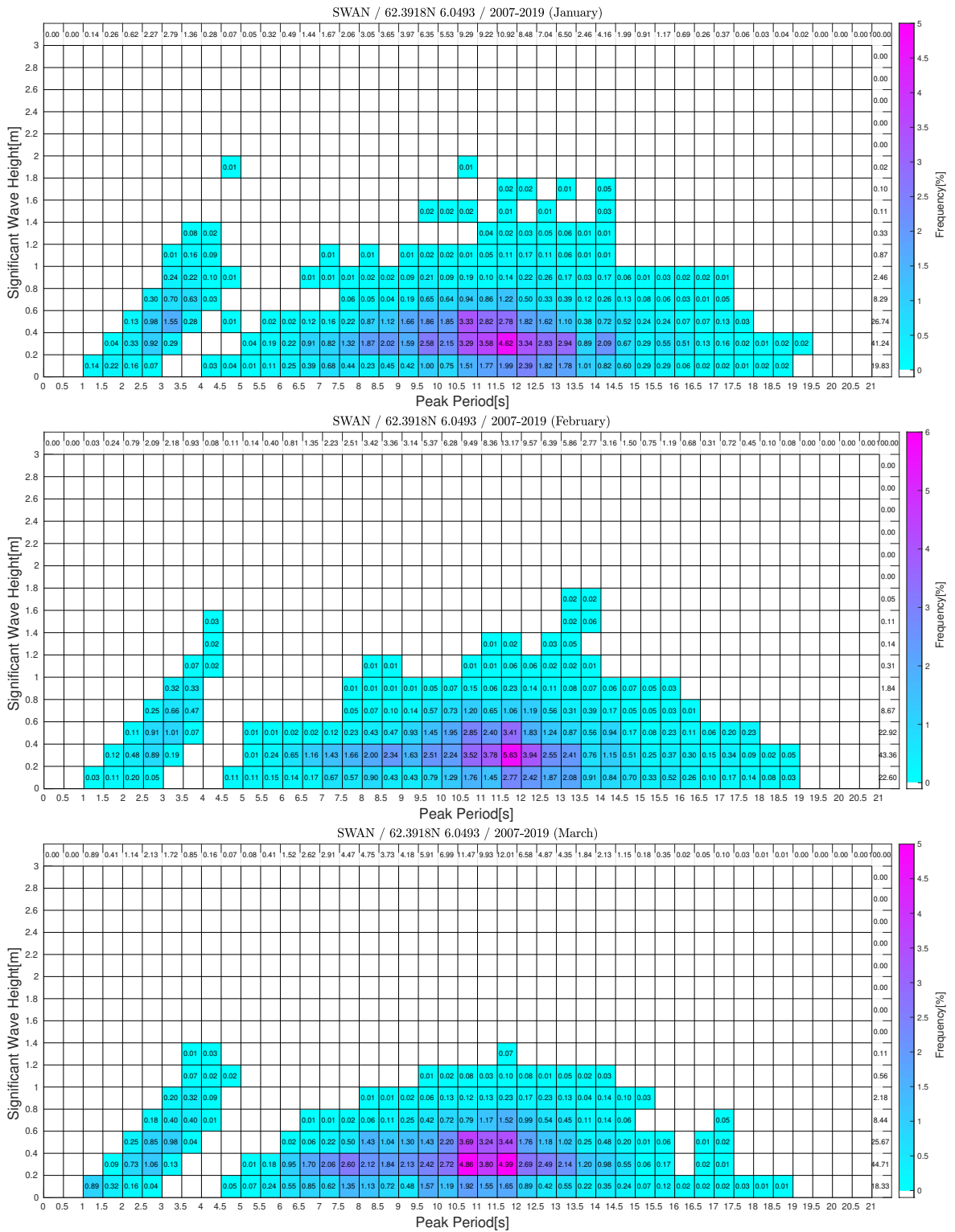


**Figure 82:** Monthly frequency tables of  $H_s/T_p$  at location C.

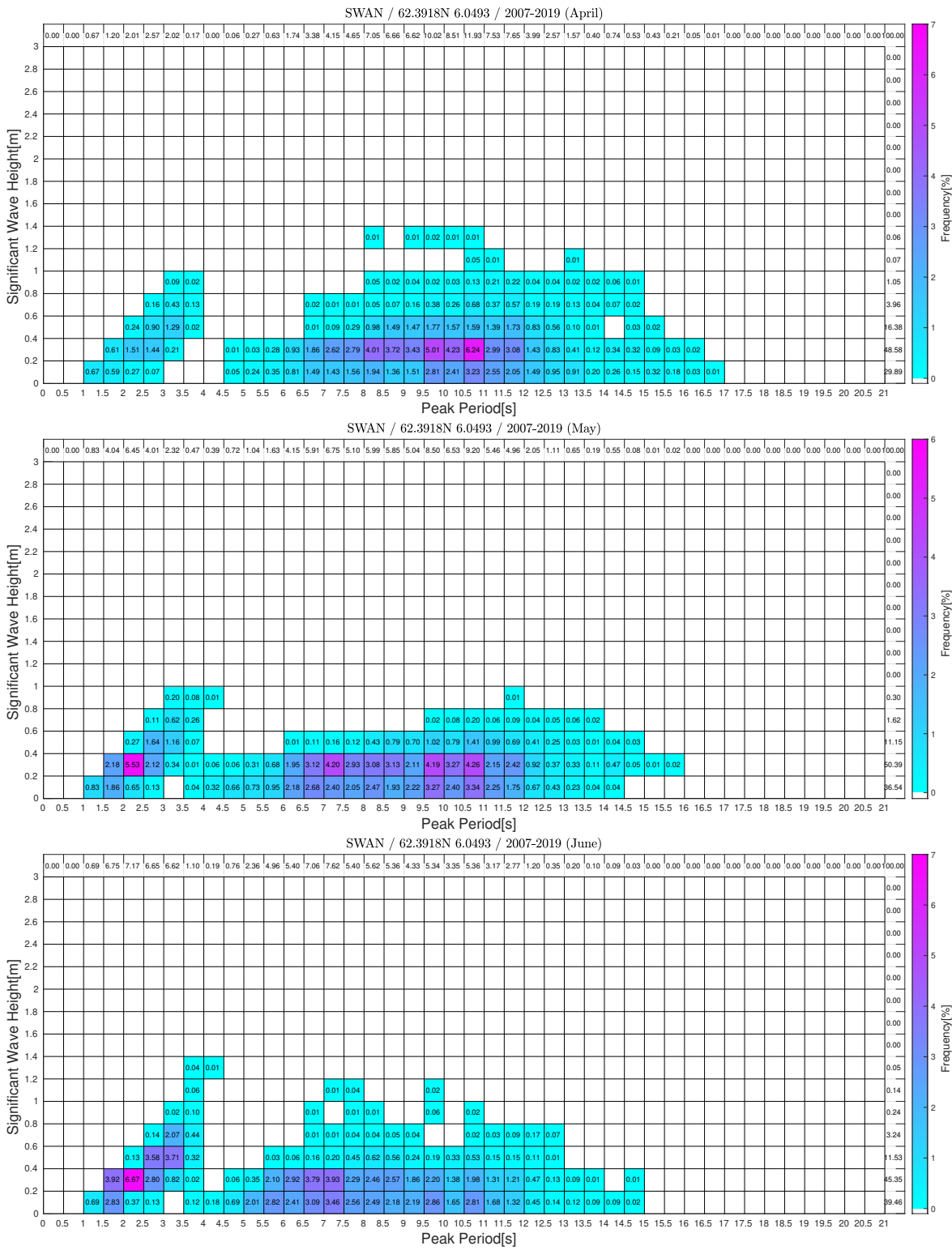


**Figure 83:** Monthly frequency tables of  $H_s/T_p$  at location C.

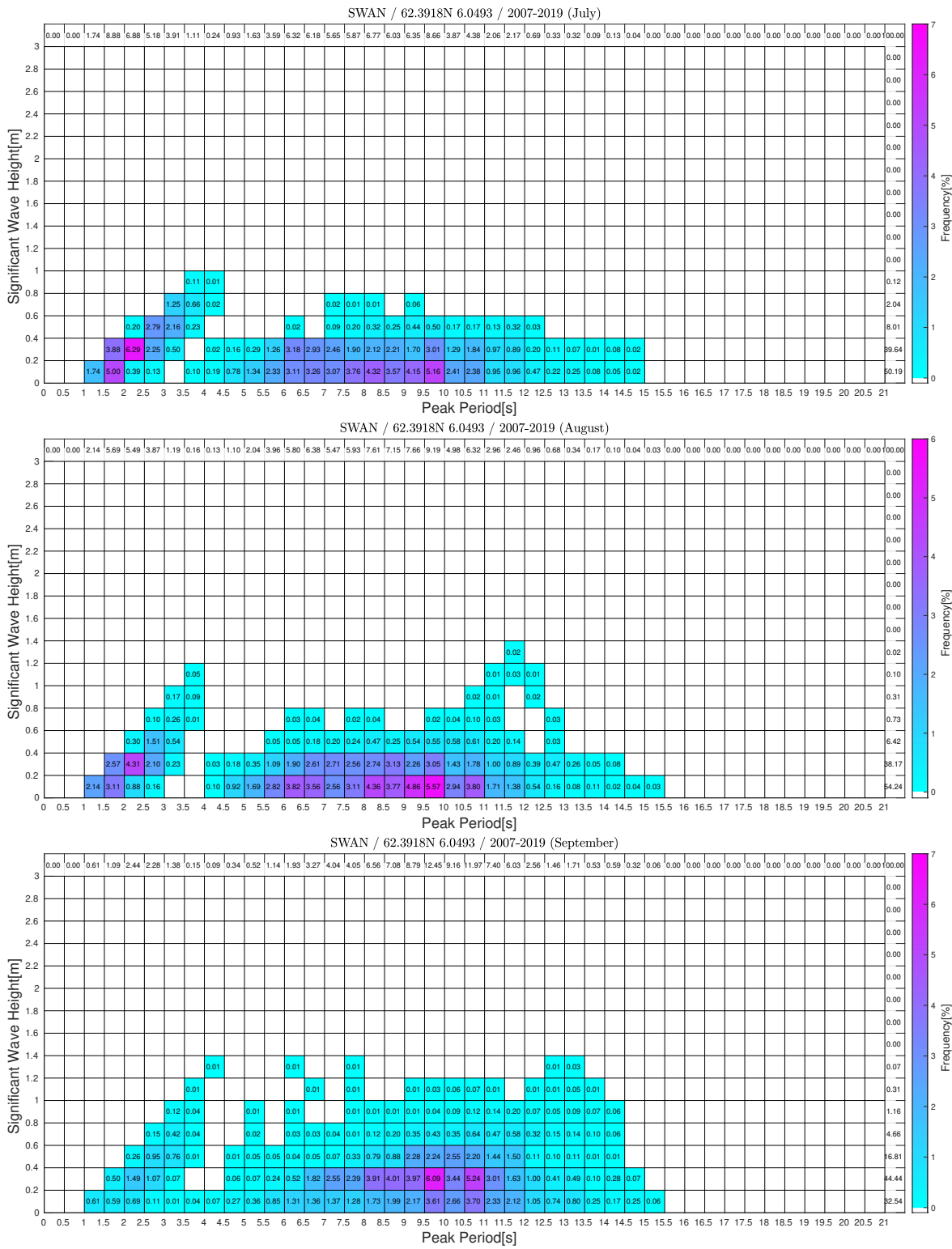


**Figure 84:** Monthly frequency tables of  $H_s/T_p$  at location C.

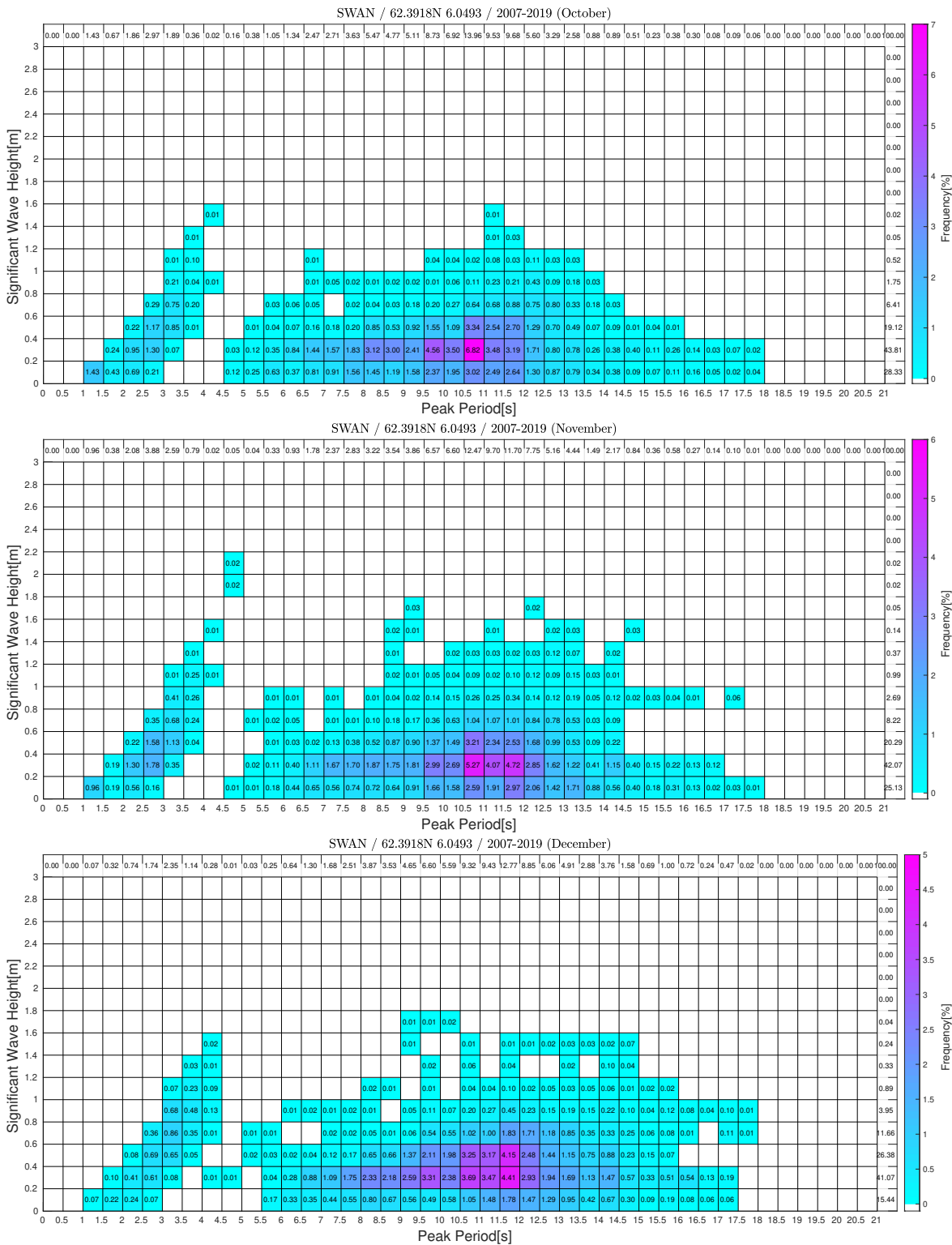


**Figure 85:** Monthly frequency tables of  $H_s/T_p$  at location C.

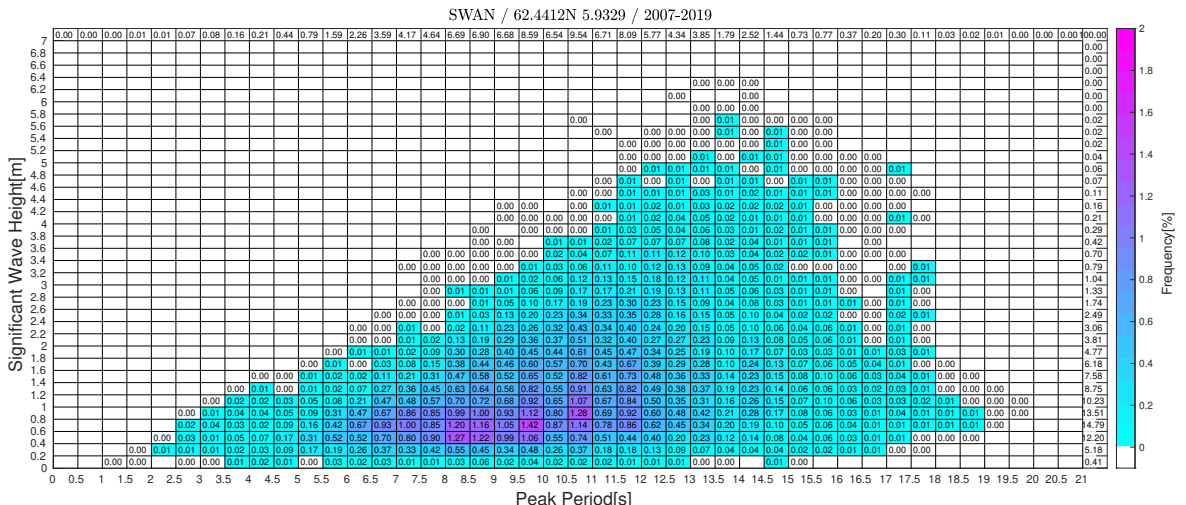


**Figure 86:** Frequency table of annual/omni  $H_s/T_p$  at location D.

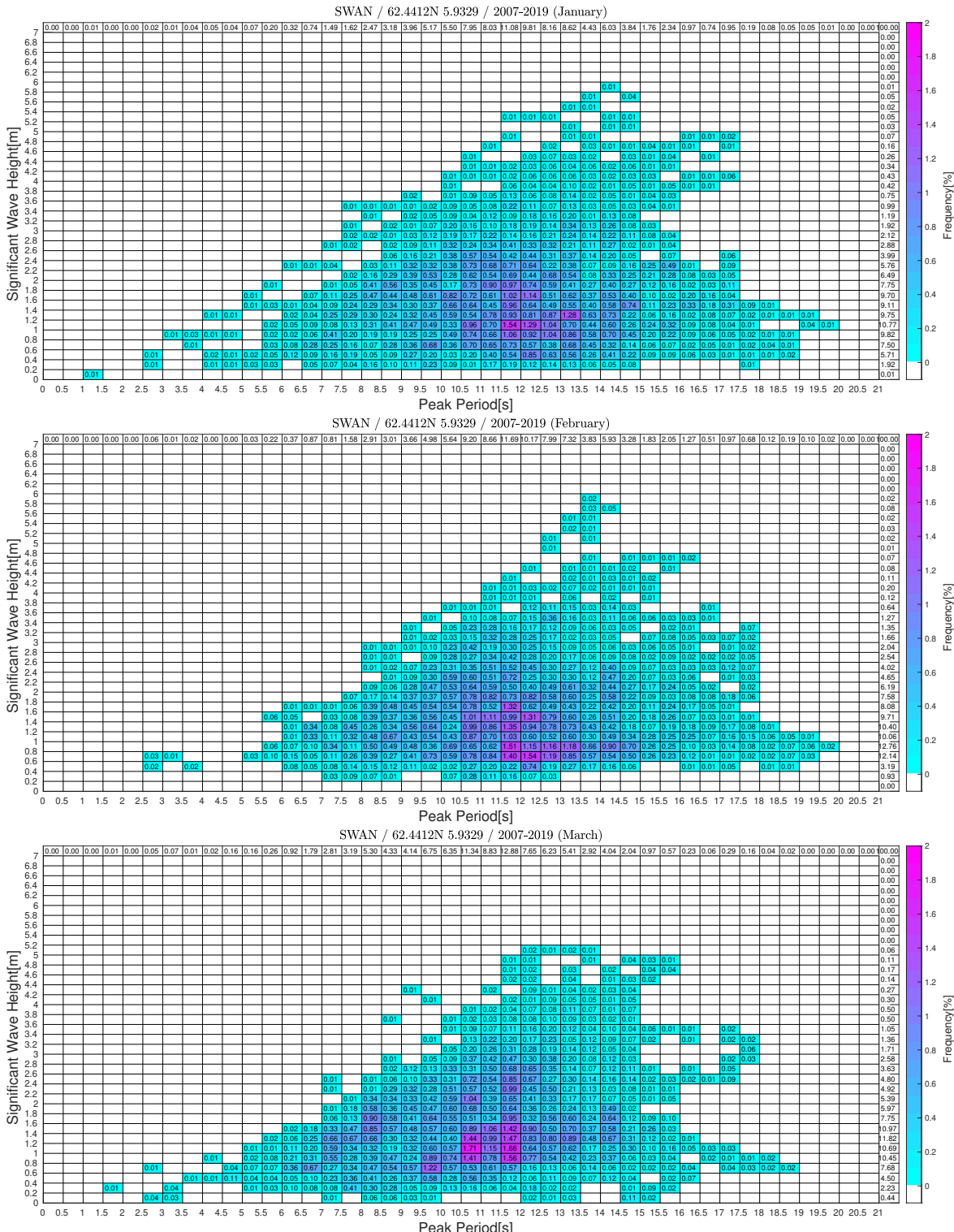


**Figure 87:** Monthly frequency tables of  $H_s/T_p$  at location D.

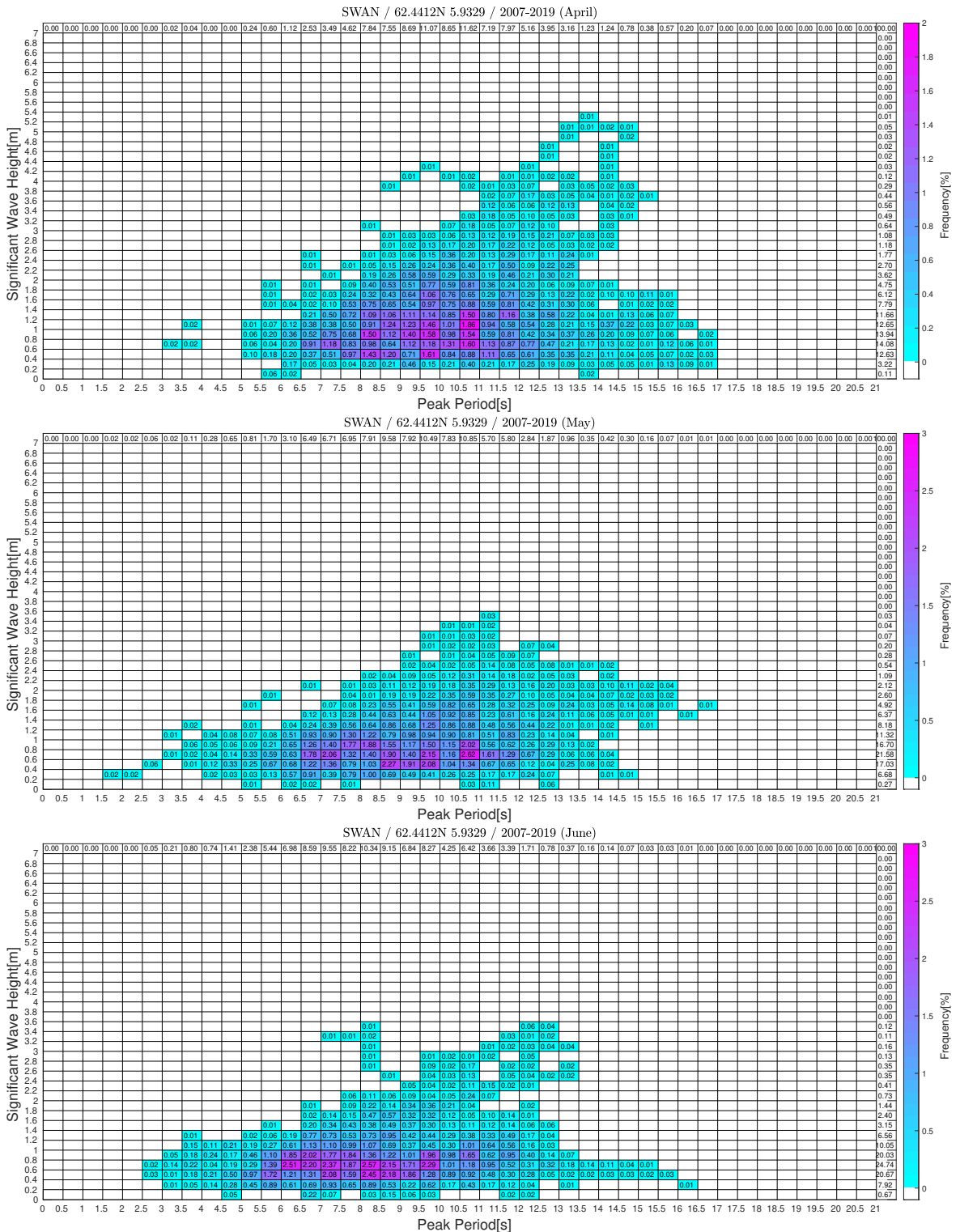


**Figure 88:** Monthly frequency tables of  $H_s/T_p$  at location D.

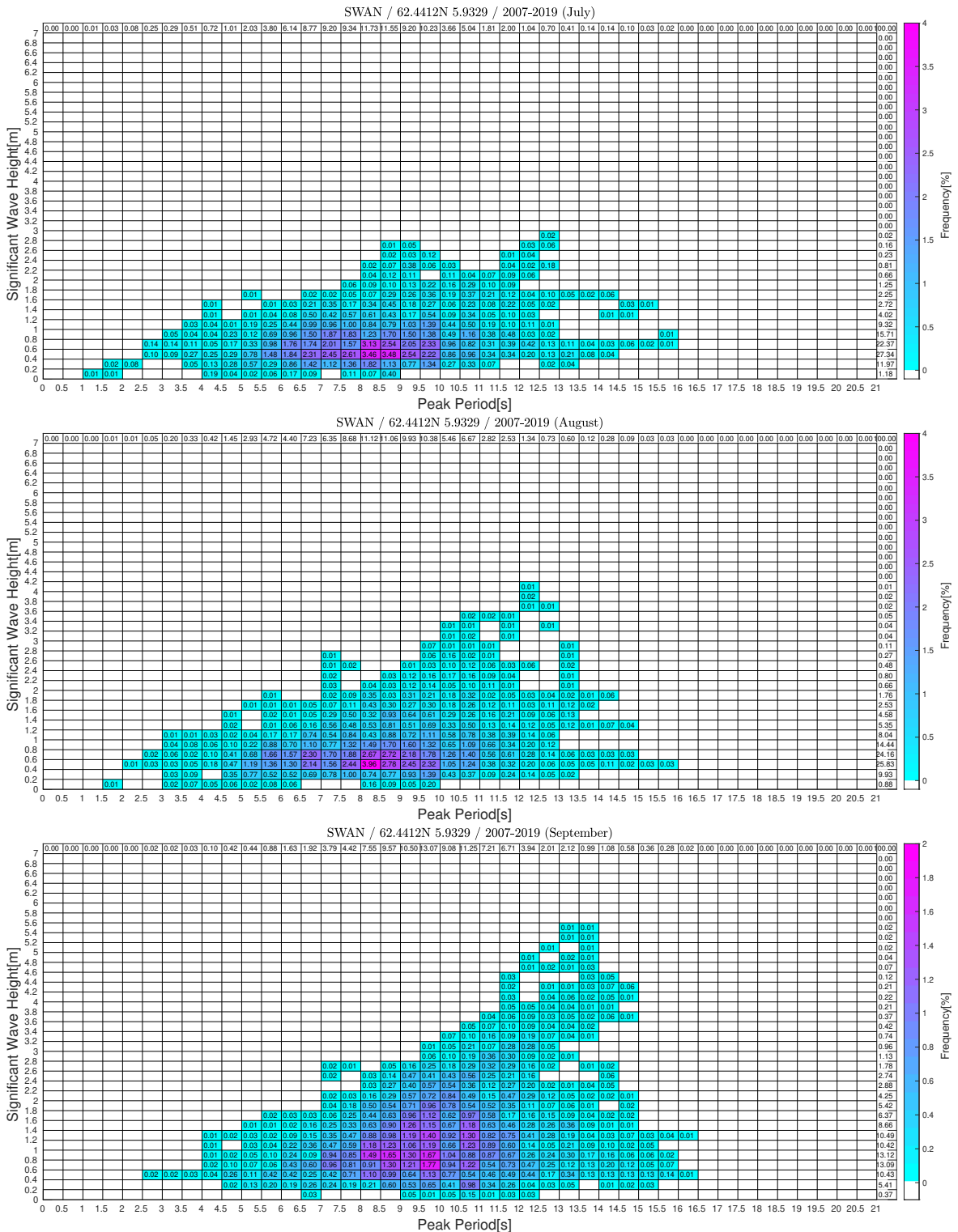


**Figure 89:** Monthly frequency tables of  $H_s/T_p$  at location D.

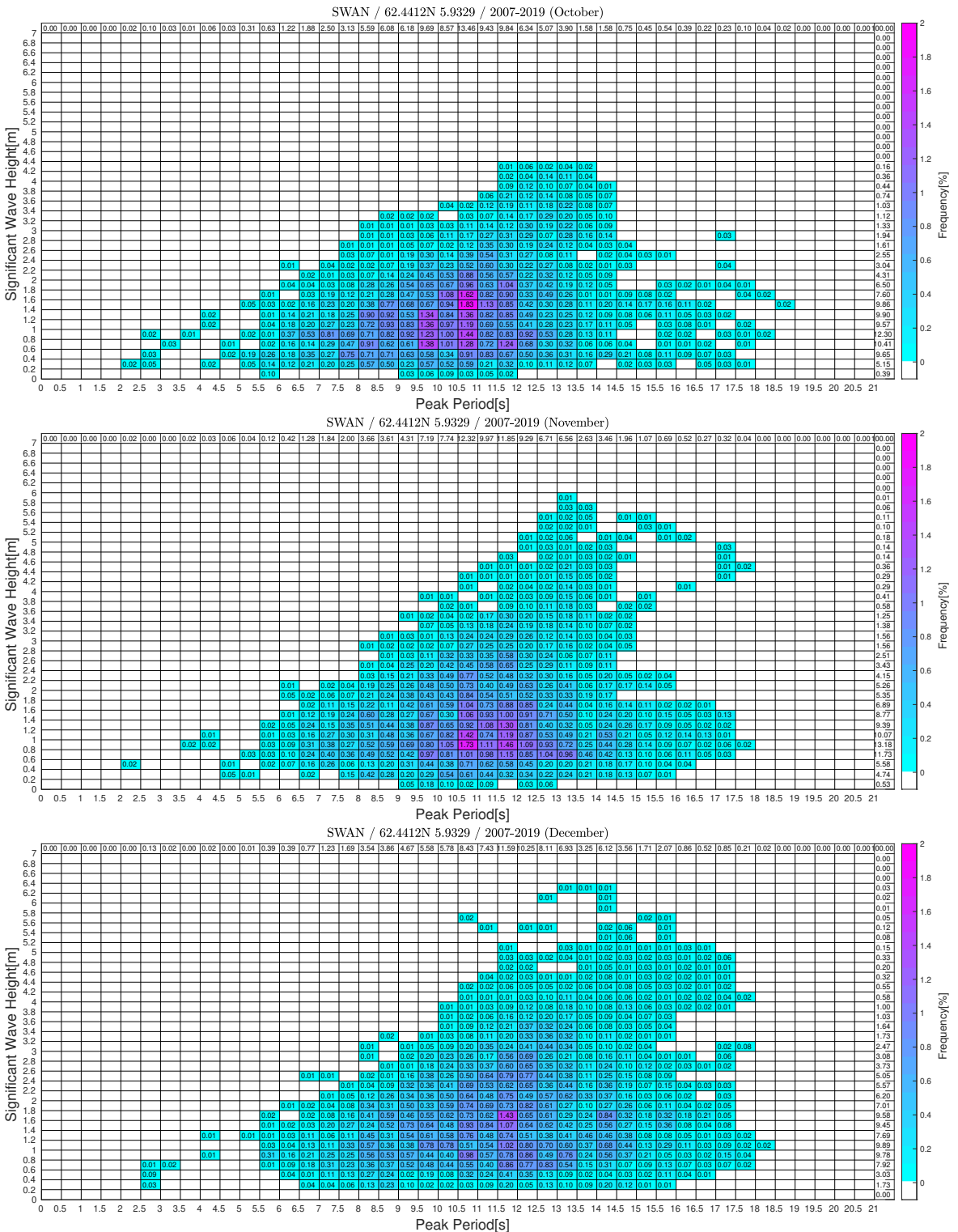


**Figure 90:** Monthly frequency tables of  $H_s/T_p$  at location D.

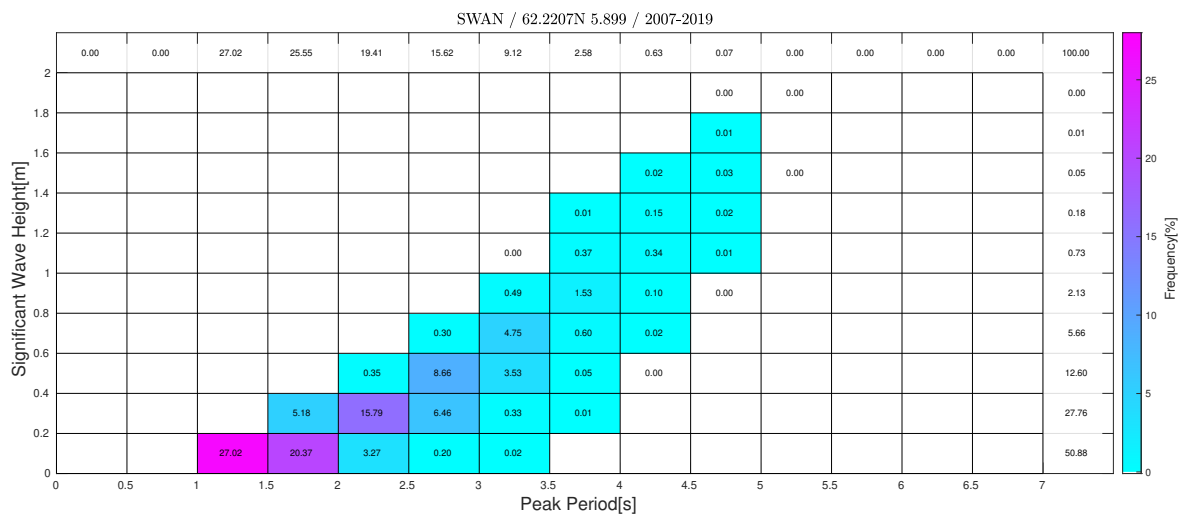


**Figure 91:** Frequency table of annual/omni  $H_s/T_p$  at location F.

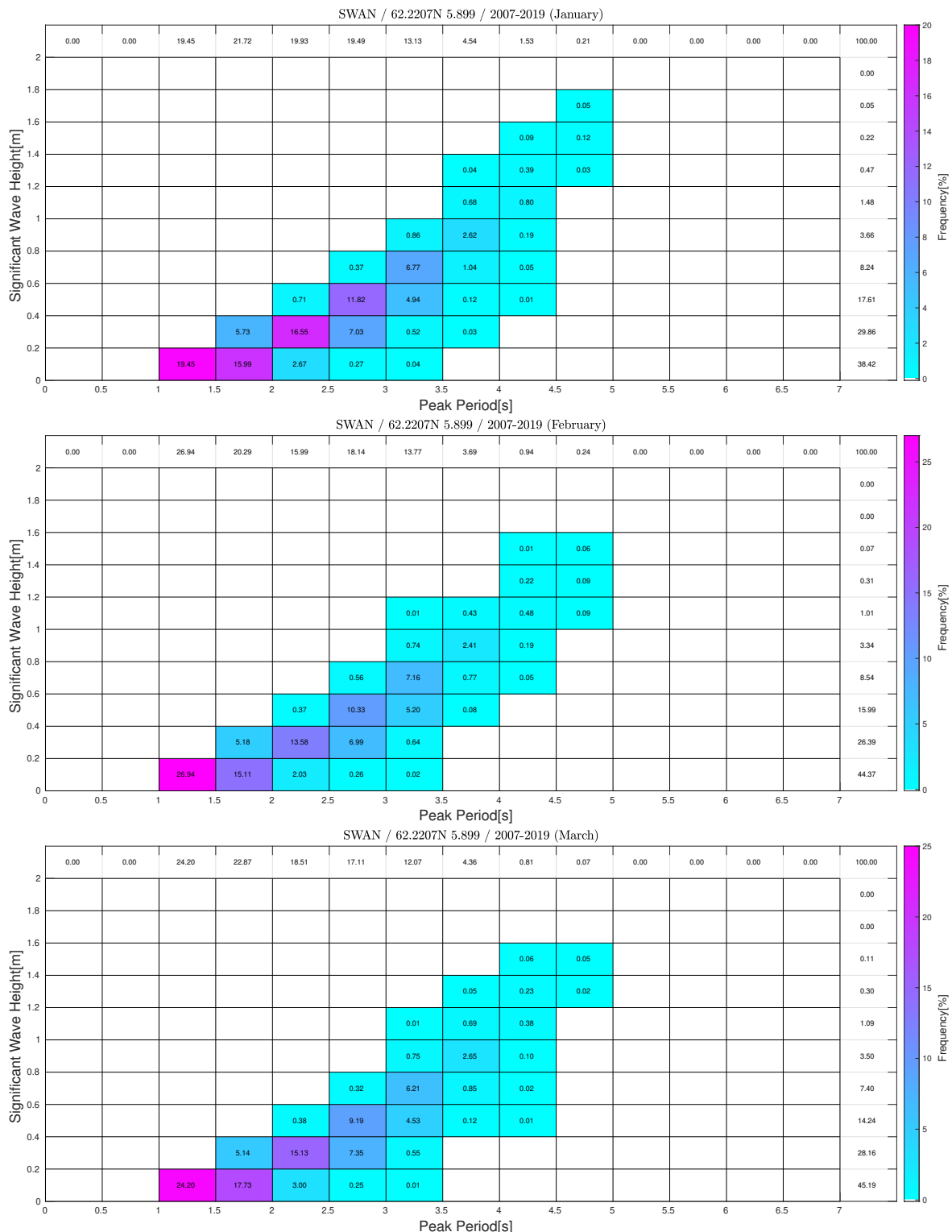


**Figure 92:** Monthly frequency tables of  $H_s/T_p$  at location F.

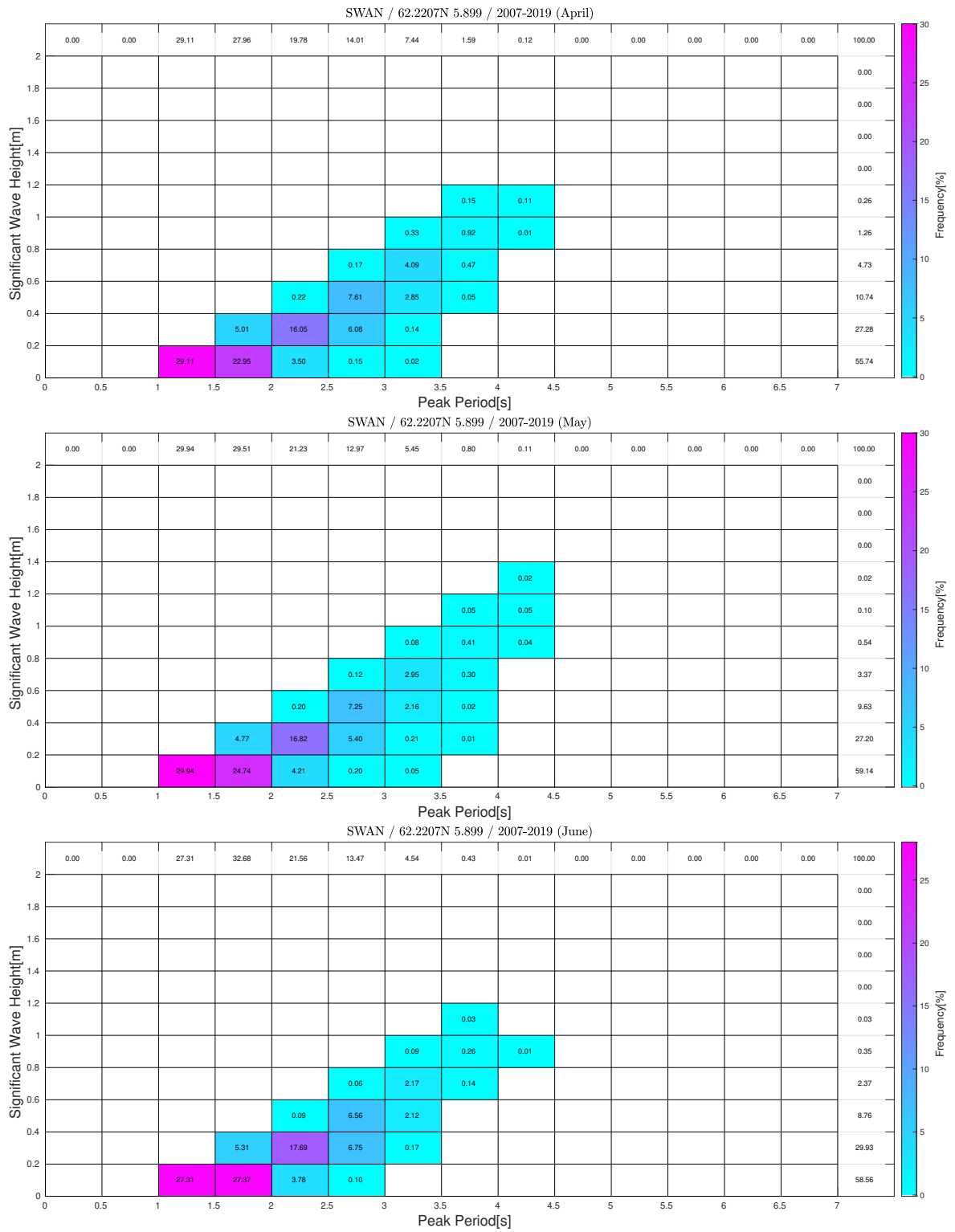


**Figure 93:** Monthly frequency tables of  $H_s/T_p$  at location F.

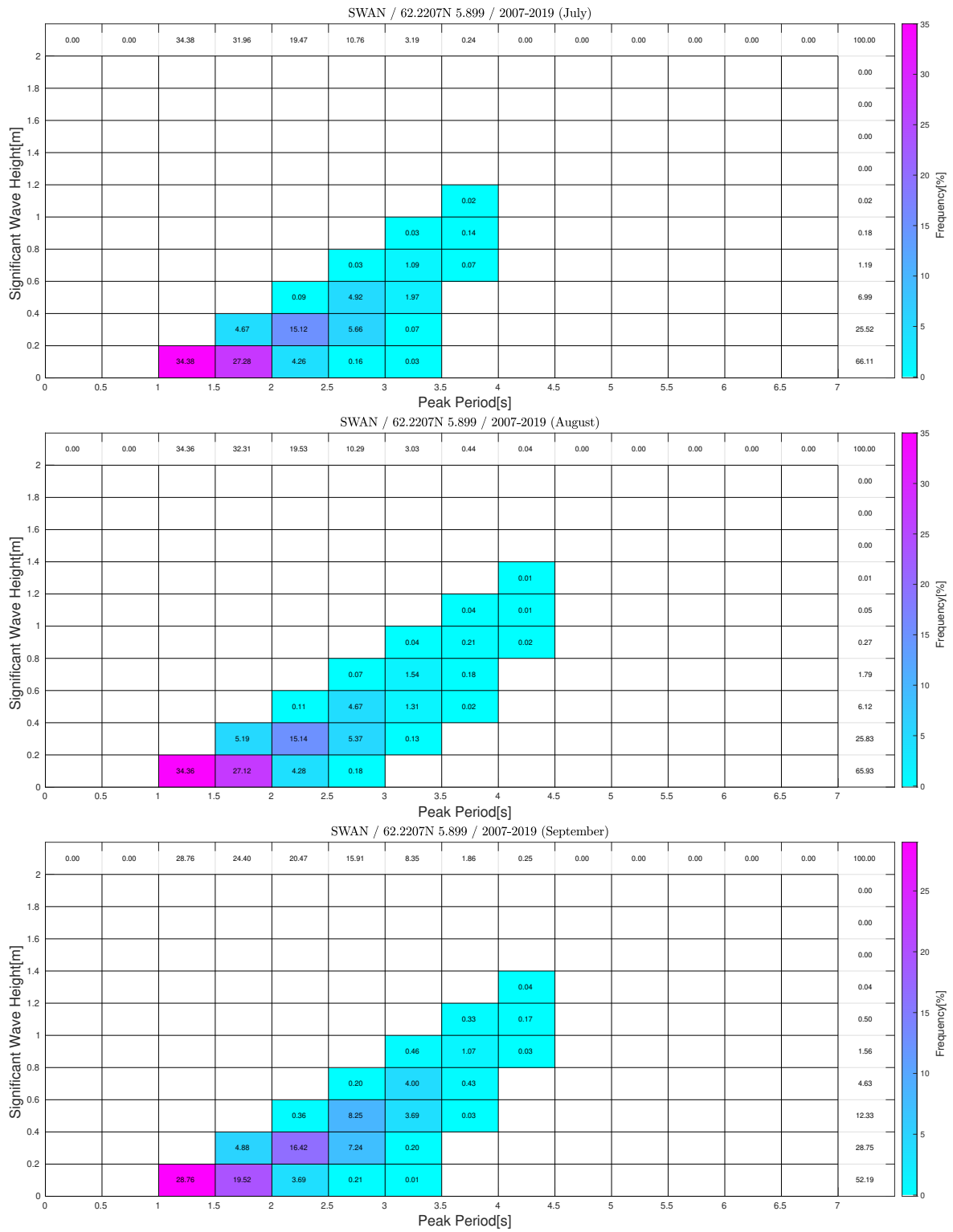


**Figure 94:** Monthly frequency tables of  $H_s/T_p$  at location F.

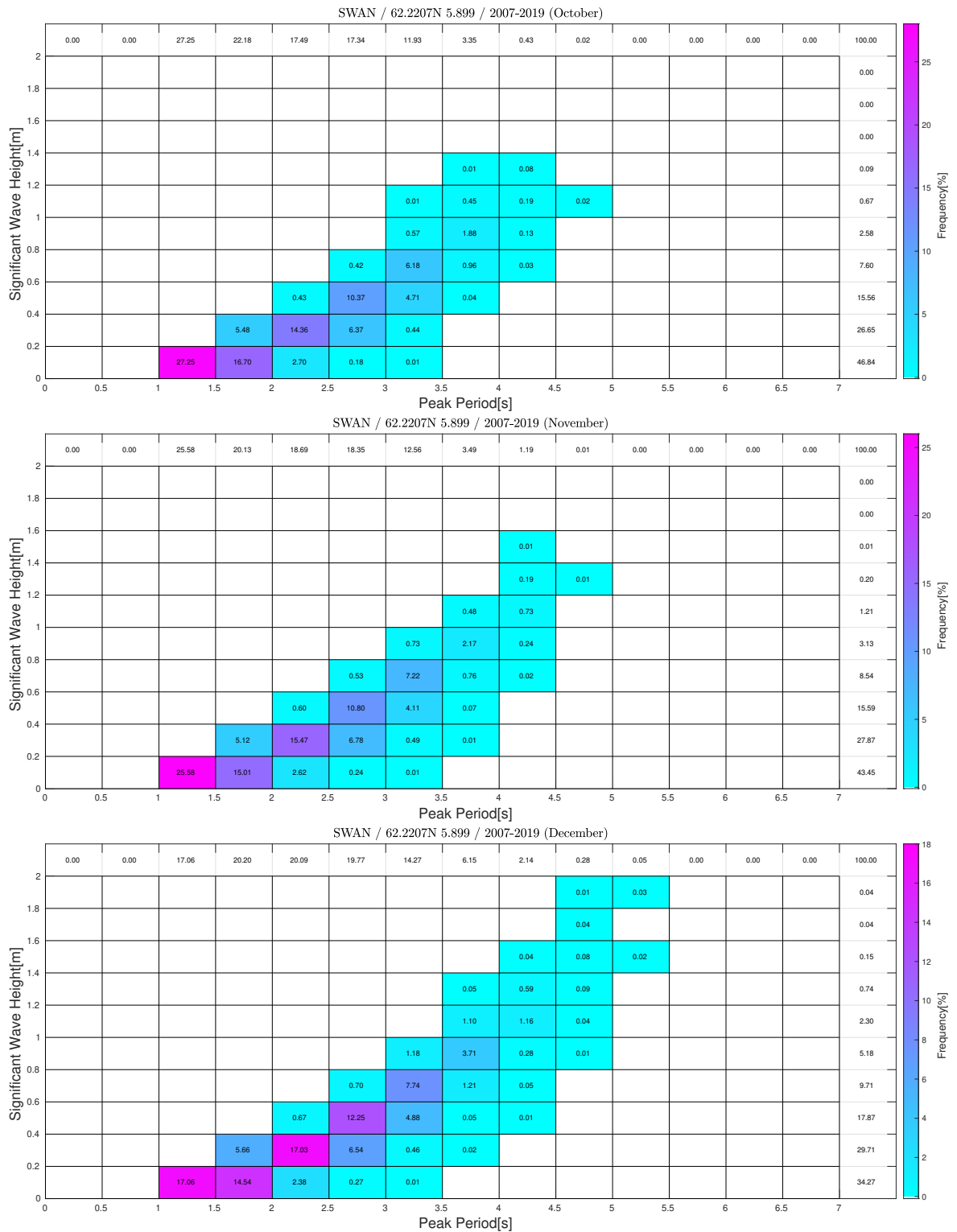


**Figure 95:** Monthly frequency tables of  $H_s/T_p$  at location F.

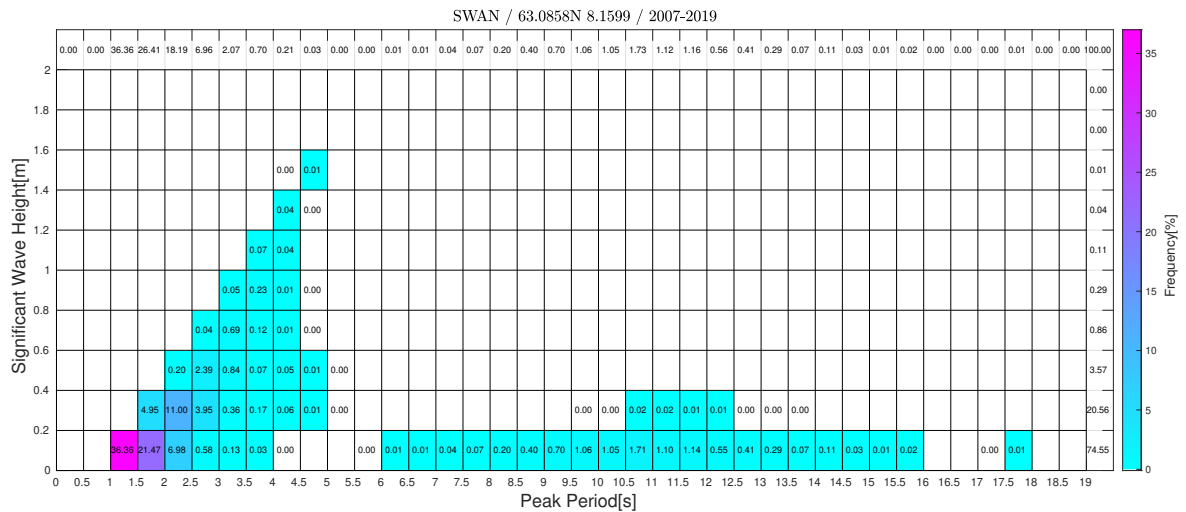


**Figure 96:** Frequency table of annual/omni  $H_s/T_p$  at location G.

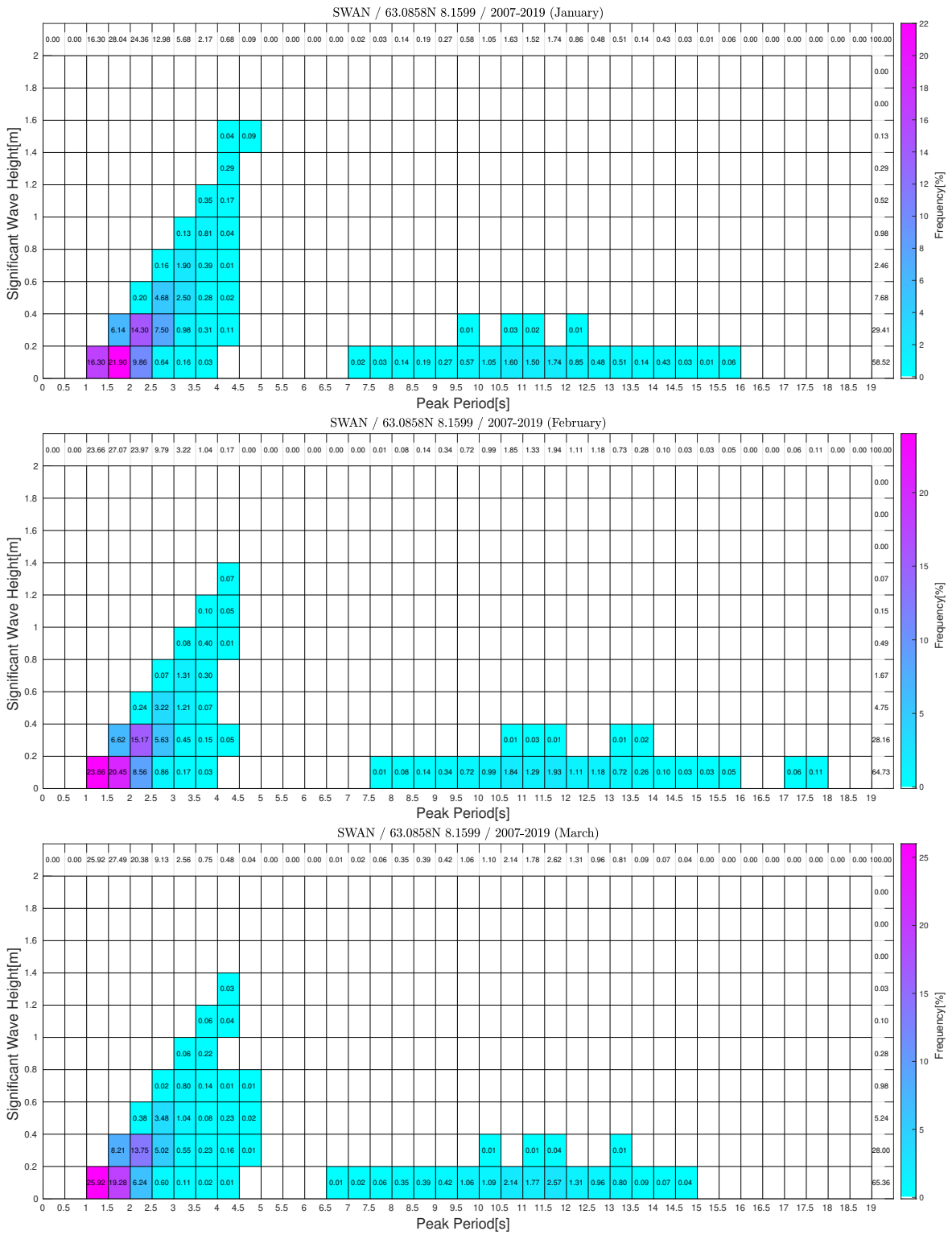


**Figure 97:** Monthly frequency tables of  $H_s/T_p$  at location G.

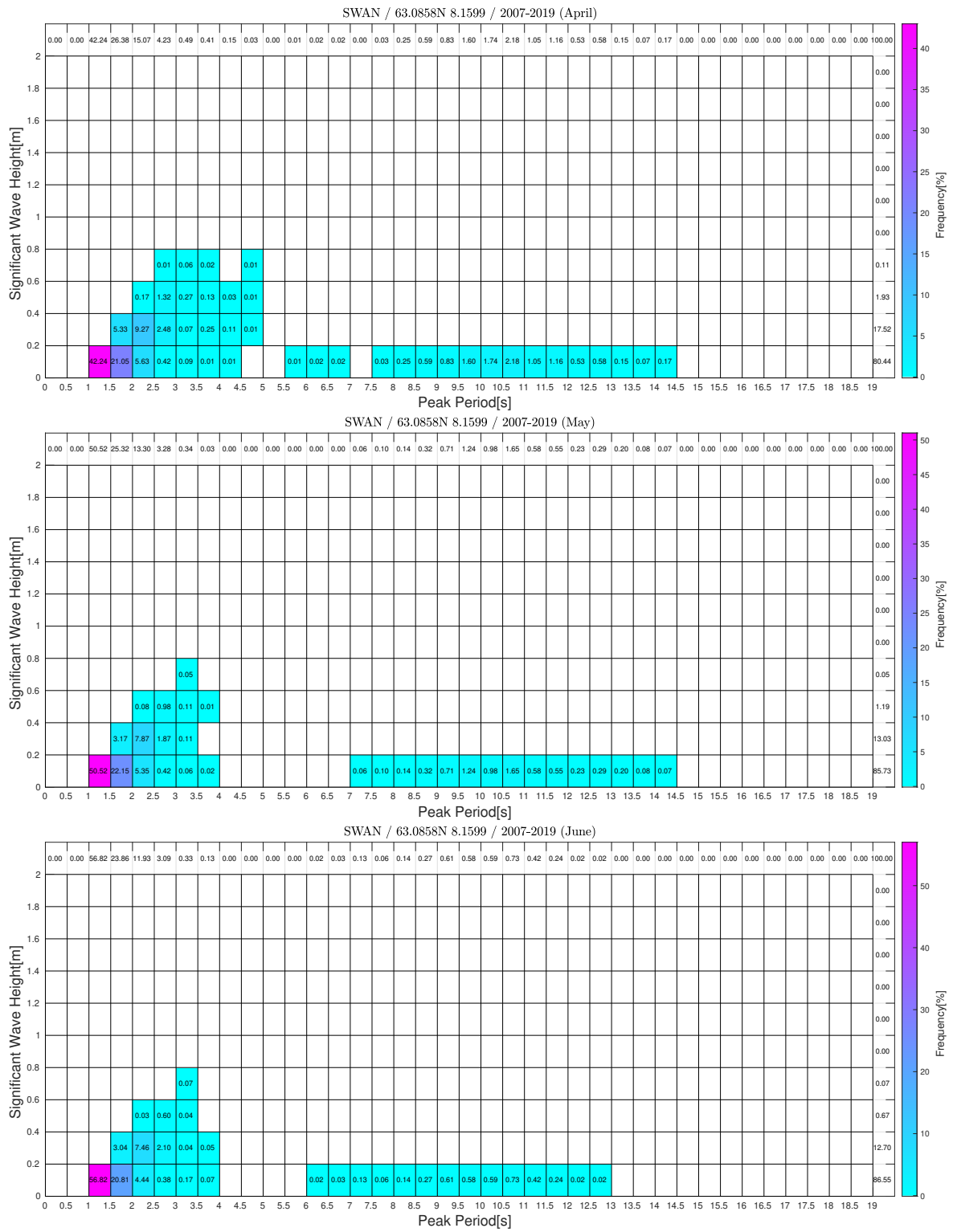


**Figure 98:** Monthly frequency tables of  $H_s/T_p$  at location G.

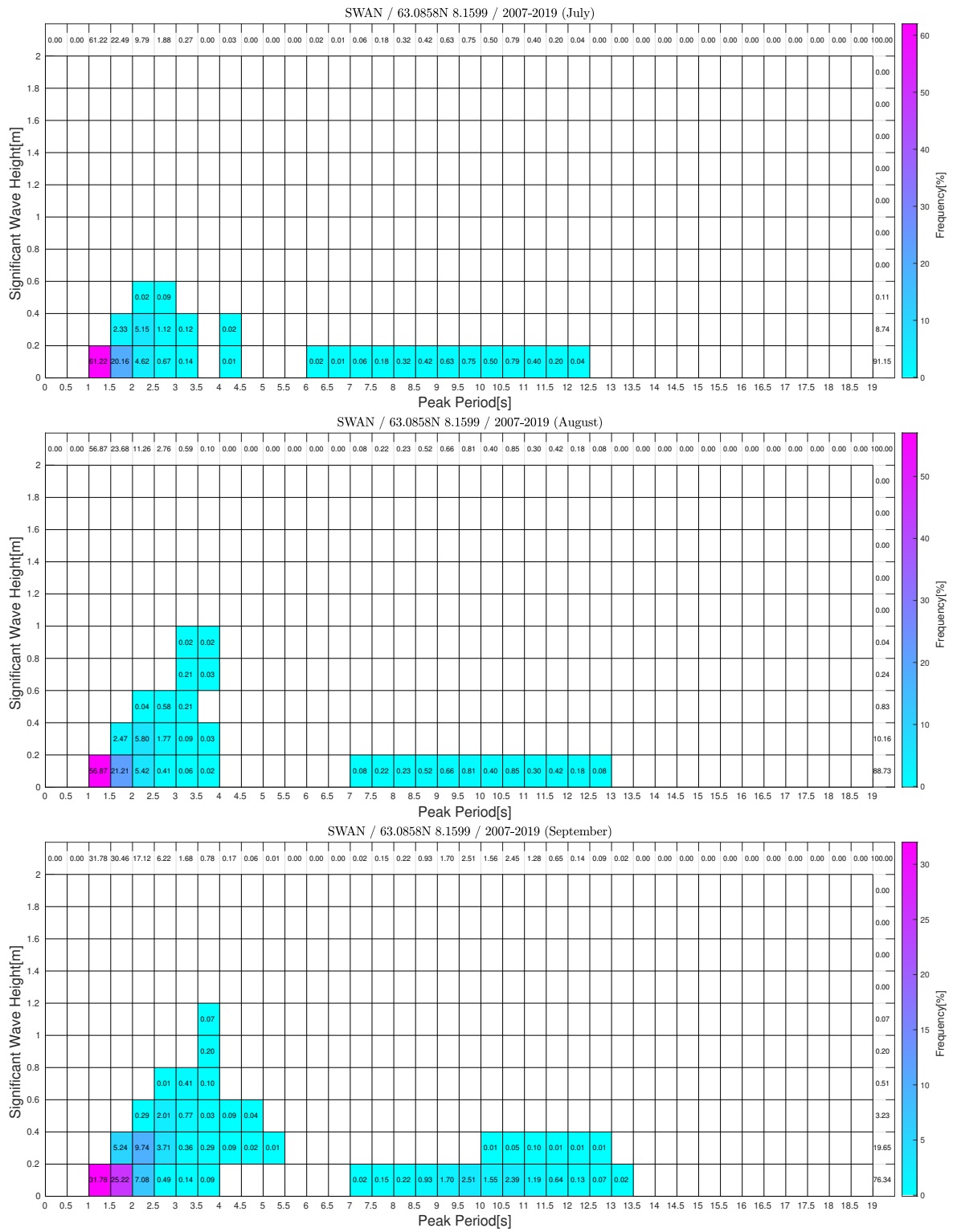


**Figure 99:** Monthly frequency tables of  $H_s/T_p$  at location G.

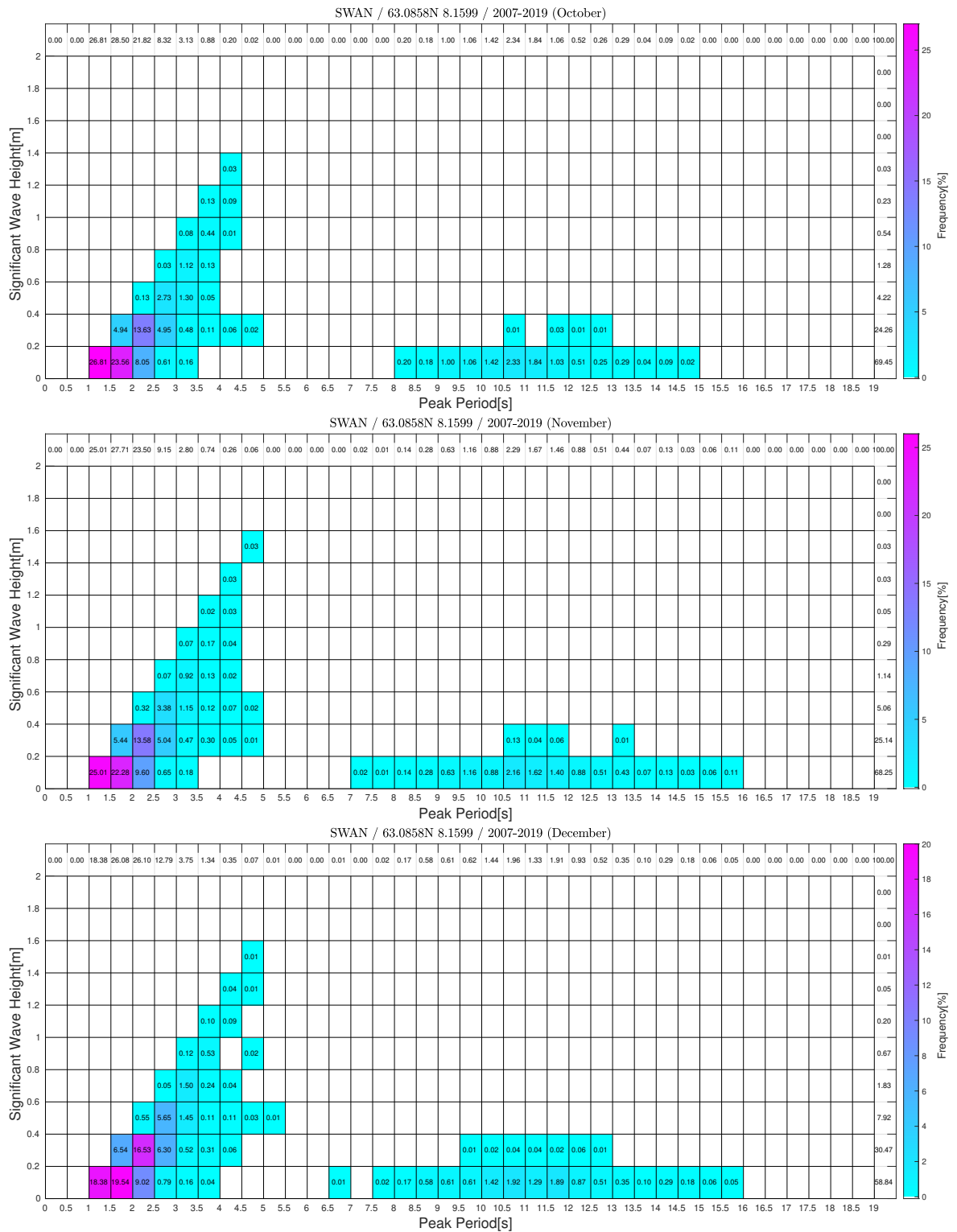


**Figure 100:** Monthly frequency tables of  $H_s/T_p$  at location G.

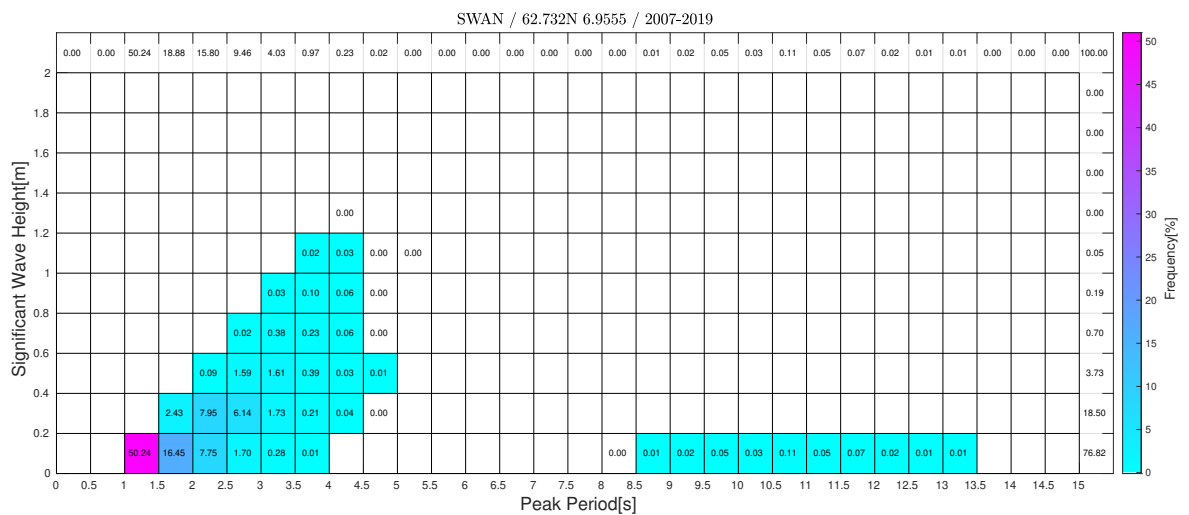


**Figure 101:** Frequency table of annual/omni  $H_s/T_p$  at location J.

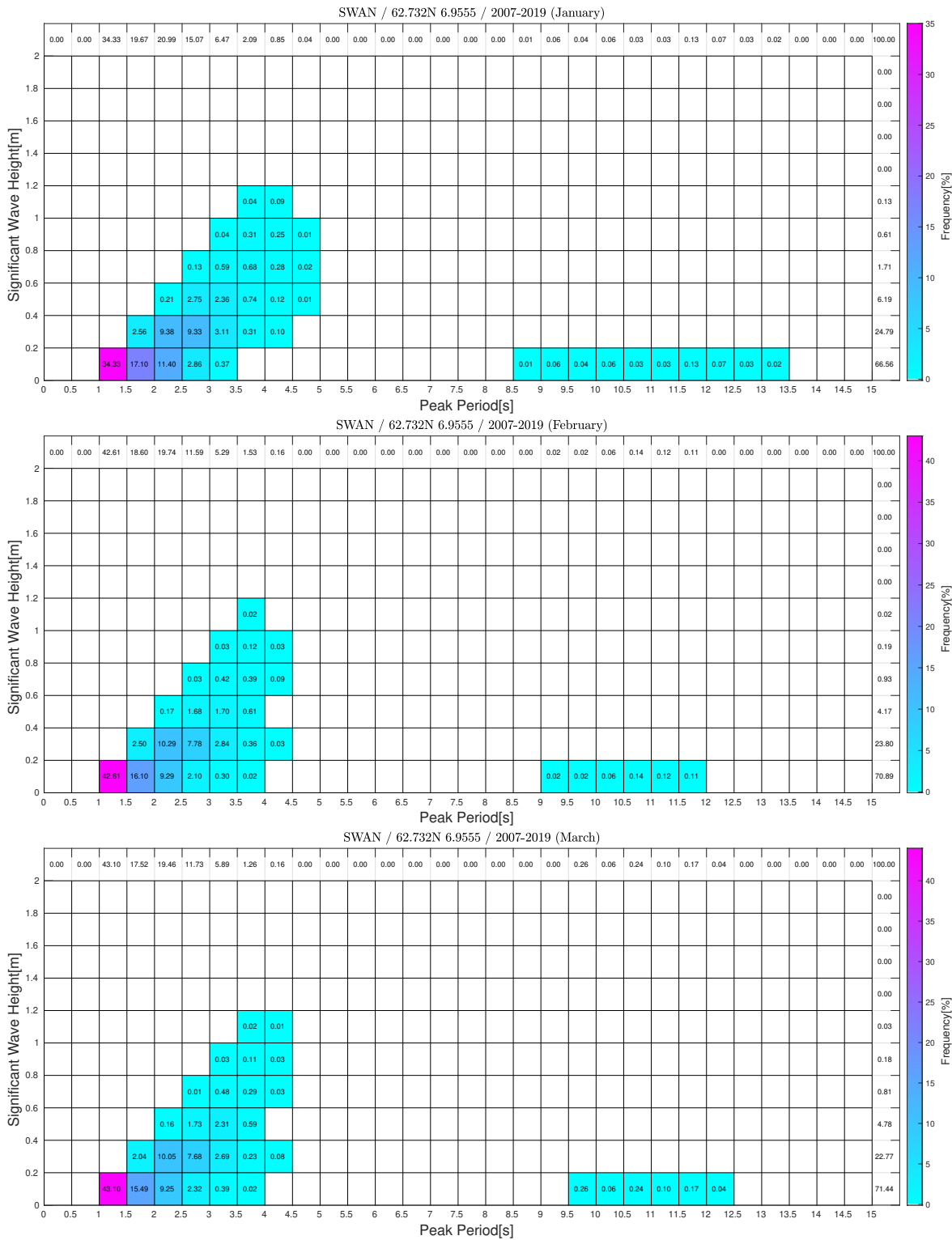


**Figure 102:** Monthly frequency tables of  $H_s/T_p$  at location J.

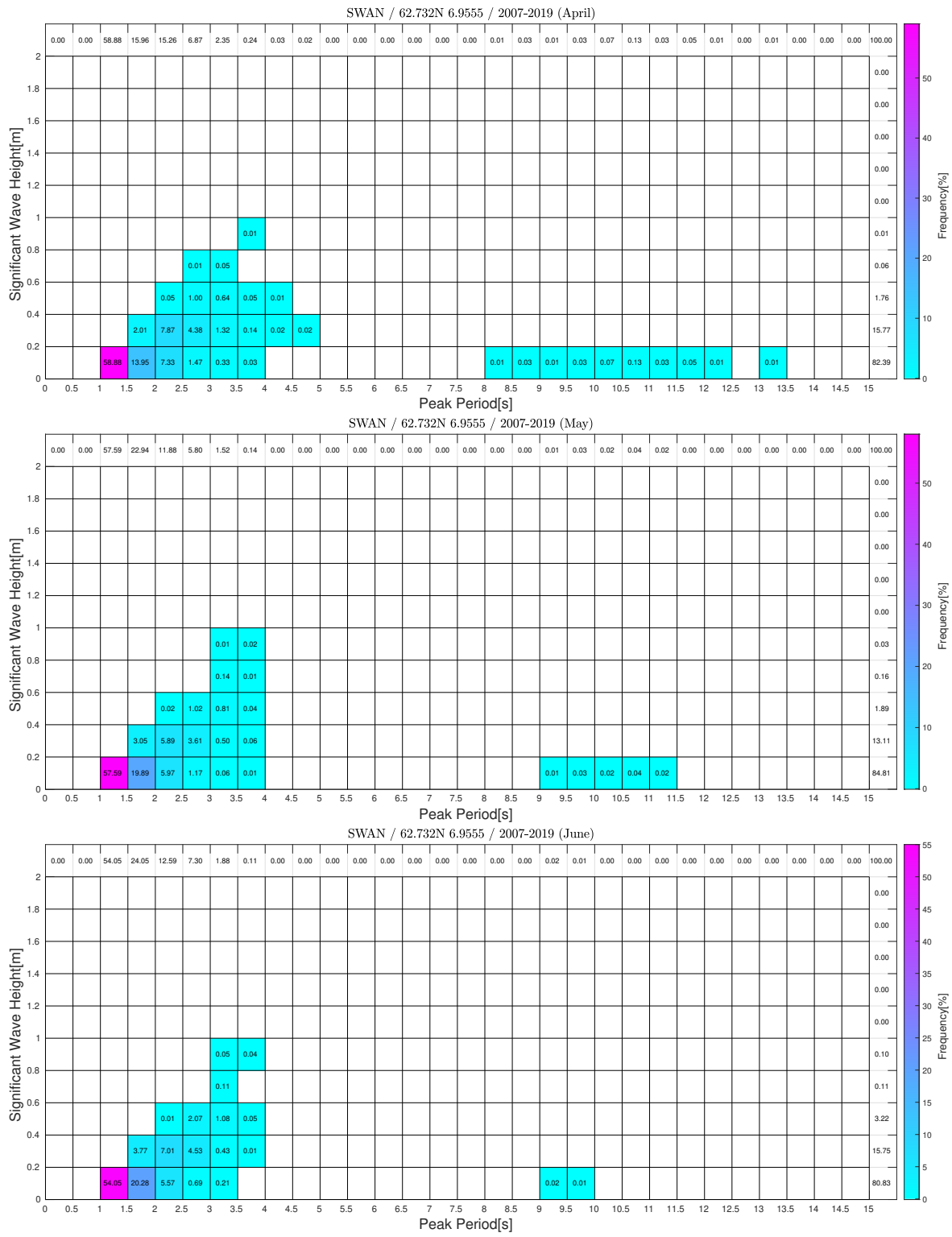


**Figure 103:** Monthly frequency tables of  $H_s/T_p$  at location J.

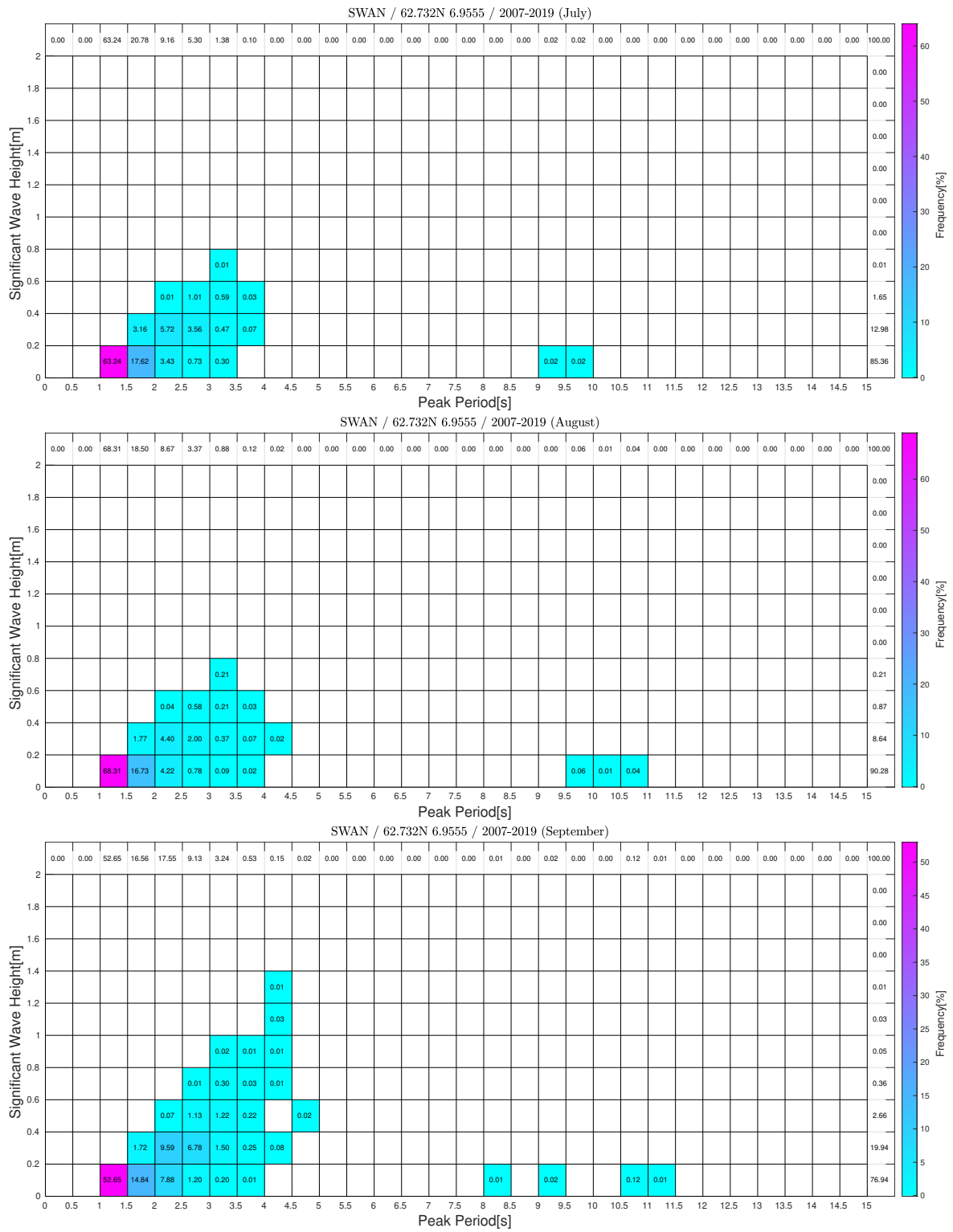


**Figure 104:** Monthly frequency tables of  $H_s/T_p$  at location J.

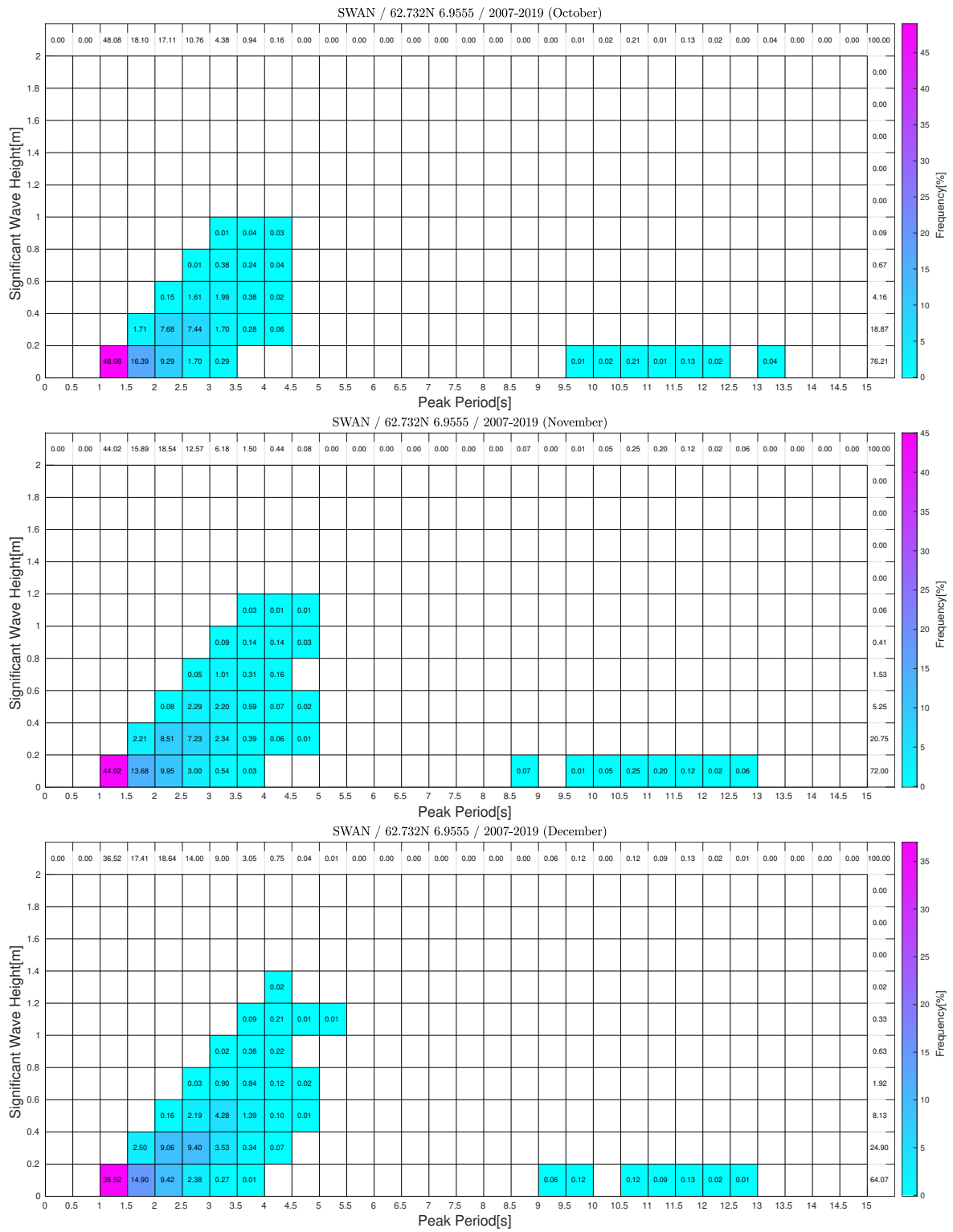


**Figure 105:** Monthly frequency tables of  $H_s/T_p$  at location J.

## **7.5.2 Significant Wave Height and Wind Speed**

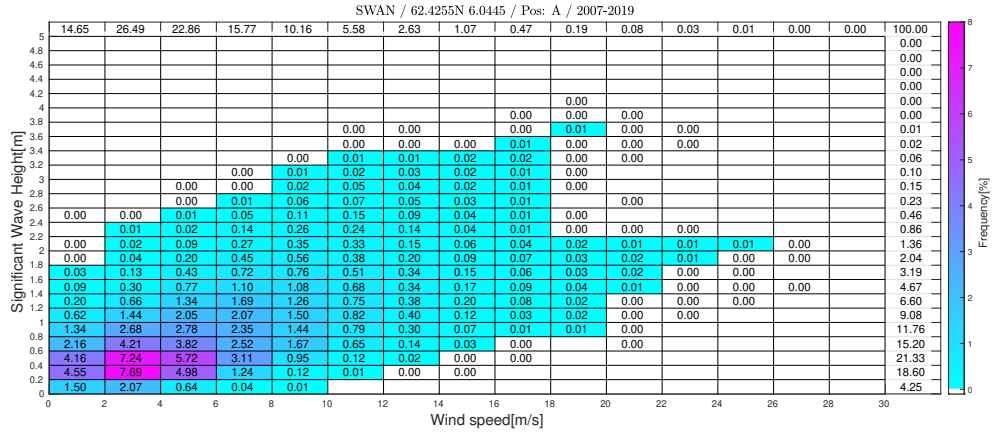


**Figure 106:** Frequency tables of  $H_s/FF$  at location A

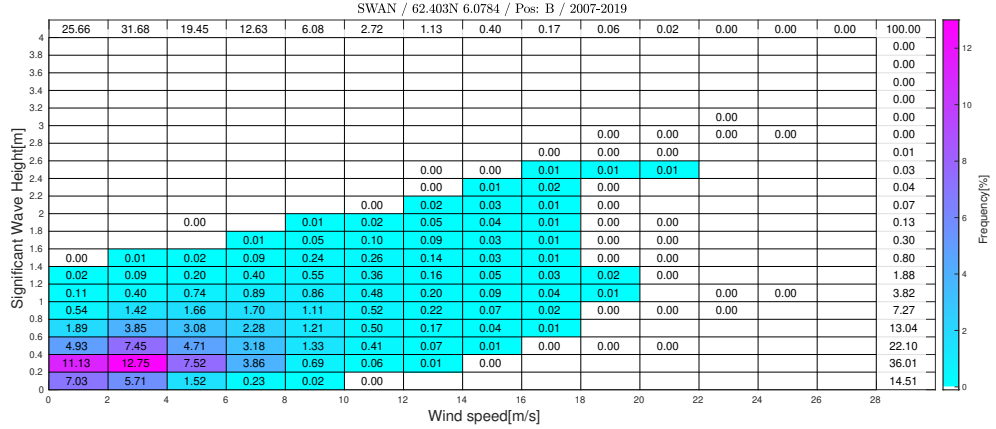


**Figure 107:** Frequency tables of  $H_s/FF$  at location B

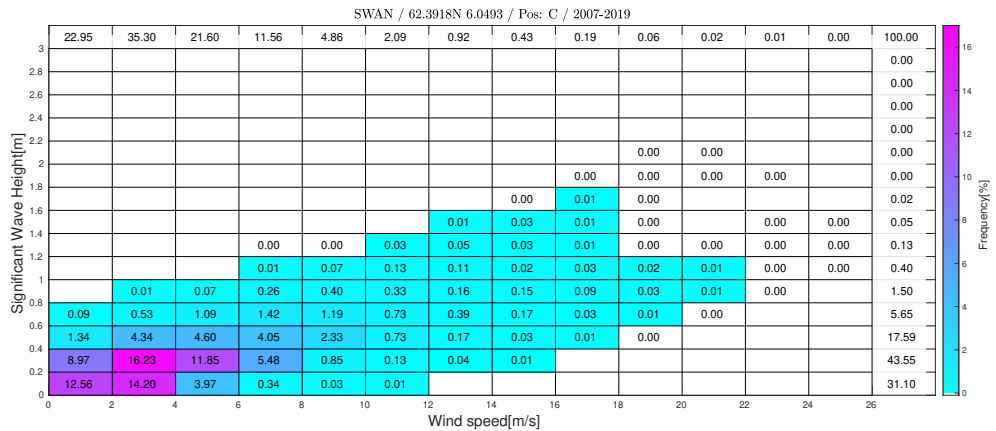


**Figure 108:** Frequency tables of  $H_s$ /FF at location C

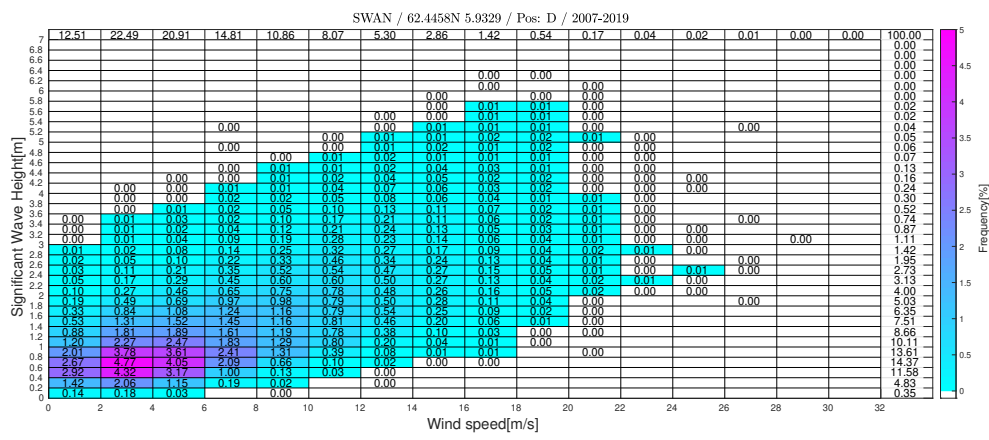


**Figure 109:** Frequency tables of  $H_s/FF$  at location D

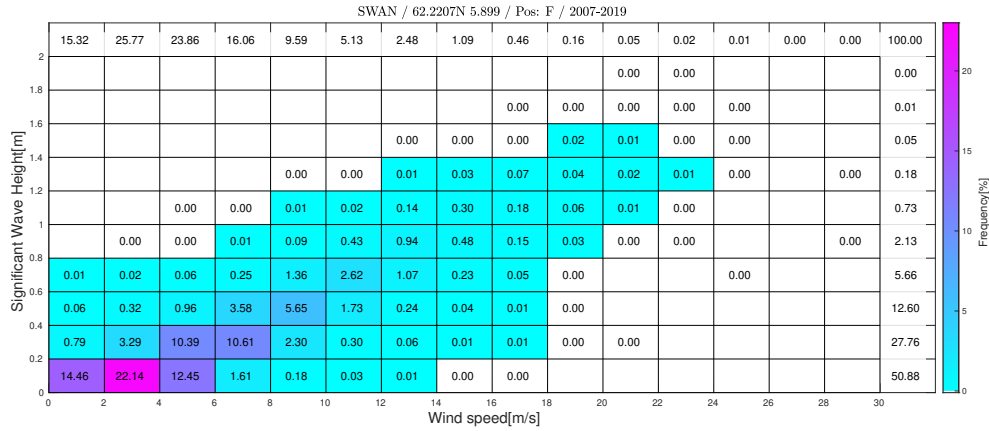


**Figure 110:** Frequency tables of  $H_s/FF$  at location F

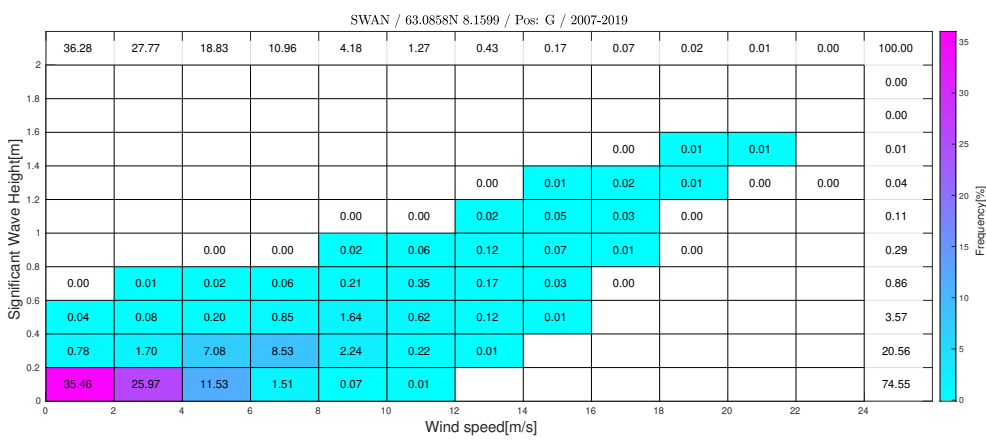


**Figure 111:** Frequency tables of  $H_s/FF$  at location G

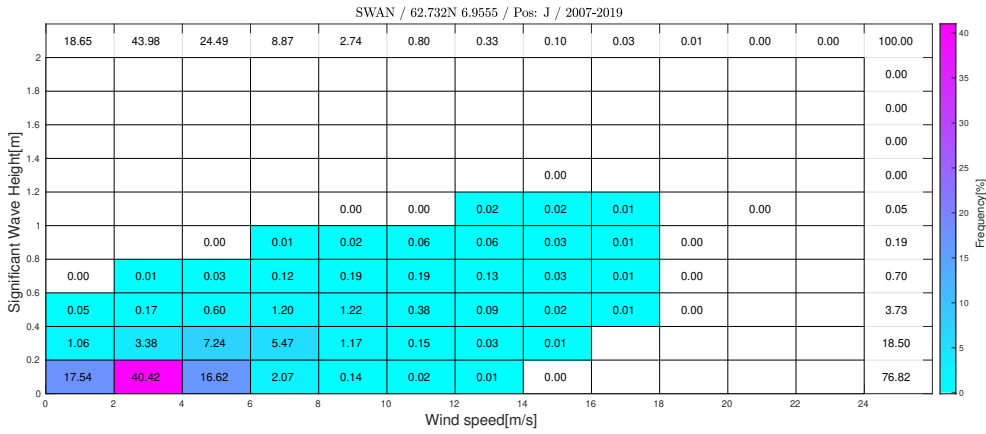


**Figure 112:** Frequency tables of  $H_s/FF$  at location J

## 7.6 Validation NORA10

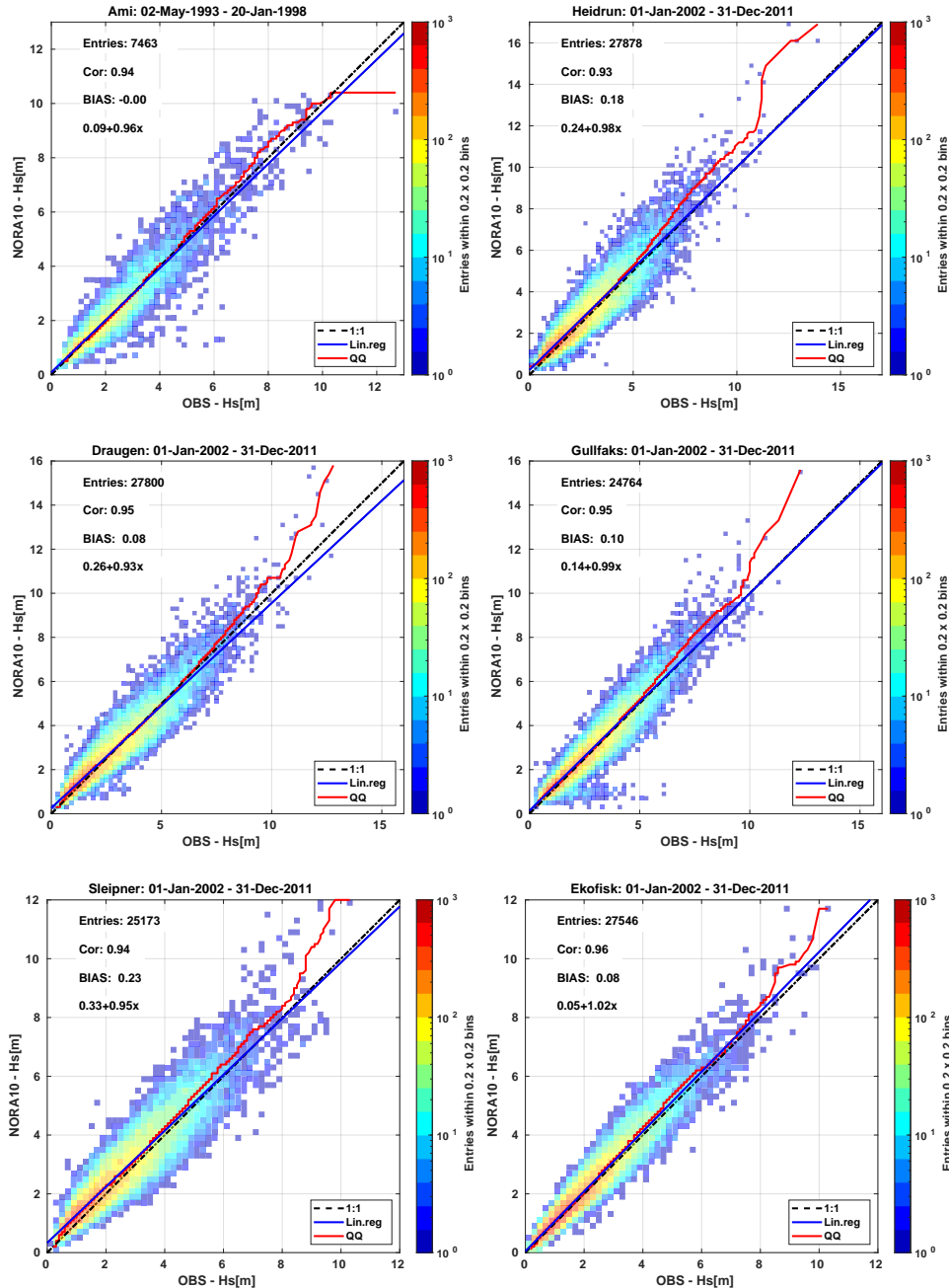


**Figure 113:** Significant wave height obtained from NORA10 validated against observed  $H_s$  over the period 2002-2011 (Ami: 1993-1998). Observations are based on 20-min periods and retained every three hours, corresponding to the hours of NORA10.

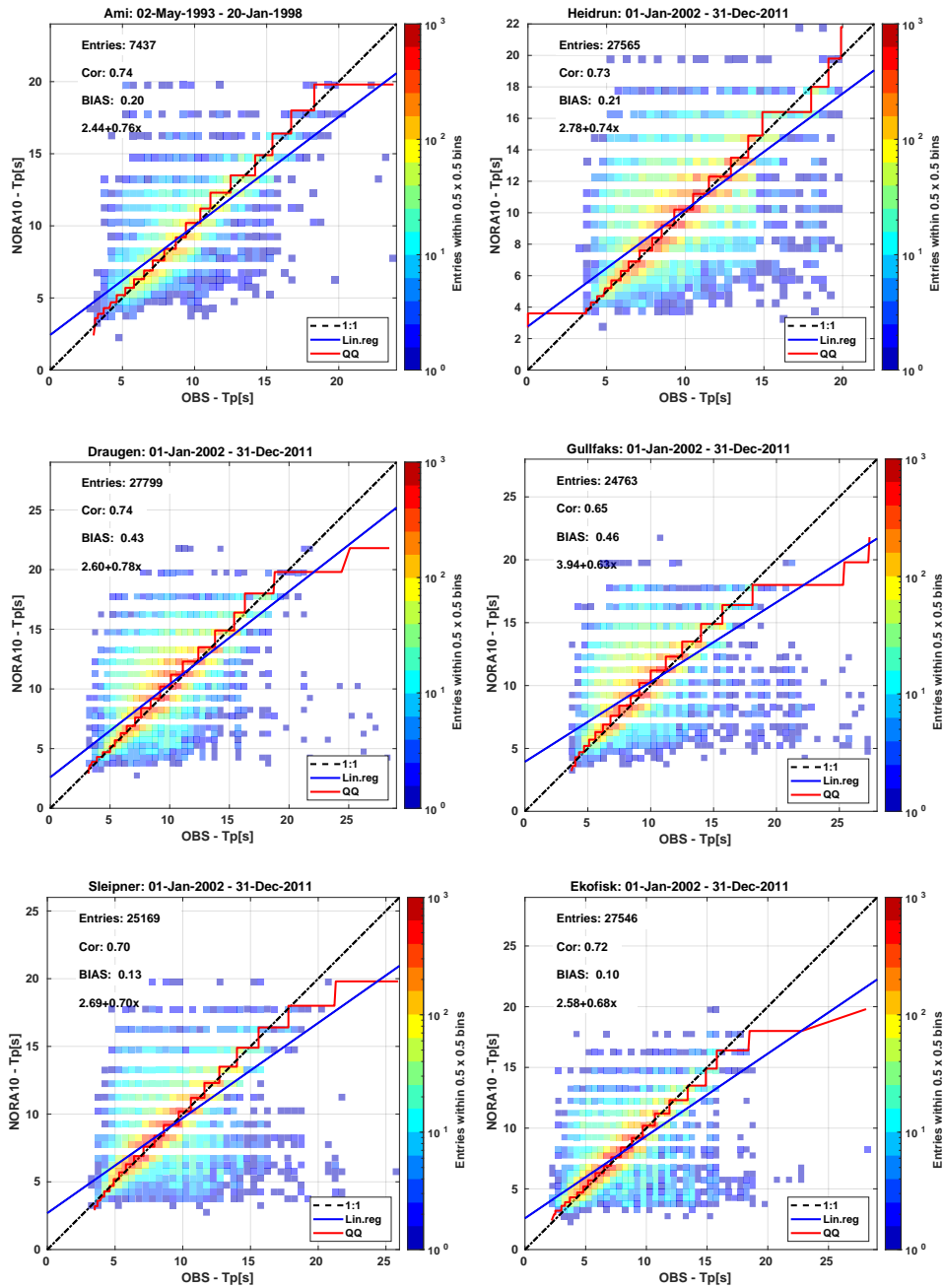


**Figure 114:** Peak period from NORA10 validated against observed  $T_p$  over the period 2002-2011 (Ami: 1993-1998). Observations are based on 20-min periods and retained every three hours, corresponding to the hours of NORA10.

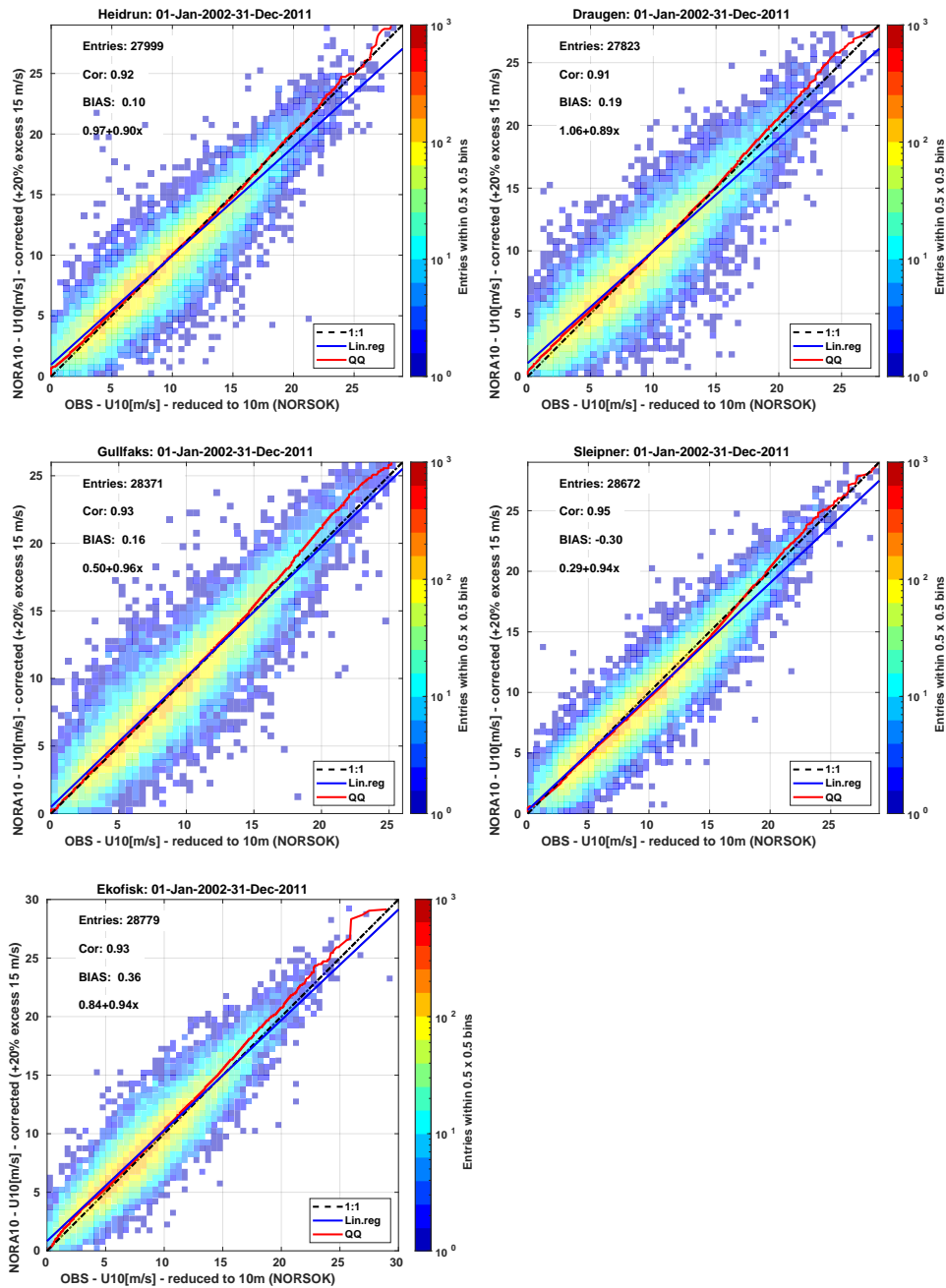


**Figure 115:** Calibrated wind speed from NORA10 validated against observed wind speed reduced to 10 m from rig height. Observed wind speed represents the mean wind condition taken over a 10 minute period and sampled every three hours, at corresponding hours with NORA10.

## References

- O. J. Aarnes, O. Breivik, and M. Reistad. Wave Extremes in the Northeast Atlantic. *Journal of Climate*, 25:1529–1543, 2012. doi: 10.1175/JCLI-D-11-00132.1.
- B. Aune and K. Harstveit. The storm of January 1, 1992. Dnmi report 23/92 klima, The Norwegian Meteorological Institute, 1992.
- K. Christakos. Metocean analysis tools for ferjefri e39 dataset. GitHub, 2020. URL [https://github.com/KonstantinChri/Ferjefri-E39\\_MET-Norway](https://github.com/KonstantinChri/Ferjefri-E39_MET-Norway). Language: Python.
- K. Christakos, B. R. Furevik, O. J. Aarnes, Ø. Breivik, L. Tuomi, and Ø. Byrkjedal. The importance of wind forcing in fjord wave modelling. *Ocean Dynamics*, 70(1):57–75, 2020.
- K. Christakos, J.-V. Björkqvist, L. Tuomi, B. R. Furevik, and Øyvind Breivik. Modelling wave growth in narrow fetch geometries: The white-capping and wind input formulations. *Ocean Modelling*, 157:101730, 2021. ISSN 1463-5003. doi: <https://doi.org/10.1016/j.ocemod.2020.101730>. URL <http://www.sciencedirect.com/science/article/pii/S1463500320302328>.
- S. Coles. *An introduction to Statistical Modelling of Extreme Values*. Springer-Verlag, 2001. doi: 10.1007/978-1-4471-3675-0.
- DNVGL. Recommended Practice DNV-RP-C205. Environmental Conditions and environmental loads. Technical report, Det Norske Veritas, 2017.
- DNVGL. Recommended Practice DNV-RP-C205. Environmental Conditions and environmental loads. Technical report, Det Norske Veritas, 2019.
- B. R. Furevik, L. Lønseth, A. L. Borg, V. Neshaug, and M. Gausen. Oceanographic observations for the coastal highway e39 project in mid-norway, 2016.
- K. Harstveit, H. Ágústsson, R. E. Bredesen, J. Lindvall, B. R. Furevik, O. J. Aarnes, and J. Albretsen. Sulafjorden og vartdalsfjorden, møre og romsdal - analyse av modellert vind, strøm og bølger for 2007 - 2017. Technical Report KVT/KH/2018/R105, Kjeller Vindteknikk, 2018.

- K. Hasselmann, T. Barnett, E. Bouws, H. Carlson, D. Cartwright, K. Enke, J. Ewing, H. Gienapp, D. Hasselmann, P. Kruseman, et al. Measurements of wind-wave growth and swell decay during the joint north sea wave project (jonswap). *Ergänzungsheft* 8-12, 1973.
- G. J. Komen, M. Cavaleri, M. Donelan, K. Hasselmann, S. Hasselmann, and P. A. E. M. Janssen. *Dynamics and Modelling of Ocean Waves*. Cambridge University Press, 1994.
- L. J. Lopatoukhin, V. A. Rozhkov, V. E. Ryabinin, V. R. Swail, A. V. Boukhanovsky, and A. B. Degtyarev. Estimation of extreme wind wave heights. Jcomm tech. rep. 9, Joint WMO/IOC Technical Commission for Oceanography and Marine Meteorology., 2000.
- L. Makkonen. Plotting Positions in Extreme Value Analysis. *J. Appl. Meteor. Climatol.*, 45(2):334–340, Feb. 2006. ISSN 1558-8424. doi: 10.1175/JAM2349.1. URL <http://dx.doi.org/10.1175/JAM2349.1>.
- T. Moan, Z. Gao, and E. Ayala-Uraga. Uncertainty of wave-induced response of marine structures due to long-term variation of extratropical wave conditions. *Marine Structures*, 18(4):359–382, May 2005. ISSN 0951-8339. URL <http://www.sciencedirect.com/science/article/pii/S0951833905000730>.
- O. Musch, A. E. Lothe, and A. Sasikumar. Fjordcrossing e39 data report 6: Sulafjorden, halsafjorden and vartdalsfjorden. Assignment 5185136, doc. nr. 6, version 3, Norconsult AS, 2019.
- M. Reistad, Breivik, and H. Haakenstad. A high-resolution hindcast study for the North Sea, the Norwegian Sea and the Barents Sea. In *Proceedings of the 10th International Workshop on Wave Hindcast and Forcasting and Coastal Hazard Symposium.*, 2007.
- M. Reistad, Øyvind Breivik, H. Haakenstad, O. J. Aarnes, B. R. Furevik, and J.-R. Bidlot. A high-resolution hindcast of wind and waves for The North Sea, The Norwegian Sea and The Barents Sea. *Journal of Geophysical Research, Oceans.*, 116, 2011. doi: 10.1029/2010JC006402. C05019.
- K. Torsethaugen, S. Haver, et al. Simplified double peak spectral model for ocean waves. In *The Fourteenth International Offshore and Polar Engineering Conference*. International Society of Offshore and Polar Engineers, 2004.

S. M. Uppala, P. Kållberg, A. Simmons, U. Andrae, V. Bechtold, M. Fiorino, J. Gibson, J. Haseler, A. Hernandez, G. Kelly, et al. The ERA-40 re-analysis. *Quarterly Journal of the Royal Meteorological Society*, 131(612):2961–3012, 2005. doi: 10.1256/qj.04.176.